Chemical Reaction Dynamics

and

Coincidence Imaging Spectroscopy

by

Anthony M. D. Lee

A thesis submitted to the

Department of Chemistry

in conformity with the requirements for

the degree of Doctor of Philosophy

Queen's University

Kingston, Ontario, Canada

March 2007

Abstract

This thesis describes and develops two experimental techniques, Time Resolved Photoelectron Spectroscopy (TRPES), and Time Resolved Coincidence Imaging Spectroscopy (TRCIS), to study ultrafast gas phase chemical dynamics. We use TRPES to investigate the effects of methyl substitution on the electronic dynamics of the simple α,β-enones acrolein, crotonaldehyde, methylvinylketone, and methacrolein following excitation to the $S_2(\pi\pi^*)$ state. We determine that following excitation, the molecules move rapidly away from the Franck-Condon region reaching a conical intersection promoting relaxation to the $S_1(n\pi^*)$ state. Once on the S_1 surface, the trajectories access another conical intersection leading them to the ground state. Only small variations between molecules are seen in their S_2 decay times. However, the position of methyl group substitution greatly affects the relaxation rate from the S_1 surface. *Ab initio* calculations used to compare the geometries, energies, and topographies of the S_1/S_0 conical intersections of the molecules are not able to explain the variations in relaxation behaviour. We propose a model that uses dynamical factors of specific motions in the molecules to explain the differing nonadiabatic S_1/S_0 crossing rates.

The second part of this thesis examines the issues involved with design and construction of a Coincidence Imaging Spectrometer. This type of spectrometer measures the 3-dimensional velocities of both photoelectrons and photoions generated from probing of laser induced photodissociation reactions. Importantly, the photoelectrons and photoions are measured in coincidence from single molecules, enabling measurements such as recoil frame photoelectron angular distributions and correlated photoelectron/photoion energy maps, inaccessible using existing techniques. How to optimize the spectrometer resolution through design, tuning, and calibration is discussed. The power of TRCIS is demonstrated with the investigation of the photodissociation dynamics of the NO dimer. TRPES experiments first identified a sequential kinetic model following 209nm excitation resulting in NO(X) (ground state) and NO(A) (excited state) products. Using TRCIS, it was possible to measure *time resolved* vibrational energy distributions of the products, indicating the extent of vibrational energy redistribution within the dimers prior to dissociation. Recoil frame photoelectron angular distributions and theoretical support allow identification of a previously disputed intermediate on the dissociation pathway.

keywords: time resolved photoelectron spectroscopy, TRPES, time resolved coincidence imaging spectroscopy, TRCIS, acrolein, crotonaldehyde, methylvinylketone, methacrolein, conical intersection dynamics, $(NO)_2$, nitric oxide dimer

Acknowledgments

First I would like to thank my PhD supervisor, Dr. Albert Stolow for making the work presented in this thesis possible. Throughout my degree, he has been insightful and extremely supportive. His guidance has allowed me to develop both academically and personally. I would also like to thank my co-supervisor Dr. David Wardlaw for help, support, and advice from afar. I thank my supervisory committee Dr. Hans-Peter Loock, and Dr. Natalie Cann, for their roles in helping me complete my degree.

I express much gratitude to my numerous collaborators, with whom I have had the pleasure of working. I would especially like to thank Dr. Carl Hayden, for giving me hands-on experience with his coincidence imaging spectrometer and for happily enduring my relentless pestering about scientific and technical matters. I thank Dr. Oliver Geßner for assistance with the building the spectrometer and our collaborative work on the NO dimer. I am deeply indebted to Allan Horner, Luc Martin, John Hanna, and other machinists at the M36 machine shop at NRC for exceptional workmanship and timely delivery of the spectrometer pieces. I also thank Doug Moffatt and Shutao Li for superb and diligent technical assistance. Many thanks go to Dr. Christer Bisgaard for proofreading large sections of this manuscript. I also acknowledge an unnamed postdoc, without whose bungling of the project I would not have learned so much about building coincidence imaging spectrometers.

On the α, β-enones project, I would like to especially thank Drs. Josh Coe and Todd Martinez and fellow collaborators M. Z. Zgierski, M.-L. Ho, S.-J. Lee, B.-M. Cheng and I-C. Chen for valuable discussions and data contributions. On the NO dimer project, I thank O. Gessner, E. t-H. Chrysostom, C. C. Hayden, J. G. Underwood, H. Reisler, S. V. Levchenko, A. I. Krylov, H. Shi, and A. L. L. East for their valuable contributions to this collaborative effort.

I would like to thank my many friends and co-workers, past and present, at the NRC for making my PhD an enjoyable experience; I regret not being able to list everybody here. A tip o' the hat goes out to fellow graduate students Rune (Fidel) Lausten, Ben 'the Animal' Sussman, Jérôme Levesque, Marc Smits: partners in crime...

A heartfelt thanks goes out to my family and friends, many of whom I have neglected over the past months while writing this thesis. Your patience and support are much appreciated. And finally, I would like to thank my wife Bojana, for encouraging me, keeping me focussed, and for being my Sunce.

This research has been financially supported by the Natural Science and Engineering Research Council (NSERC) Canada and the National Research Council of Canada's Graduate Student Scholarship Supplement Program.

Statement of Originality

This thesis is original and all the ideas and inventions attributed to others have been properly referenced.

Contents

List of Tables

List of Figures

List of Schemes

Glossary

AC Acrolein *Page 11.*

ADC Analog to Digital Converter *Page 129.*

CFD Constant Fraction Discriminator *Page 125.*

CI Conical Intersection *Page 9.*

CR Crotonaldehyde *Page 11.*

DNL Differential Non-Linearity *Page 127.*

DS Doppler Spectroscopy *Page 3.*

FWHM Full Width Half Maximum.

INL Integral Non-Linearity *Page 127.*

IP Ionization Potential. The energy required to remove an electron from the highest occupied molecular orbital to the continuum.

ISC Intersystem Crossing *Page 11.*

IVR Intramolecular Vibrational energy Redistribution *Page 209.*

KER Kinetic Energy Release *Page 3.*

LF-PAD Lab Frame PAD *Page 3.*

MA Methacrloein *Page 11.*

MCP Microchannel Plate. A device in which a high voltage is placed across an array of tiny coated glass channels that causes avalanche amplification of charged particles *Page 65.*

MECI Minimum Energy Conical Intersection *Page 23.*

MVK Methylvinylketone *Page 11.*

PAD Photoelectron Angular Distribution *Page 2.*

PEPICO Photoelectron Photoion Coincidence *Page 4.*

PES Potential Energy Surface *Page 9.*

PTS Photofragment Translational Spectroscopy *Page 3.*

RF-PAD Recoil Frame PAD *Page 6.*

Space Focussing The use of a multi-region spectrometer with appropriate voltages such that the first derivative of the time-of-flight with respect to the position of ionization is zero *Page 59.*

TDC Time to Digital Converter.

TOF Time-Of-Flight *Page 56.*

TRCIS Time Resolved Coincidence Imaging Spectroscopy *Page 3.*

TRPEI Time Resolved Photoelectron Imaging *Page 2.*

TRPES Time Resolved Photoelectron Spectroscopy *Page 1.*

UHV Ultrahigh Vacuum.

VMI Velocity Map Imaging *Page 3.*

XDL Crossed Delay Line *Page 97.*

Chapter 1

Introduction

In studying chemical reaction dynamics, we wish to observe the intricate 'dance' of electrons and nuclei during chemical reactions. Ultrafast lasers, whose pulse durations are on the order of vibrations within molecules, can be used to probe these dynamics [1]. In addition to vibrational motions, nonadiabatic dynamics such as internal conversion occur on this timescale. Fast nonadiabatic dynamics are important in determining the primary steps and branching ratios in many photochemical processes such as photosynthetic bacteria [2], vision [3], and photochemical switches [4]. Here, we use time resolved photoelectron spectroscopy (TRPES) to study ultrafast processes occurring in polyatomic molecules.

TRPES is a well developed technique that uses a pair of short duration laser pulses to first excite molecules, and then probe the excited state dynamics via ionization [5]. Analogous experiments can be performed with negative ions [6]. The energies of the emitted photoelectrons are often measured using time-of-flight 'magnetic-bottle' spectrometers [7] with high detection efficiency. Photoionization is an ideal probing technique because it is always allowed (i.e. there are no dark states), and charged

particle metrology and detection is very sensitive and well developed. By analyzing the kinetic energy spectrum of the photoelectrons, the electronic and vibrational dynamics occurring on the excited potential energy surfaces can be followed. Vibrational wavepacket dynamics are revealed by changes in the Franck-Condon overlap between the excited and ionic states. Changes in the photoelectron spectra can also indicate nonadiabatic electronic state dynamics [8]. An extension of TRPES is to use 2-dimensional imaging detectors to reconstruct the photoelectron angular distributions (PADs) as well as the energy distributions in a technique called time resolved photoelectron imaging (TRPEI) [9, 10, 11]. The more differential information revealed in the PADs can give information about the symmetries of the evolving states [12, 13].

Photodissociation of molecules is another process that can occur on the timescale of a few vibrational periods. In photodissociation reactions that are not direct, there can be a complex series of steps leading to molecular dissociation [14]. In the generic reaction $AB \rightarrow A + B$, we wish to learn about the dynamics (vibrational motions, electronic motions, energy flow) occurring inside the proverbial chemistry 'arrow'. In some cases, TRPES can be used to follow these dynamics from the reactants through to products. However, in large, conformationally floppy, polyatomic molecules, large amplitude motions often result in very broad photoelectron spectra at long time delays that are difficult to interpret. A complementary approach to TRPES is to measure properties of the nascent photodissociation products. Just as in TRPES, these product attributes can be measured as a function of time: the pump pulse starts the chemical process; and the delayed probe pulse ionizes the products formed up to that point in time. The simplest measure is to record the kinetics for the

appearance of the products. Being a highly integrated quantity, the product kinetics are a coarse measure of the dynamics occurring in the molecule. More differential measurements of the product properties can potentially be a more sensitive probe of the photodissociation dynamics. Here we develop a new technique which is capable of accessing existing and new photodissociation product attributes as a function of time. This technique is time resolved coincidence imaging spectroscopy (TRCIS).

Coincidence imaging spectroscopy is an extension of previously developed single particle techniques. Photofragment kinetic energy release (KER) spectra and angular distributions have been obtained using techniques such as Doppler spectroscopy (DS) (for examples see [15, 16, 17]), photofragment translational spectroscopy (PTS) [18, 19, 20], and photofragment imaging [21]. These photofragment energy and angular distributions relate to the shapes of the potential energy surfaces which the molecular trajectories traverse. In the case of DS and PTS, the measured KER spectra and angular distributions are 1-dimensional projections of the 3-dimensional quantities. As such, the data must be fit to retrieve the desired information. Processes resulting in broad spectra or multiple channels can have 1-D profiles that are quite complex, complicating the fitting procedure and introducing ambiguity in the results [22]. Photofragment imaging and its higher resolution progeny velocity map imaging (VMI) [23] use imaging detectors to measure 2-D projections of the photodissociation products. Laboratory frame PADs (LF-PADs) and KER spectra can be reconstructed from the 2-D images using an inverse Abel (or similar) transformation. This image inversion procedure requires cylindrical symmetry about a vector parallel to the face of the detector. To circumvent the need for the 2-D→3-D transformation (that can

introduce noise into the reconstructed image, and restricts the laser polarization geometry), sliced imaging techniques have been developed to extract the central slice of the photofragment distribution [24, 25].

TRCIS is a coincidence imaging technique that measures the full 3-dimensional momenta of photofragments and photoelectrons in coincidence from individual molecules. Specifically we are interested in photodissociation of neutral gas phase polyatomic molecules [26, 27]; similar techniques had been previously developed for looking at anionic photodetachment fragmentation [28, 29], and atomic/diatomic photoionization [30]. In TRCIS, a pair of time and position sensitive detectors are employed, with particle hit position determining two dimensions of the velocities, and time-of-flight determining the third. TRCIS data sets consist not of spectra, but of event pairs of photoelectron and photoion 3-dimensional momenta. From these data events, previously available distributions such as photoelectron spectra, ion kinetic energy release spectra, and lab frame angular distributions can be constructed. Since coincidence imaging spectroscopy uses imaging and timing to measure the 3-D momentum and angular distributions directly, it is unnecessary to fit or transform the data to achieve the desired measurement. Therefore, there are no restrictions on laser polarization schemes, or experimental symmetry conditions. This simplifies the data analysis procedure and allows the opportunity to use any laser polarization geometry.

Correlation of photoelectron spectra with photoion mass has been developed previously and is called photoelectron photoion coincidence (PEPICO) spectroscopy (for example, see [31]). This technique has great applicability in studying neutral cluster photoelectron spectra or electronic dynamics because neutral cluster beams usually contain a large range of cluster sizes. Thus, disentangling photoelectron spectra

according to their mass is essential. One inherent complication incurred by only measuring the mass of the photoion in PEPICO spectroscopy is cluster fragmentation. Weakly bound mass clusters can fragment upon excitation/ionization to create smaller clusters. Therefore, there can be multiple channels leading to the same mass fragment. A similar problem exists in pump-probe photodissociation experiments: a molecule can fragment first, then be ionized; or fragment following ionization, leading to the same photoion. For example, consider the following three processes resulting in the detected mass fragment A^+:

$$\begin{aligned} (1) \qquad & A + h\nu_{pump} \rightarrow A^* \\ & A^* + h\nu_{probe} \rightarrow A^+ + e^-, \end{aligned} \tag{1.1}$$

$$\begin{aligned} (2) \qquad & AB + h\nu_{pump} \rightarrow AB^* \\ & AB^* + h\nu_{probe} \rightarrow A^+ + B + e^-, \end{aligned} \tag{1.2}$$

$$\begin{aligned} (3) \qquad & AB + h\nu_{pump} \rightarrow A + B \\ & A + h\nu_{probe} \rightarrow A^+ + e^-. \end{aligned} \tag{1.3}$$

If correlating the photoelectron only with mass A, the photoelectron energy and angular distributions can be completely overlapping. Coincidence imaging spectroscopy has some ability to distinguish between these reaction channels using photofragment/photoelectron energy correlation maps. In such maps, all data events are histogrammed on a 2-dimensional grid with photofragment KER on one axis and photoelectron energy on the other. A^+ formed by Channel 1.1 is almost completely separable because the A^+ ions are formed without ion recoil velocity, whereas A^+ ions from both Channels 1.2 and 1.3 do have recoil velocity. Separation of A^+ formed by Channels 1.2 and 1.3 is possible if there are distinguishing features in the energy

correlation map identifying the process. For example, in 1.2, the measured photoelectron spectrum is that of AB, whereas in 1.3, it is of A. We deal with this exact problem in the photodissociation of the NO dimer in Chapter 7.

If the axial recoil approximation holds during photodissociation, the coincidence imaging technique allows the determination of the recoil frame PADs (RF-PADs). The photoion emission direction defines the recoil axis alignment, to which the photoelectron emission angle can be measured. RF-PADs contain more information than LF-PADs because they are measured in the reference frame of the photodissociating molecule; they are only averaged azimuthally around the recoil axis. On the other hand, LF-PADs are averaged over all possible orientations. A comparison of molecular frame PADs (MF-PADs) with LF-PADs demonstrates how the richness of PAD structure is lost upon lab frame orientational averaging [32].

Armed with these highly differential product property measurements described above, we hope to gain a greater grasp on the processes occurring during photodissociation reactions. It should be stressed that TRCIS is a time resolved technique, such that all product spectra and distributions can be followed as a function of time. One significant question that we can address is whether products formed at early times during the reaction are identical to those formed at later times, and whether this information allows us to discern the mechanism of photodissociation. Using a combined approach of TRPES to follow initial electronic dynamics, and TRCIS to follow product dynamics, we can now approach the chemistry 'arrow' from both sides.

Thesis Outline

In Chapter 2 we present a TRPES study on the α,β-enones acrolein, crotonaldehyde, methylvinylketone, and methacrolein following excitation to the $S_2(\pi\pi^*)$ state. We are able to follow the rapid relaxation to, and subsequent relaxation from, the $S_1(n\pi^*)$ state. In combination with theoretical results, our experiments suggest that the location of methyl substitution on the α,β-enone backbone strongly affects the dynamics occurring at the S_1/S_0 conical intersection. These experiments demonstrate the importance of dynamical, not just structural factors, in determining reaction branching ratios and relaxation timescales.

In Chapters 3 through 6 we explain the design, construction, calibration of our time resolved coincidence imaging spectrometer apparatus located at the National Research Council's (NRC) Steacie Institute for Molecular Sciences in Ottawa, ON, Canada. Although this spectrometer is not the first of its kind (this credit belongs to C. C. Hayden at Sandia National Laboratories in Livermore, CA, USA [26]), to my knowledge, the intricate workings of this type of spectrometer have not been documented in much detail in the literature. An improvement in the NRC spectrometer is the use of crossed delay line detectors [33], as opposed to the wedge and strip detectors [34] in the Sandia spectrometer. These detectors rely on timing differences rather than charge division to infer the 2-D hit positions. We predict better stability, performance, and ability to screen out stray UV light events using these detectors. We also install a vertically oriented piezoelectrically adjustable slit in the molecular beam path to improve the velocity resolution along the laser propagation direction.

In Chapter 7, we demonstrate the full power of the time resolved spectroscopies described in this thesis to unravel the photodissociation dynamics of the NO dimer.

In this photodissociation, TRPES is able to follow the electronic dynamics all the way from the initially excited molecule to the final products. Analysis of the TRPES results allow determination of the timescales of the steps involved in the transformation to products. We then apply TRCIS to examine the electronic configurations in more detail. Through analysis of the correlated energy maps, we are able to follow the total vibrational energy in the products as a function of time. With time resolved RF-PADs and assistance from theoretical results, we identify the electronic nature of the dissociation pathway. Far from making the earlier TRPES obsolete, this study demonstrates the complementary information that is obtainable using a combined TRPES and TRCIS experimental approach.

Chapter 2

Substituent Effects on Conical Intersection Dynamics: α, β-enones

2.1 Introduction

Conical intersections (CI's) continue to find increasing importance in descriptions of nonadiabatic dynamics in excited states of polyatomic molecules [35, 36, 37]. They can lead to very fast electronic relaxation dynamics (internal conversion) on the femtosecond and picosecond timescales. The literature contains numerous examples where the discovery of a CI in a polyatomic molecule leads to conclusions being drawn about its excited state chemical dynamics and branching ratios. Yet, merely finding a CI does not indicate how or even if a molecular trajectory passes through it.

Consideration of CI's as important features on potential energy surfaces (PES's) is dependent on a number of factors. The first, trivial concern is whether or not the CI is conformationally and energetically accessible from the initially excited state. For CI's that are accessible, the energy of the CI relative to nearby minima is important

because this represents an effective barrier over which the molecular trajectory must pass. Analogous to the behaviour of a barrier in statistical transition state theory, CI's with low barriers generally have faster relaxation rates than those with large barriers. Closely related is the amount of excess energy available to reach the CI. Molecules with large amounts of excess internal energy are expected to have faster nonadiabatic relaxation through CI's than those with little excess energy. The topography (tilt and asymmetry) of the CI is also important. Atchity et al [38] and Yarkony [37] have examined CI's and classified them into two categories: 'peaked' and 'sloped'. Peaked topographies lead to fast internal conversion by funneling the trajectories towards the CI, while trajectories that do make it through sloped topographies are more likely to recross back onto the upper state, leading to slower net internal conversion. Ben-Nun et al. [36] have used this reasoning to explain the selectivity of cis-trans isomerization about the C_{11} double bond versus the C_{13} double bond in retinal. Often overlooked, but arguably equally important to the topographical features of the potential energy surface are dynamical factors affecting excited state trajectories. Just as in the 1-dimensional avoided crossing surface hopping probability analysis of Landau and Zener [39, 40], the velocity of the trajectory near a CI is expected to affect the branching ratio between adiabatic and nonadiabatic dynamics.

Here we investigate the effect of methyl substitution on the timescales of ultrafast non-adiabatic processes in the simplest α,β-enones using time resolved photoelectron spectroscopy (TRPES). We attempt to rationalize the different observed dynamical timescales between the molecules using high level theoretical calculations to analyze the structures and energies of the ground and important excited states. In addition,

we map the topographies of the conical intersections relevant to the dynamics we observe. The ultimate goal of this research is to help develop a theory that incorporates the elements of CI energetics, CI topography, and dynamical factors near CI's, to explain and predict nonadiabatic excited state dynamics in polyatomic molecules.

The α,β-enones contain the conjugated –C=C–C=O chromophore. Unlike the conjugated hydrocarbons, additional excited states exist and different photochemical pathways are available due to the presence of the non-bonding electrons on the oxygen atom. The simplest α,β-enone, acrolein (AC) is an important theoretical system for quantitatively studying configuration interaction with dynamic electron correlation effects. The potential energy surface (PES) landscape of AC is predicted to abound with conical intersections and intersystem crossings (ISC) that control the initial excited state relaxation pathways [41, 42, 43]. We compare the dynamics of AC with its singly methyl-substituted analogs crotonaldehyde (CR), methylvinylketone (MVK), and methacrolein (MA). These molecules are depicted in Figure 2.1.

Figure 2.1: The α, β-enones: acrolein, crotonaldehyde, methylvinylketone, and methacrolein.

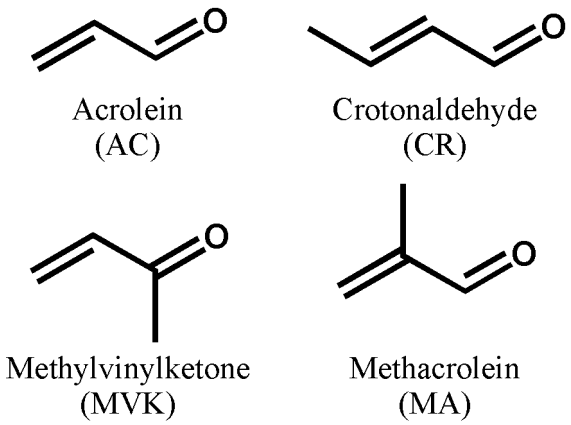

In the ground state, conjugation across the central C–C bond restricts internal rotation and AC is found to have a planar *s-trans* structure at room temperature. A strong, broad electronic transition at 193nm (6.4eV) is attributed to the $S_2(\pi\pi^*)$ state while weak transitions at 387nm (3.2eV) and 412nm (3.0eV) have been assigned to the $S_1(n\pi^*)$ and $T_1(n\pi^*)$ states respectively [44].

The $S_2 \leftarrow S_0$ absorption in AC is qualitatively the transition of an electron from the bonding π orbital to the antibonding π^* orbital. The large orbital overlap between these states results in the large oscillator strength for this transition. A simple molecular orbital analysis indicates this state is biradicaloid in nature with significant bond reversal relative to the ground state, strengthening the central C–C bond, and weakening the C=C and C=O double bonds. Treatment of dynamical electron correlation is important to calculate the vertical excitation energies correctly [45]. Theoretical studies predict that the bond reversal in this excited state results in the minimum energy geometry having the terminal CH_2 group rotated out of plane by approximately 90° [41, 42, 45].

The S_1 electronic state in AC is approximately the ground state configuration with a non-bonding electron on oxygen (n_O) removed and placed in the π^* orbital. The poor overlap between these orbitals of differing symmetry explains why the observed transition is weak. Bond order reversal is expected, although to a lesser extent than in S_2 because only one electron occupies the antibonding π^* orbital whereas two occupy the bonding π orbital. Charge reversal along the C=O bond is also expected with the oxygen becoming more positively charged since the n_O electron nominally residing on oxygen is delocalized into the π-system. Bond length increases of $\sim$0.12Å for the C=C and C=O bonds were observed spectroscopically after excitation to the S_1 state

[46, 47, 44]. Detailed studies of the vibronic spectra of the S_1 state were performed on AC [48, 47, 49, 50], and CR, MVK, and MA [51]. Unlike the other molecules, MA shows richer structure in its S_1 vibronic spectrum due to a series of C=C vibrational bands.

In AC, the ordering of the lowest triplet states ($^3n\pi^*$ and $^3\pi\pi^*$) depends on geometry. For vertical excitation from the ground state, the $^3n\pi^*$ is the lowest state. However, by twisting the terminal CH_2 to $\sim 90^\circ$, the triplet states are nearly degenerate, with the $^3\pi\pi^*$ state slightly lower in energy [45, 42]. The minimum energy conformations of both triplet states lie below the S_1 minimum energy.

At 193nm, the AC S_2 state adiabatically correlates with energetically unavailable, highly excited dissociation products and, therefore, is assumed to rapidly internally convert to the lower lying singlet state, S_1 [52, 42]. Reguerro and coworkers [41] suggest three possible relaxation mechanisms from S_1: internal conversion to S_0 from a $\sim 90^\circ$ twisted S_1 state; fluorescence from the S_1 minimum to the ground state; or inter-system crossing to the triplet manifold, with $T_2(\pi\pi^*) \leftarrow S_1(n\pi^*)$ being the dominant channel according to El-Sayed's Rules [53].

Numerous researchers have performed laser photodissociation experiments at 193nm on AC [52, 54, 55, 56, 57], and CR [58]. Photodissociation experiments near 300nm have also been performed on AC in the gas phase [59], and in argon matrices [60]. Following 193nm photoexcitation to the S_2 state in AC, the main fragmentation

pathways are

$$\begin{aligned} CH_2{=}CH\text{-}CHO &\longrightarrow CH_2{=}CH(X\ ^2A') + HCO(X\ ^2A') && (2.1)\\ &\longrightarrow CH_2{=}CH(X\ ^2A') + HCO(A\ ^2A'') && (2.2)\\ &\longrightarrow CH_2{=}CH\text{-}CO + H && (2.3)\\ &\longrightarrow CH_3CH{=}C{=}O \longrightarrow CH_3CH + CO \\ &\qquad\longrightarrow CH_2{=}CH_2 + CO && (2.4) \end{aligned}$$

The most extensive *ab initio* electronic structure calculations on AC to date have been conducted by Fang[42]. The HCO(X $^2A'$) product channel (2.1) was found to correlate directly with the ground and $^3\pi\pi^*$ states, while the HCO(A $^2A''$) product channel correlates with S_1. However, the HCO(A) state is predissociative on the picosecond time scale [61] and is not easily detectable using laser or mass spectrometric techniques. The molecular CO formation channel (2.4) is believed to occur via a 1,3-H sigmatropic shift on the $^3\pi\pi^*$ surface followed by fragmentation and rearrangement.

2.2 Experimental

2.2.1 VUV absorption spectra

Absolute absorption cross sections of AC, CR, and MA were measured using synchrotron radiation from the HF-CGM beamline at the NSRRC in Hsinchu, Taiwan. This beamline is equipped with a cylindrical grating (600 lines/mm, focal length 6m and variable slit width) for usage in the wavelength range of 105-230nm. A LiF window eliminated short-wavelength, high order light diffracted from the grating. A double beam absorption cell of 8.9cm length simultaneously recorded the incident and

transmitted light intensities to obtain the absorbance. The samples were purified at least twice via vacuum distillation prior to use. The absolute wavelength positions were calibrated with lines of CO, NO and O_2 in the same wavelength region.

The UV absorption spectra of AC, CR, and MA are shown in Figure 2.2. The UV absorption spectrum of MVK has been reported previously [62, 63]. AC was measured with 0.1nm resolution between 223-177nm and 0.02nm between 177-105nm. CR was measured with 0.1nm resolution between 230-184.5nm and 0.02nm between 184.5-105nm. MA was measured with 0.1nm resolution between 230-190nm, 0.02nm resolution between 190-129nm, and 0.05nm resolution between 129-105nm. The broad, featureless absorption band of the S_2 state can been seen near 200 nm in all cases. The excitation wavelengths used in the time resolved experiments (200nm and 209nm) are indicated by dotted lines in the figures.

2.2.2 Time Resolved Photoelectron Spectroscopy

We briefly describe our femtosecond time resolved magnetic bottle photoelectron spectrometer experiments, detailed elsewhere [64]. Harmonic generation of an amplified femtosecond Ti:sapphire system was used to produce pump and probe laser pulses for two complete sets of experiments: one using 209nm pump and 279nm probe pulses; the other using 200nm pump and 267nm probe pulses. The UV pulses were individually recompressed using CaF_2 prism pairs, combined collinearly, and then gently focussed using $f/80$ spherical reflective optics to intersect a seeded molecular beam in the interaction region of a magnetic bottle spectrometer. Time delays between pump and probe pulses were scanned using a computer controlled stepper motor in 25fs steps. Typically, pump pulse energies were $\sim$100nJ, and probe pulse energies were

Figure 2.2: Absolute UV absorption cross sections of acrolein, crotonaldehyde, and methacrolein measured with synchrotron radiation. Acrolein was measured with 0.1nm resolution between 223-177nm and 0.02nm between 177-105nm. Crotonaldehyde was measured with 0.1nm resolution between 230-184.5nm and 0.02nm between 184.5-105nm. Methacrolein was measured with 0.1nm resolution between 230-190nm, 0.02nm resolution between 190-129nm, and 0.05nm resolution between 129-105nm. The excitation wavelengths (200nm and 209nm) used in the time resolved photoelectron experiments are indicated by dotted lines.

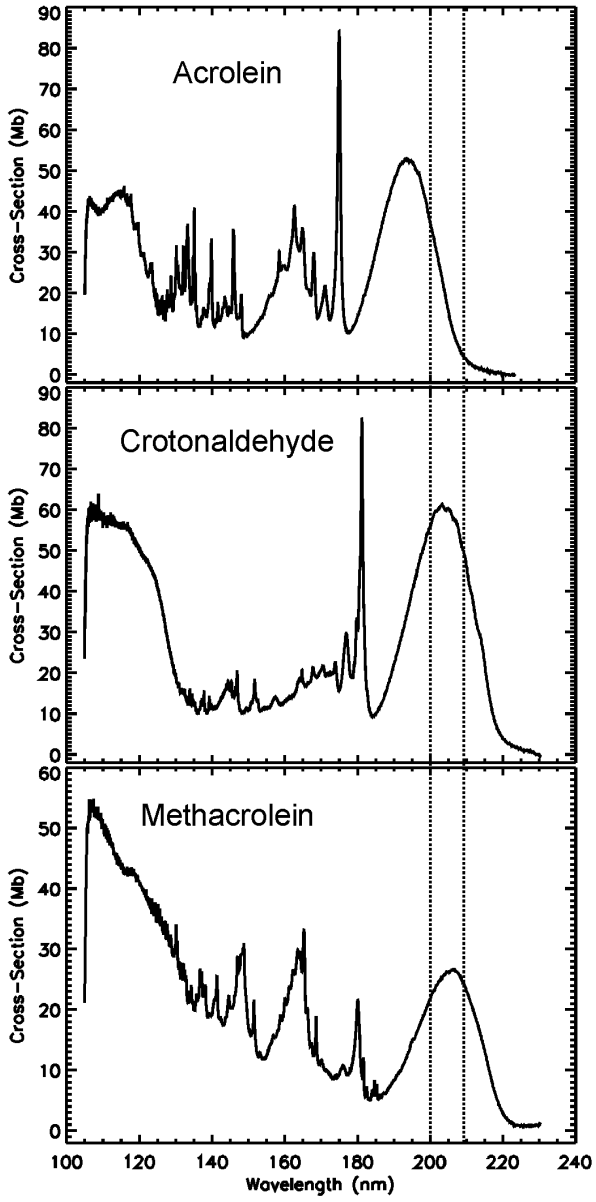

$\sim$2.5μJ. Supersonic molecular beams of AC, CR, MVK, and MA were made by bubbling helium through the respective neat liquid. The liquids were pre-cooled in a temperature controlled bath in order to choose a desired vapour pressure. The 200nm or 209nm pump pulse excited the molecules from their S_0 ground state into their $S_2(\pi\pi^*)$ excited state. The delayed 267nm or 279nm probe pulse produced photoelectrons via one- and/or two- photon ionization of the excited molecule. Photoelectron spectra arising from the pump laser alone and probe laser alone were subtracted to correct for background photoelectrons generated from single-colour multiphoton ionization. For each particular molecule, the pump-probe time delays were scanned back and forth multiple times to minimize any effects of temporal and/or spatial laser drift.

The electron kinetic energy calibration and time zero overlap of the two laser pulses were achieved using the well characterized 1+1' photoionization of nitric oxide. Measured 1+1' pump-probe cross correlations (*i.e.* instrumental response or time resolution) ranged between 150fs and 170fs. The energy and time calibration scans were performed both before and after each experiment.

Single colour multi-photon photoelectron spectra at 209nm (2×5.93eV = 11.86eV), 200nm (2×6.2eV = 12.4eV), 279nm (3×4.44eV = 13.32eV), and 267nm (3×4.65eV = 13.95eV) for AC, CR, MVK, and MA are shown in Figures 2.3-2.6 respectively. As determined by He(I) photoelectron spectroscopy, the n-hole and π-hole ionization energies for the molecules are [65]: AC (10.11eV, 10.93eV); CR (9.75eV, 10.20eV); MVK (9.66eV, 10.53eV); and MA (9.92eV, 10.38eV). Due to the resonant nature of the multiphoton ionization process (1+1 for 209nm/200nm and 2+1 for 279nm/267nm), bands are present in the 11-12eV region not seen previously in the one photon He(I) spectra [65, 66, 67]. The shapes of the spectra from our experiments are determined

by fast dynamics of the molecules occurring within the duration of the laser pulses. Rapid, large amplitude motions of the molecules allow ionization to ionic states with geometries different from the ground state. Ionic state energies ($D_0 \ldots D_4$) calculated at the TD/B3LYP/cc-pvdz level of theory using D_0 optimized geometries are shown in Table 2.1. The ordering of the ionization energies is predicted correctly when compared to experiment. The presence of ionic states in the 11-12eV region agrees well with our measured photoelectron spectra.

Table 2.1: Energies of ionic states optimized at the D_0 geometry using TD/B3LYP/cc-pvdz level of theory. Values obtained from the literature for He(I) photoionization are shown in parentheses [65]. The energies are reported in eV and are relative to the neutral ground state.

State	Acrolein	Crotonaldehyde	Methylvinylketone	Methacrolein
D_0	9.78 (10.11)	9.29 (9.75)	9.26 (9.66)	9.56 (9.92)
D_1	10.62 (10.93)	9.78 (10.20)	10.28 (10.53)	9.93 (10.38)
D_2	12.84	12.37	12.40	12.28
D_3	13.46	12.49	12.84	12.31
D_4	13.80	13.09	12.50	12.63

2.2.3 *Ab Initio* Calculations

Excited state geometries were optimized using the complete active space self-consistent field (CASSCF) [68] method with a (6,5) active space. To optimize the states in an equivalent manner, the orbitals were optimized to yield the lowest average energy for the first three singlet states, using the state-averaged [69] approach (SA3-CAS). Ground state geometries were minimized at the MP2 level. All calculations employed a 6-31G* basis set and were performed with the MolPro suite [70].

The optimized geometries for the S_0 minimum, the S_1 minimum, and the minimum

Figure 2.3: Multiphoton photoionization spectra of acrolein. The energy axis is labeled for 2-photon ionization at 200nm and 209nm, and 3-photon ionization at 267nm and 279nm. The He(I) photoionization energies from the n and π orbitals are indicated with vertical lines.

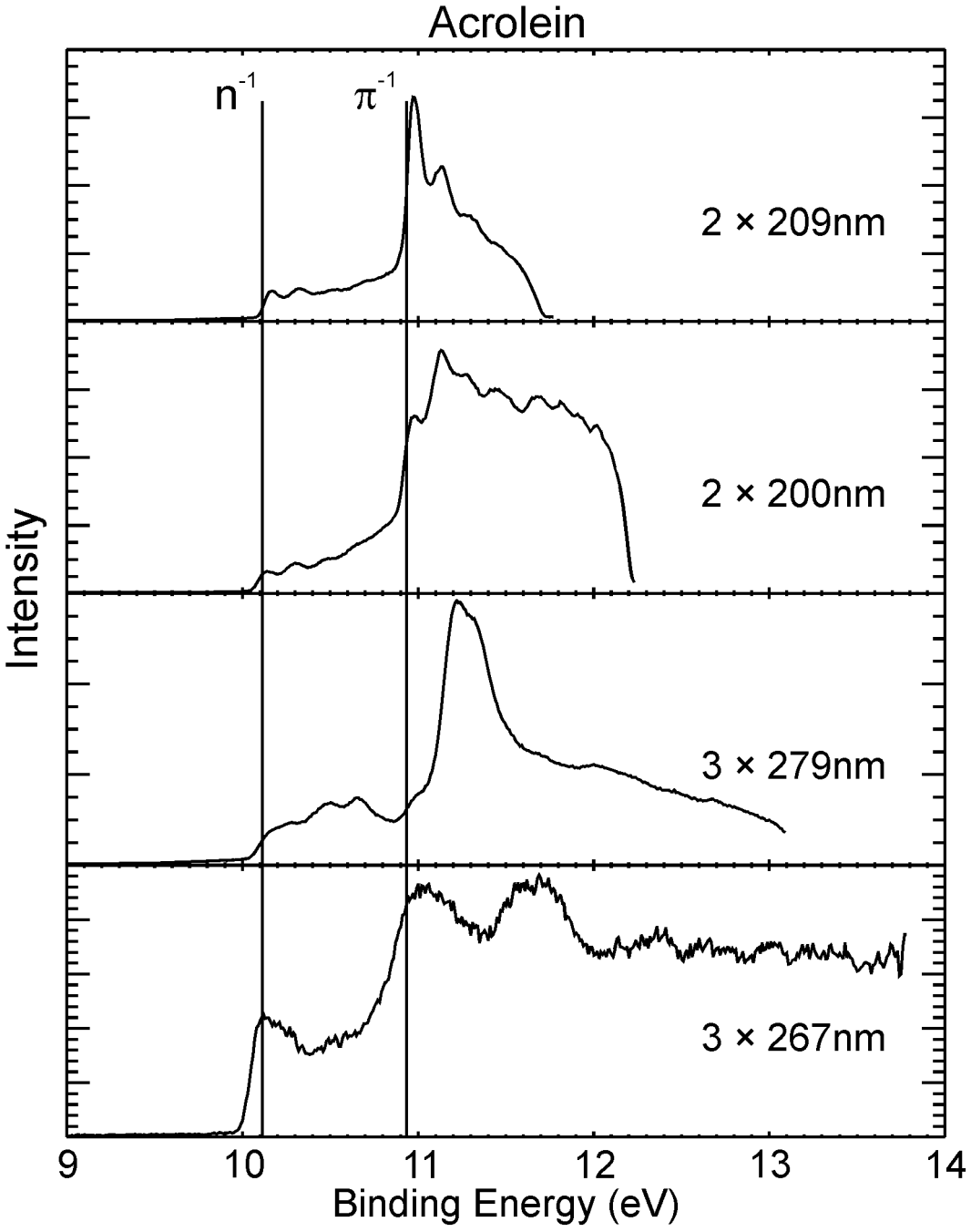

Figure 2.4: Multiphoton photoionization spectra of crotonaldehyde. The energy axis is labeled for 2-photon ionization at 200nm and 209nm, and 3-photon ionization at 267nm and 279nm. The He(I) photoionization energies from the n and π orbitals are indicated with vertical lines.

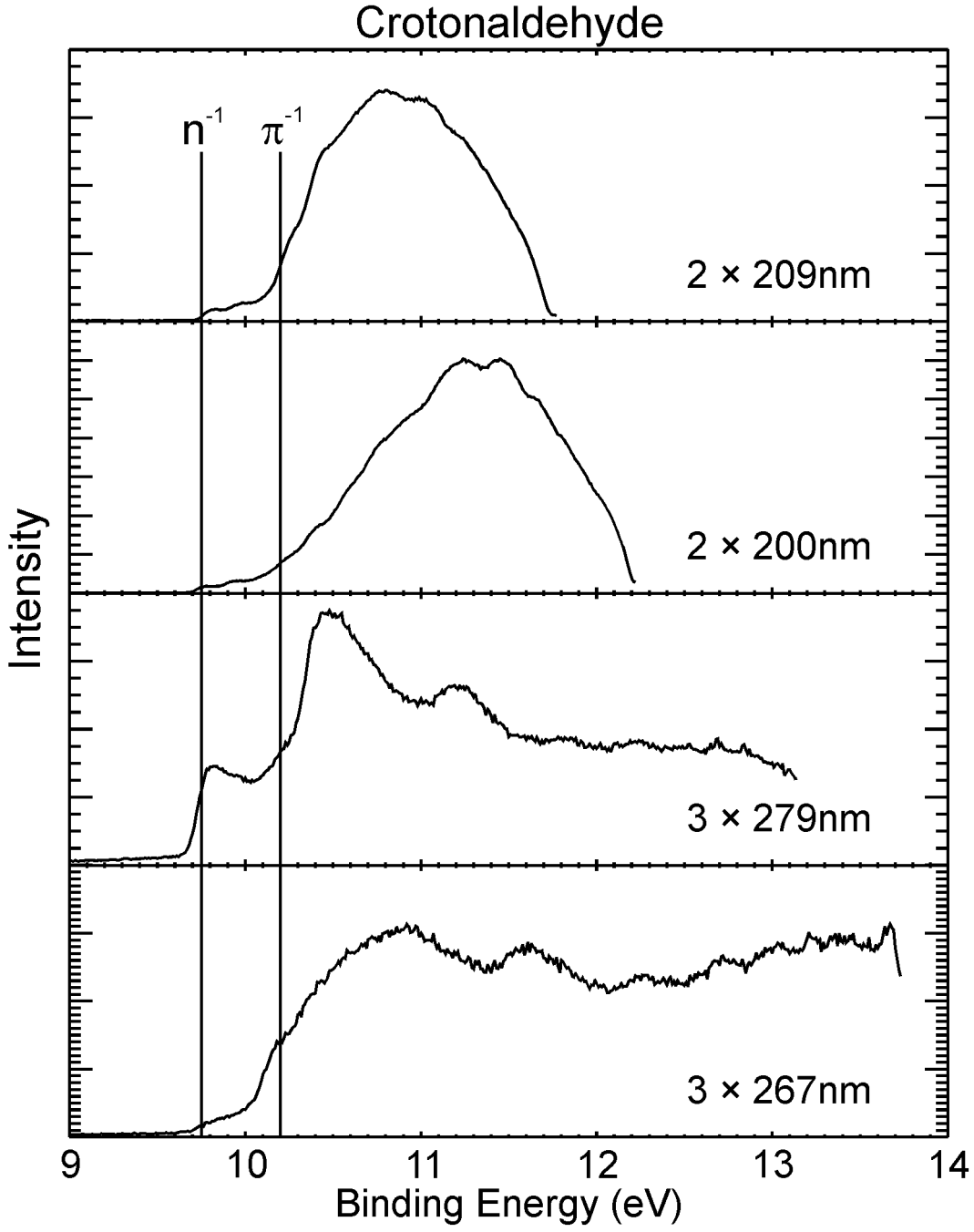

Figure 2.5: Multiphoton photoionization spectra of methylvinylketone. The energy axis is labeled for 2-photon ionization at 200nm and 209nm, and 3-photon ionization at 267nm and 279nm. The He(I) photoionization energies from the n and π orbitals are indicated with vertical lines.

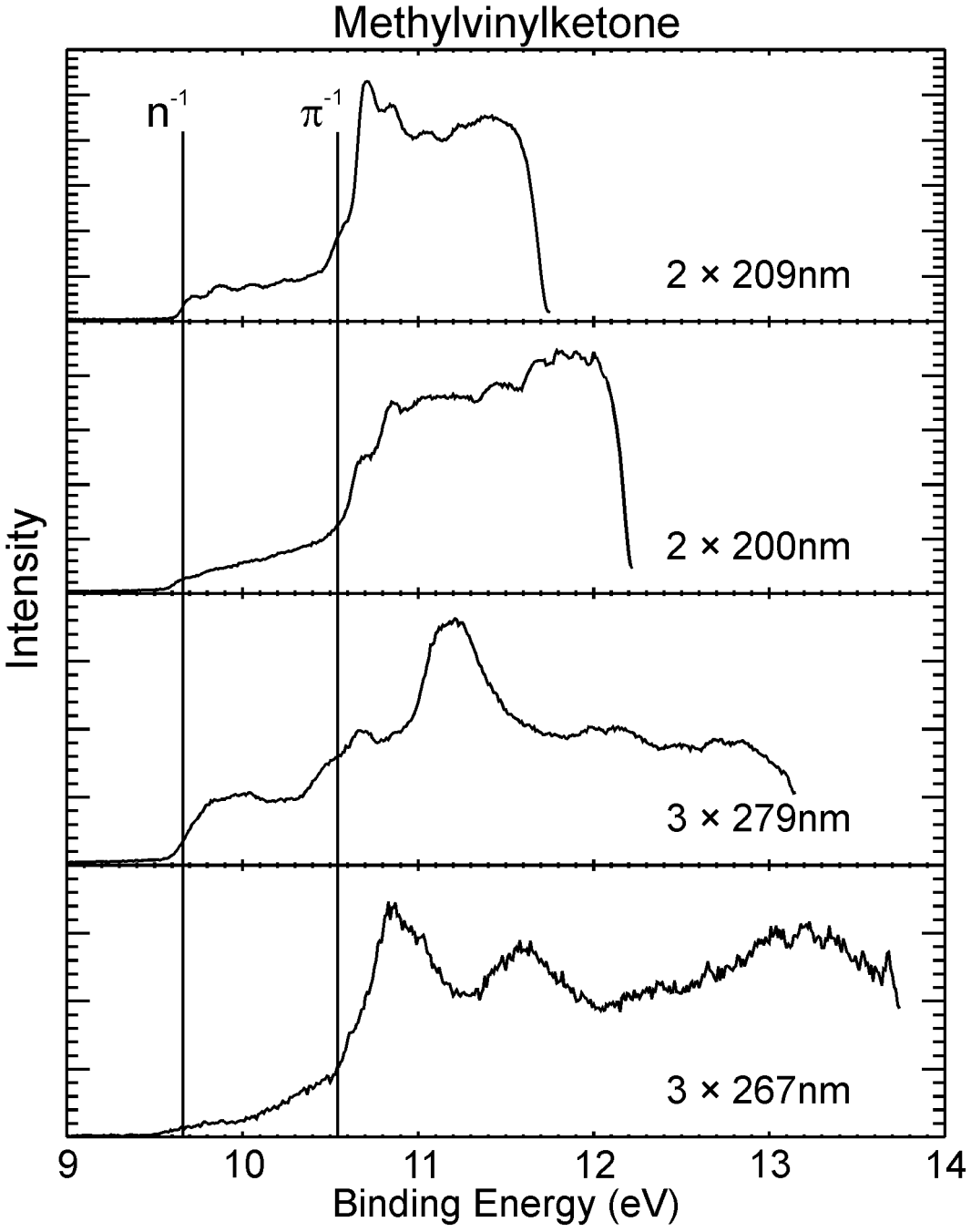

Figure 2.6: Multiphoton photoionization spectra of methacrolein. The energy axis is labeled for 2-photon ionization at 200nm and 209nm, and 3-photon ionization at 267nm and 279nm. The He(I) photoionization energies from the n and π orbitals are indicated with vertical lines.

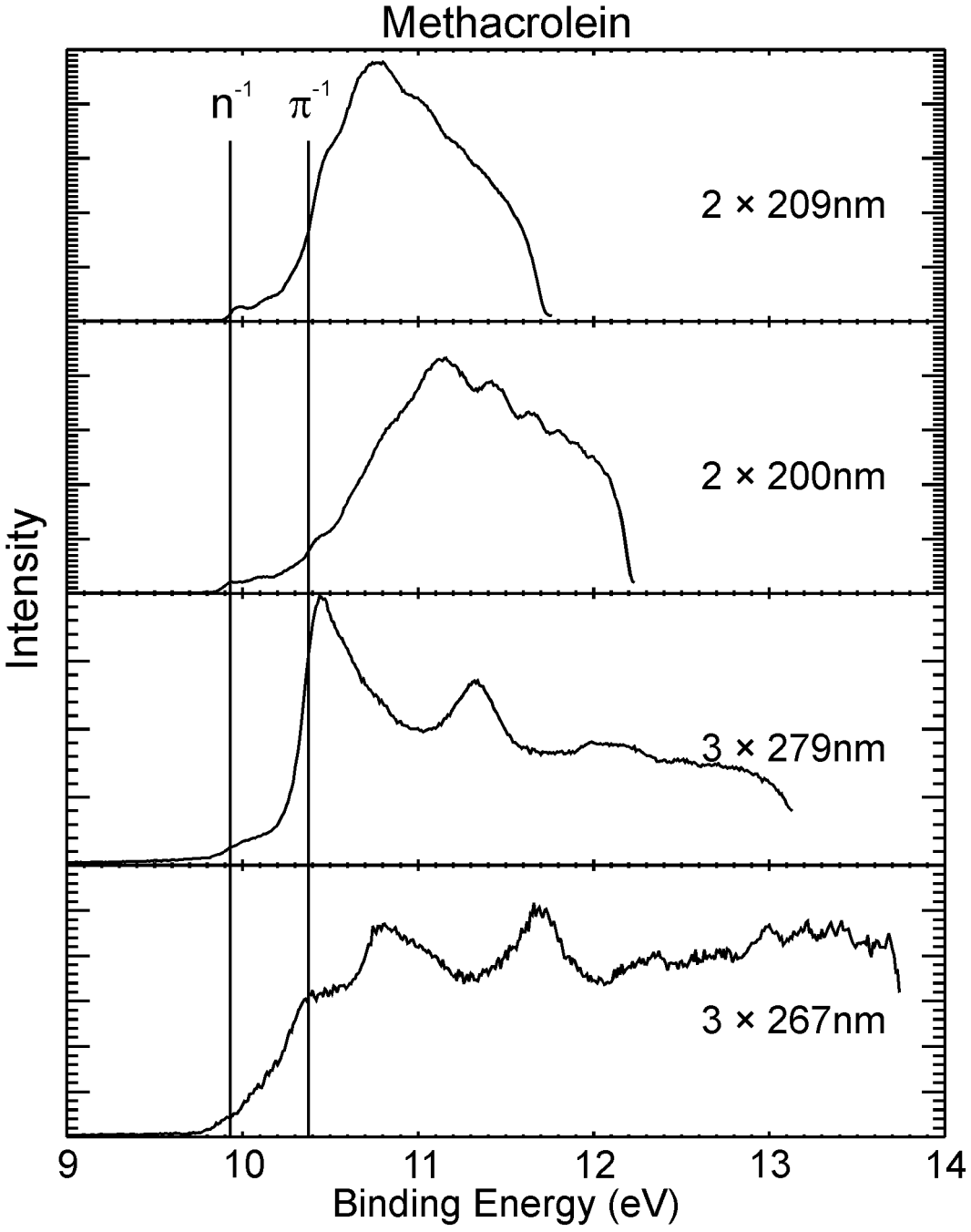

energy conical intersections (MECI) points connecting S_2 with S_1, and S_1 with S_0 are shown in Figures 2.7 through 2.10 respectively. The energies of these structures are shown in Table 2.2. Attempts to locate a true minimum with all real vibrational frequencies on S_2 were unsuccessful. Bond alternation progresses smoothly from C=C–C=O at the S_2 FC point, to a resonant pattern in which all three bond lengths are roughly equal at the S_1 minimum, to full reversal as C–C=C–O at the S_1/S_0 MECI.

With the exception of the S_2/S_1 MECIs, the four molecules have very similar geometries at the ground state (S_0) minimum, the S_1 minimum, and the S_1/S_0 MECI's. All are planar at the S_0 and S_1 minima, but twisted and pyramidalized to roughly the same degree at the S_1/S_0 MECI. Pyramidalization is a common feature of intersection geometries [36, 71, 72]. The pyramidalization angles indicated in Figure 2.10 are defined as:

$$\tau_{pyr} = \cos^{-1}\left(\left(\mathbf{e}_{C_pR_1} \times \mathbf{e}_{C_pR_2}\right) \cdot \mathbf{e}_{C_pC_2}\right) - \frac{\pi}{2} \tag{2.5}$$

where unit vectors pointing along a bond from atom A to atom B are denoted by $\mathbf{e}_{AB}$. The S_2/S_1 MECI geometries vary to a slightly larger extent than the other points, but all are twisted along the CCC backbone.

2.3 Results and Discussion

Excerpts from the time-resolved photoelectron scans at selected pump-probe time delays are shown in Figures 2.11 and 2.12. Each time delay in the plot is offset vertically downwards as pump probe time delay increases. The scans start from 0.2eV because the magnetic bottle transmission below this energy is unreliable.

Figure 2.7: MP2/6-31G* S_0 minima structures of the α,β-enones studied here.

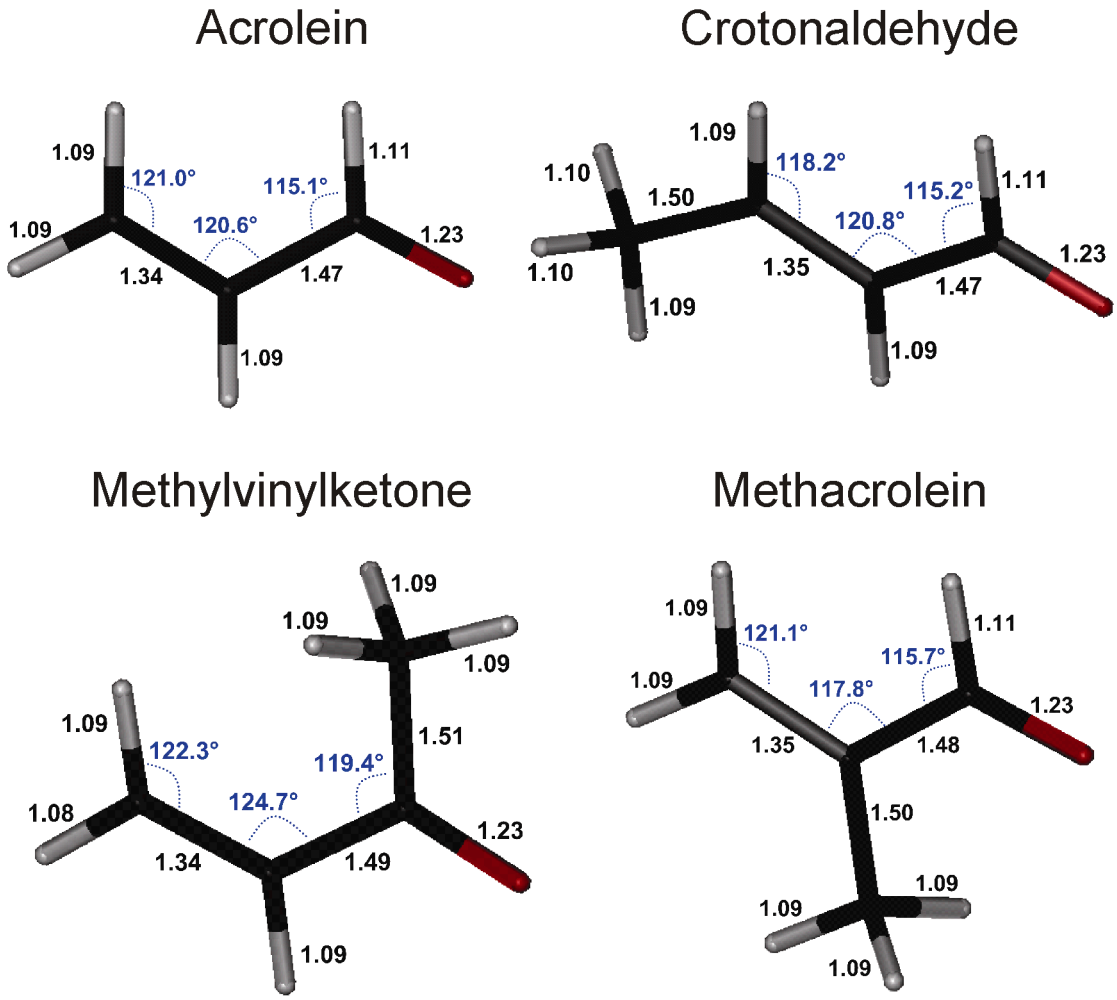

Figure 2.8: CASSCF(6,5) 6-31G* optimized $S_1(n\pi^*)$ minima geometries of the α,β-enones. Apart from the methyl groups, all of the structures are planar.

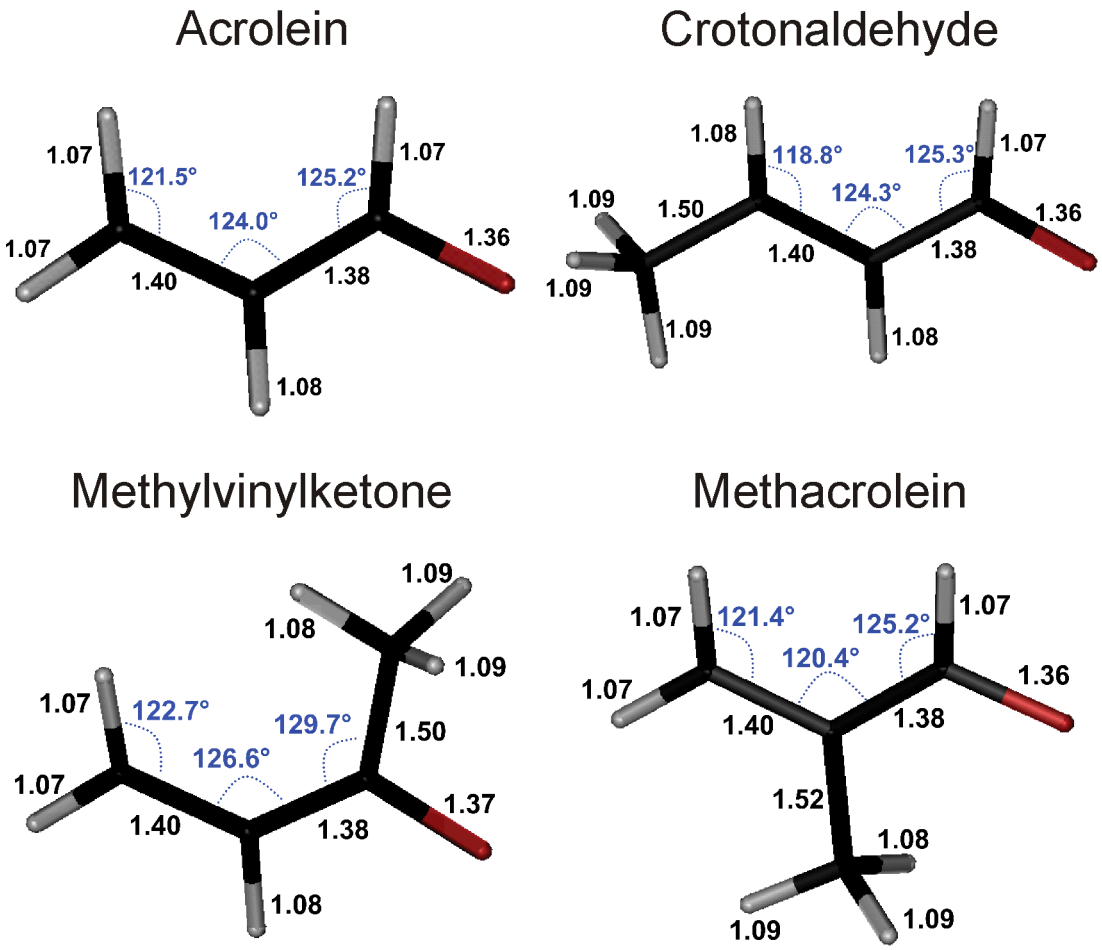

Figure 2.9: SA3-CAS(6,5)/6-31G* S_2/S_1 minimum energy conical intersection structures for the α,β-enones studied here. All four molecules are twisted about both CC bonds of the molecular backbone.

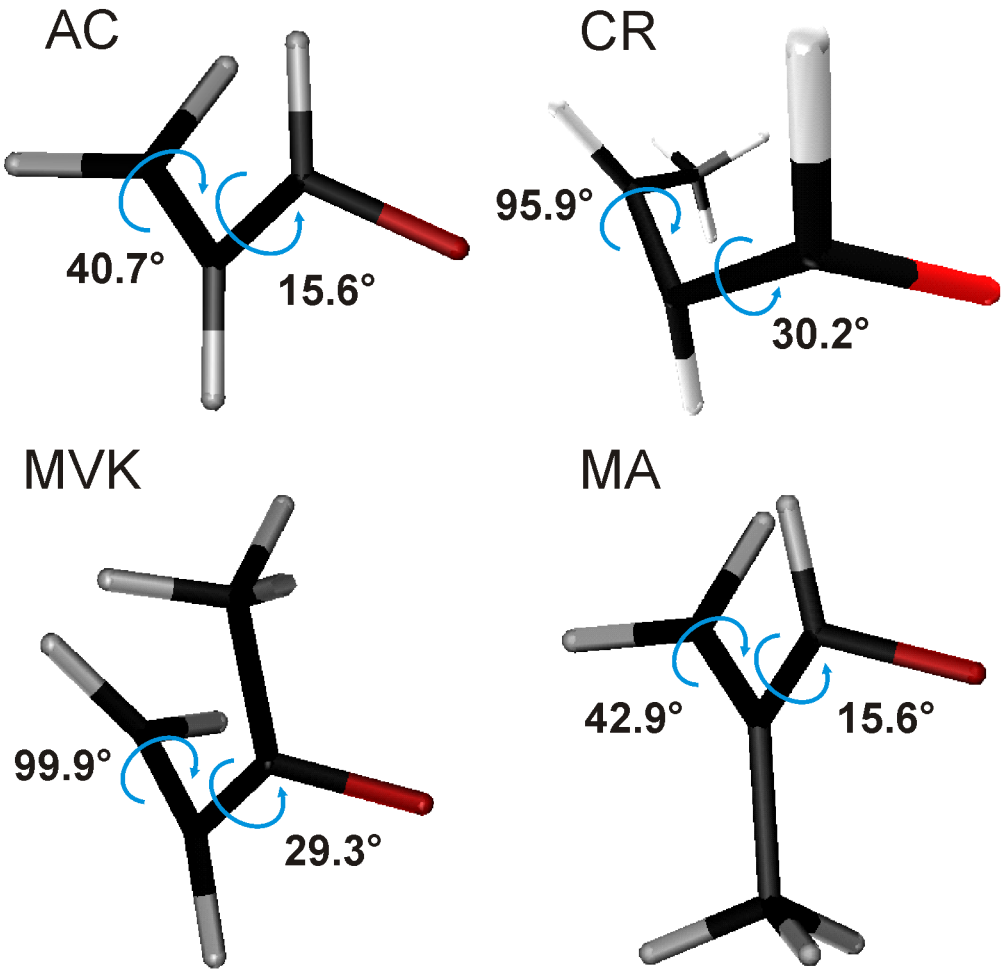

Figure 2.10: SA3-CAS(6,5)/6-31G* S_1/S_0 minimum energy conical intersection structures for the α,β-enones studied here. Structures are twisted 90° about the nominally C=C bond and the terminal carbon is slightly pyramidalized in all four cases. The pyramidalization angle τ_{pyr} is explicitly defined in the text.

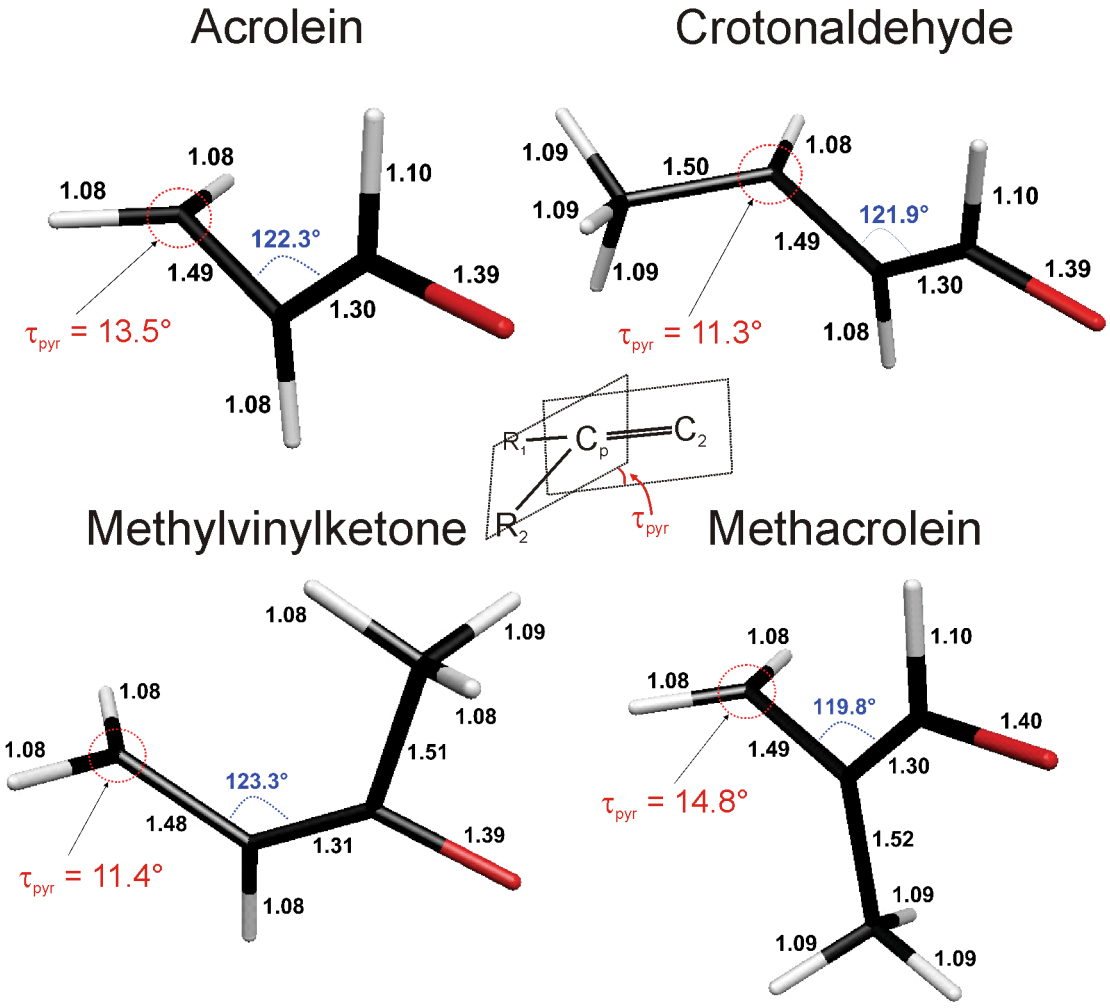

Figure 2.11: Selected time dependent photoelectron spectra for acrolein, crotonaldehyde, methylvinylketone, and methacrolein using 209nm pump and 279nm probe. Each time spectrum is offset downwards with increasing time delay. The 1+1' n-hole ionization energies are shown as dotted vertical lines.

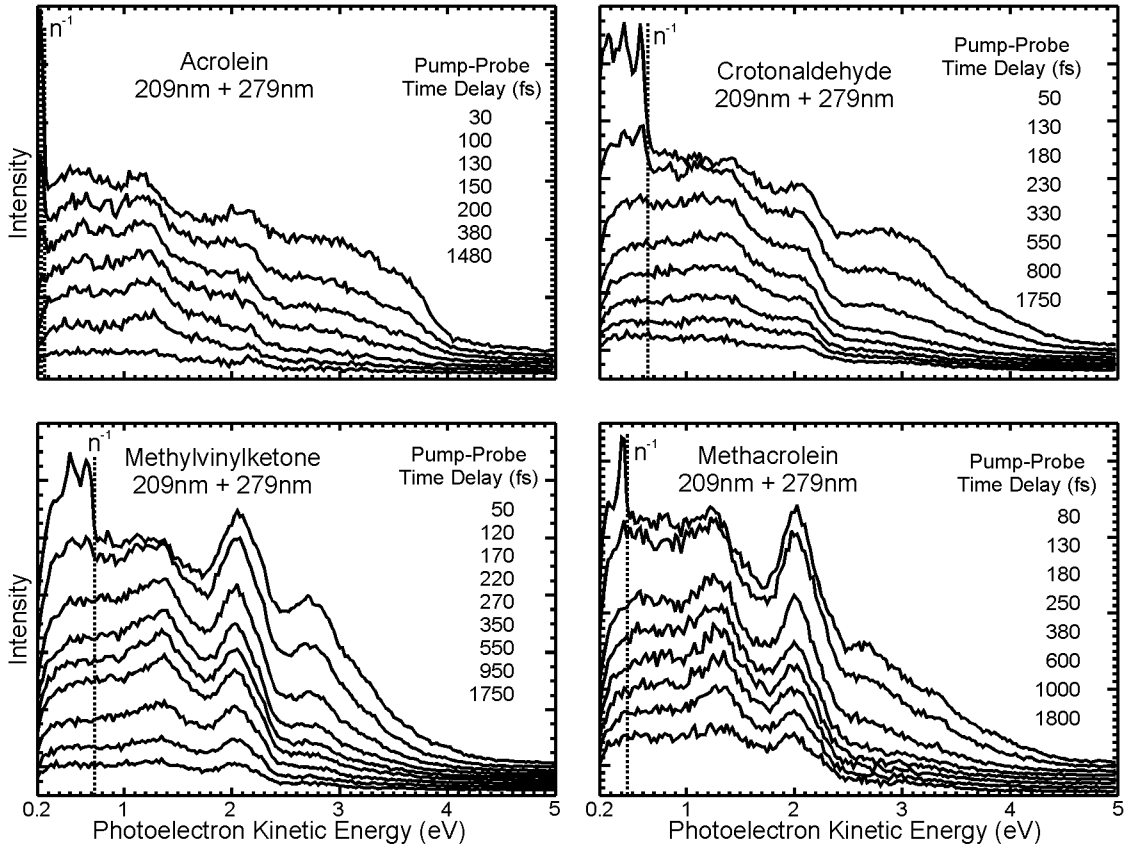

Figure 2.12: Selected time dependent photoelectron spectra for acrolein, crotonaldehyde, methylvinylketone, and methacrolein using 200nm pump and 267nm probe. Each time spectrum is offset downwards with increasing time delay. The 1+1' n-hole and π-hole ionization energies are shown as dotted vertical lines.

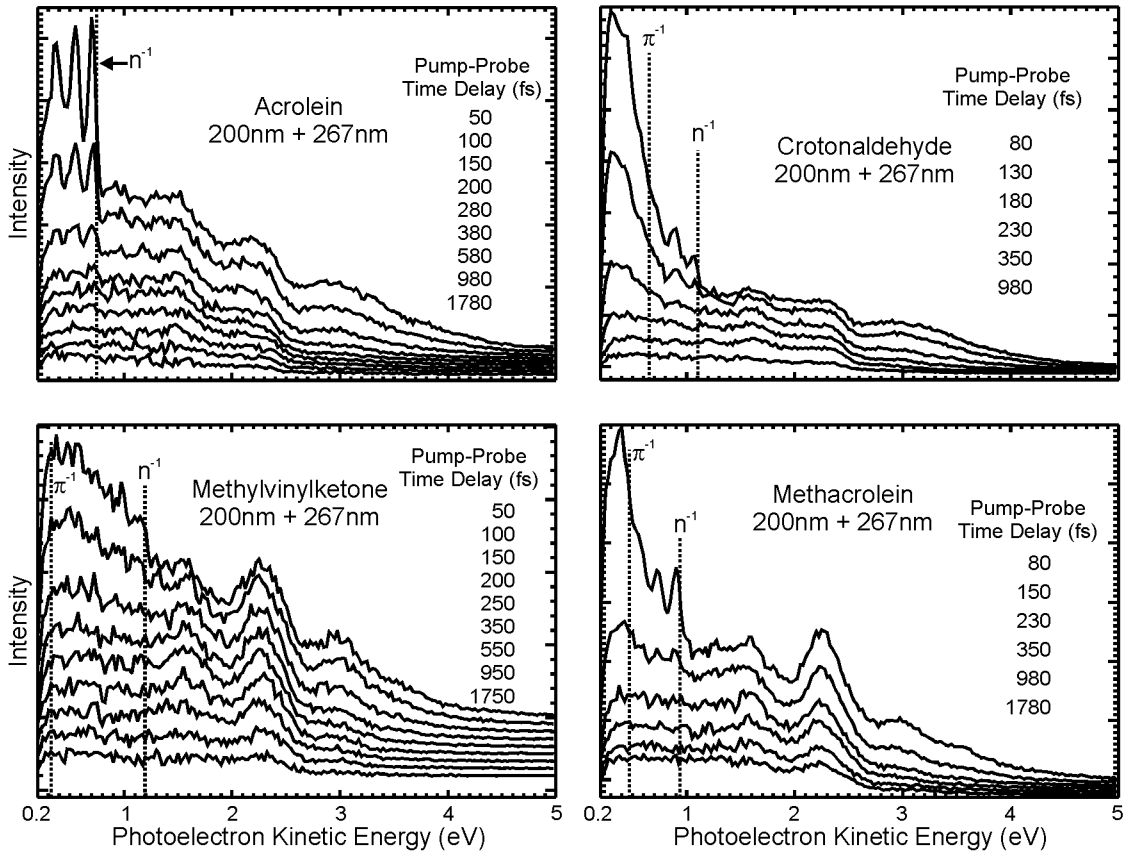

Table 2.2: SA3-CAS(6,5)/6-31G* calculated energies for the Franck-Condon vertical excitation to S_2 (S_2 FC), the S_2/S_1 MECI (minimum energy conical intersection), the S_1 minimum, and the S_1/S_0 MECI, of the α,β-enones examined in the text. All energies are relative to the ground state and reported in eV.

	S_2 FC	S_2/S_1 MECI	S_1 min	S_1/S_0 MECI
AC	7.55	5.91	2.96	3.94
CR	6.92	5.51	2.90	3.89
MVK	6.98	5.52	2.93	3.75
MA	6.96	5.29	2.98	3.80

For the 209nm + 279nm experiments, the 1+1' and 1+2' total photon energies are 10.38eV and 14.81eV, respectively. Likewise, for the 200nm + 267nm experiments, the total photon energies are 10.85eV and 15.50eV. Thus, there are two regions in the photoelectron spectra, resulting from ionization via these two processes. In the low electron kinetic energy region of the spectra, photoelectrons are produced from both types of pump-probe processes: single photon ionization of the excited states by the probe laser (1+1'); and two photon ionization by the probe laser (1+2'). In the high electron kinetic energy region of the spectra, all photoelectrons result from 1+2' ionization.

As a first step in the analysis, the photoelectron energy / time delay scans were sliced into 0.025eV bins to yield time dependent transients. Each time transient was fit using an exponential kinetic model convoluted with the appropriate Gaussian instrumental response function. In the 1+1' region, the instrumental response was taken to be the Gaussian fit of the measured NO 1+1' cross correlation with FWHM $\tau_{1+1'}$. In the 1+2' region of the spectra, the pump and probe laser pulses were assumed to be of the same duration such that the 1+2' instrumental response $\tau_{1+2'}$ could be

calculated using $\tau_{1+2'} = \tau_{1+1'} \times \sqrt{3}/2$.

The time constants and spectral amplitudes were varied to minimize the weighted χ^2 value of the fit to the data. Initially, the time constants were allowed to vary independently from slice to slice. In all slices, for all molecules, it was found that the simplest model to fit all the time transients reasonably was one which contained 4 components. One component, referred to here as X, was only present during the cross correlation of the two laser pulses. The other 3 components were fit according to a sequential decay kinetic model in which an immediately prepared component A, decayed with time constant t_1 to an intermediate component I, which in turn decayed with time constant t_2 to a long-lived component P.

AC, MVK, and MA were found to have t_2 values approximately constant across the entire photoelectron spectrum using both excitation/probing schemes. To fit t_2 more accurately for these molecules, photoelectron spectra at short pump-probe delay times were removed to yield time transients consisting of only the I and P components. A global fitting procedure then was used in which t_2 was optimized but held constant across the entire spectrum. The complete time transient was then re-fit with all components (X, A, I, P), this time holding t_2 constant at the value from the previous analysis step. In contrast to the fitting of t_2, t_1 was found to vary across the spectrum for all molecules. This is indicative of large amplitude motion occurring on this timescale. Nevertheless, in sub-regions of the spectra, the t_1 values were found to be relatively constant. In these sub-regions, each roughly encompassing broad spectral features, the time transients were co-added and the resulting transient was fit once again for t_1 and the spectral amplitude. An example of one of the fits, for AC, is shown in Figure 2.13.

Figure 2.13: Example fit of acrolein 209nm pump/279nm probe data between 1.5eV and 2.5eV using a 4 component sequential model: an instrumental response component X, an immediately excited species A, which decays to an intermediate I, which in turn decays to a product P. The decay times of the A and I components are 65fs and 900fs respectively.

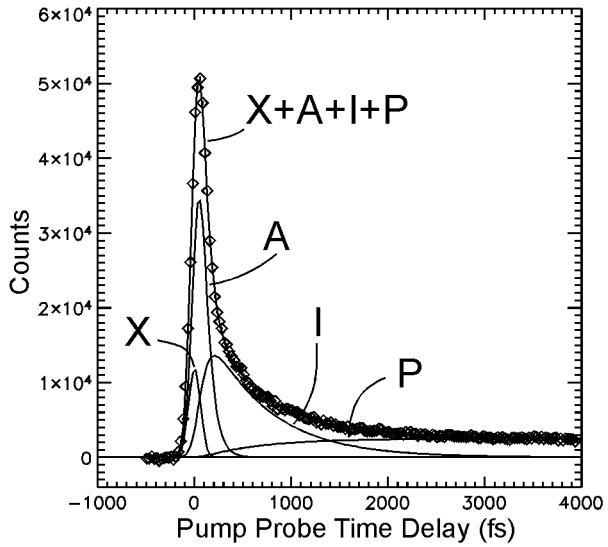

For CR, the dynamics were sufficiently fast such that the time transients could not be fit with time constants in the piecewise fashion described above for the other molecules. In addition, both t_1 and t_2 were found to vary across the photoelectron spectrum so no global fitting procedure could be applied, indicating that CR in some way behaves differently from the other molecules. The full energy range was divided into 3 sub-regions where t_1 and t_2 were approximately constant. Within these regions, the spectral slices were co-added and the integrated transient was fit again for t_1, t_2, and the spectral amplitudes.

The time constants and spectral amplitudes for all molecules are summarized in Tables 2.3 (209nm pump/279nm probe) and 2.4 (200nm pump/267nm probe). The spectral amplitudes are determined such that direct comparisons should only be

made for individual species across the different energy regions, not between species within a single energy region. The time constants for t_1 are comparable or shorter than the instrumental response yet are still easily observed and fit as seen in Figure 2.13. Uncertainty in the pump-probe overlap time and limitations in the Gaussian instrumental response function approximation results in large error bars for the values of t_1.

Table 2.3: Time constants and normalized spectral amplitudes for time dependent photoelectron spectra of acrolein, crotonaldehyde, methylvinylketone, and methacrolein using 209nm pump and 279nm probe wavelengths. The model used to fit the spectra consisted of a cross correlation response X, an immediately excited species A, that decays with time constant t_1 to intermediate I, which in turn decays with time constant t_2 to product P. The spectral amplitudes are determined such that direct comparisons should only be made for individual species across the different energy regions, not between the species within a single energy region.

Molecule	Energy Range (eV)	t_1 (fs)	t_2 (fs)	Normalized Spectral Amplitudes				
				X	A	I	P	A/I
Acrolein	0.23 - 0.28	90 ± 20	900 ± 100	4600	25.	4.6	1.2	5.4
	0.28 - 1.5	100 ± 20		1300	35.	7.0	1.4	5.0
	1.5 - 2.5	65 ± 25		980	36.	4.0	0.80	9.0
	2.5 - 5.0	45 ± 25		550	19.	0.58	0.16	32.
Croton-aldehyde	0.25 - 0.65	70 ± 30	380 ± 50	5100	120	36.	9.7	3.4
	0.65 - 2.4	90 ± 30	500 ± 70	1100	93.	29.	6.8	3.3
	2.4 - 5.0	50 ± 15	360 ± 50	520	49.	3.4	1.2	15.
Methylvinyl-ketone	0.30 - 0.73	170 ± 20	1080 ± 80	4300	93.	18.	3.2	5.0
	0.73 - 1.7	190 ± 30		1200	94.	21.	2.7	4.6
	1.7 - 2.6	140 ± 40		1300	100	21.	1.3	4.8
	2.6 - 5.0	90 ± 20		480	37.	2.3	0.24	16.
Methacrolein	0.30 - 0.46	150 ± 20	2020 ± 80	2000	35.	11.	2.1	3.2
	0.46 - 1.7	150 ± 30		490	37.	14.	1.6	2.7
	1.7 - 2.4	90 ± 20		150	45.	10.	0.87	4.4
	2.4 - 5.0	70 ± 20		130	15.	1.0	0.15	14.

Table 2.4: Time constants and normalized spectral amplitudes for time dependent photoelectron spectra of acrolein, crotonaldehyde, methylvinylketone, and methacrolein using 200nm pump and 267nm probe wavelengths. The model used to fit the spectra consisted of a cross correlation response X, an immediately excited species A, that decays with time constant t_1 to intermediate I, which in turn decays with time constant t_2 to product P. The spectral amplitudes are determined such that direct comparisons should only be made for individual species across the different energy regions, not between the species within a single energy region.

Molecule	Energy Range (eV)	t_1 (fs)	t_2 (fs)	Normalized Spectral Amplitudes				
				X	A	I	P	A/I
Acrolein	0.30 - 0.75	100 ± 30	620 ± 80	3200	29.	7.3	1.5	4.0
	0.75 - 1.8	110 ± 30		580	30.	8.0	1.2	3.7
	1.8 - 2.6	75 ± 25		370	25.	4.8	0.63	5.2
	2.6 - 5.0	60 ± 20		180	9.7	0.46	0.076	21.
Croton-aldehyde	0.25 - 1.12	70 ± 25	480 ± 25	5700	71.	14.	3.5	5.2
	1.12 - 2.6	70 ± 25	580 ± 50	37.	47.	11.	1.6	4.3
	2.6 - 5.0	50 ± 20	530 ± 50	82.	24.	0.93	0.23	25.
Methylvinyl-ketone	0.30 - 1.2	170 ± 40	1040 ± 100	990	13.	3.1	0.62	4.0
	1.2 - 2.0	190 ± 30		260	11.	3.0	0.46	3.5
	2.0 - 2.6	170 ± 40		230	9.8	3.2	0.31	3.1
	2.6 - 5.0	90 ± 30		78.	3.2	0.33	0.028	9.6
Methacrolein	0.30 - 0.93	110 ± 25	1800 ± 100	2600	33.	7.2	1.7	4.7
	0.93 - 2.0	130 ± 30		170	26.	8.3	1.2	3.2
	2.0 - 2.7	95 ± 25		130	27.	6.6	0.58	4.1
	2.7 - 5.0	70 ± 20		64.	8.7	0.56	0.085	15.

The validity and implications of this fitting model should be discussed. It is always possible to achieve a better fit by adding more components to the fitting procedure. Therefore, to justify this model over a 3 component model, it is necessary to provide spectral evidence for 4 identifiable components. Simply adding components until an 'acceptable' fit is achieved is not a satisfactory method to determine the number of components.

The long-lived component P is easily distinguished because, at long time delays, it is the only component remaining after all other components have decayed to zero. It does not decay appreciably on the timescale of our experiment (i.e. $\sim$100's of ps).

The instrumental response component X is also easily recognized because it follows the laser cross correlation. The only part of the spectrum where the X component has significant amplitude is in the low energy region where 1+1' ionization dominates. Small X amplitudes in the 1+2' region are most likely due to the limitations of fitting with a Gaussian laser cross correlation. The 1+1' ionization regime is the only region of the spectrum where the C–C stretching vibrations are resolved. The X component can arise from either resonant or non-resonant ionization of the molecules. If non-resonant ionization is primarily responsible for the spectra, they should resemble the He(I) photoelectron spectra [65, 66, 67], where n-hole and π-hole photoelectron bands are approximately equal in intensity with one or two vibrations bands visible. However, the 200nm spectra obtained here (see Figure 2.12) show that the X components for the molecules are quite different in appearance from the He(I) spectra, with several vibrational bands seen in AC, and π-hole ionization much more favoured than n-hole ionization in CR and MA. If the ionization process resonantly involves the $\pi\pi^*$ state, we would expect that ionization correlates to the π-hole ionic

state. The change in ionization propensity to favour π-orbital ionization can also be seen in the pump only (2×200nm and 2×209nm) spectra in Figures 2.3-2.6. These single-colour spectra can be thought of as a pump-probe experiment using 200nm for both pump and probe pulses with a very short time delay between them. These compelling reasons provide strong evidence that the X component is a resonant signal and is part of the excited state dynamical process.

The remaining components A and I, are more difficult to separate because they are spectrally broad and overlap to a large extent. The spectral amplitudes from the fit provide the key in separating these two components. In Tables 2.3 and 2.4, the rightmost column displays the ratio of the A to I spectral amplitudes for the different energy regions. For the 3 lowest energy regions (2 lowest energy regions in the case of CR), the ratio of A to I is approximately constant. However, for the highest energy region, the ratio increases dramatically. This means that A and I have different photoelectron spectra, suggesting that they arise from ionization of two different electronic states.

It is important to state that this 4 component sequential model is limited in several ways. It is constructed with exponential kinetics convoluted with fitted 1+1' or 1+2' Gaussian cross correlations. The real measured 1+1' cross correlation can be used in some regions when convoluting with the exponential dynamics, but this correction is minor. The assumption of exponential dynamics is the more restrictive assumption, especially at short pump-probe delay times that are on the timescale of molecular vibrations. In addition, there is a somewhat hidden restriction implied by fitting the X component. By fitting it with the instrumental response function, it is equivalent to fitting an initially excited component that decays instantaneously with

zero lifetime. It would be ideal to be able to relax this restriction since all resonant processes have some nonzero lifetime, however small. Yet this restriction is necessary because the observed t_1 values are shorter or on the order of the instrumental response function ($\sim$160fs). Regardless of the fitting procedure, two time constants cannot be fit that are close together (i.e. the same order of magnitude). Thus, the t_1 values are probably the upper limit for the $A \rightarrow I$ process.

For the above reasons, we conclude that the 4 component fitting model used in this work describes a resonant process that starts with X decaying very rapidly to A, which decays with a maximum time constant t_1 to I, which subsequently decays with time constant t_2 to P. As detailed below, we propose the relaxation pathway from S_2 for the α,β-enones shown in Scheme 2.1. In this scheme, relaxation rapidly occurs from the S_2 Franck-Condon (FC) region (X), towards the S_2/S_1 MECI. We assign the decay time t_1 of component A to the residence time on the S_2 surface. Fast internal conversion through a conical intersection leads the molecules onto the S_1 surface (I). From this surface, the molecules proceed through another conical intersection to produce hot ground state molecules, or intersystem cross to long-lived states in the triplet manifold. These "products" are the TRPES component identified as P.

The pump laser initially excites the planar ground state molecules into the FC region of the $S_2(\pi\pi^*)$ PES. The molecules are expected to move rapidly away from the FC region towards more energetically favoured geometries via torsion about the terminal CH_2 group and stretching to achieve different CC bond lengths. Only while the molecules are near the FC region are their photoelectron spectra expected to be somewhat similar to their non-resonant He(I) spectra. Accordingly, we assign the structured X component as this FC region on the S_2 surface.

Scheme 2.1: Proposed scheme for ultrafast S_2 relaxation of the α,β-enones. X is the Franck-Condon region on the S_2 surface, A is away from the Franck-Condon region on the S_2 surface, I is the S_1 state, and P is long-lived (>100's of picoseconds) hot ground state or triplet state products. The decay of X to A is very fast (i.e. $\ll$160fs, our laser cross-correlation). t_1 and t_2 are the decay times for A and I respectively.

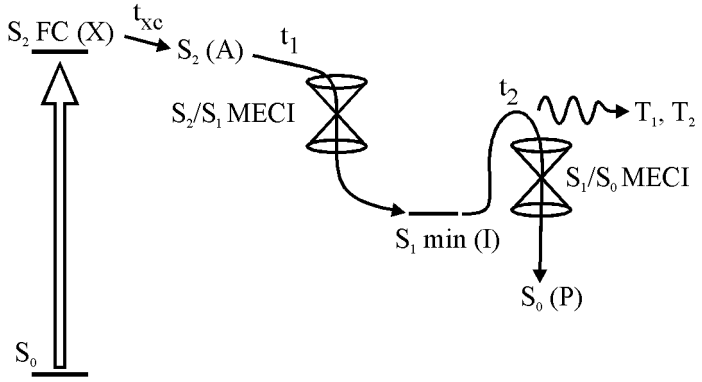

At 209nm, the X components of all molecules show vibrational resolution in the 1 + 1' (low kinetic energy) region of the photoelectron spectrum. In CR and MVK, a vibrational progression with spacing of roughly 0.15eV or 1200cm^{-1} is seen. This progression is assigned to C=C stretching in the ionic states of the molecules, and matches the previously reported value for CR [67]. At 200nm, all molecules show the C=C stretch vibrational progression.

Upon leaving the FC region, the molecules make their way towards the S_2/S_1 conical intersection located roughly 1.5eV below the S_2 FC region. We propose the A signal arises from these molecules still on the S_2 surface but located away from the FC region. From the apparent absence of a true minimum for S_2, one would expect very rapid internal conversion to S_1, as seems to be reflected by the short A lifetimes (t_1) in Tables 2.3 and 2.4. There are small differences in t_1 between the molecules, with CR being the fastest (50-90fs), followed by AC (45-110fs), MA (65-155fs), and finally MVK (90-190fs). However, we draw no conclusions from these small differences due to

the uncertainties in the fitting procedure as described previously. The differences in t_1 at 200nm and 209nm appear to be minimal, suggesting similar dynamics are occurring on the t_1 timescale at both wavelengths for all molecules. For all of the enones, the t_1 decay times at low photoelectron kinetic energies are longer compared to those at higher kinetic energies. Spectrally, this means that the photoelectron spectrum of A is shifting to lower kinetic energies as time progresses. Correspondingly, this means that the excited molecules preferentially ionize to more highly excited vibrational states at later times. This observation is indicative of large deformations (bond stretching and torsion) occurring on the S_2 surface.

After passing through the S_2/S_1 conical intersection, the molecules reside on the S_1 surface. This is component I in our model, with its lifetime described by t_2. By referring to Tables 2.3 and 2.4, we come to the most striking observation that the t_2 relaxation times are very different for the different α,β-enones. At 209nm, CR (360-560fs) appears to have the fastest t_2 relaxation time by a factor of $\sim$2 compared to AC (900$\pm$100fs) and MVK (1080$\pm$80fs), while MA (2020$\pm$80fs) is the slowest by a factor of $\sim$2. At 200nm, AC (615$\pm$80fs) and MA (1800$\pm$100fs) speed up slightly, while CR (480-580fs) and MVK (1040$\pm$100fs) stay approximately the same, compared to their relaxation times at 209nm.

Three possibilities exist for relaxation from the S_1 state: fluorescence from S_1; intersystem crossing to the triplet manifold; or decay through a conical intersection to the ground state S_0. From the short lifetimes of the S_1 states, fluorescence can be ruled out. Intersystem crossing as the major relaxation pathway remains somewhat dubious, as it seems unlikely that a spin-forbidden process can compete with spin-allowed internal conversion. Thus, we conclude the dominant S_1 relaxation pathway

is rapid decay through the S_1/S_0 conical intersection.

The significance of differences in the S_1 decay times for the enones is supported by HCO(X) quantum yield measurements on AC and CR photolysis at 193nm [73]. Using laser induced fluorescence, HCO ground state photoproducts, HCO(X), thought to be formed exclusively via the triplet manifold [42, 56], were observed only from AC, while no detectable production (<0.35%) was found from CR. (The observation of triplet products does not contradict with the statement that intersystem crossing may not be the major relaxation pathway because the singlet-triplet branching ratios are not known.) Due to an increase in the density of states, it might be expected that the rate of intersystem crossing increases for CR relative to AC, resulting in increased triplet product yields. In contrast, the entire triplet yield seems to be shut off by the addition of the methyl group. Two explanations are possible: 1) the opening of another channel on the S_1 surface in CR that depletes the S_1 population; or 2) remarkably faster internal conversion in CR via the S_1/S_0 conical intersection as compared to AC.

The accessibility of a new channel in CR cannot be excluded by energetic reasons because fragmentation to produce the excited state fragment HCO(A) is possible at wavelengths used in our TRPES experiments. However, no new channel is seen in the TRPES data up to ∼100ps suggesting that a new pathway is present. The 193nm photolysis experiments [73] were only able to detect ground state HCO(X), not HCO(A). Experiments using synchrotron VUV light as the ionization source following 193nm excitation [58] speculate that this channel might be present. However, direct observation of the HCO(A) photoproduct is impossible because it is unstable relative to further fragmentation. There are a number of drawbacks for this explanation of

the observed S_1 relaxation times. A barrier restricts HCO(A) formation in AC [42]. Thus, this explanation requires the unlikely result that simple addition of the methyl group at the end of AC substantially lowers the barrier to HCO(A) formation. Also, by Hammond's postulate, one would expect that corresponding formation of the more stable acetyl radical CH_3CO from MVK, would be more favourable and should have a shorter S_1 relaxation time than CR, which it does not. In addition, this explanation cannot describe why the S_1 relaxation time is slower for MA.

The more probable explanation for the differing S_1 decay times between the enones are differences occurring at or near the S_1/S_0 conical intersection, resulting in promotion or retardation of internal conversion to the ground state. We attempted to find correlations between the S_1 decay times and properties defining the CI. Table 2.5 shows the computed values for the barrier $E^{\dagger}$ (difference between the S_1 minimum and the S_1/S_0 MECI); the total excess E_{xs} energy (difference between S_2 FC and S_1/S_0 MECI), and the excess averaged over the number of modes, $E_{xs,avg}$, for each of the four molecules. From these values, it is clear that energetics alone cannot explain the difference in S_1 lifetimes - it fails to discriminate between CR, MVK and MA (whose lifetimes differ by a factor of two), and would dictate that AC decay faster than CR (which it does not).

Next, we examined the topographical features of the S_1/S_0 intersection itself. In the case of a two-surface crossing, in the two coordinates that create the degeneracy the potential energy surfaces resemble a double cone with the CI at the apex. Far from being mere isolated points, CI's form N-2 dimensional seams along which two (and possibly three [74, 72], in which case the seam is N-5 dimensional) electronic states are degenerate. The two dimensions along which the degeneracy is broken form

Table 2.5: Calculated properties near the S_1/S_0 conical intersections for the α,β-enones discussed here. $E^{\dagger}$ is the energy between the S_1 minimum and the S_1/S_0 MECI. E_{xs} is the excess energy available at the S_1/S_0 MECI (i.e. the energy difference between S_2 FC and S_1/S_0 MECI). $E_{xs,avg}$ is the excess energy averaged over the number of vibrational modes. Projections of the gradient difference ($\mathbf{g}$) and nonadiabatic coupling ($\mathbf{h}$) vectors onto the seam gradient vector ($\mathbf{s}$) are given by s_x and s_y, respectively. d_{gh} represents the distance metric in the branching space, and Δ_{gh} the asymmetry of the conical intersection. ν_t is the torsional frequency determined by SA3-CAS(6,5)/6-31G* at the S_1 minimum about the terminal methylenic CHX bond (X=H for AC, MVK, MA; X=CH_3 for CR). The final row provides relative S_1 lifetimes based upon the 209nm t_2 data provided in Table 2.3, taking AC as the reference (value of unity).

	AC	CR	MVK	MA
$E^{\dagger}$ (eV)	0.98	0.99	0.82	0.82
E_{xs} (eV)	3.61	3.03	3.23	3.16
$E_{xs,avg}$ (eV)	0.20	0.11	0.12	0.12
s_x	0.439	0.440	0.394	0.467
s_y	0.0000	0.0003	0.0006	0.0002
d_{gh}	0.112	0.112	0.106	0.114
Δ_{gh}	0.973	0.972	0.968	0.954
ν_t (cm^{-1})	518	249	524	530
$t_2^{(AC)}/t_2(209nm)$	1.00	1.80	0.95	0.45

the branching [38], or $\mathbf{g}-\mathbf{h}$ [75] plane. We begin by considering two electronic states $|I\rangle$ and $|J\rangle$. For state energies E_I and E_J, the $\mathbf{g}$ (gradient difference) vector is defined by

$$2\mathbf{g}_{IJ} = \nabla_{\mathbf{R}}(E_I - E_J) \tag{2.6}$$

in which the $\nabla_{\mathbf{R}}$ operator indicates differentiation with respect to nuclear coordinates. Likewise, the nonadiabatic coupling vector $\mathbf{h}$ between electronic states $|I\rangle$ and $|J\rangle$ is

defined as

$$\mathbf{h}_{IJ} = \langle I|\nabla_{\mathbf{R}}|J\rangle = \frac{\langle I|\nabla_{\mathbf{R}}H|J\rangle}{E_I - E_J}. \tag{2.7}$$

The classification of conical intersections as 'peaked' or 'sloped' is based on the projections

$$s_x = \mathbf{s}\cdot\mathbf{x} \tag{2.8}$$

$$s_y = \mathbf{s}\cdot\mathbf{y} \tag{2.9}$$

in which $\mathbf{x}$ and $\mathbf{y}$ are normalized versions of the branching plane vectors $\mathbf{g}$ and $\mathbf{h}$ respectively:

$$\mathbf{x} = \frac{\mathbf{g}}{||\mathbf{g}||} \tag{2.10}$$

$$\mathbf{y} = \frac{\mathbf{h}}{||\mathbf{h}||}. \tag{2.11}$$

The seam coordinate $\mathbf{s}$ is

$$2\mathbf{s} = \nabla_{\mathbf{R}}(E_I + E_J) \tag{2.12}$$

representing the gradient of the average energy of the intersection seam.

In addition to the projections, two additional parameters are needed to fully characterize the seam space [76]. The first of these,

$$\Delta_{gh} = \frac{||\mathbf{g}||^2 - ||\mathbf{h}||^2}{||\mathbf{g}||^2 + ||\mathbf{h}||^2} \tag{2.13}$$

measures the intersection asymmetry, or ellipticity of the intersection. The final parameter,

$$d_{gh} = \sqrt{||\mathbf{g}||^2 + ||\mathbf{h}||^2} \tag{2.14}$$

provides a distance metric for the branching space. Larger values of d_{gh} represent steeper pitched (narrower) CI's than smaller values.

Previous studies [38, 37] attempted to correlate intersection topography with decay efficiency, and we summarize the relevant points here. Intersections with branching plane vectors having zero projection (s_x=0, s_y=0) onto the seam coordinate are described as vertical or "peaked" cones. In this situation, the upper surface lies entirely above the CI in energy, while the lower surface lies entirely below. This topography conforms closely to the classical picture of a funnel, meaning that population on the upper state is very efficiently directed to and through the intersection located at the apex of the cone. Intersections with branching space axes having nonzero projection onto the seam coordinate ($s_x \neq 0$ and/or $s_y \neq 0$), on the other hand, are tilted or "sloped". In this case, the cone axis can be tilted significantly such that parts of the upper surface lie below the CI energy while parts of the lower surface lie above the CI energy. Some trajectories pass efficiently through these sloped CI's, while others do not. In addition, recrossing of the CI is possible for such geometries. More than in the peaked pattern, the direction by which a sloped CI is approached can be critical in determining whether the adiabatic or non-adiabatic pathway is followed. The symmetry and pitch of the CI, defined by Δ_{gh} and d_{gh} can also affect the efficiency of passage through the CI.

The parameters defining the conical intersections are illustrated with two examples shown in Figure 2.14. Figure 2.14a shows two views of a vertical asymmetric CI. A nonzero Δ_{gh} is readily seen as a difference in slopes of the PES's along the **g** and **h** vectors. The projections of the seam coordinate (**s**) onto the branching space vectors is zero and the cone axis is completely vertical. Figure 2.14b shows two views of a symmetric sloped CI, whose cone axis is only tilted along the gradient difference vector **g**. The CI is not tilted along the nonadiabatic coupling vector **h**, thus only

$s_x \neq 0$ and $s_y = 0$. The CI is symmetric since Δ_{gh} is zero. Unlike the idealized examples presented here, real conical intersections in general contain some degree of both tilt and asymmetry. The preceding parameterization of conical intersections only describes a small, local PES subspace near the CI. Other more global PES features may affect the CI accessibility or crossing dynamics.

The gradient difference **g** and nonadiabatic coupling **h** vectors for AC are shown in Figure 2.15. The gradient difference vector is bond alternation (strongest on the central C–C bond), but due to motions of the aldehyde H and O, it effectively looks like scissoring motion of the CCOH. The nonadiabatic coupling vector is pyramidalization of the central backbone carbon. The **g** and **h** vectors for CR, MVK, and MA are qualitatively the same as those for AC, providing no evidence to explain the differences in S_1 lifetimes between the molecules.

In Table 2.5, we show the calculated +parameters $s_x, s_y, \Delta_{gh}, d_{gh}$ describing the topography of the S_1/S_0 CI's for the α,β-enones. The results reveal intersections sloped sharply along the gradient difference axis but almost perfectly peaked along that of the nonadiabatic coupling ($s_y \approx 0$). Qualitatively, they resemble the CI presented in Figure 2.14b. The values of s_x differ by approximately <10% between the molecules. The magnitude of s_x fails to distinguish between AC and CR, and values for both are larger than that for MVK, even though their t_2 decay rates are higher (contrary to the correlation anticipated by Yarkony [37]). Lack of a clear pattern relating the **s** projection values with t_2 is, perhaps, not surprising in this context. The relative differences in tilt and asymmetry examined here are quite small in comparison to those studied previously [37] (in which they are greater than 0.5 for both s_x and Δ_{gh}).

Figure 2.14: Examples of conical intersections in the space defined by the gradient difference **g** and nonadiabatic coupling **h** vectors. The upper and lower surfaces are coloured red and blue respectively. The left and right diagrams are different views of the same intersection. (a) an asymmetric, peaked conical intersection. The asymmetry, parameterized by Δ_{gh}, is easily seen as the differing slopes along the **g** and **h** vectors near the intersection. $s_x = s_y = 0$ indicate that the cone axis is vertical. (b) a symmetric, sloped intersection. $s_x \neq 0$ and $s_y = 0$ indicate that the cone axis is only tilted along the **g** direction.

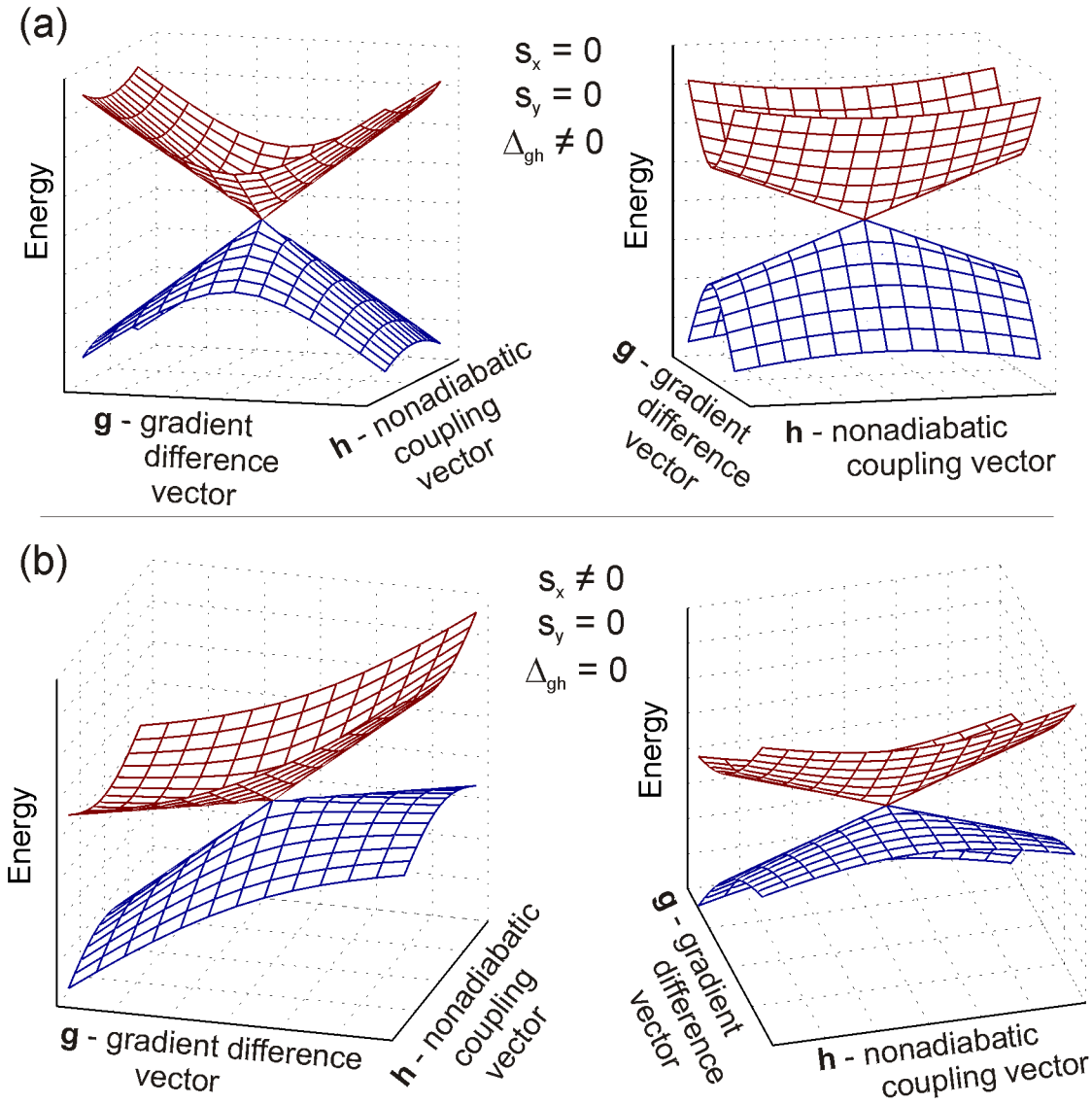

Figure 2.15: Gradient difference and nonadiabatic coupling vectors for acrolein. The gradient difference vector is essentially bond alternation (strongest on the nominally C–C bond), but due to motions of the aldehyde H and O, effectively looks like scissoring motion of the CCOH. The nonadiabatic coupling vector is pyramidalization of the central backbone carbon.

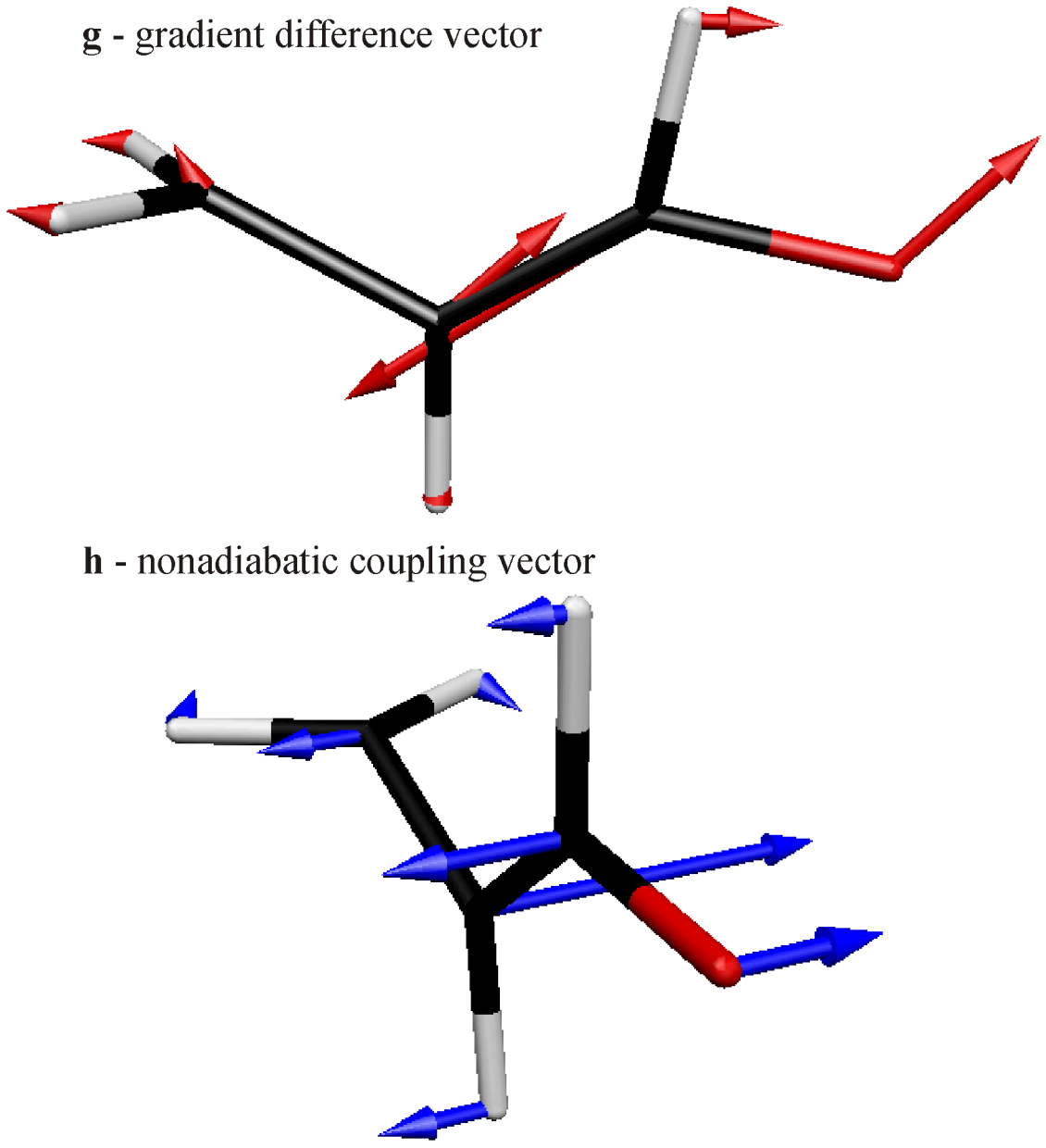

The CI's for the molecules are also quite asymmetric, as indicated by the values of Δ_{gh} in Table 2.5. The intersections all are steeply sloped along the gradient difference vectors while the degeneracy is barely broken along the nonadiabatic coupling vector. Again there does not appear to be appreciable differences in the CI asymmetries that would explain the trends seen in the S_1 relaxation behaviour.

The analysis thus far deals with static features on the potential energy surfaces of the molecules, and the energies and topographies of the conical intersections. It fails to find a consistent explanation for the observed differences in relaxation rates between the four molecules. Therefore, the remaining important issue is the vibrational dynamics occurring near the S_1/S_0 CI and their relationship to surface hopping probabilities. Because the geometric changes required to move from the S_1 minimum to the S_1/S_0 MECI are dominated by torsion about the terminal CH_2 (or $CHCH_3$ in CR), this mode was chosen as an approximate reaction coordinate. CASSCF normal modes (as calculated at the S_1 minimum) allowed unambiguous identification of a single mode corresponding to such motion, enabling assignment of an approximate vibrational frequency. The calculated torsional frequencies ν_t, included in Table 2.5, are roughly equal for all but CR, which differs by a factor of $\sim$2 as a result of methylation at the twisted end of the molecule. We speculate that this slower torsional frequency is responsible for faster internal conversion in CR. Assuming that the torsional velocity is constant, the torsional period for AC, MVK, and MA, is half that of CR. Thus, for CR, it appears that although sampling of the space near the S_1/S_0 CI occurs at half the frequency as the others, efficiency of internal conversion to the ground state is doubled.

This leads us to propose a mechanism for the faster internal conversion in CR.

Vertically oriented CI's funnel the trajectories towards the intersection to promote fast internal conversion. However, the direction of approach is important in determining the efficiency of crossing in sloped CI's. As indicated above, the S_1/S_0 MECI's for all the enones are of this latter type. Figure 2.10 indicates that the MECI geometries for the molecules are all twisted $\sim$90° about the terminal –C=CHX. A complete rotation about the methylene bond takes the trajectory from the S_1 minimum at 0° and 180° (planar geometry) to regions nearby the S_1/S_0 CI at 90° and 270° (twisted geometry). We speculate that *slow* torsion through the CI region promotes internal conversion. In CR, more time is spent near the intersection region on each pass near the CI region, during which other molecular motions can occur. Importantly, these motions can bring the molecular trajectory to the S_1/S_0 CI, resulting in rapid internal conversion to the ground state. Conversely, for the faster twisting molecules (AC, MVK, MA), the trajectories pass though the CI region relatively quickly, bypassing the opportunity pass through the CI. Interestingly, this postulate is opposite in nature to the analysis of 1-dimensional Landau-Zener avoided crossings, where faster moving trajectories are more likely to follow the diabatic pathway to end up on the other surface, while slower moving trajectories follow the adiabatic pathway and remain on the same surface. However, this difference in behaviour is not surprising considering that for CI's, the upper and lower surfaces do meet at a degenerate point, unlike the case in avoided crossings.

While faster rotation of the CH_2 group is consistent with the relatively longer S_1 decay times observed for AC and MVK, we note that of MA appears anomalously long. With similar torsional frequency about the terminal CH_2 bond, reasons outlined above would predict MA to have a similar S_1 decay time to AC and MVK. However,

this is not the case. For MA, we propose a different effect responsible for the slower S_1 relaxation dynamics. Examination of the branching space vectors for AC in Figure 2.15 reveals that the non-adiabatic coupling vector ($mathbf{fh}$) is primarily pyramidalization around the middle carbon. The magnitude and speed of the motion of this carbon is affected by substitution of the hydrogen with a relatively heavy methyl group at this location, as is the case in MA. As such, the **h** motion in MA is expected to move slower relative to that in CR, AC, and MVK. A key difference in this situation compared to the anomalous decay rate in CR is that fact that the methyl group in MA is directly affecting one of the branching space vectors (in this case **h**). We expect that MA, AC, and MVK access the intersection region, with the terminal methylene group twisted by 90°, at approximately the same rate. We speculate that AC and MVK have overall faster S_1 relaxation because they have faster moving **g** and **h** vectors which allow them to access the S_1/S_0 CI more efficiently than MA.

We postulate that the relative speeds of specific motions is important in controlling relaxation rates in sloped conical intersections. Motions that are required to reach the CI, but are not necessarily responsible for creating the intersection (e.g. the torsional mode), speed up the crossing rate (as in CR). Conversely, motions that create the intersection (i.e. the g and h vectors) speed up the crossing rate when they are fast because they quickly shoot the trajectory through the CI. This reasoning seems consistent with the experimentally observed trend in S_1 relaxation rates. CR has the fastest decay because both effects, slow torsional motion to reach the CI region, and fast motion of the **h** coordinate, drive nonadiabatic crossing. At the other extreme in decay rates, MA is the slowest because both effects, fast torsional motion by the CI region, and slow motion of the **h** coordinate, are detrimental to

nonadiabatic crossing. AC and MVK fall in between because the effects operate in a canceling fashion, with fast torsional motion retarding relaxation, and fast motion of the **h** coordinate promoting relaxation. We stress that this analysis applies only to sloped conical intersections where the excited state trajectories are expected to come from points on the PES lower in energy.

Clearly, more experimental and theoretical investigations are needed to prove or disprove the postulates presented here. Full quantum mechanical dynamics calculations are currently underway to explore these issues. In addition, it would be useful to perform further experiments using the di-methyl substituted α, β-enones to emphasize the strengths and/or weaknesses of this model.

2.4 Conclusion

We measured the ultrafast dynamics of the α,β-enones acrolein (AC), crotonaldehyde (CR), methylvinylketone (MVK), and methacrolein (MA) after excitation to the S_2 electronic surface at 200nm and 209nm. The molecules initially move quickly away from the Franck-Condon overlap region toward the S_2 minimum. Large amplitude motions are observed as they make their way towards an S_2/S_1 conical intersection to land on the S_1 state roughly 50-200fs later. The molecules then pass through another conical intersection to the ground state. Intersystem crossing to the triplet manifold is predicted to be minimal. Small differences between the molecules are seen in the S_2 relaxation times. However, large differences are seen in the S_1 relaxation times, with CR decaying the quickest, followed by AC and MVK approximately equal, and MA considerably slower. Thus, the S_1 decay dynamics are greatly affected by the position of the methyl group substituent. Theoretical calculations of the geometries,

topographies, and energies of the S_1/S_0 conical intersections do not reveal reasons for the observed differences. We conclude that dynamical factors (i.e. motions of the atoms on the potential energy surface) play a large role in the S_1 decay rates through the sloped S_1/S_0 conical intersections.

We propose a model in which the speeds of specific motions in the molecules affects their nonadiabatic crossing rate. We identify two important types of motions in the molecules that we studied. The first are the motions which are responsible for the formation of the conical intersection, the gradient difference **g** and nonadiabatic coupling **h** vectors. The second are the modes required to reach the CI geometry. In the case of the α, β-enones, this mode is the terminal methylene torsional mode. Fast motion of the **g** and **h** vectors promotes non-adiabatic crossing by speeding passage of the trajectory to and through the CI. Correspondingly, slow motion of these modes results in slow relaxation through the CI. For the modes that bring molecules to the correct CI geometry, slow motion promotes nonadiabatic crossing while fast motion slows crossing. The reason for this effect is that slower motions allow more time for the CI modes (**g** and **h**) to reach the CI. These reasons are consistent with the measured S_1 relaxation rates in the α, β-enones. CR has the fastest decay because it has the slowest methylene torsion and also fast motion of the **g** and **h** vectors. AC and MVK are of intermediate decay rate because the effects of the fast methylene torsion and fast CI modes oppose each other. MA has the slowest decay rate because it has fast methylene torsion and the methyl group substituent slows **h**.

Chapter 3

Designing a Coincidence Imaging Spectrometer

3.1 Introduction

In coincidence imaging spectroscopy, we wish to measure the three dimensional velocities of a photoelectron/photoion pair from a single photoionization event. This measurement is accomplished using time and position sensitive detectors in an arrangement shown in Figure 3.1. Pump and probe laser pulses intersect a molecular beam to initiate a chemical reaction and then photoionize the products. Ions and electrons are directed towards their respective detectors. The three dimensional velocities are translated into timing and position measurements at the detectors. It is important to stress that each photoelectron/photoion pair is measured on an event by event basis. As such, all distributions such as kinetic energy distributions, photoelectron angular distributions, photoelectron spectra, are directly constructed from the raw data; no assumptions about experimental symmetry, no transformations, nor

modeling of the measured data is required.

This chapter investigates the basic issues of mass, velocity, and energy resolution involved in design of a coincidence imaging spectrometer. A general overview of coincidence imaging spectrometers is given here; design specifics for our own spectrometer are given in Chapter 4. This study was motivated by our desire to optimize our spectrometer design within the constraints of our existing vacuum chamber and commercially purchased detectors.

Figure 3.1: Schematic diagram of the Coincidence Imaging Spectrometer. The molecular beam, laser beam, and spectrometer axis are all mutually perpendicular.

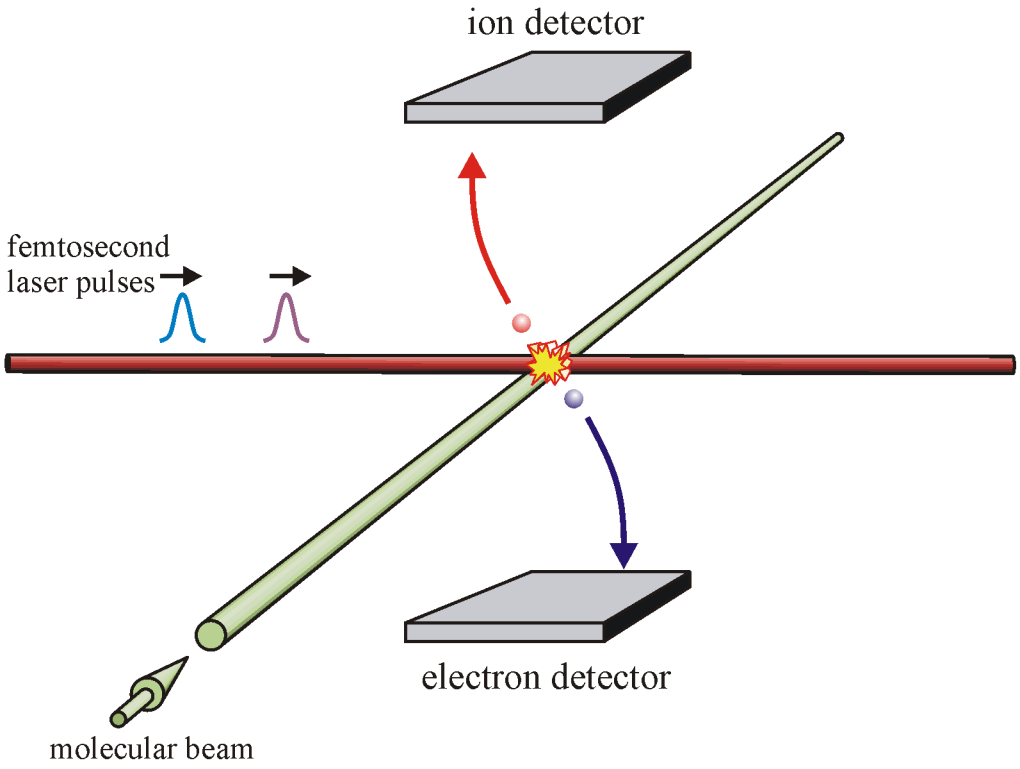

3.2 Measuring Three Dimensional Velocities

The experimental setup axis definition is shown in Figure 3.2, with the molecular beam, laser beams, and the spectrometer axis residing along the mutually perpendicular x, y, and z axes respectively. The interaction region is defined as the volume of intersection between the molecular and laser beams. The geometric centre of this interaction region is defined as the origin of the spectrometer.

In order to detect electrons or ions emitted in all directions, electric and/or magnetic fields must be used to direct the particles onto the detector. If only electric fields are used to image the electrons, relatively high fields must be used to accelerate the electrons towards the detector. This places very high requirements on the timing measurement electronics. An alternate solution is to use magnetic fields aligned along the spectrometer axis to contain electrons that would otherwise fly out of the field of view of the detector [77]. Using this method, the electrons follow helical trajectories towards the detectors. Very small electric fields can be used to force the electrons onto the detector, greatly relaxing the time resolution requirements. A problem with using magnetic fields is that there is an ambiguity that arises because after each electron cyclotron period, the electron position projects onto the detector xy origin. Thus, if a particle hits the detector origin, it becomes impossible to determine how many cyclotron orbits the electron has completed. Due to this ambiguity, we explored only the use of electric fields for our spectrometer. Thus, one of our major tasks in building our spectrometer was ensuring accurate and precise timing from our electronics. This issue is dealt with explicitly in later sections.

Particle velocities along the z-axis, v_z are measured by recording the time-of-flight (TOF) that particles take to travel from the interaction region to the detector.

Particles initially flying away from the detector arrive later than those initially flying towards the detector. If the spectrometer is designed such that there are no forces exerted on the particles in the xy plane, the x and y velocities, v_x and v_y remain constant throughout the entire trajectory of the particle. If the projection of the origin onto the detector face is known, v_x and v_y can be calculated by dividing the spatial distances measured on the detector by the particle TOF.

Figure 3.2: Experimental geometry for a time resolved photoelectron or photoion experiment using crossed molecular and laser beams. The molecular beam, laser beam, and spectrometer axis are located along the x, y, and z axes respectively.

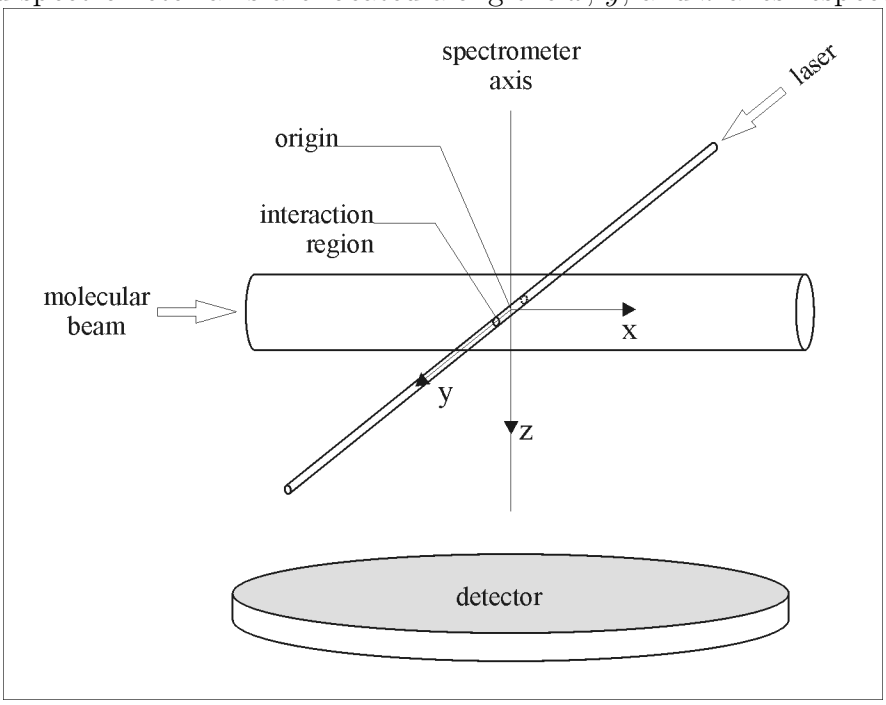

3.3 Spectrometer Resolution Issues

A number of different factors can limit the resolution of the three velocity components v_x, v_y, and v_z. A summary of these effects is shown in Table 3.1 and described following.

Table 3.1: Resolution Limiting Factors for Electron and Ion Coincidence Imaging Spectrometers

velocity component	Resolution Limiting Factors
v_z	spatial extent of interaction region in z dimension
	turnaround time spread & spectrometer timing errors
	calibration of t_0 for $v_z = 0$
v_y	spatial extent of interaction region in y dimension
	detector spatial resolution
	calibration of t_0 for $v_z = 0$
v_x	spatial extent of interaction region in x dimension
	detector spatial resolution
	molecular beam velocity spread
	calibration of t_0 for $v_z = 0$

3.3.1 Spatial Extent of the Interaction Region

Ideally all photoelectrons and photoions are produced at a point source located at the origin. However, in reality, they are produced from the entire volume of the interaction region. Typically molecular beams are on the order of 2-3mm diameter at the interaction region. Focussing a 200nm gaussian laser beam of 5mm diameter using a $f = 500mm$ lens produces a 25μm diameter spot size at the focus. The Rayleigh range of such a beam is about 2.5mm. Thus, the interaction volume is shaped like a thin cylinder aligned along the y-axis. As such, the v_y resolution is degraded more

by the spatial extent of the ionization region than is either the v_x or v_z resolution.

Particles with identical initial velocity vectors but different initial locations of birth along the spectrometer axis (z-axis) will arrive at different times at the detector. This will result in a blurring of the time of arrival at the detector and hence v_z resolution. If deemed necessary, the resolution loss due to the z extent of the ionization volume can be minimized using a so-called Wiley-McLaren spectrometer[78]. A Wiley-McLaren spectrometer contains one or two acceleration regions followed by a field free drift region. By adjusting spectrometer lengths and voltages appropriately, the first derivative of the TOF with respect to the displacement from the origin along the z-axis can be minimized. Thus, the first order dependence of TOF upon ionization position along the z-axis can be removed. This process of guiding identical particles with different initial starting positions to arrive at the same time at the detector is called Space Focussing.

Resolution loss in the plane of the detector (xy plane) due to the size of the interaction region has been handled by the technique of Velocity Map Imaging developed by Eppink and Parker[23]. In this technique, open electrostatic lenses are used to focus particles with the same initial velocity vector onto the same point on the detector regardless of where they are produced within the ionization volume. Unfortunately, the improvement in x and y spatial resolution on the detector comes at the expense of resolution in v_z. A high electric field is needed for this technique, which compresses the TOF spread. For this reason, this technique has only limited applicability for 3D velocity measurements.

A hybrid technique developed by Lebech and coworkers[79] is a compromise between the Wiley-McLaren and Velocity Map Imaging setups. However calibration

and simulation issues make this technique difficult to use in practise.

Homogeneous fields were chosen for our spectrometer because back-transformation of the initial particle velocities is straightforward in this case. Therefore, the spatial extent of the interaction region is directly mapped onto the detector (e.g. a 2mm interaction region in the y dimension causes 2mm of blurring at the detector). To minimize the effect of the spatial extent of the interaction region, the spectrometer voltages should be chosen such that the image is expanded to cover the largest area as possible on the detector. In this way, the blurring is small compared to the displacement on the detector caused by initial v_x and/or v_y.

3.3.2 Turnaround Time Spread and Spectrometer Timing Error

The turnaround time spread is the TOF difference between particles initially travelling towards the detector and those initially travelling away from the detector. The spectrometer timing error is the total uncertainty in the measurement of the time when a particle hits the detector. For best resolution in v_z, it is necessary to have the largest possible ratio of turnaround time spread to spectrometer timing error.

3.3.3 Molecular Beam Velocity Spread

A good supersonic molecular beam expansion of a heavy molecule seeded in helium will be moving on the order of 1800m/s with a speed ratio of 20, meaning that the beam will have a velocity beam spread of 5%, or 90m/s. The molecular beam velocity and its spread are negligible when measuring electrons because even 0.01eV electrons move at a speed of almost 6×10^4m/s. However, beam velocity spread cannot be

ignored if ions are the particles of interest. An ion of mass 40amu with 0.5eV of energy moves at only 1.5×10^3m/s. In this case, the molecular beam velocity spread is 6% of the velocity to be measured which translates into a 12% error in the measured kinetic energy. For ions, it is difficult to correct or even minimize the loss of resolution due to the beam velocity spread when using a continuous molecular beam source.

If the detector and spectrometer axes are coincident, the beam velocity carries the ions in the direction of the molecular beam and reduces the amount of usable space on the detector. It is possible to somewhat compensate for this effect by shifting the detector off the spectrometer axis in the direction of the molecular beam. The combined effects of average beam velocity and beam velocity spread are shown in Figure 3.3.

3.3.4 Detector Spatial Resolution

The accuracy with which a detector can determine the position that a particle hits is the detector spatial resolution. Both v_x and v_y are calculated from the displacement of the particle hit position from the origin's projection onto the detector. Therefore, the detector spatial resolution can be a limiting factor for the velocities in the plane of the detector.

Figure 3.3: The effect of average molecular beam velocity and beam velocity spread on measuring an ion's energy release from a chemical process. The average beam velocity causes the image to be shifted from the centre of the detector. The beam velocity spread causes blurring in the direction of the molecular beam travel.

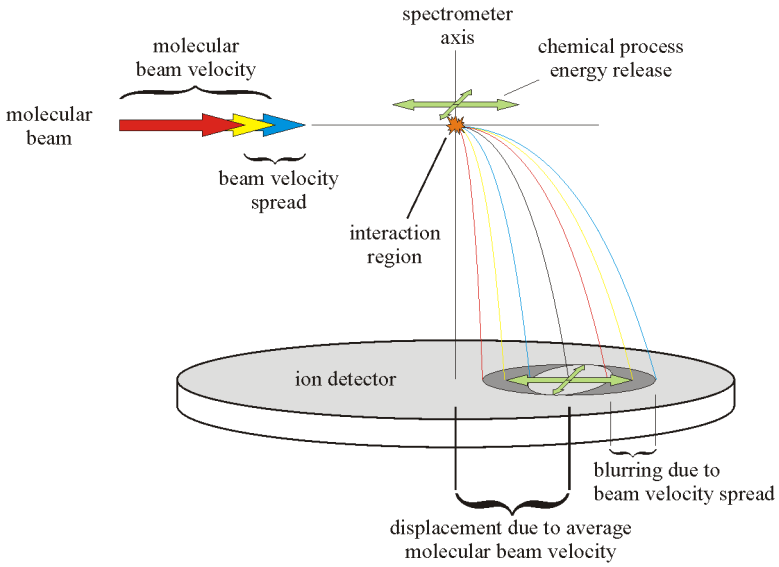

3.4 Energy Measurement Error

The photoelectron energy or photoion kinetic energy release for an event E, and its associated error are

$$E = \frac{1}{2}m\left(v_x^2 + v_y^2 + v_z^2\right) \tag{3.1}$$

$$\Delta E = m\left((\Delta v_x v_x)^2 + (\Delta v_y v_y)^2 + (\Delta v_z v_z)^2\right)^{1/2} \tag{3.2}$$

where m is the mass of the particle and v_i is the velocity of the i^{th} component.

The radial (x and y) velocity components are

$$v_x = \left(\frac{x}{t}\right) \tag{3.3}$$

$$v_y = \left(\frac{y}{t}\right) \tag{3.4}$$

where x and y are the displacements from the origin and t is the time of flight of the particle.

Ideally the TOF of a particle will vary linearly with initial velocity along the z-axis, v_{0z}:

$$v_{0z} = -K(t - t_0) \tag{3.5}$$

where K is a proportionality constant, and t_0 is the TOF for a particle with no initial z velocity. Later it will be shown that K is approximately the acceleration of the electron in the extraction region.

The errors associated with the individual velocity components are:

$$\begin{aligned} \Delta v_x &= v_x \sqrt{\left(\frac{\Delta x}{x}\right)^2 + \left(\frac{\Delta t}{t}\right)^2} \\ \Delta v_y &= v_y \sqrt{\left(\frac{\Delta y}{y}\right)^2 + \left(\frac{\Delta t}{t}\right)^2} \\ \Delta v_z &= K\sqrt{(\Delta t^2 + \Delta t_0^2)} \end{aligned} \tag{3.6}$$

The error Δt_0 is the error in finding the TOF for particles with zero initial velocity along the spectrometer axis. The spectrometer timing error Δt is due to the timing error of the detector Δt_{det}, the apparent error due to the z-spatial time spread Δt_{sf}, and the timing error of the electronics that are used to measure the TOF, Δt_{el}. Since these errors are uncorrelated, Δt can be expressed as:

$$\Delta t = \sqrt{\Delta t_{sf}^2 + \Delta t_{det}^2 + \Delta t_{el}^2} \tag{3.7}$$

3.5 Designing an Imaging Electron Spectrometer

The electron spectrometer is simpler to design compared to the ion spectrometer because: 1) mass separation is not necessary; and 2) as previously mentioned, the molecular beam velocity and the beam velocity spread are negligible compared to typical electron velocities.

The objectives when designing an electron spectrometer are the following:

- To minimize the effect of the spatial extent of the interaction region on the electron TOF.
- To ensure linearity of the TOF with v_{0z}.
- To maximize v_{0z} resolution by maximizing the ratio of the turnaround time spread to the spectrometer timing error.
- To maximize the radial hit position on the detector to maximize (v_x, v_y) resolution.

As can be expected, some of these objectives are conflicting, so compromises must be made when designing a spectrometer.

The electron spectrometer discussed here was designed for electrons with kinetic energy $\leq$2.0eV. The anticipated detector characteristics were 100ps timing resolution and 100 micron spatial resolution. The accuracy with which the laser focus was able to be placed through the origin was estimated to be $\pm$100 microns. The detector active area was taken to be a 40mm diameter circle.

3.5.1 Spectrometer Overview

Only spectrometers using grids, or fine wire meshes, were considered for use in constructing our spectrometer. Grids allow for simple analytical simulation of particle trajectories because the electric fields can be assumed to be constant between a pair of grids. In contrast, trajectories through open electrode spectrometers must be simulated numerically using actual electrode shapes. This is a serious computational issue if some spectrometer parameters are unknown, and can only be fit by forward propagating trajectories to obtain a measured TOF spectrum. The main disadvantage of gridded spectrometers is that they are much less efficient at particle detection because they have reduced open areas resulting in reduced particle transmission. Also, large differences in electric fields across the grids can create small aperture lenses that deflect the particle trajectories. This complication will be discussed in Section 3.6.9.

Two designs were considered for the electron spectrometer: the constant field spectrometer, and the single-field Wiley-McLaren spectrometer. Both are schematically shown in Figure 3.4. The constant field spectrometer uses a single electric field to accelerate the electrons onto the detector. The single-field Wiley-McLaren Spectrometer has two regions separated by a grid (grid 1 in Figure 3.4b). In the first region, the extraction region, there is a constant electric field, the extraction field E_{ext}, that forces all the electrons towards the detector. The second region, the drift region, contains no electric field. In both spectrometers, a conductive grid is required in front of the detector to define an additional field region in which the electrons are accelerated onto the detector microchannel plates (MCPs).

Figure 3.4: (a) The constant field electron spectrometer, and (b) the single-field Wiley-McLaren electron spectrometer.

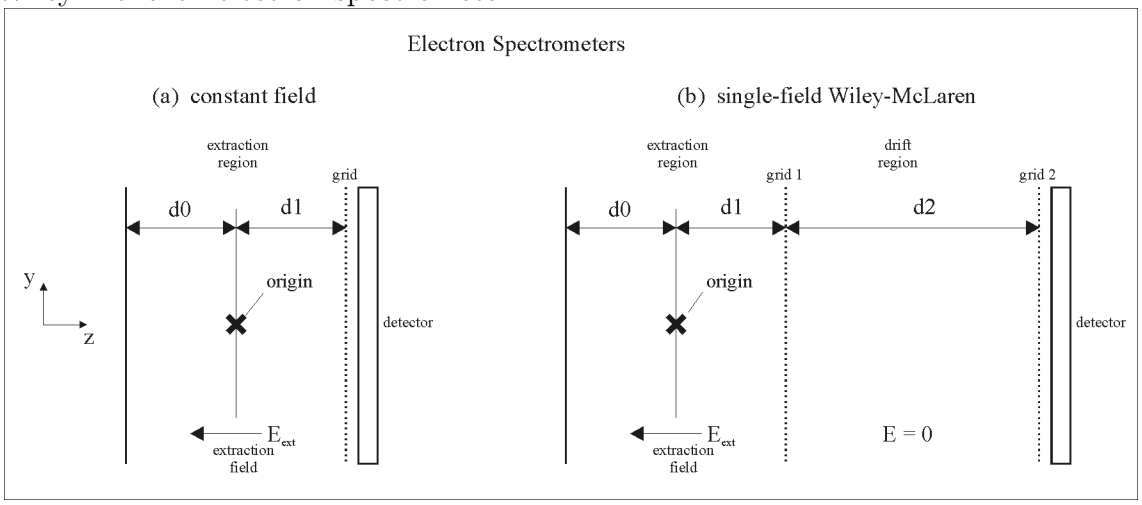

3.5.2 Electron Spectrometer Simulations

The electron trajectories were simulated analytically using basic kinematics equations and assuming constant field regions. Electron trajectories $[x(t), y(t), z(t)]$ are defined by their initial conditions: v_0, the initial electron velocity; θ, the angle the initial electron velocity makes with the spectrometer axis; and z_0, the z distance from the origin to where the electron is born. These quantities are shown in Figure 3.5. Since the molecular beam velocity and its spread are negligible, the simulated trajectories are almost cylindrically symmetric, with the only difference between x and y being differing dimensions of the interaction region along the respective axes, and different possible x and y errors on the detector.

The following conditions were used for the electron spectrometer simulations:

1. Direct comparisons were be made between constant field and single-field Wiley-McLaren spectrometers that are equivalent. To be equivalent, the spectrometers

Figure 3.5: Parameters determining an electron trajectory. v_0 is the initial electron velocity, z_0 is the z distance from the origin, and θ is the angle the electron trajectory makes with the spectrometer axis.

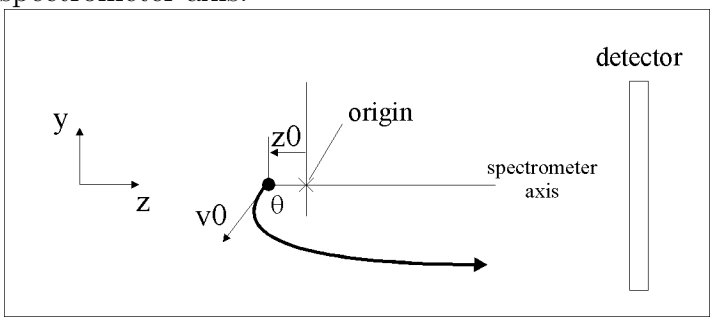

were required to have the same total length and have voltages adjusted such that they fully image spherically symmetric electron distributions up to the same maximum kinetic energy.

2. The grids were assumed to be perfect grids: i.e. the electric field changed in a discontinuous fashion across the grid and there was no field penetration across the grid. Using this assumption, electron trajectories can be easily simulated analytically. Relaxation of this assumption is discussed in Section 3.6.9.

3. The trajectories are simulated only until the final grid. There is usually a gap between the final grid and the detector. This last region contains a relatively large electric field that must not be overlooked when designing the real spectrometer electrodes.

3.5.3 Electron Spectrometer: X-Y Resolution

For either type of spectrometer, the voltage can be chosen such that electrons of the same energy fill the same area of the detector of equivalent spectrometers. Since no

forces are exerted in the x and y dimensions, this means that the v_x and v_y resolutions of the constant field and single field Wiley McLaren spectrometers are roughly the same.

3.5.4 Electron Spectrometer: Space Focussing

For the constant field spectrometer, the electron TOF is given by

$$TOF_{CF} = \frac{-v_{0z} + (v_{0z}^2 + 2a(d_1 + z_0))^{\frac{1}{2}}}{a} \tag{3.8}$$

where $v_{0z} = v_0 \cos\theta$ and acceleration $a = qE_{ext}/m_e$. No space focussing condition exists for the constant field spectrometer because the first derivative $d(TOF_{CF})/d(z_0)$ is always non-zero.

The single-field Wiley-McLaren Spectrometer has an electron TOF of

$$TOF_{WM} = \frac{-v_{0z} + (v_{0z}^2 + 2a(d_1 + z_0))^{\frac{1}{2}}}{a} + \frac{d2}{(v_{0z}^2 + 2a(d_1 + z_0))^{\frac{1}{2}}} \tag{3.9}$$

By applying the space focussing condition $d(TOF_{WM})/d(z_0) = 0$, and temporarily assuming $v_{0z} = 0$, it is found that all single-field Wiley-McLaren spectrometers must have $d_2 = 2d_1$. The effect of non-zero v_{0z} is to shift the extremum of the TOF_{WM} vs. z_0 plot away from $z_0 = 0$. Even with the inclusion of non-zero v_{0z}, the beneficial effect of space-focussing can be easily seen in Figure 3.6, where comparisons of equivalent Wiley-McLaren and constant field spectrometers are shown.

Figure 3.7 shows the time spread due to the spatial extent of the interaction region in the z dimension, t_{sf}, as a function of the total spectrometer length for equivalent single field Wiley-McLaren and constant field spectrometers. As expected, the Wiley-McLaren spectrometer shows a much smaller time spread.

Figure 3.6: Comparison of TOF vs. z_0 profiles for equivalent (a,c) constant field and (b,d) space focussing single field Wiley-McLaren spectrometers. (a,c) d_1=45mm, E_{ext}=944V/m. (b,d) d_1=15mm, d_2=30mm, E_{ext}=1232V/m. In (a) and (b), the electron energies were 2.0eV and initial velocities were directed towards the detector ($\theta = 0°$). In (c) and (d), the electron energies were 2.0eV and initial velocities were directed perpendicular to the spectrometer axis ($\theta = 90°$). Note the much smaller time spread for the Wiley-McLaren spectrometer (b,d).

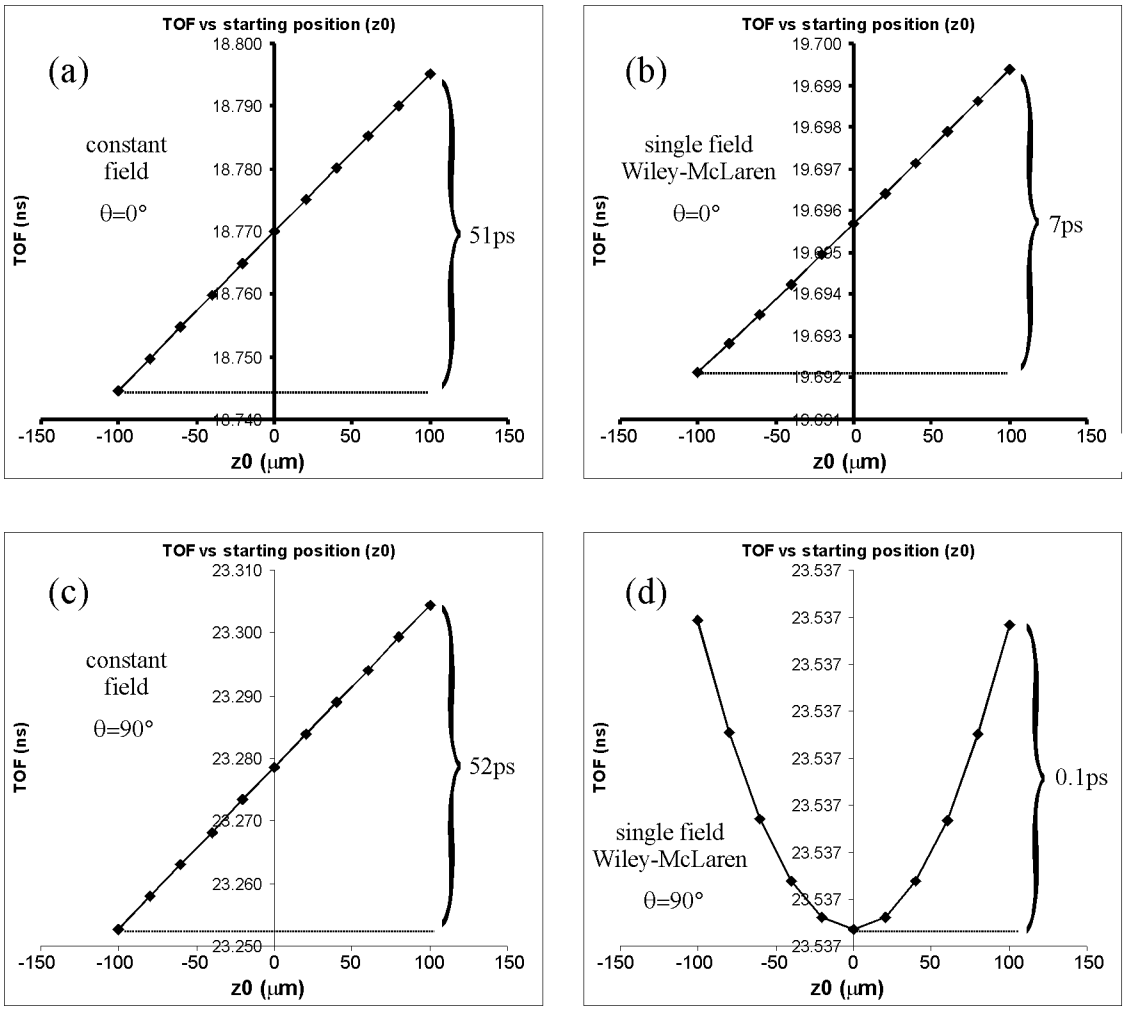

Figure 3.7: The time spread due to the spatial extent of the interaction region in the z-dimension versus the total spectrometer length for equivalent constant field and single field Wiley-McLaren spectrometers. The electrons are simulated for initial velocity directly along the spectrometer axis ($\theta = 0°$), the worst case scenario for the Wiley-McLaren spectrometer.

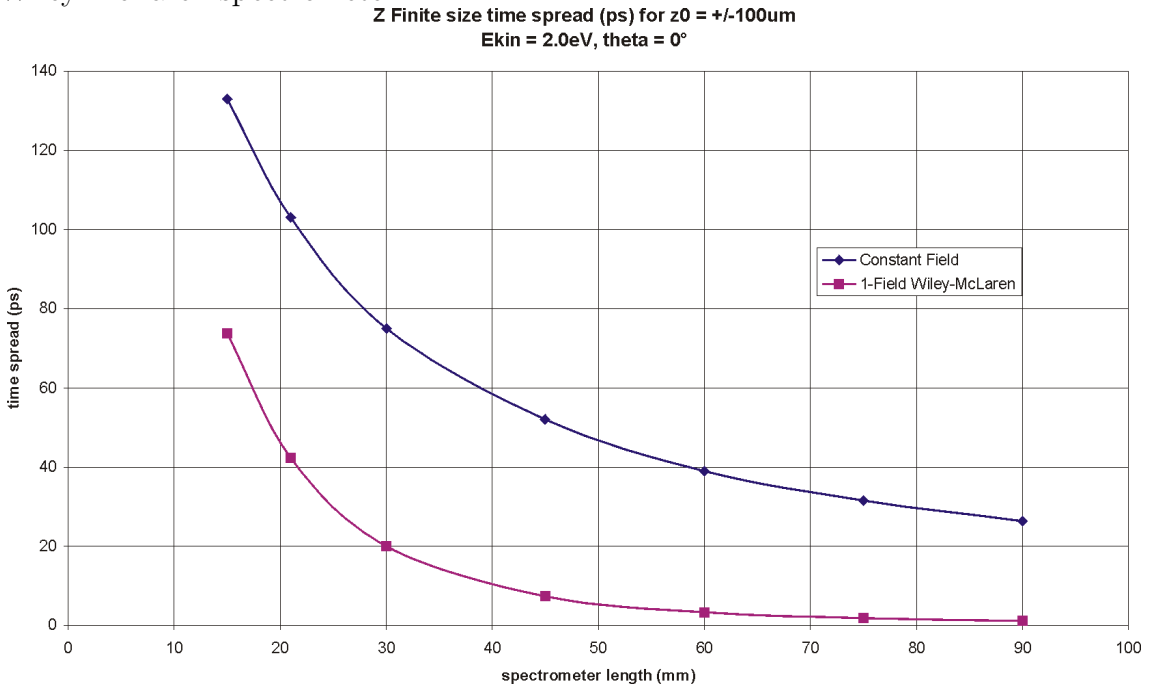

3.5.5 Electron Spectrometer: TOF Linearity

In a spectrometer it is desirable to have the TOF vary linearly with the initial v_{0z}. This allows for simple calibration and constant resolution for all v_{0z}. Both equations 3.8 and 3.9 can be rearranged to become

$$TOF = \frac{-v_{0z}}{a} + t_0 \tag{3.10}$$

where in the case of the constant field spectrometer

$$t_0 = t_{0,CF} = \frac{(v_{0z}^2 + 2a(d_1 + z_0))^{\frac{1}{2}}}{a} \tag{3.11}$$

and in the case of the single field Wiley-McLaren spectrometer

$$t_0 = t_{0,WM} = \frac{(v_{0z}^2 + 2a(d_1 + z_0))^{\frac{1}{2}}}{a} + \frac{d_2}{(v_{0z}^2 + 2a(d_1 + z_0))^{\frac{1}{2}}} \tag{3.12}$$

In the limit

$$v_{0z}^2 \ll 2a(d_1 + z_0) \tag{3.13}$$

both $t_{0,CF}$ and $t_{0,WM}$ become approximately constant and Equation 3.10 becomes linear with respect to v_{0z}. The condition expressed by Equation 3.13 is equivalent to a comparison of the initial electron energy in eV with the extraction voltage. If the initial energy of the electron is much less than the extraction voltage, Equation 3.13 holds true. The degree of linearity of Equation 3.10 for actual spectrometers is different for the two types of spectrometers. In the Wiley-McLaren spectrometer, the higher-order contribution of v_{0z} to the TOF is partially cancelled because it appears in the numerator of the first term and the denominator in the second term of Equation 3.12 whereas in the constant field spectrometer, there is only a single positive contribution (Equation 3.11). Also, extraction voltages are higher for Wiley-McLaren spectrometers compared to equivalent constant field spectrometers, so the

condition in Equation 3.13 becomes valid at shorter values of d_1. Thus, the Wiley-McLaren spectrometer approaches v_{0z} linearity faster than equivalent constant field spectrometers. "TOF vs. v_{0z}" plots are shown for equivalent spectrometers with total lengths 15, 30, and 45mm in Figure 3.8 (constant field) and Figure 3.9 (single field Wiley-McLaren). Notice the Wiley-McLaren spectrometer linear fits are significantly better than those for the constant field spectrometer.

3.5.6 Electron Spectrometer : v_z Resolution

Velocity resolution along the spectrometer axis is determined by the relative magnitudes of the turnaround time spread and the total timing error. Figure 3.10 shows the comparison of the turnaround time spread for both constant field and single field Wiley-McLaren spectrometers of varying lengths. Notice that the constant field spectrometer always has a larger turnaround time spread than the Wiley-McLaren spectrometer. This is because in the Wiley-McLaren spectrometer, larger extraction fields are needed to force the same energy electrons onto the same sized detector, thus the TOF spread is compressed more than in the case of the constant field spectrometer.

The time resolution, and therefore v_z resolution depends on how many 'effective' bins into which the electron TOF can be sorted. By 'effective' bins, we mean the turnaround time divided by the total timing error of the spectrometer. As stated above, this timing error depends on the electronics used, the timing error of the detector, and the apparent timing error due to electrons being produced at different locations within the ionizing volume. Figure 3.11 shows the number of 'effective' TOF bins for 2.0eV electrons for equivalent constant field and single field Wiley-McLaren

Figure 3.8: Linearity of "TOF vs v_z" for Constant Field electron spectrometers of lengths d_1=15, 30, and 45mm. Voltages were adjusted such that the maximum kinetic energies of electrons that were detected with 4π solid angle acceptance was 2.0eV.

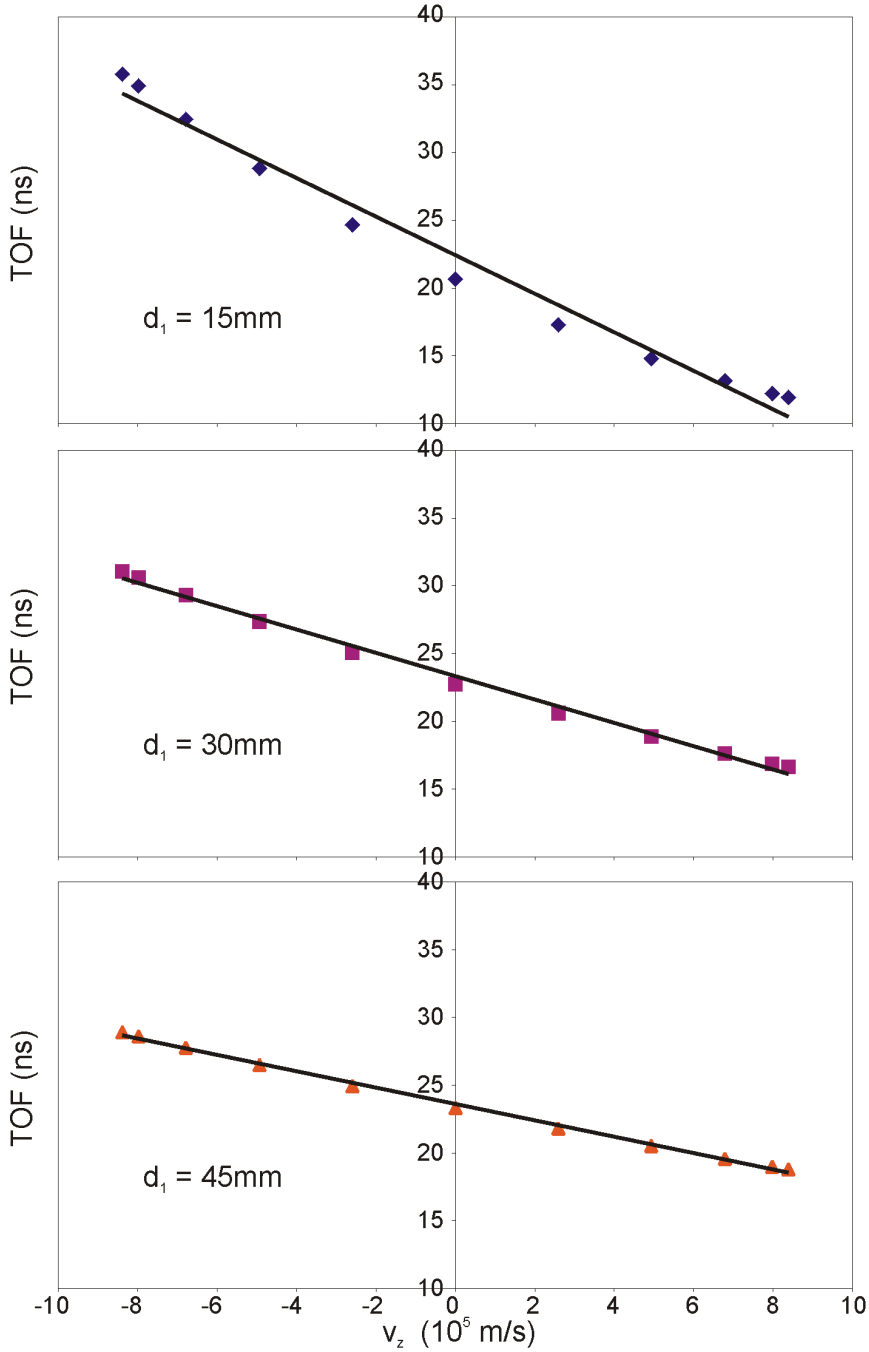

Figure 3.9: Linearity of "TOF vs. v_z" for single field Wiley-McLaren electron spectrometers of lengths d_1+d_2=15, 30, and 45mm. $d_2 = 2d_1$. Voltages were adjusted such that the maximum kinetic energies of electrons that were detected with 4π solid angle acceptance was 2.0eV. Note the better linearity of the single field Wiley-McLaren spectrometers compared to the constant field spectrometers shown in Figure 3.8.

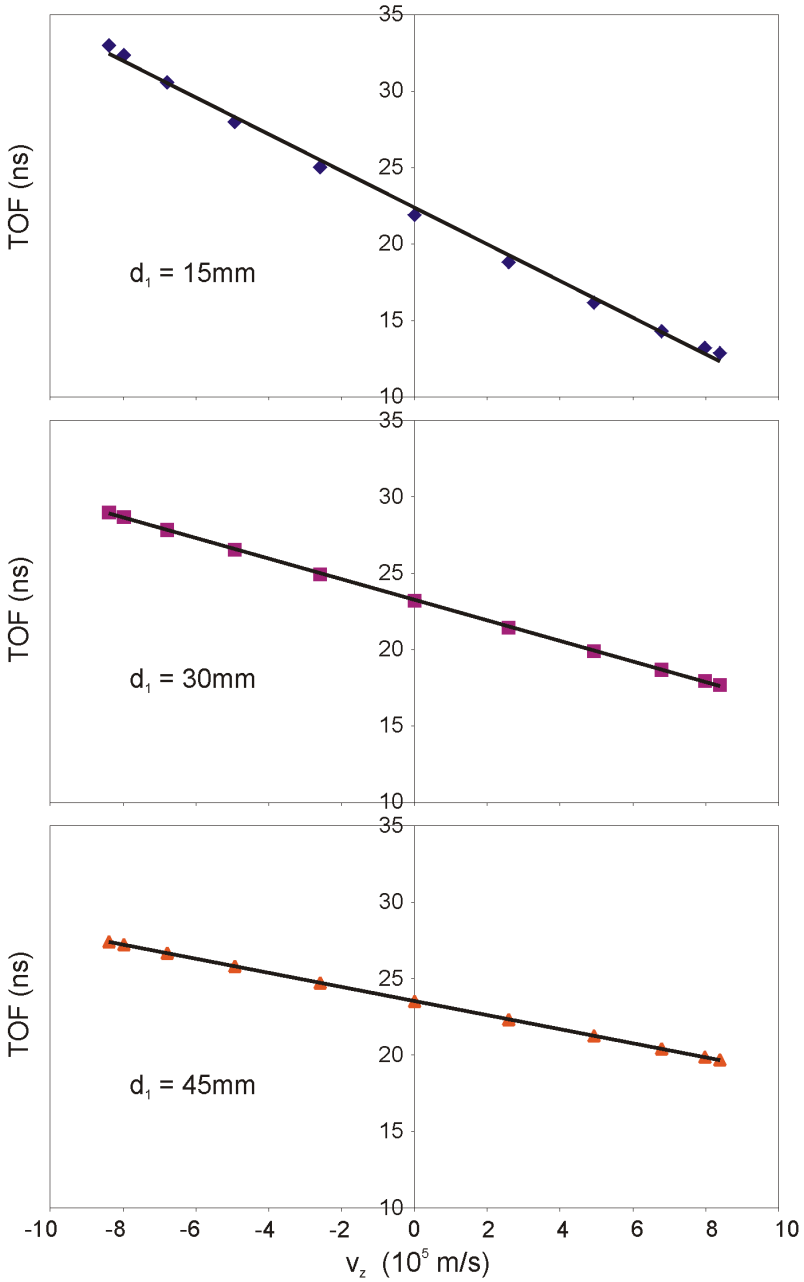

Figure 3.10: Turnaround time spread for equivalent constant field and single field Wiley-McLaren spectrometers of different lengths. Voltages were adjusted such that the maximum kinetic energies of electrons that were detected with 4π solid angle acceptance was 2.0eV.

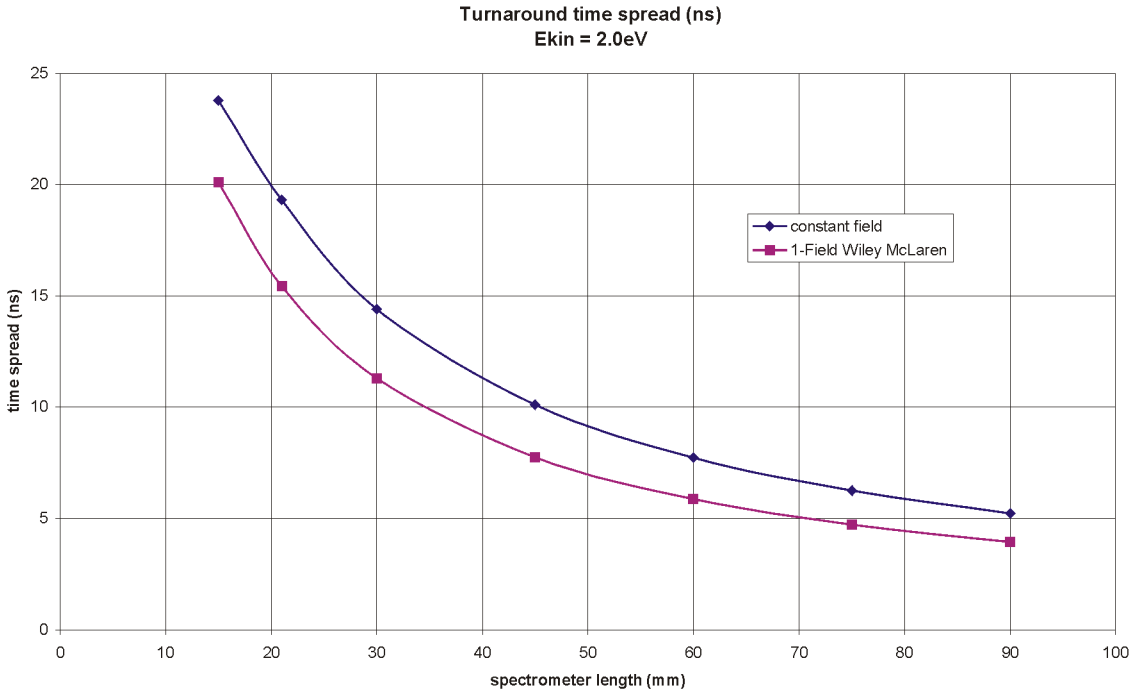

spectrometers of lengths between 15mm and 90mm, detector time resolution of 100ps, and spatial time spread origination from electrons born $\pm 100\mu m$ from the laser focus. Timing errors due to electronics were neglected. Error in determination of $t(v_{0z} = 0)$ was also ignored. On an absolute basis, the shorter spectrometers have more time bins in the z dimension and so also have better v_z resolution. The single-field Wiley-McLaren spectrometer is better than the constant field spectrometer at shorter spectrometer lengths up to about 30mm, beyond which the situation is reversed. The reason for this behaviour is that the constant field spectrometer always has the larger turnaround time spread (as seen in Figure 3.10) but for short spectrometers the timing uncertainty due to the spatial extent of the interaction region is larger and thus determines v_z resolution.

3.5.7 Electron Spectrometer Summary

There is no single perfect imaging electron spectrometer that covers all electron energies. In general, one should avoid making the spectrometer extremely short, to avoid nonlinear TOF profiles; or extremely long, which degrades v_z resolution by requiring high electric fields to keep the electrons on the detector.

3.6 Designing an Imaging Mass Spectrometer

In addition to obtaining accurate ion velocities, the ion spectrometer must be able to separate ions of differing charge to mass ratios. For the analysis presented here, a mass spectrometer is said to have resolution of M if it is separated in time from adjacent masses $M + 1$, and $M - 1$. For ions with kinetic energy release, this means

Figure 3.11: Overall resolution comparison of equivalent constant field and single field Wiley-McLaren spectrometers with varying lengths. The turnaround time spread divided by the total timing error is the number of 'bins' into which the v_z velocity can be sorted. Detector time resolution = 100ps. Spatial time spread originating from electrons $\pm$ 100μm from the laser focus. Errors due to the timing electronics and determination of t_0 were assumed to be negligible. Voltages were adjusted such that the maximum kinetic energies of electrons that were detected with 4π solid angle acceptance was 2.0eV.

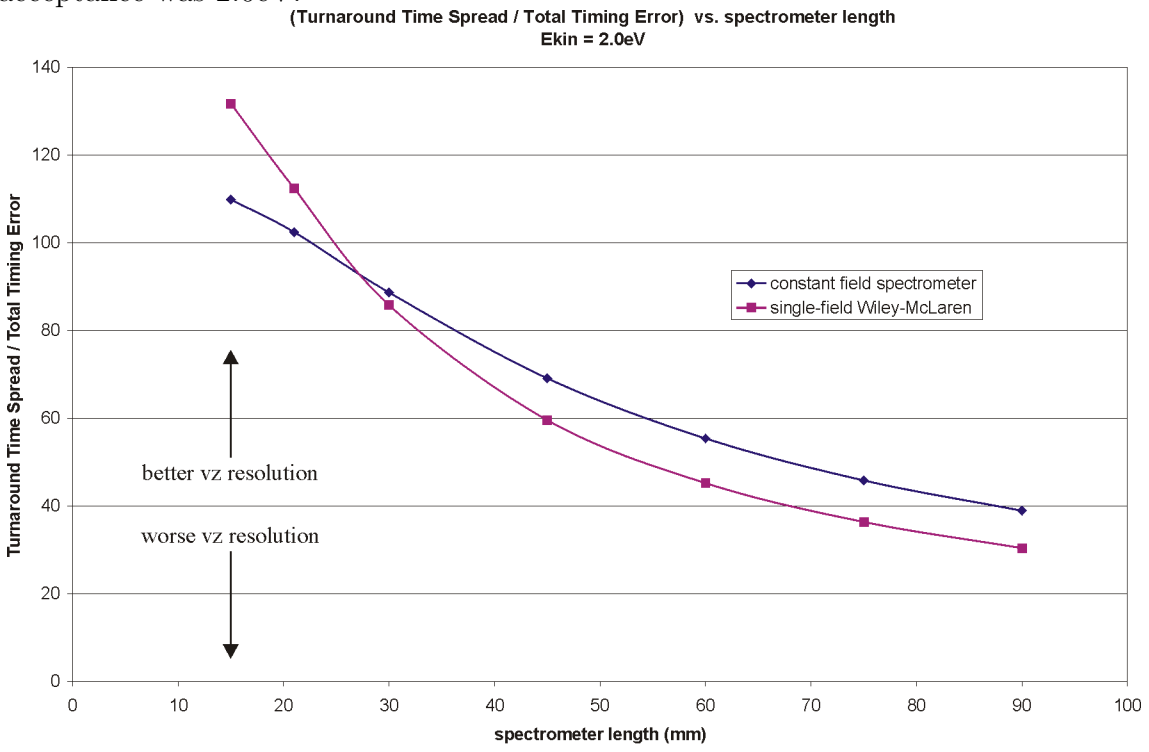

that ions of mass $M-1$ initially traveling away from the detector arrive before ions of mass M initially traveling towards the detector, and ions of mass M initially traveling away from the detector arrive before ions of mass $M+1$ initially traveling towards the detector.

Important objectives when designing an imaging mass spectrometer are the following:

- To minimize the effect of the spatial extent of the interaction region on ion TOF.
- To ensure linearity of the TOF with v_{0z}.
- To maximize v_{0z} resolution by maximizing the ratio of the turnaround time spread to the spectrometer timing error.
- To maximize radial hit position on the detector for greatest (v_x, v_y) resolution.
- To ensure 4π acceptance of ions taking into account the kinetic energy release of the reaction under study and the molecular beam velocity.
- To ensure high transmission efficiency of ions.
- To maximize mass resolution.

The spectrometer chosen for this study was the two field Wiley-McLaren spectrometer shown in Figure 3.12. This spectrometer consists of an extraction region, an acceleration region, and a field-free drift region each separated by conductive grids. The electric fields are designed to be as homogeneous as possible. As with the single field Wiley-McLaren spectrometer, by choosing the applied voltages appropriately,

the spectrometer is space focussing, having the first derivative of the ion TOF with respect to the ionization position along the z-axis equal to zero.

Figure 3.12: The two field Wiley-McLaren spectrometer, consisting of extraction region, acceleration region, and field-free drift region.

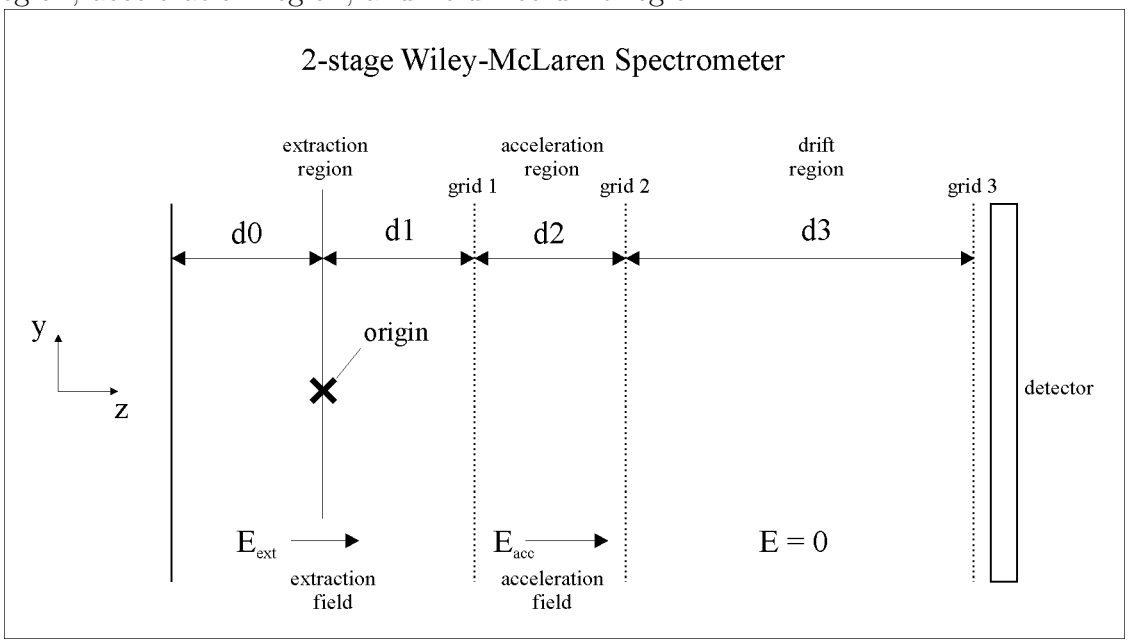

3.6.1 Imaging Ion Spectrometer Simulations

Ion trajectories $[x(t), y(t), z(t)]$ were simulated using the same initial parameters v_0, θ, and z_0 as defined for the electron trajectories in the preceding section. In addition, there are the initial parameters of molecular beam velocity, v_b, and the molecular beam velocity spread, Δv_b, oriented along the x-axis.

The following conditions were used in simulations described in this section:

1. The molecular beam velocity was taken to be 1800m/s ± 5%. These values approximately correspond to a supersonic expansion of helium containing a

low concentration of seed molecule though a 0.2mm nozzle from 300torr into vacuum.

2. When detecting photoelectrons and photoions in coincidence, it is necessary to first extract the electrons from the interaction region with a relatively weak field. Once the electrons have left the interaction region a larger field is needed to extract the considerably heavier ions. It was assumed that the electron extraction field was 1000V/m. The ion extraction field was applied 80ns after the ionization event.

3. The grids separating regions were assumed to be perfect grids: ie. the electric field changed abruptly at the grid boundary and there was no field penetration across the grid. Relaxation of this assumption is discussed in Section 3.6.9.

4. The trajectories were simulated only until the final grid. As with the electron spectrometer, there is usually a gap between the final grid and the detector enclosing a region with a relatively large electric field. This must not be overlooked when designing the actual spectrometer electrodes.

5. When an ion with a certain energy, E, is said to fit on the detector, it is meant that a spherical distribution of ions with energy E completely fits on the detector. (ie. the spectrometer's acceptance solid angle is 4π for ions with energy E)

3.6.2 The Wiley-McLaren Spectrometer: Space Focussing

The Wiley-McLaren spectrometer is by definition space focussing. Ignoring the effect of the extraction pulse delay, the TOF for an ion in the 2-stage Wiley-McLaren

spectrometer is

$$\begin{aligned} TOF_{2WM} &= \frac{-v_{0z}+\sqrt{v_{0z}^2+2a_1(z_0+d_1)}}{a_1} \\ &+\frac{-\sqrt{v_{0z}^2+2a_1(z_0+d_1)}+\sqrt{v_{0z}^2+2a_1(z_0+d_1)+2a_2d_2}}{a_2} \\ &+\frac{d_3}{\sqrt{v_{0z}^2+2a_1(z_0+d_1)+2a_2d_2}} \end{aligned} \tag{3.14}$$

where a_1 and a_2 are the accelerations of the ions in the extraction and acceleration regions respectively. The accelerations are $a_1 = qE_{ext}/m$ and $a_2 = qE_{acc}/m$, m being the mass of the ion.

By setting the first derivative of the TOF with respect to z_0 to zero and assuming $v_z = 0$, we arrive at the Wiley-McLaren constraint for space focussing:

$$\frac{a_2-a_1}{\sqrt{a_1(z_0+d_1)}}+\frac{a_1}{\sqrt{a_1(z_0+d_1)+a_2d_2}}-\frac{a_1a_2d_3}{2(a_1(z_0+d_1)+a_2d_2)^{\frac{3}{2}}}=0 \tag{3.15}$$

As in the case for the single field Wiley-McLaren spectrometer, when the initial ion kinetic energy is non-zero, the ability to space focus is slightly degraded. For a given Wiley-McLaren spectrometer with lengths d_1, d_2, and d_3, the Wiley-McLaren condition is a single constraint that specifies the ratio between the applied fields E_{ext}, and E_{acc}. Our second constraint is to maximize the image size on the detector to obtain maximal (v_x, v_y) resolution.

3.6.3 The Wiley-McLaren Spectrometer: The Extraction Region

The extraction field turns around ions that are initially travelling away from the detector. Mass resolution can be improved by employing a high field in this region. This is because the initial velocity distribution of the ions is compressed in time by

the high field making the TOF through the spectrometer less dependent on the initial velocity. However, this increase in mass resolution is offset by loss of resolution in v_z, and v_x and v_y: the former because of a decrease in the TOF spread; and the latter because of an overall TOF decrease causing the image to be smaller on the detector. Figure 3.13 shows the dependence of mass resolution and turnaround time spread vs. E_{ext} for a Wiley-McLaren spectrometer with dimensions d_1=15mm, d_2=10mm, and d_3=300mm. Space focussing time spread error for ions originating $\pm$ 100μm from the origin is on the order of a few ps. Since this is negligible compared to the timing error of the detector, the number of effective bins for v_z is directly proportional to the turnaround time spread of the ions.

Figure 3.13: Dependence of mass resolution and turnaround time spread on extraction voltage E_{ext}. Initial ion energies were 0.1eV. For simulation of turnaround times, m/z = 40 was used. d_1=15mm, d_2=10mm, d_3=300mm. E_{acc} was adjusted to fulfill the Wiley-McLaren constraint.

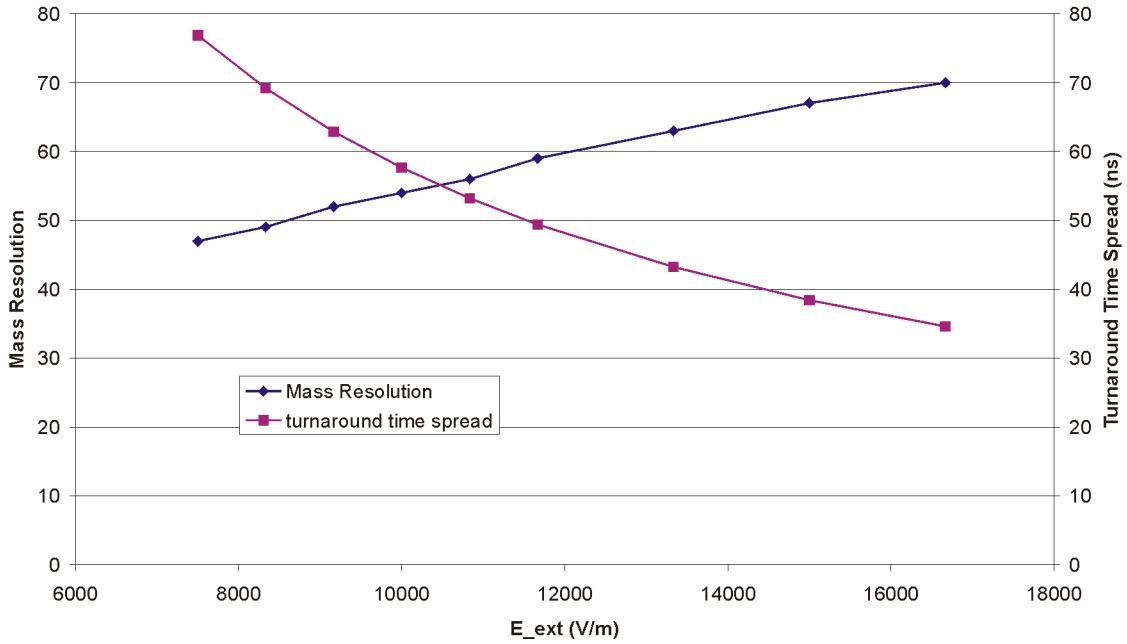

The mass resolution is not greatly affected by the length of the extraction region. Figure 3.14 shows the mass resolution dependence on the extraction region length for 0.1eV ions using extraction fields of 10,000V/m and 15,000V/m.

Figure 3.14: Dependence of mass resolution on d_1, the extraction region length, for extraction fields 10000V/m and 15000V/m. d_2=10mm, d_3=300mm. E_{acc} was adjusted to fulfill the Wiley-McLaren constraint. The initial energies of the ions were 0.1eV.

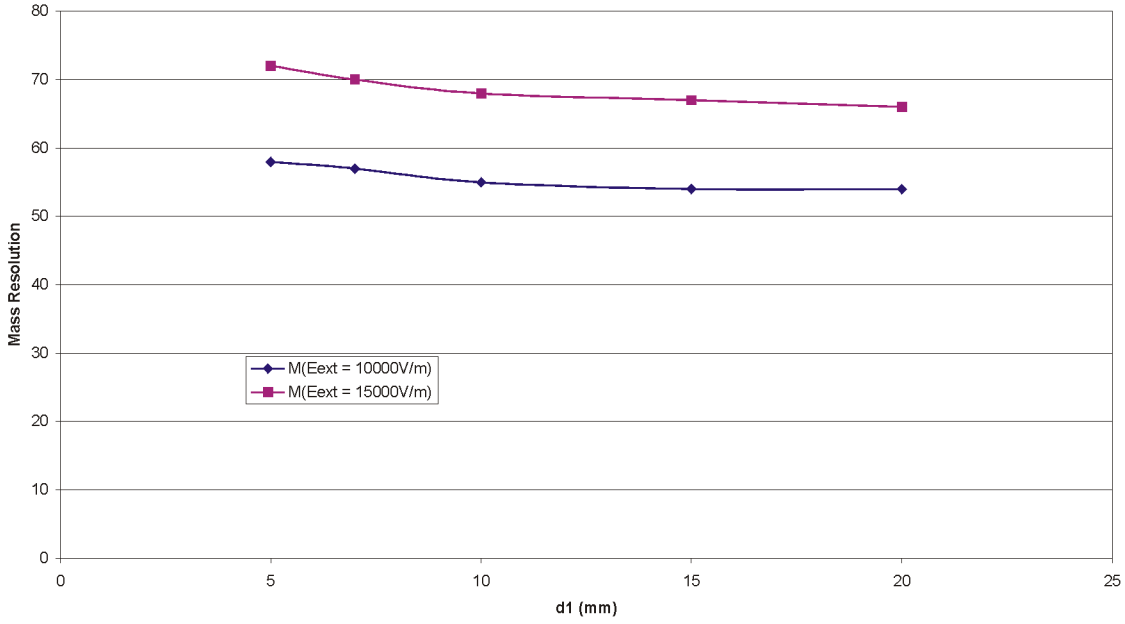

3.6.4 The Wiley-McLaren Spectrometer: The Acceleration Region

The purpose of the acceleration region is to give the ions an extra kick of energy following the extraction region. This increases the distance between the centre of interaction and the point where space focussing occurs in the field free drift region (ie. where ions with equal v_z but different z_0 pass at the same TOF). This increase is

desirable because better mass separation is possible with longer drift regions. If the acceleration region was removed, the two field Wiley-McLaren spectrometer becomes the single field Wiley-McLaren and space focussing occurs at twice the interaction region flight length.

The length of the acceleration region is not critical for mass resolution as can be seen in Figure 3.15, where mass resolution as a function of d_2 is plotted. Usually this region is chosen to be reasonably short to keep the overall length of the spectrometer shorter. Although having little effect on the mass resolution, the length of the acceleration region does affect the magnitude of the electric field in the acceleration region. The magnitude of the acceleration field can improve or worsen the effect of grid lensing, which destroys (v_x, v_y) resolution. This point will be discussed in detail in Section 3.6.9.

3.6.5 The Wiley-McLaren Spectrometer: The Drift Region

As stated earlier, the mass resolution greatly depends on the length of the drift region. This is shown in Figure 3.16 where mass resolution is plotted against length of the drift tube. Mass resolution improvements can be made with longer flight tubes, but cannot be made excessively long or else the average molecular beam velocity carries the ions off the edge of the detector.

To alleviate the problems of the molecular beam carrying the ions off the detector, the detector axis can be offset from the spectrometer axis in the direction of the molecular beam. This can extend the high mass range of the ion spectrometer to include ions that would otherwise miss the detector. Ramifications of displacing the detector off axis are discussed in following sections.

Figure 3.15: Dependence of mass resolution on d_2, the acceleration region length, for extraction fields 10000 V/m and 16667 V/m. d_1=15mm, d_3=300mm. E_{acc} was adjusted to fulfill the Wiley-McLaren constraint. The initial energies of the ions were 0.1eV.

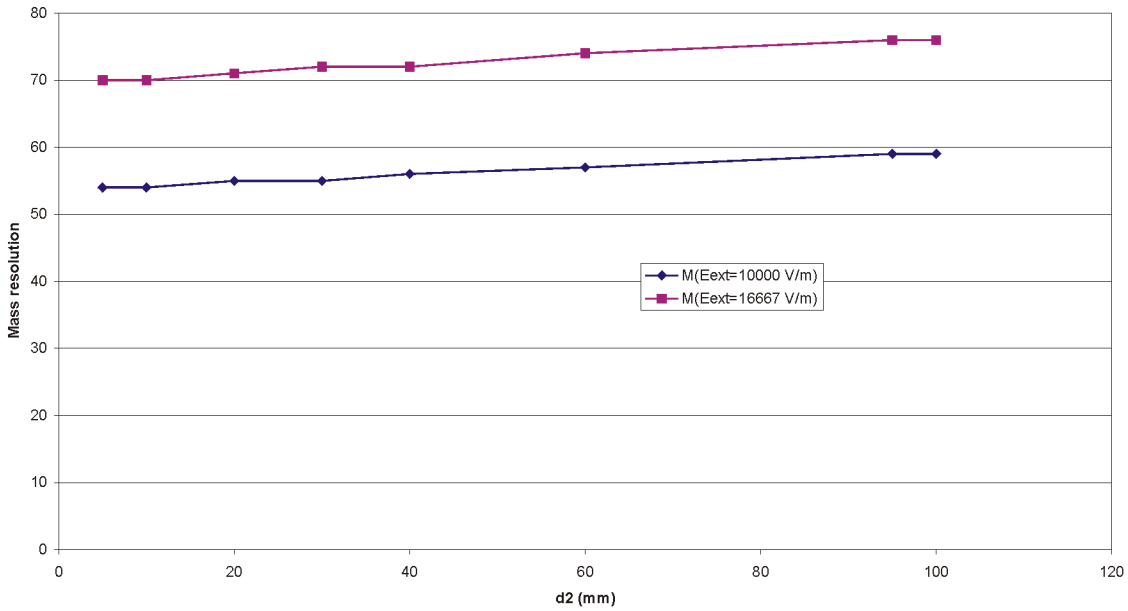

3.6.6 Ion TOF and Linearity

Inspection of Equation 3.14 reveals that the TOF is approximately linear with v_{0z} if the following condition is valid:

$$v_{0z}^2 \ll 2a_1(z_0 + d_1) \tag{3.16}$$

Similar to the electron spectrometer, this condition is equivalent to a comparison of the initial ion energy in eV with the ion extraction voltage. If the initial energy of the ion is much less than the extraction voltage, the condition of Equation 3.16 holds true. We expect ion energies to be on the order of 1eV, while extraction voltages are typically several 10's or 100's of volts. Thus, the TOF linearity condition is easily fulfilled. The constant of proportionality between the ion TOF and v_{0z} is the

Figure 3.16: Mass resolution dependence on drift tube length, d_3 for extraction fields 10000V/m and 16667V/m. d_1=15mm, d_2=10mm. E_{acc} was adjusted to fulfill the Wiley-McLaren constraint. The initial energies of the ions were 0.1eV.

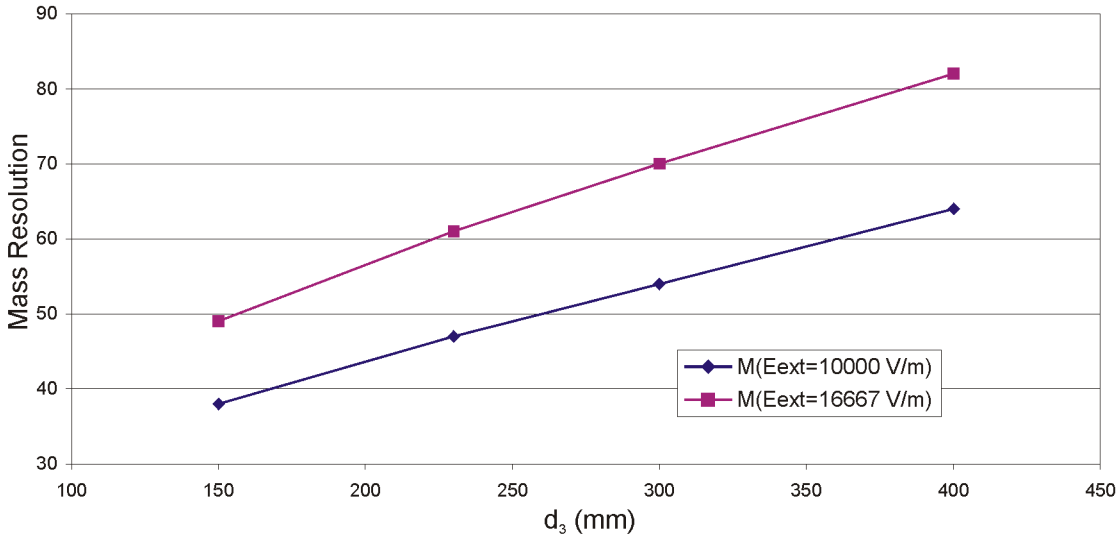

reciprocal of the acceleration in the extraction region $1/a_1 = m/qE_{ext}$.

If v_{0z} and z_0 are temporarily assumed to be zero, Equation 3.14 can be rearranged to show that the TOF for a mass m, simplifies to

$$TOF_m(v_{0z} = 0, z_0 = 0) = t_0 = km^{\frac{1}{2}} \tag{3.17}$$

where k is a spectrometer constant. k can be calculated if the TOF is known for a particular mass. Combining Equation 3.17 with the TOF linearity approximation, we arrive at a much simplified expression for the ion TOF t:

$$\begin{aligned} t &= km^{\frac{1}{2}} - \frac{m}{qE_{ext}}v_{0z} \\ &= m^{\frac{1}{2}}(k - c) \end{aligned} \tag{3.18}$$

It is useful to parameterize the quantity c in terms of the initial ion kinetic energy E:

$$c = \frac{v_{0z}\sqrt{m}}{qE_{ext}} = \frac{\sqrt{2E}}{qE_{ext}}. \tag{3.19}$$

3.6.7 Mass Range Detection and Beam Velocity

Often, unit mass resolution is not necessary for a particular experiment (eg. if H atom loss is not involved, or the sample is sufficiently isotopically pure). In this case, an ion spectrometer is still successful in separating masses higher than the previously defined mass resolution. Yet, due to the average molecular beam velocity, the maximum mass that can be forced onto the detector is not infinite. The maximum mass with energy E that can be measured by the spectrometer, $m_{\max}$, is approximately

$$m_{\max} \approx \frac{1}{v_b^2}\left(\frac{x_{\text{det,max}}}{k} - \sqrt{2E}\right)^2 \tag{3.20}$$

where v_b is the molecular beam velocity. $x_{\text{det,max}}$ is the maximum extent of the detector in the x dimension, which is the sum of the detector radius r_{det} and any offset in the direction of the molecular beam x_{offset}:

$$x_{\text{det,max}} = r_{\text{det}} + x_{\text{offset}} \tag{3.21}$$

If the term inside the brackets in Equation 3.20 is negative, no mass with kinetic energy E can be fully imaged onto the detector using that particular set of electric fields and spectrometer distances.

If the detector is offset from the spectrometer axis, there is also the possibility that light ions with high kinetic energy release traveling back towards the molecular beam source will not hit the detector. The minimum mass with energy E that can be measured by the spectrometer $m_{\min}$, is approximately

$$m_{\min} \approx \frac{1}{v_b^2}\left(\frac{x_{\text{det,max}}}{k} + \sqrt{2E}\right)^2. \tag{3.22}$$

$x_{\text{det,min}}$ is the minimum extent of the detector in the x dimension, which is

$$x_{\text{det,min}} = -r_{\text{det}} + x_{\text{offset}}. \tag{3.23}$$

3.6.8 Maximum Resolvable Mass

A useful quantity to estimate is the maximum mass M that is resolvable by the spectrometer. This can be calculated by using Equation 3.18 to equate the TOFs for M ions travelling away from the detector and $M+1$ ions towards the detector, and then solving for M. For ions with initial energy E, the maximum resolvable mass in amu is

$$M \leq \frac{(k-c)^2}{4kc} \tag{3.24}$$

where k and c are defined previously.

If a mass m is greater than the maximum resolvable mass M, it is interesting to know what are the closest masses to m that are resolved. These are referred to as adjacent resolvable masses. The closest resolved more massive ion m_+, and less massive ion m_- are

$$m_+ \geq m\frac{(k+c)^2}{(k-c)^2} \tag{3.25}$$

$$m_- \leq m\frac{(k-c)^2}{(k+c)^2}. \tag{3.26}$$

3.6.9 Non-Ideality of Spectrometer Grids

Unfortunately, due to the requirement that large fields are needed to accelerate ions inside the spectrometer, the assumption of perfect grids becomes invalid. An aperture behaves like an electrostatic lens when there are differing fields on either side of the aperture. The field lines from the higher field region bulge through the aperture and cause the aperture to act as either a positive or negative lens. Conductive grids act as an array of these aperture lenses that can severely damage (x, y) imaging.

When the energy of the particle passing through the lens is much larger than the

energy change caused by the lens, ie. when the grid deflection is small, the lens' focal length, f, of a particle passing from a region with field E_1 to a region with field E_2 can be approximated as[80][81]:

$$f = \frac{4T}{q(E_2 - E_1)} \tag{3.27}$$

where T is the kinetic energy of the particle, and q is its charge. The maximum deflection, θ_{defl}, occurring when the particles pass close to the edge of the aperture is approximately

$$\theta_{defl} = \frac{a}{2f} \tag{3.28}$$

where a is the diameter of the aperture. Therefore, to reduce the angular deflection, it is desirable to use very fine meshes with very small apertures. However, small aperture meshes generally have low open areas with low transmission leading to low ion detection efficiency. In coincidence experiments, high detection efficiency is critical to obtaining high coincidence rates. Therefore, some compromise must be made between blurred (x, y) resolution (caused by aperture lensing), and detection efficiency.

In the spectrometer, when positively charged ions pass through the first grid from the lower field extraction region to the higher field acceleration region, they experience a positive lensing effect. On passing through the second grid into the field free drift region, they experience a negative lensing effect. The signs of the lensing effects from the two grids are insignificant.

In this work, the effects of the two grid lenses were treated individually and the blurring they introduce was assumed to be uncorrelated. The maximum spatial errors at the detector caused by the first and second grids, Δr_{g1} and Δr_{g2}, were taken to be $\theta_{defl,1} \times (d_2 + d_3)$ and $\theta_{defl,1} \times d_3$ respectively. The total deflection, Δr_g was is then

the square root of the sum of the squares of the individual errors:

$$\Delta r_g = \sqrt{(\Delta r_{g1})^2 + (\Delta r_{g2})^2} \tag{3.29}$$

Deflections at the detector due to the two grids were calculated using a selection of commercially available conductive meshes[1]. Meshes with 1500, 1000, 750, 500, 333, 200, and 117 lines/inch grids with transmissions 44, 50, 55, 60, 70, 78, 86% respectively were chosen for investigation [2]. The spectrometer lengths were varied and the voltages were optimized using the Wiley-McLaren constraint at each set of spectrometer distances. The results of these simulations are shown in Figure 3.17 (d_1 varied), Figure 3.18 (d_2 varied), and Figure 3.19 (d_3 varied). Note for the same mesh density, the grid between the extraction and acceleration regions deflects the particles significantly more than the grid between the acceleration and drifts regions.

The lensing effect of both grids can be greatly reduced by increasing the length of the acceleration region because the electric field differences across the grids decreases dramatically. With smaller lensing effects, a sparser mesh can be used which increases the detection efficiency of the ions.

3.6.10 Ion Y Resolution: Along the laser beam

In the y-dimension, along the laser axis, the size of the interaction region blurs the image at the detector. The effect of the blurring can be minimized by expanding the image as widely as possible onto the detector. This means reducing the extraction

[1]Mesh selection taken from InterNet Incorporated.
http://www.internetplastic.com/intromesh.html

[2]After these simulations were complete, we discovered another supplier of electroformed meshes with significantly higher transmission (80, 40, 20, 8, 4 lines/mm with transmissions 47, 59, 79, 89, 91% respectively, distributed through GPTA, Berlin, Germany). These grids were used in our spectrometer.

Figure 3.17: Grid 1 (a) and Grid 2 (b) deflection effects at the detector for d_2=10mm, d_3=300mm and varying dimensions of d_1. Deflections for 1500, 1000, 750, 500, 333, 200, 117 lines/inch grids with transmissions 44, 50, 55, 60, 70, 78, 86% respectively were calculated. Electric fields were calculated using the Wiley-McLaren constraint. Note that deflections due to Grid 1 are many times greater than deflections due to Grid 2.

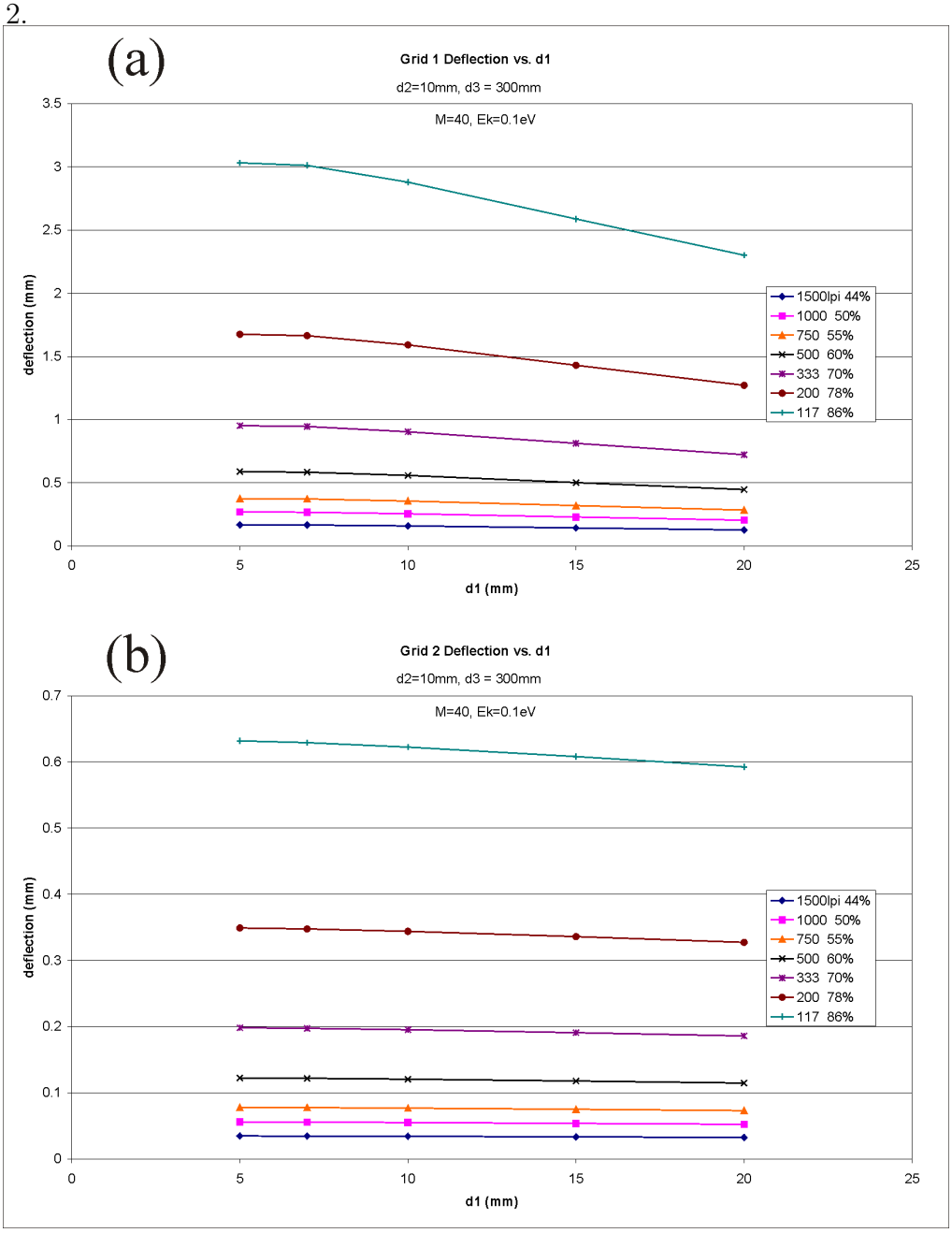

Figure 3.18: Grid 1 (a) and Grid 2 (b) deflection effects at the detector for d_1=15mm, d_3=300mm and varying dimensions of d_2. Deflections for 1500, 1000, 750, 500, 333, 200, 117 lines/inch grids with transmissions 44, 50, 55, 60, 70, 78, 86% respectively were calculated. Electric fields were calculated using the Wiley-McLaren constraint. Note that deflections due to Grid 1 are many times greater than deflections due to Grid 2.

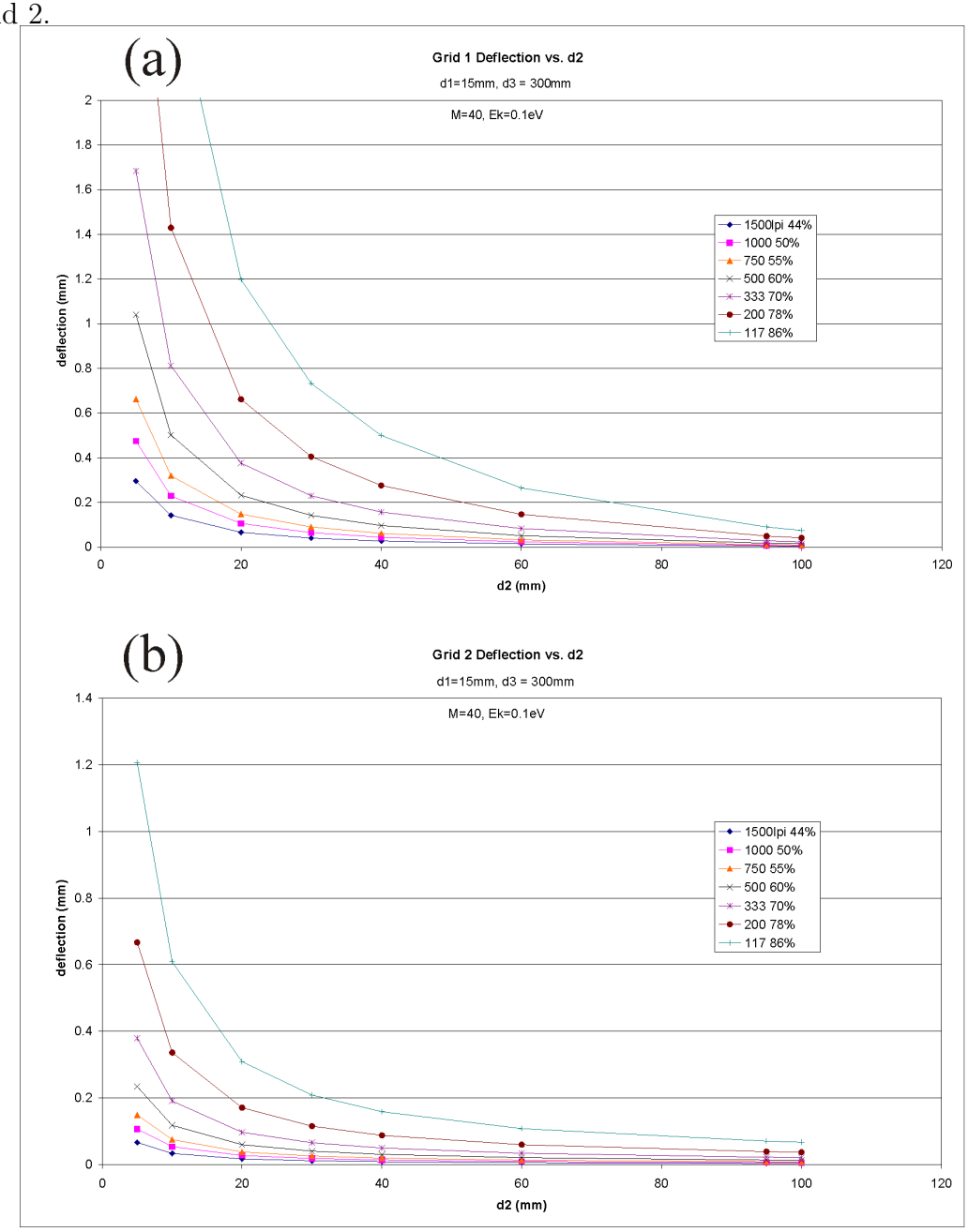

Figure 3.19: Grid 1 (a) and Grid 2 (b) deflection effects at the detector for d_1=15mm, d_2=300mm and varying dimensions of d_3. Deflections for 1500, 1000, 750, 500, 333, 200, 117 lines/inch grids with transmissions 44, 50, 55, 60, 70, 78, 86% respectively were calculated. Electric fields were calculated using the Wiley-McLaren constraint. Note that deflections due to Grid 1 are many times greater than deflections due to Grid 2.

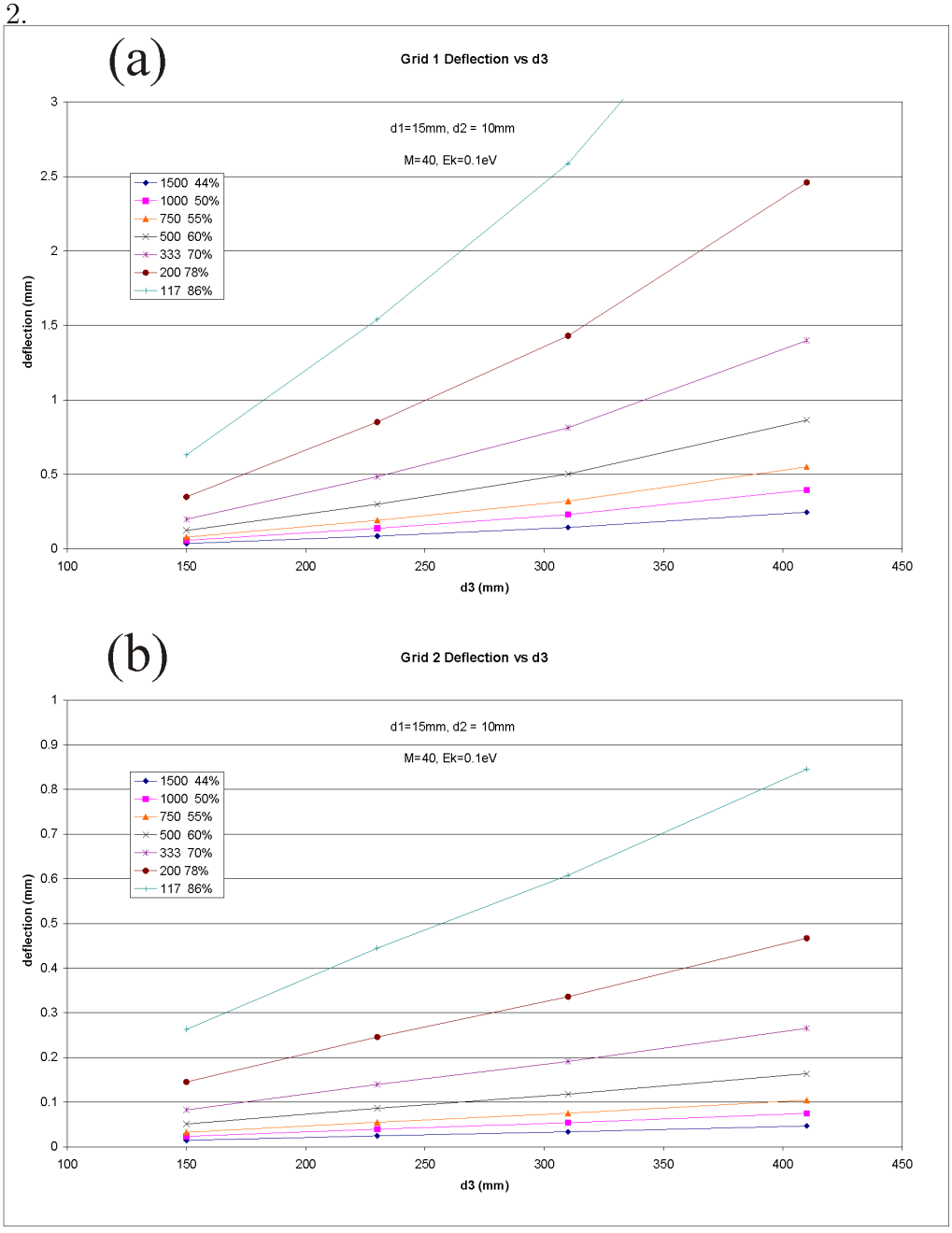

field of the spectrometer. Unfortunately, by reducing the extraction field, the ion TOF increases, which can result in the ion of interest flying out of the view of the detector because of the average molecular beam velocity. As discussed previously, shifting the detector axis in the direction of the molecular beam can help mediate this problem.

The width of the interaction region in the y-dimension can be narrowed by using a small diameter molecular beam skimmer or aperturing the beam. Both of these solutions reduce the signal intensity so they cannot be made arbitrarily small. Also, care must be taken to avoid heating of the molecular beam due to scattering from the apertures. The molecular beam skimmer or aperture should be placed as close as possible to the laser focus to reduce the angular spread of the molecular beam.

3.6.11 Ion X Resolution: Along the molecular beam

In the x-dimension, resolution is degraded by the interaction region's finite size and the molecular beam velocity spread. The size in the x-dimension is only the width of the laser focus (10's of μm) so the primary problem is the molecular beam velocity spread. The beam velocity spread can be reduced if a very short pulsed molecular beam is used. Recent advances in pulsed valve construction have permitted sub-10μs gas pulse production at kilohertz repetition rates These valves allow backing pressures of >100 bar to be used with minimal pumping requirements [82]. High backing pressure enables the production of very cold molecular beams with small velocity spread. Also, the velocities within short gas pulses can temporally disperse such that the laser pulse selects a subset of molecular beam velocities, thus reducing the velocity spread blurring at the detector.

3.6.12 Imaging Ion Spectrometer Summary

There is no perfect ion spectrometer for all ions and ion energies. One must have an estimate of ions and energies that are expected. A compromise must be made weighing the factors of mass resolution, minimum-maximum measurable masses, v_{0z} resolution, grid deflection, and ion detection efficiency.

Chapter 4

The NRC CIS Spectrometer

4.1 Introduction

In the preceding chapter, general spectrometer design issues were explored. This chapter describes the specifications for the coincidence imaging spectrometer built at the National Research Council's Steacie Institute for Molecular Sciences Labs in Ottawa. The first step in designing a spectrometer is to define the expected mass and energy ranges for the ions and electrons to be measured. The dimensions of the spectrometer must be chosen to measure these ions and electrons as precisely as possible. The time and position sensitive detectors are critical to the realization of the spectrometer. The detectors chosen for this spectrometer are a considerable improvement over previous ones because they are able to distinguish between real events and events caused by scattered UV light. Numerical simulations used to ensure electric field homogeneity for the designed electrodes are described here. Also explained are the detailed specifics for the electron and ion spectrometers, and their design into a unified instrument inside the vacuum chamber.

4.2 Energy Ranges of Interest in Chemical Dynamics Experiments

For our chemical dynamics experiments, we have the ability to tune our pump and probe lasers from the UV (∼200nm) throughout the visible range. Therefore, we have some choice over the energies of photoelectrons that are generated. Usually, these are chosen to lie in the range of $\lessapprox$2eV.

For ions, we also expect to have energies $\lessapprox$2eV. For the NO dimer photodissociation to NO(A) and NO(X) described in Chapter 7 using 208.8nm light, the maximum kinetic energy release for the NO fragments is 0.4eV. Hydrogen atoms are best detected using spectrometers designed for their detection, so the lowest mass fragment that we wish to detect is likely M∼15 (CH_3). The upper mass limit is somewhat harder to predict. The highest mass atomic species is probably M∼127 (iodine). Molecular species have the possibility of being much higher in mass.

4.3 Crossed Delay Line (XDL) Detectors

For our detectors, we chose the Crossed Delay Line (XDL) electron and ion detectors purchased from Siegmund Scientific (now Sensor Sciences LLC, Pleasant Hill, CA) [33]. These are schematically shown in Figure 4.1. Microchannel plates (MCPs) are used to amplify single ions or electrons into easily detectable electrical signals. Our plates are approximately 1mm thick and 46mm in diameter. They consist of an array of micron-sized diameter glass channels oriented with their channel axes at a slight angle to the surface normal of the disk. High voltage is placed across these channels. Amplification occurs when a particle is accelerated into the wall of the channels,

causing multiple electrons to be emitted. These secondary electrons are accelerated down the channel by the increasing potential, striking the walls of the channels to emit more electrons. This process is repeated many times until the electrons exit the channel. Amplification factors of 10^3 to 10^7 are common for single MCP and triple MCP stacks (Z-stacks) respectively. Since particles enter a single channel and the electron avalanche at most spreads to a few neighbouring channels, the position information of the incident particle is preserved from entrance to exit.

Figure 4.1: Schematic drawing of the Crossed Delay Line (XDL) detector. Modified from [33].

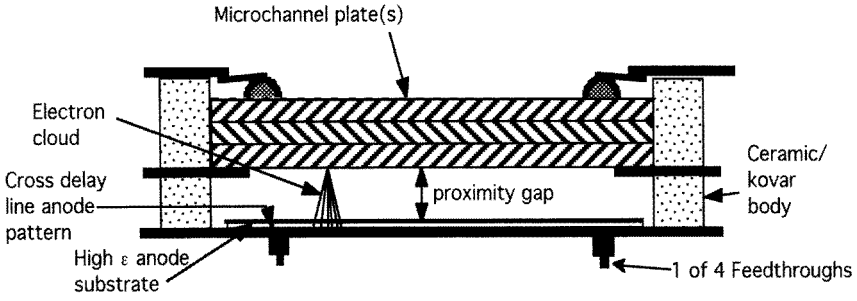

The charge cloud from the MCP falls on a specially patterned multilayered anode. The top and bottom layers are a set of conductive fingers that extend over the MCP active area in either the x or y directions. A schematic of this finger arrangement is shown in Figure 4.2. A photograph of the actual XDL anode is shown in Figure 4.3. The top and bottom layers are separated by a three layer insulator-ground-insulator sandwich patterned like the top layer of conductive fingers. The purpose of the ground layer is to reduce cross talk between the x and y fingers and provide a ground plane against which pulses hitting the top layer can propagate. The electron charge cloud falling on the anode divides between the x and y fingers. Typically, the spreading charge cloud from the back of the MCP covers 3 fingers in each dimension. One end

of the x and y fingers connect to separate serpentine delay lines. Upon reaching the serpentine delay line, the pulse resistively bifurcates to travel towards both ends of the delay line. Each end of the delay line (2 for each direction, 4 in total) is wired to a signal feedthrough. By measuring the time delay between the arrival of the pulses on either end of the delay line, it is possible to measure the position along that dimension. The second delay line allows the 2-dimensional hit position of the charge cloud, and thus the original particle hit position on the MCP, to be determined. Since the position measurement by these detectors requires only the timing measurement of 4 electronic pulses per event, these detectors can easily measure at 100s of kHz[33].

By managing the detector voltages and electronics very carefully, this type of XDL detector has been shown to have resolution better than 25μm. This is significantly better than that of similar wire-wound detectors ($\sim$ 200μm) [83]. The tuning of the electronics associated with these XDL detectors is non-trivial and will be discussed in Chapter 5.

The active area of our XDL detectors is 40.5mm in diameter. The lengths of the x and y delay lines are approximately 20ns for both detectors. This delay line length is important because it is shorter than the electron TOF. Previous experimental setups revealed that scattered UV laser light impinging on the detectors can be a significant source of spurious counts on the detectors. By having such short propagation times, the signals from scattered light are completely off the anode by the time that the first electrons arrive at the detector. Thus, it is possible to remove the interference from the spurious events by gating with the data acquisition electronics.

Figure 4.2: Schematic drawing of the XDL detector anode. The x and y fingers are separated by insulators and a ground plane. Pulses from the electron charge cloud from the MCP travel along the fingers to the serpentine delay line where they bifurcate and travel to the ends of the delay line. The time difference between arrival of the pulses indicates the hit location.

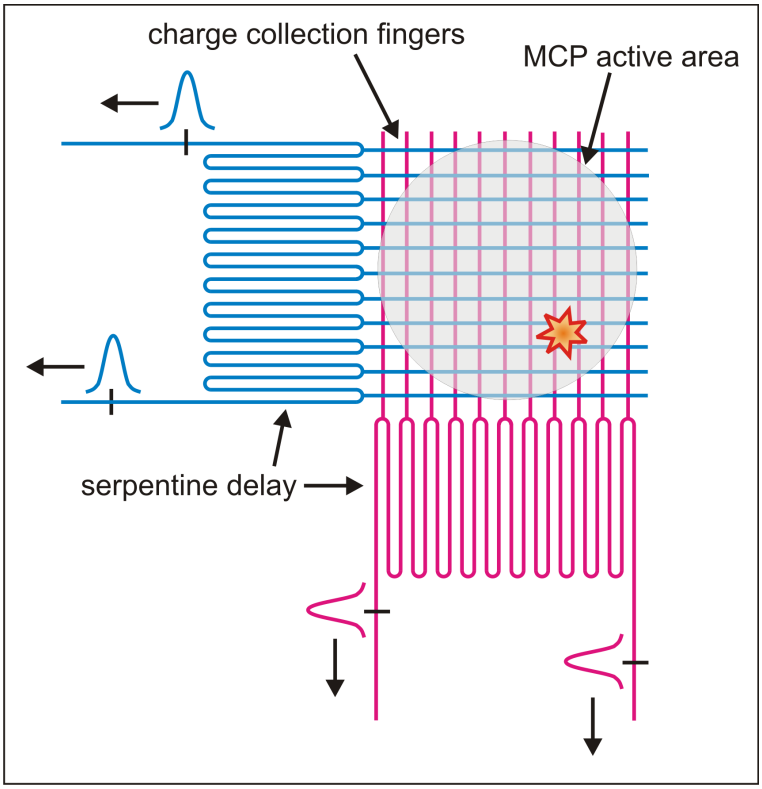

4.3.1 Ion Detector vs. Electron Detector

It is convenient to have one of the electrodes near the spectrometer interaction region to be held at earth ground. For a Wiley-McLaren spectrometer, the potential differences required for mass separation and energy resolution of ions are typically in the hundreds to a few kilovolts range. To make sure that the ions are accelerated all the way to the detector, the front face of the MCP must be biased to negative high voltage. At the MCP front face, the impacting ions cause the release of electrons that

Figure 4.3: Photograph of an XDL anode.

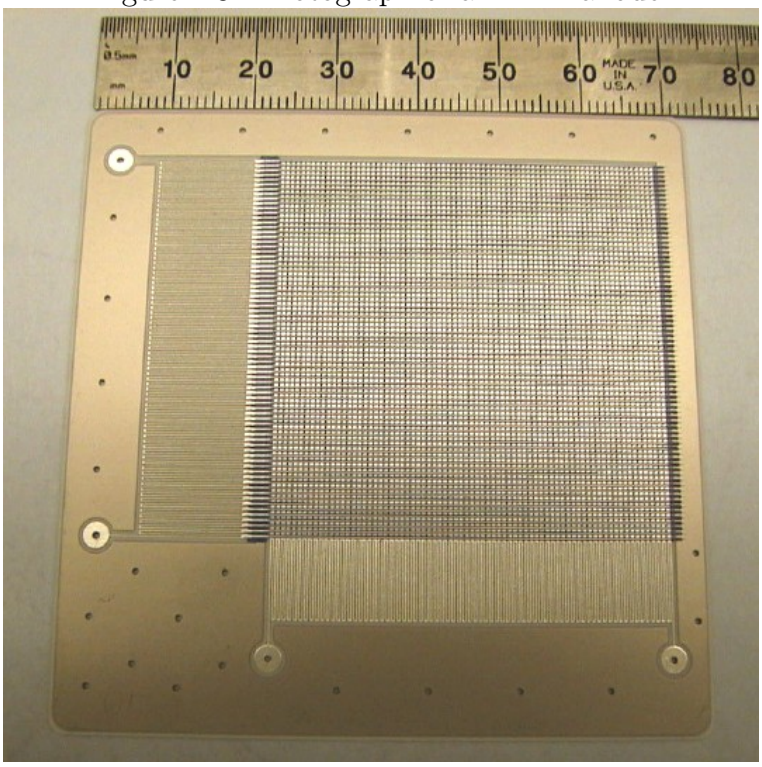

must be accelerated towards the detector anode. By holding the ion detector anode at ground, the anode delay lines can be directly coupled to their respective amplifiers.

The electron detector must be biased differently. The front face of the MCP must be biased positively to a few hundred volts so that impinging electrons have a high propensity for generating secondary electrons. These must be accelerated with increasing positive voltage all the way to the anode. This means that positive high voltage must be placed on the anode. Since amplifiers floating at high voltage are not desirable, the anode delay lines must be decoupled using capacitors. In addition, a layer of capacitors must be used to mimic an effective ground plane against which the anode pulses propagate. The presence of the capacitors means that the pulses

from the ion and electron detectors differ significantly in shape.

4.4 Spectrometer Simulation

4.4.1 Simulations with Simion

The first step in designing a coincidence imaging spectrometer is to decide on the lengths of the spectrometer regions, and approximate shapes for the electrodes. For our spectrometer design, we aimed for homogeneous electric fields (ie. planar equipotential surfaces) to allow for simpler back-transformation of the TOF and image positions to initial velocities. Homogenous fields are always an approximation in the real world because of fringing field effects near the edges of the electrodes. Edge effects can never be entirely eliminated, but by carefully designing the shapes of the electrodes, the fringe fields can be minimized to make the electric fields homogeneous over as large an area as possible. The only way to test if an electric field is constant enough to be considered homogeneous is to simulate particle trajectories numerically through calculated electric fields. These simulations are critical to ensure that the spectrometer preserves the information about the photoelectron and photoion velocities at the interaction region via unique mappings to the detectors.

The ion and electron spectrometers were simulated using Simion 6.0 (Scientific Instrument Services, Inc., Ringoes, NJ). Simion uses finite difference methods to solve Poisson's equation ($\nabla^2 V = -4\pi\rho$) on a grid in the spectrometer volume exclusive of the electrodes. Particles of certain charge, mass, and initial velocity vector were then placed at desired locations in the spectrometer and their trajectories propagated numerically until they hit an electrode or detector. By comparing the results of the

numerically calculated trajectories with analytically determined trajectories assuming homogeneous fields, it was possible to judge whether the chosen electrode designs were within the detector resolution capabilities, which were taken to be 100ps temporally, and 50μm spatially. Converging to the optimal electrode shape was an iterative, trial and error procedure. The following design criteria were enforced on the simulated spectrometer pieces:

1. Structural stiffness and robustness to be dimensionally stable.
2. Easy machinability to reasonable tolerances.
3. Sufficient distance between electrodes at high voltage to prevent arcing.
4. For parts to be attached together, allotting space for fasteners.

4.4.2 Electron Spectrometer Simulations & Design

As shown in Figure 3.11, shorter electron spectrometers generally have better v_z resolution than longer ones. We chose the single-field Wiley-McLaren setup for our electron spectrometer to eliminate the need for calibrating the z position of the interaction region. The extraction and drift regions were chosen to be 8mm and 16mm respectively. This was deemed to be a reasonable length for the extraction region because we wanted to have a very open interaction region to prevent the proximity of surfaces off of which the UV photons could create spurious photoelectrons.

Simulated electron trajectories for the final electron spectrometer design are shown in Figure 4.4. The most problematic part of the design was in the region between the electrode drift tube and the electron detector, due to the curved electric field lines caused by the bumpiness of the electron MCP housing. The field in this region is

high due to the large voltage needed to slam the electrons into the MCP to produce secondary electrons. Since the TOF through this region is small, one might expect that any deviations from non-homogeneous fields are negligible. This is true for the electron TOF, as the differences between the analytical and numerical results are on the order of picoseconds. However, the spatial deflections due to the non-homogenous fields in this region are not negligible, with deflections on the millimetre scale possible with improper electrode design. The final electrode design compensates for the electron detector shape by introducing field distortions at the exit of the drift tube to oppose the effect of the detector face irregularities. Due to the high electric field difference across the grid at the exit of the drift tube, we required the use of a 20 lines/mm grid to prevent severe grid lensing. The field difference between the extraction region and drift tube is much less so we were able to use a higher transmission 8 lines/mm grid for the extraction grid.

For a point source of electrons, we predicted that the electron spectrometer spatial and temporal resolutions to be $\sim$100μm and 50ps respectively out to about 17mm radius on the electron detector. Grid lensing was expected to degrade this resolution by approximately a factor of 2. For electrode voltages chosen to expand a 1eV electron image to 17mm radius on the detector, assuming a $25\mu m \times 2mm \times 25\mu m$ interaction region, Equation 3.2 predicts $\Delta E/E$ of 1%, 10%, and 3% for 1eV electrons emitted along the x (molecular beam), y (laser beam), and z axes respectively.

4.4.3 Ion Spectrometer Simulations & Design

To maintain symmetry about the interaction region, the ion detector extraction region was also set to 8mm. The overall length of the ion spectrometer was constrained to

Figure 4.4: Simion simulated trajectories for the electron spectrometer. The figure shows a radial cut through the cylindrically symmetric spectrometer. The simulated electrons were emitted in angles from 0 to 180° with 2eV of energy. Electrode voltages were chosen to image the electrons over most of the detector face. The red lines show equipotentials but are not equally spaced.

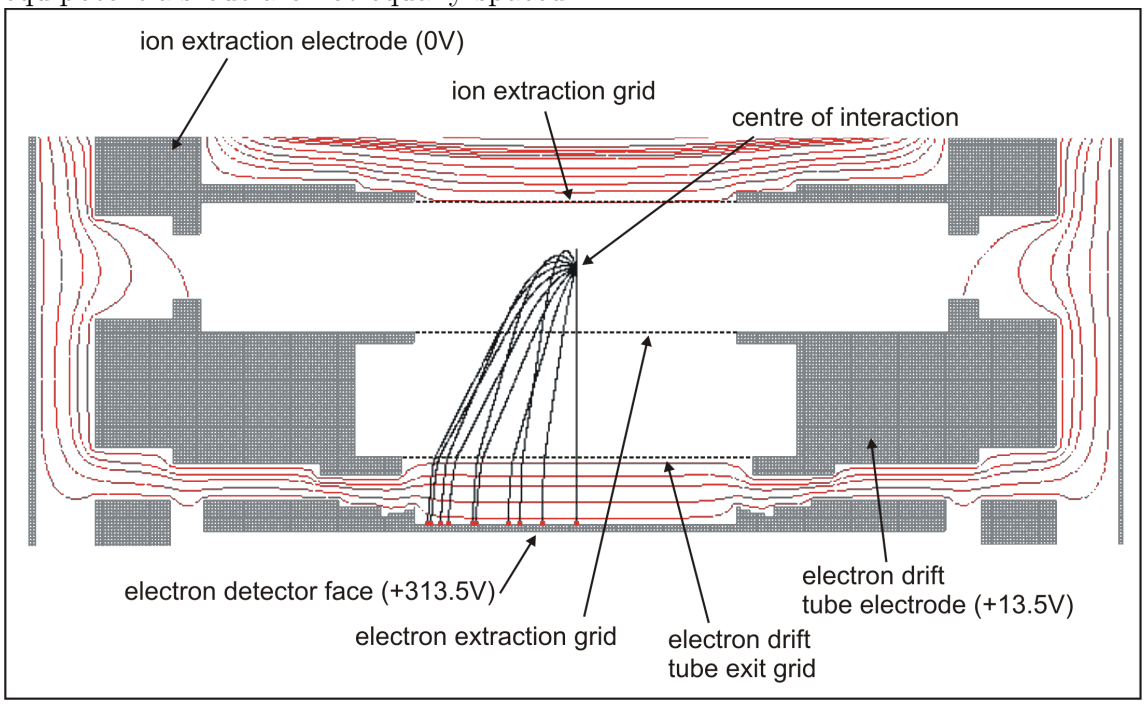

about 250mm by the size of the existing vacuum chamber that we planned to use. To help reduce grid deflections, we chose an acceleration region length of 30mm and a drift region length of 200mm. Longer lengths for both of these regions is desired to lessen grid lensing effects and increase mass resolution. For ease of simulation, the ion extraction plate was held at constant voltage and not pulsed as it is in the real experiment.

Figure 4.5 shows simulated ion trajectories for the final ion spectrometer design. Again the mounting hardware caused field inhomogeneity problems near the face of the detector. Unfortunately, the field is so high in this region because the detector

face sits at several kilovolts: the only solution was to put another grid in front of the detector to create a flat equipotential surface. Another area of careful design was the acceleration region. Small deflections felt in this region are magnified because they occur early in the flight trajectory and trajectory deviations accumulate over a long distance.

An einzel lens was incorporated into the setup for detector uniformity calibration tests. Biasing the lens appropriately can spray ions throughout the drift tube creating quasi-uniform illumination of the detector. A high density grid (20 lines/mm, 79%) was required for the extraction grid, with all other grids showing acceptable trajectory deviations using 8 lines/mm (89%) grids.

For a point source of ions, we predict that the ion spectrometer spatial and temporal resolutions to be $\sim 100\mu m$ and 50ps respectively out to about 17mm radius on the ion detector. Grid lensing is expected to degrade this resolution by approximately a factor of 2. For electrode voltages chosen to expand 0.78eV, M=127 (iodine) ions image to 17mm radius on the detector, assuming a $25\mu m \times 2mm \times 25\mu m$ interaction region, and beam velocity of $1500 \pm 5\%$, the predicted energy resolution $\Delta E/E$ is 3%, 15%, and <1% for 0.78eV ions emitted along the x (molecular beam), y (laser beam), and z axes respectively. Without any detector offset, this spectrometer has the capability to measure 1eV ions up to M=500. A 15mm offset extends the mass range to M$\sim$2600 while also improving the radial resolution of lower mass ions by allowing expansion over greater area of the detector.

Figure 4.5: Simion simulated trajectories for the ion spectrometer. The figure shows a radial cut through the cylindrically symmetric spectrometer. The simulated ions had mass 100 and were emitted in angles from 0 to 180° with 2eV of energy. Electrode voltages were chosen to meet the Wiley-McLaren space-focussing condition. The red lines show equipotentials but are not equally spaced.

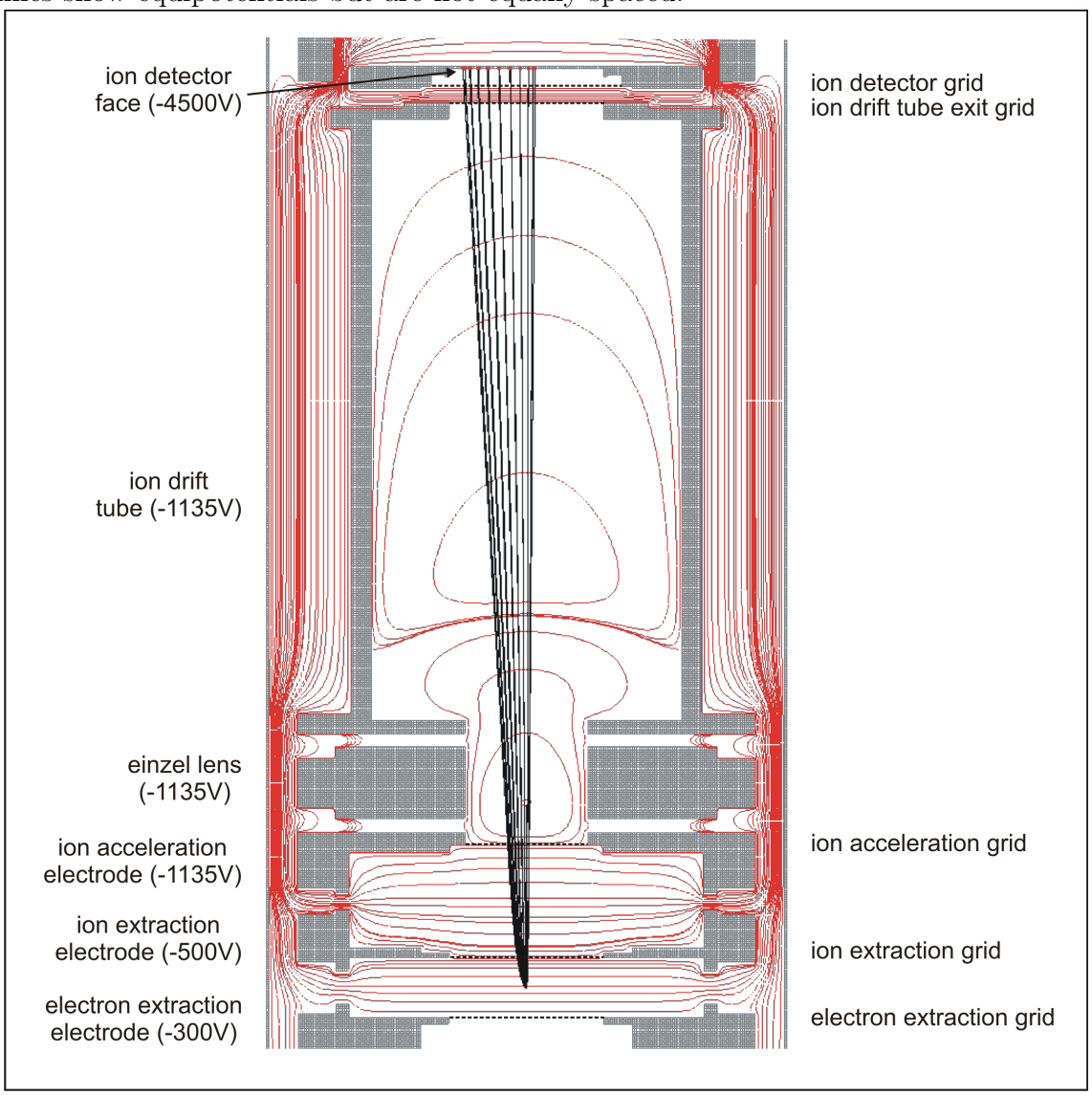

4.4.4 Analytical Simulations

By ensuring the electric fields were homogeneous using Simion, all further simulations can be performed analytically, requiring only knowledge of the lengths of the spectrometer regions and the electrode voltages. The spectrometer lengths and voltage designations for our spectrometer are shown in Figure 4.6. In addition to these parameters, the magnitude and arrival time at the interaction region of the high voltage ion extraction pulse must be known.

4.5 Design Specifications

4.5.1 Materials

To avoid large signals due to ionization of background gases, it is necessary to work in ultrahigh vacuum chambers with base pressures of $\sim 10^{-9}$ torr. This means that materials containing compounds with high vapour pressures, such as volatile organics, sulfur, and zinc, must be avoided. Additionally, since small magnetic fields can cause electrons trajectories to deflect, strongly magnetic materials cannot be used. Most metallic alloys contain nickel and/or zinc, so they must be carefully screened before being used. The primary materials used in our spectrometer are listed in Appendix A. An additional helpful resource for determining vacuum compatible materials is the NASA online space materials database [1].

[1] http://outgassing.nasa.gov/

Figure 4.6: Schematic of the CIS spectrometer. Dimensions indicated are in mm.

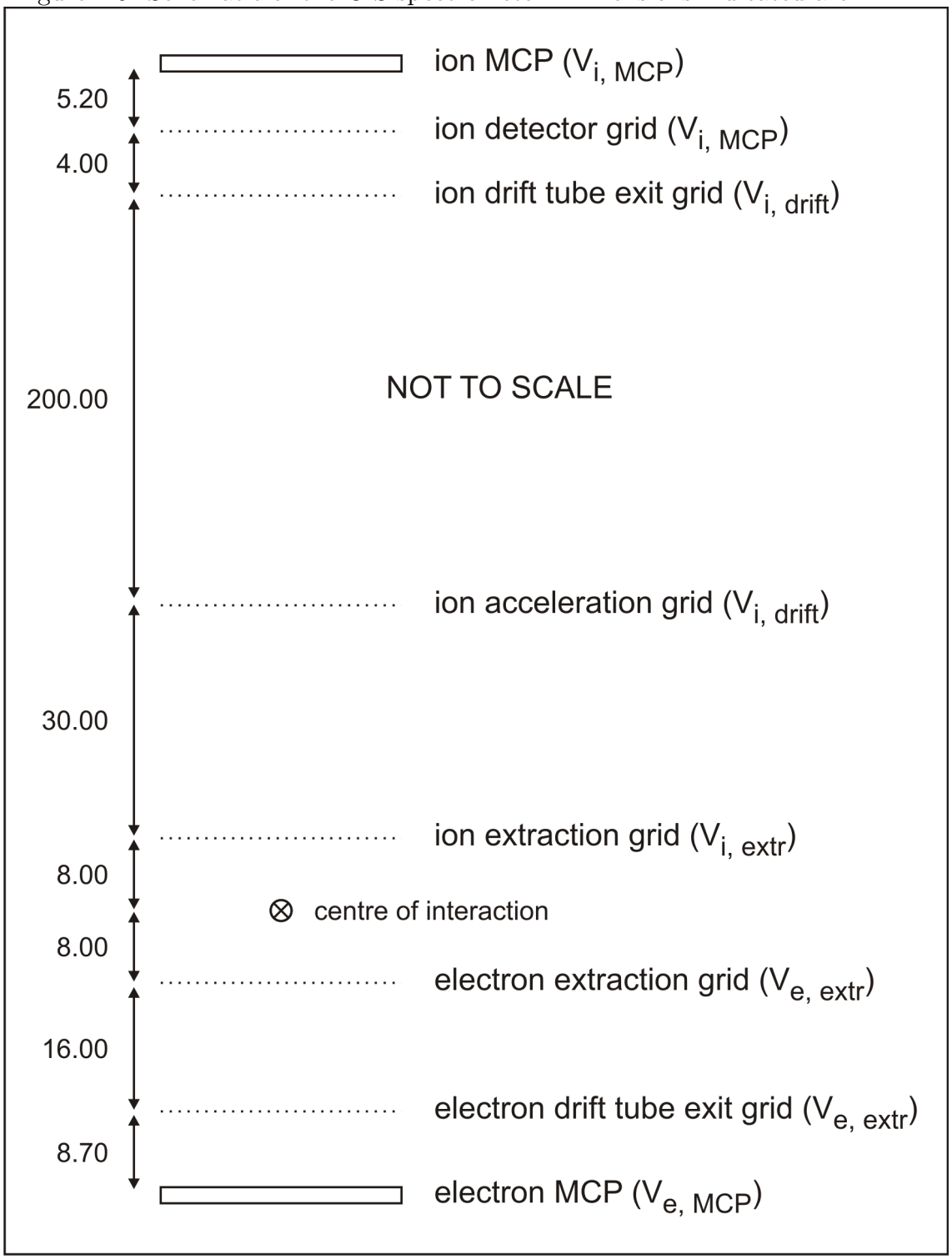

4.5.2 Magnetic Shielding

Magnetic shielding is needed to prevent the earth's magnetic field from influencing the electron trajectories to a large extent. The design of such shields using so-called μ-metal, an alloy with very high magnetic permeability, is well documented in the literature [84, 85, 86]. Ideally, to eliminate magnetic fields, it is desirable to completely enclose the apparatus with multi-layered μ-metal shields. However, due to space constraints and the need for holes in the shield for electrical feedthroughs, laser and molecular beam access, the magnetic shield used here was designed as a cylindrical shell with open ends. Extension tubes were added around the holes for the molecular and laser beams to reduce penetration of external fields into the shielded region.

Our magnetic shield is made from 0.76mm thick μ-metal (Co-netic AA, Magnetic Shield Corporation, Bensenville, IL). It is 160mm in diameter and approximately 500mm in length. For the earth's magnetic field in Ottawa, ON, Canada (0.523 gauss vertical, 0.177 gauss horizontal), the shielding factors are 375 for the transverse field, and 217 for the longitudinal field, at the interaction region. These shielding factors are assumed to be constant over the entire electron flight distance of $\sim$6cm. The longitudinal shielding factor includes the effect of field penetration from the ends of the magnetic shield. Outside of the magnetic shield, 1eV electrons have cyclotron radii of 19cm in the vertical plane and 6.4cm in the horizontal plane. Inside the magnetic shield, these radii increase to 71m and 14m respectively. Since our electron flight distances are at most a few centimetres, the residual magnetic field inside the magnetic shield is negligible.

4.5.3 General Spectrometer Design

Our desire to use an existing vacuum chamber imposed many constraints on our spectrometer design. The chamber is roughly cubic but half of the usable space is filled with a cylindrical structure holding a molecular beam skimmer and UHV gate valve. The magnetic shield defines a volume in which the spectrometer column resides and is differentially pumped by two 400L/s magnetically levitated turbo pumps (Seiko-Seiki). A third 400L/s turbo pump pumps the main chamber where most of the gas load is dumped.

The spectrometer electrodes were mainly made out of aluminum to negate any possibility of magnetism. Aluminum has an insulating oxide layer that can cause problems with field homogeneity. To eliminate this problem, the aluminum electrodes were plated with 5μm of copper followed by 0.25μm of gold (Electroloh Plating, Dorval, QC). The electrodes were mounted on PEEK rods and separated by ceramic spacers. The cylindrical ceramic spacers were coated on their exterior surface with a thin layer of vapour deposited germanium. The Ge layer serves two purposes: it drops the voltage uniformly along the length of the spacer; and it eliminates charge buildup on the surface of the spacers. The ends of the spacers were carefully painted with colloidal graphite (Aerodag G, Acheson Chemicals, Port Huron, MI) to ensure good contact with the adjacent electrodes. The thickness of the germanium layer should be carefully controlled if large voltages are to be applied across the plates that the spacers separate because of the possibility of high current flows through the germanium layer. High currents cause the germanium coated spacers to heat slightly, which in turn reduces their resistance and causes even more current to be drawn.

Due to the size and fragility of the spectrometer grids, they were designed to be

mounted on small rings for easy replacement in case of breakage. The mounting rings were machined from beryllium copper (BeCu) for rigidity and also to have a thermal expansion coefficient almost exactly the same as the copper grids. Previous experience revealed temperature cycling sometimes fractured the grid if different materials were used for the mounting rings. A special jig was designed for mounting the grids. Briefly, the grid was placed over the grid mounting ring. A metal lip pressing down on a soft neoprene o-ring was used to push the grid onto the mounting ring and tension the grid to smooth out wrinkles along its surface. A mixture of Aerodag G and methanol was painted around the edge to fix the grid to the mounting ring. Following trimming of the excess grid material, the grids were inspected by microscope for defects and flatness. The grid flatness was measured to be $< 10\mu m$. The copper grids were evaporatively coated with a thin ($\sim$100nm) layer of gold to prevent oxidation.

The mounting of the ion detector to the spectrometer stack was designed so that the ion detector could be placed at an offset relative to the spectrometer axis in an attempt to compensate for the molecular beam velocity. Initial assembly placed the detector with a 15mm offset.

To reduce the spatial spread of the molecular beam at the interaction region, we installed a vertically oriented piezoelectrically driven slit at the entrance to the spectrometer region. The slit (PZS-3V, PiezoSystemJena, Jena, Germany) opens from 0 to 1.5mm. For experiments where high signal levels are required the slit can be fully opened, whereas high resolution experiments can be carried out with the slits almost closed. Use of the slit can improve the y resolution to better than that of the x resolution.

The input laser window was chosen to be a 2mm thick magnesium fluoride window

with the birefringent axis cut at 0° to the window normal. Magnesium fluoride allows transmission to <200nm with high resistance to colour-centre formation. The input laser window was mounted at 0° incidence to reduce any rotation of the polarization due to the angular error of the crystal alignment or cut. A set of optical baffles coated with Aerodag G were placed along the laser axis to reject non-collimated laser light traveling in a similar direction to the laser beam that might cause spurious photoelectrons to be produced. The 1/4″ thickness fused silica laser output window was mounted at 45° to route reflections into a beam dump.

Stainless steel was used sparingly in parts requiring higher strength or in locations where any residual magnetism would not affect the electron trajectories. Prior to assembly into the vacuum chamber, all pieces were demagnetized with a demagnetizing coil to remove any residual magnetism. The support structures for the spectrometer were constructed from aluminum and stainless steel and designed for maximal gas throughput to maintain adequate vacuum pumping throughout the chamber.

4.5.4 Electrical Connections

The electrical connectivity of the spectrometer is schematically shown in Figure 4.7. The spectrometer and ion detector wiring were fed upwards through a 8” CF tee, while the electron detector wiring was dropped downwards through a 6” CF tee. Each detector requires five coaxial outputs, four for the delay line anode, and one for the MCP pick-off. The delay line and MCP connections were made using high bandwidth, vacuum compatible SMA connectors and PFA-insulated silver plated copper (SPC) coaxial cabling with dimensions similar to RG-174. The cables were connected through double-ended SMA connectors to atmosphere. High voltage for the MCPs

was supplied using high voltage cabling (600 Series connectors, type 'L' cabling, Teledyne Reynolds, CA) feeding through single-ended SHV connectors to atmosphere.

Shielded cabling (Astrolabe boaflex-V, Warren, NJ) for biasing the spectrometer electrodes was attached using copper brackets and connected to atmosphere using SHV feedthroughs. The high voltage pulse was introduced into the vacuum chamber through a double-ended SMA feedthrough connecting via 75Ω coaxial cable (Astrolabe boaflex-V) to the ion extraction plate. Due to the fast risetime of the high voltage pulse used to extract the ions, a circuit of compensation capacitors had to be constructed. The capacitors serve two functions: to tune the load that the pulse generator drives; and to maintain a quasi-continuous shield for pulse transmission. The tuning capacitor was chosen to be 22pF (2.5kV, Voltronics 25-220-J-2500-S) and the transmission capacitors were chosen to be 1500pF (500V, Voltronics 25-152-J-500-S) and 430pF (2.5kV, TPL Microelectronics MPH1C431JPXBB). All capacitors were non-magnetic, vacuum compatible ceramic chip capacitors. The values of the compensation capacitors were chosen to obtain the best possible approximation to a square pulse (i.e. minimal ringing) measured using a high voltage oscilloscope probe (Tektronix 5100) at the ion extraction electrode with the high voltage pulser (HVC-1000, GPTA, Berlin, Germany). A note of caution regarding the pulser: the HV output of this pulser produces noise at semi-random times when the power is on, but pulsing is disabled. When not in use, the pulser should be powered off to avoid spurious signal pickup. Care should be taken to shield and properly ground the voltage supplies biasing the electrodes as relatively small voltage fluctuations can cause significant degradation in the spectrometer resolution.

Several tin-plated, braided copper straps connect the ion detector baseplate to the

Figure 4.7: Spectrometer wiring diagram. Resistor values are given in ohms. *MCP resistances change slowly over time; the labels indicate resistance at time of construction. Capacitor values and their recommended maximum working voltages are specified. Normally, $V_{i,drift}$, $V_{i,einzel}$, and $V_{i,acc}$ are supplied from the same high voltage power supply and are thus equal. $V_{i,extr}$ is provided from a high voltage pulse generator that pulses relative to ground.

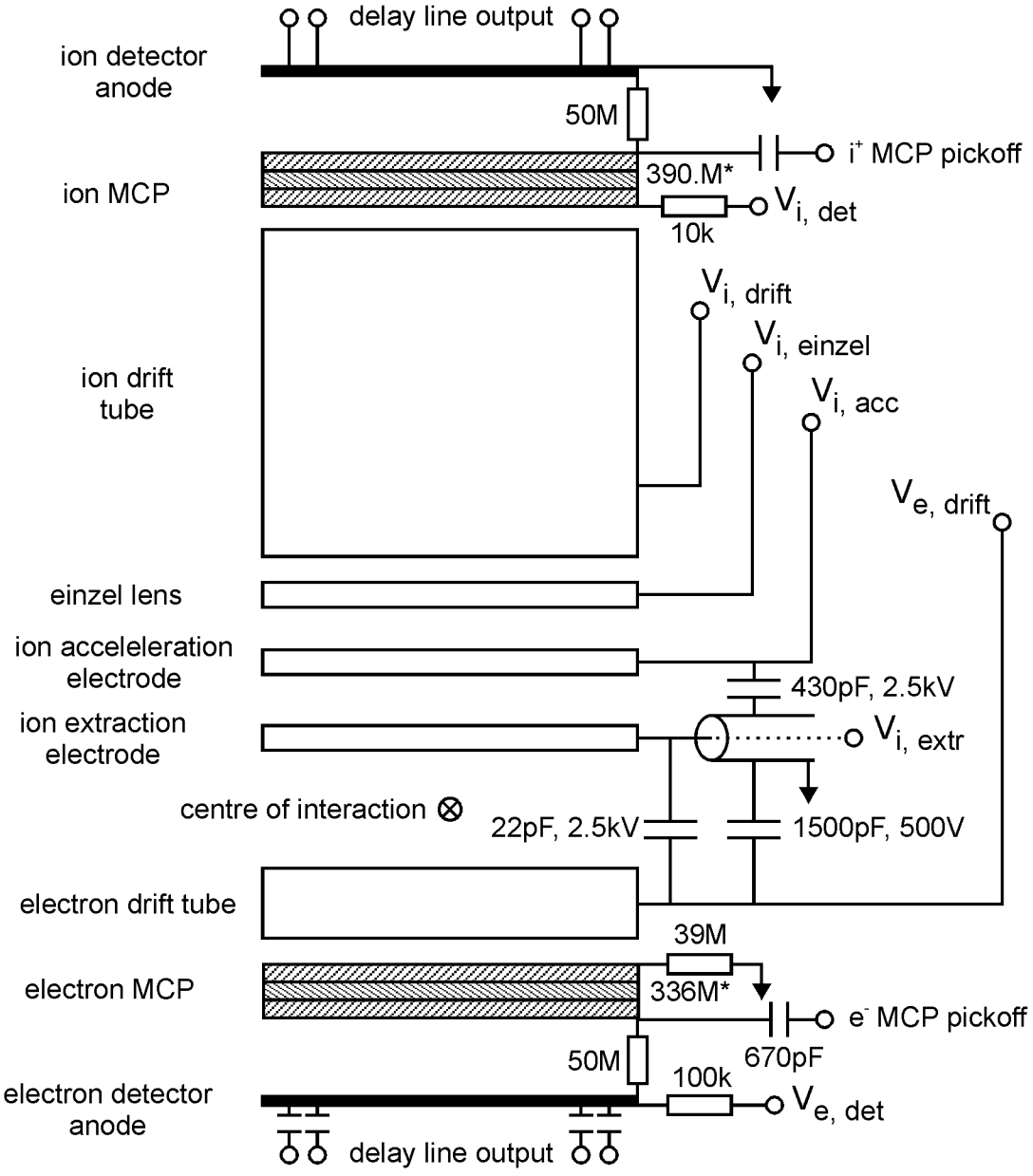

vacuum chamber ensuring a high quality ground plane for the detector. The electron detector baseplate is grounded through the spectrometer support assembly to the vacuum chamber.

Four halogen bake-out lamps were installed to heat the vacuum chamber internally. Elevating the chamber greatly reduces the time required to reach base pressure. Each lamp required a pair of electrical feedthroughs. Heating tape was wrapped externally around the upper and lower vacuum chamber tees leading to the spectrometer turbo pumps. The temperature at various locations within the vacuum chamber: the o-ring seal at laser window; the piezoslit (max. temperature 120°C); and the front chamber wall were monitored using type K (chromel/alumel) thermocouples. These were wired to atmosphere using type K thermocouple feedthroughs. The magnetic properties of commonly available and affordable thermocouples precluded their use inside the magnetic shield. Thus, we used resistive temperature devices (RTDs) affixed to the backs of the detectors to monitor their temperature during bake-out. They each require a pair of electrical vacuum feedthroughs. The maximum temperature of the detectors was specified to be 100°C. Variac settings of 35VAC on the halogen lamps, and 50VAC on the heating tapes resulted in the following temperatures: electron detector, 107°C; ion detector, 93°C; piezoslit, 91°C; laser window, 55°C; front vacuum chamber wall, 47°C. After baking, the base pressure was measured to be 3.0×10^{-9} torr in the main chamber, and 7.4×10^{-9} and 5.4×10^{-9} torr in the ion and electron cabling regions respectively.

4.5.5 Spectrometer Drawings

A cross-sectional slice along the laser propagation direction through the spectrometer is shown in Figure 4.8. Cross-sectional slices through the complete vacuum chamber and spectrometer along the laser and molecular beam propagation directions are shown in Figures 4.9 and 4.10 respectively.

Figure 4.8: Cross-sectional slice along the laser propagation direction through the spectrometer.

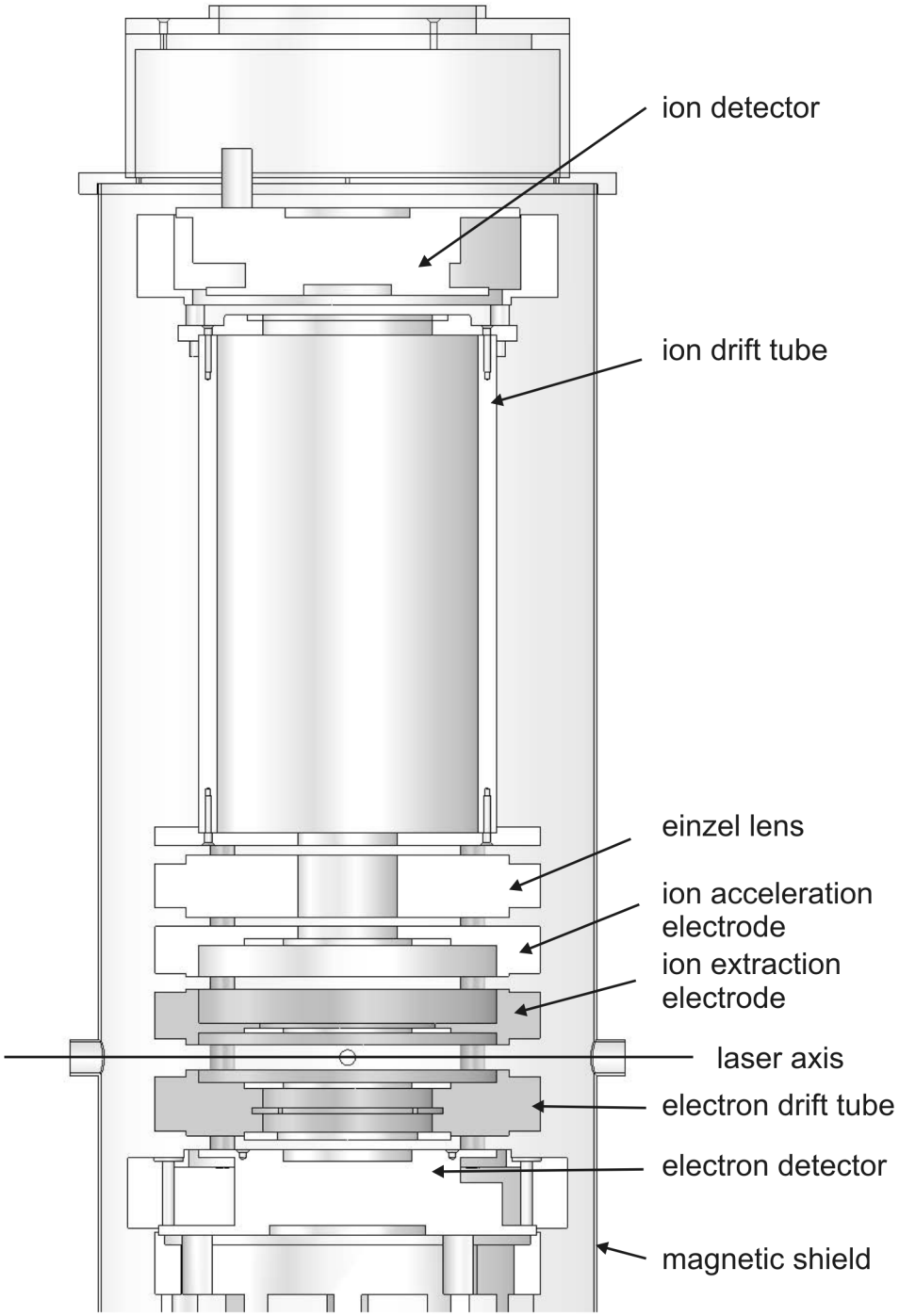

Figure 4.9: Cross-sectional slice of the vacuum chamber and spectrometer along the laser propagation direction.

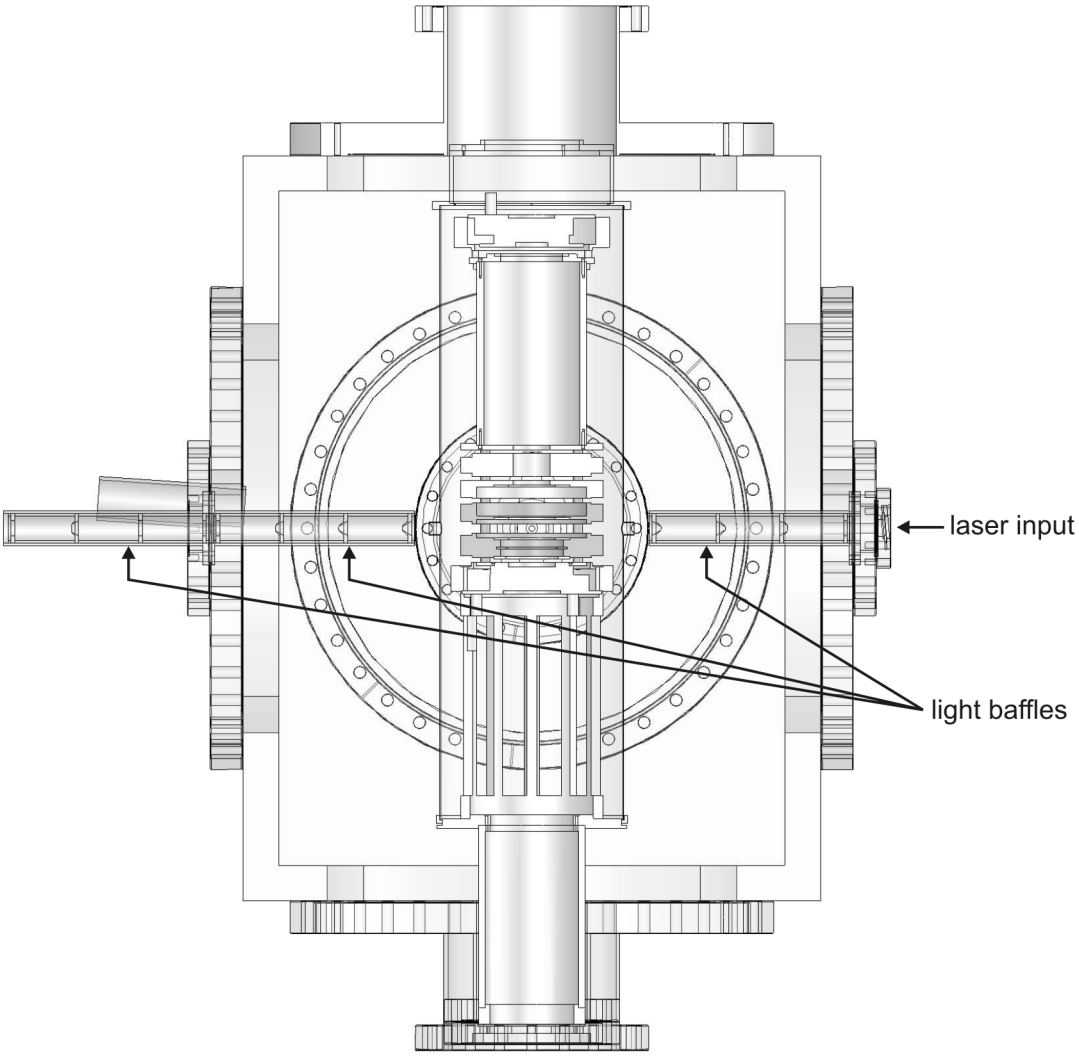

Figure 4.10: Cross-sectional slice of the vacuum chamber and spectrometer along the molecular beam propagation direction.

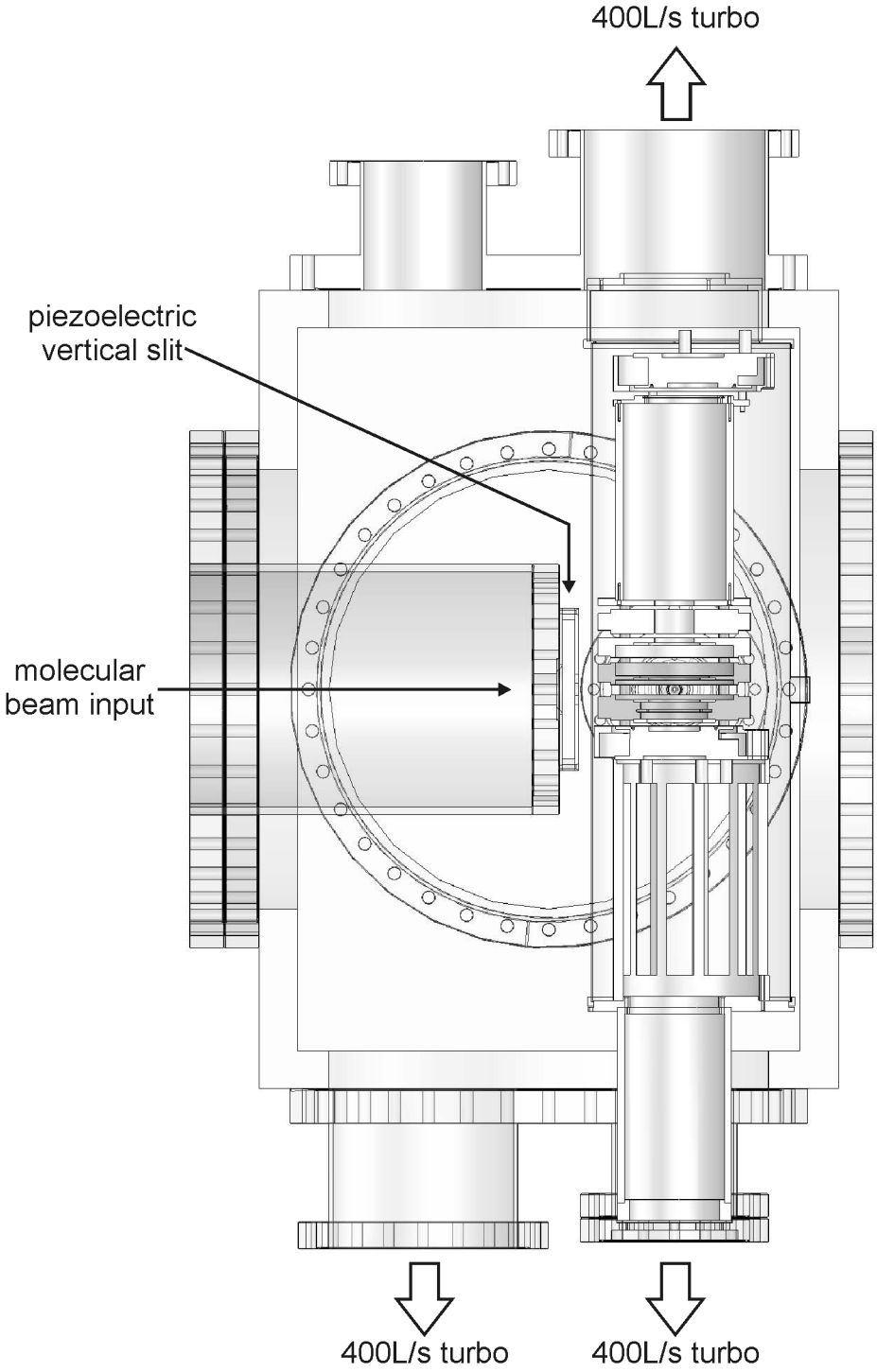

Chapter 5

CIS Data Acquisition Electronics and Tuning

5.1 Introduction

This chapter describes the Coincidence Imaging Spectroscopy data acquisition system. The system design, calibration, and tuning is explained. In particular, the XDL detectors were quite laborious to tune to achieve optimal timing and spatial resolution, and are thus deserving of some discussion.

The velocity and mass measurements require us to measure the electron hit position (ePos), TOF (eTOF); and the ion hit position (iPos), and TOF (iTOF). In addition, to allow us to discriminate whether we detect multiple particles simultaneously on the detector, we measure the charge deposited on both detectors (eQ and iQ). We must also measure the number of different mass ions that hit the ion detector (iCount) to check if there is ambiguity to which ion a coincidently detected electron belongs. We must ensure that all of these pieces of information are measured

and stored before the next laser shot arrives to prevent scrambling of the coincidence data. Also, the data acquisition system must be cleared and readied for subsequent data events prior to each laser shot. In addition to the electronics hardware, a brief description of the computer data acquisition software is presented.

5.2 XDL Detector Tuning

5.2.1 Detector High Voltage Supply

Appropriate voltages are necessary to achieve good spatial resolution from the XDL detectors. The electric field between the back of the MCP and the anode determines how much the electron cloud spreads before it hits the anode. Sufficient cloud spreading is required to cover multiple charge collection fingers. Temporal merging of the pulses as they enter the delay line effectively interpolates between the charge collection fingers to enable resolution much finer than the finger spacing. A single high voltage supply and in-vacuum dividing resistors fix the relative voltages within the detector. The high voltage for the ion detector was set at the manufacturer recommended 4.2kV. We added a 39MΩ resistor to ground on the front of the electron detector MCP to achieve proper spectrometer biasing while correspondingly raising the electron detector voltage to 4.8kV. The addition of the resistor changed the voltage ratio between the back of the MCP and the anode, but spatial resolution tests before and after the resistor change did not show significant differences. Both detector voltages should be kept the same to have consistency between measurements. The temperature of the detectors should also be kept constant except during bakeout. As shown in Figure 4.7, the voltages within the detectors are defined by the MCP resistances

and the MΩ biasing resistors. While the resistors have relatively small temperature coefficients, the MCP channels are semiconductive, with resistance falling as the temperature is increased. Thus, temperature changes cause large changes in the detector gain.

5.2.2 Detector Signals

The electron and ion detectors have a total of 5 outputs each: a pair for each of the dimensions connected to the ends of the delay lines, and one for the MCP pick-off. The pulses from the anode are negative-going because their origin is from electrons. The 4 anode lines are connected to a pair of dual channel, polarity preserving, high frequency (∼1GHz) AC amplifiers (Sensor Sciences LLC, Pleasant Hill, CA) capable of driving 50Ω loads. A typical output pulse from one of these channels is shown in Figure 5.1. The dip at ∼40ns is due a reflection of the pulse traveling the other direction along the delay line when it exits the anode. The position of the reflection relative to the primary peak (at 22ns) varies depending on the hit location on the anode.

The MCP pick-off pulses are positive-going pulses because they arise from electrons leaving the back of the MCP. The electron and ion MCP pulses are fed into inverting high frequency amplifiers (Sensor Sciences LLC TLA-101, and Phillips 6955-SD-20 respectively). A typical MCP signal from the electron detector is shown in Figure 5.2.

Figure 5.1: A typical anode delay line pulse from the electron detector following the amplifier. The voltage supplied to the detector is 4.8kV. The dip at ∼40ns is due to a reflection of the pulse traveling the other direction along the delay line when it exits the anode.

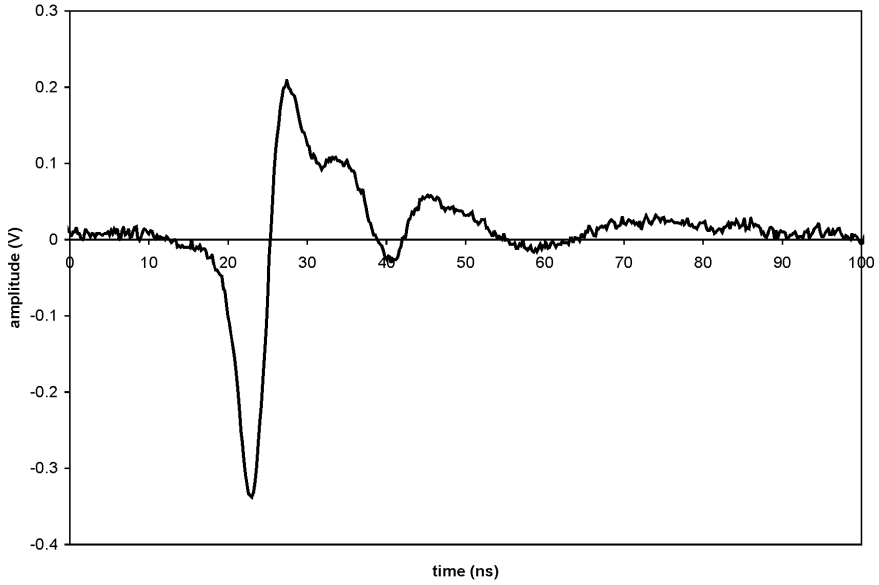

5.2.3 Constant Fraction Discrimination

Our detector spatial resolution and TOF resolution rely on accurately transforming the analog pulses from the anode and MCP pick-off into digital signals that preserve the timing of the original pulse. For our pulses, there is significant pulse height variation due to MCP pulse height variability. Using a level triggering discriminator is disadvantageous in this situation because the output timing will vary with pulse height as well as real timing change. Constant Fraction (CF) discrimination is an attempt to eliminate this amplitude jitter problem.

In CF discrimination, the analog input pulse is divided into two, not necessarily equal parts. One part is delayed in time using cabling. Both the prompt and delayed

Figure 5.2: A typical MCP pick-off pulse from the electron detector following amplification. The voltage supplied to the detector is 4.8kV. The dip at ∼58ns is due to a reflection from the amplifier input.

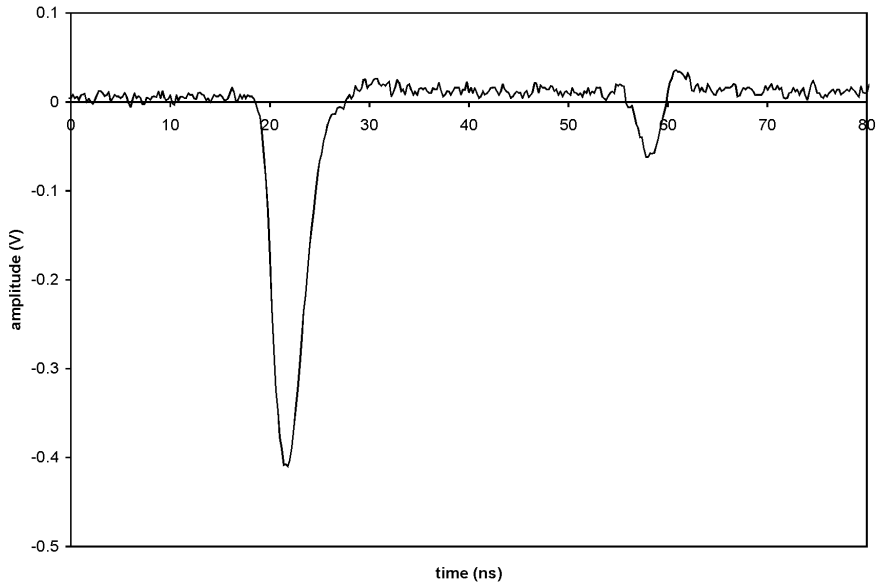

pulses are input into a fast comparator. The Constant Fraction Discriminator (CFD) output is triggered when the comparator output switches state (i.e. when the two comparator inputs are equal). The time independence of the crossing point is easily seen in Figure 5.3 for identically timed pulses that only vary in amplitude.

Electronic implementation of the CFD usually yields four user-adjustable parameters: the delay between the two pulse replicas; the relative amplitudes, or fraction (F), of the prompt and delayed pulses; the walk setting (Z) that biases the comparator inputs slightly to prevent output oscillation; and the threshold setting (T) which sets the minimum measurable pulse height. The tuning of these four parameters is far from trivial and is critical to obtain good timing and position resolution from XDL detectors. Appendix B describes the tuning of these CFD parameters in detail. It

Figure 5.3: Timing independence for different amplitude pulses of the crossing point between a pulse which has been split in two with one part delayed by a constant amount.

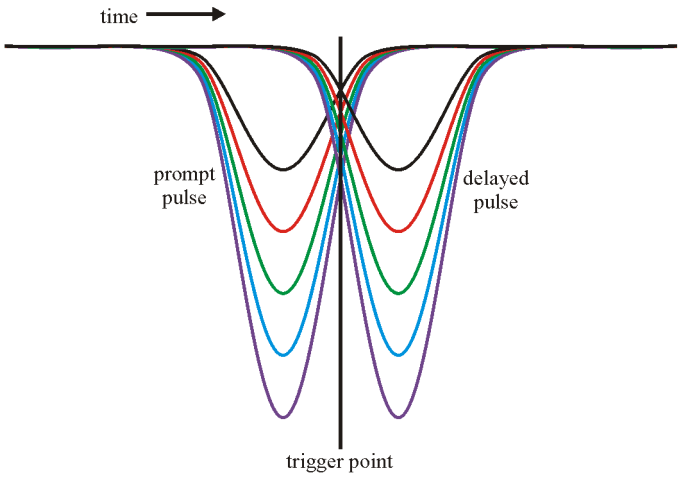

should be stressed that CFDs are designed to compensate only for amplitude variation in analog signals; changes in the shapes of the pulses with amplitude are not explicitly accounted for. Although designed to be as shape invariant as possible, the pulses from our detector still show some variation in pulse shape across the detector. To compensate as best as possible, the CFD parameters were tweaked to try to minimize both shape and amplitude timing jitter.

5.2.4 Time to Digital Conversion

We had two types of Time to Digital Converter (TDC) instruments at our disposal for measuring time differences between the arrival of two pulses: a pair of dual channel Double Sampled Time to Digital Converters (DSTDC) (Sensor Sciences LLC, Pleasant Hill, CA); and a 16 channel Phillips 7187 TDC (Phillips Scientific, Mahwah, NJ).

The Sensor Sciences DSTDC's are actually modules with combined CFD and TDC functions. They were designed specifically for collecting high resolution images using XDL detectors at high data rates. As such, certain modifications had to be made to the modules to suit our goal of detecting events one by one at regular intervals at the relatively low data rate of 1kHz, the repetition rate of our laser. Notably, this required bypassing the multiple event buffering capabilities of the modules and modifying their hardware handshaking behaviour. A disadvantage of these DSTDC's is that since both CFD and TDC functions are combined into a single module there is no intermediate feedback to indicate when the CFD's are tuned appropriately. In spite of their drawbacks, the DSTDCs are very precise, digitizing at 14-bits over approximately 55ns to yield bins with about 3ps width. Additionally, a dither circuit eliminates the effects of differential non-linearity (DNL)[33], a problem where different TDC bins have different effective widths, resulting in reduced timing precision.

The Phillips TDC module requires the use of separate CFD modules. For our implementation we used the Quad Tennelec 454 CFD modules. As stated above, the separation of CFD from TDC allows for simpler CFD tuning. The main drawback of this system is the susceptibility of the Phillips TDC to crosstalk between different channels, generally poorer resolution (25ps bins), and more severe DNL and integral non-linearity (INL). INL is the deviation form linear time to digital conversion resulting in reduced accuracy of the timing measurements.

5.2.5 Detector Timing Resolution

We tested many schemes for measuring the electron TOF (eTOF) and position (ePos) with the goal of pushing the limits of XDL detector timing and spatial resolution:

two will be described here. For testing both methods, we used the higher resolution DSTDC's. One method was to use a discriminated, laser-triggered photodiode signal and the MCP pick-off as the Start and Stop respectively to directly measure eTOF. The photodiode was set to monitor our 800nm amplifier pulse which has amplitude stability of $< 1\%$. Thus, a simple level discriminator was used (Phillips Scientific 6904). Alone, the eTOF resolution obtained by this method is limited by the average transit time of a pulse across the back of the MCP, which is about 200ps for our 40mm diameter MCPs. We thought we could improve on this resolution by correlating the eTOF measurement with the hit position on the detector. The position measurement was accomplished by wiring one of the ends of the anode delay line for each dimension to the Starts of the DSTDC, and running the other ends through cable delays before connecting them to the Stops. The extra cabling ensured that the Starts always arrived before the Stops. The positions were read directly from the TDC. This setup is shown in Scheme 5.1A.

The other method again used the laser photodiode signal as the Start but the ends of the delay line anode as the Stops for the DSTDCs. Four times were measured, two from each end of the x and y anode delay lines: t_{x1}, t_{x2}, t_{y1}, and t_{y2}. Measured this way eTOF can be calculated as

$$\begin{aligned} t_{e,TOF} &= \frac{1}{2}t_{x,sum} - \frac{1}{2}t_{x,delay} - t_{x,finger}(x,y) \\ t_{x,sum} &= t_{x1} + t_{x2} \end{aligned} \tag{5.1}$$

where $t_{x,delay}$ is the length of the x delay line, and $t_{x,finger}(x,y)$ is the x,y-position dependent transit time along the x direction charge collection fingers. A similar redundant expression exists using $t_{y,sum}$. The (x,y) position of a particular event is calculated by taking the difference between the times from the ends of the anode. We

postulated that $t_{x,finger}(x, y)$ would be a simple function that just increased linearly with increasing y. This measurement setup is shown in Scheme 5.1B.

Scheme 5.1: Test TDC measurement schemes for ePos, and eTOF.

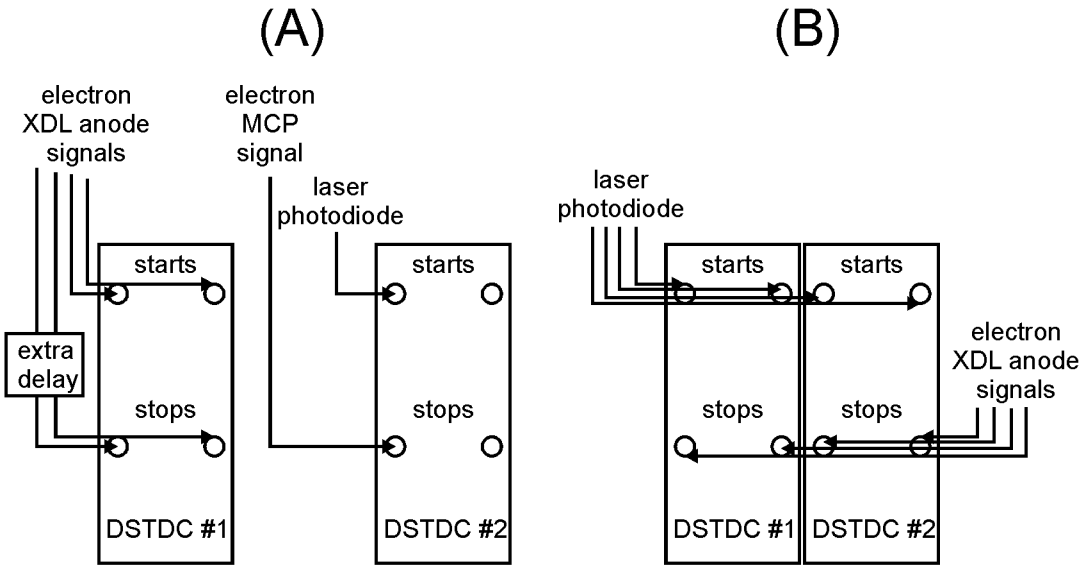

Using either of these two methods for measuring eTOF and ePos, we hoped to get below the 200ps timing resolution limit by applying a position dependent correction to the eTOF. To test this hypothesis, we used 300nm laser pulses of ∼1ps duration to create events on the electron detector face. The spread in the arrival times of the photons at the detector face was negligible relative to electronic timing capabilities and was ignored. In addition to the timing information of the events, we also used a gated analog-to-digital converter (ADC, LeCroy 2249A) to measure the pulse heights of the electron clouds hitting the anode. For each setup, we adjusted the threshold and walk settings to achieve optimal timing characteristics. We collected around 10^6 events for each experiment. The detector images were cropped to eliminate large distortions near the edges. A pinhole mask with 10μm holes on a 1mm spacing was

placed on the face of the detector to verify the detector spatial resolution.

A histogram of the time sum of the x anode lines ($t_{x,sum}$) for Scheme 5.1B shows that it is a peak with FWHM ≈400ps (see Figure 5.4). Half of this peak width (200ps) is the approximate transit time across the detector anode. Images correlated with values of $t_{x,sum}$ are shown in Figure 5.5. Although we hoped to see horizontal stripes confirming simple linear dependence of $t_{x,finger}(x, y)$ on y, we did not. Similarly, we did not see any vertical stripes when plotting images correlated with values of $t_{y,sum}$. In reality, the images from small $t_{x,sum}$ seemed to be concentrated near the center of the detector and spread towards the edges with increasing $t_{x,sum}$. Charge distribution measurements correlated with $t_{x,sum}$ values were approximately invariant with charge, indicating proper adjustment of the CFDs. Thus, we concluded that sub-200ps timing resolution was not possible using Scheme 5.1B for measuring eTOF.

Experiments using Scheme 5.1A also attempted to find a TOF-position correlation by looking at images sliced by the MCP pick-off timing. This also proved fruitless in obtaining improved timing resolution. These and other frustrations eventually led us to conclude that these XDL detectors are not capable of sub-200ps timing resolution. There are several explanations why better timing resolution might not be possible: dispersion along the XDL anode; non-uniform MCP pulse shape; and/or improper termination of the charge collection fingers.

Dispersion caused by non-uniform propagation speed for different frequency components of a pulse tends to lengthen short signal pulses as they travel. This manifests itself as a changing pulse shape as the signal propagates, thus hampering the CFD technique. Dispersion affects $t_{x,sum}$ and $t_{y,sum}$ in an additive manner whereas it subtracts when calculating the anode hit positions. Evidence of this is seen in different

Figure 5.4: Histogram of the time sums for the x axis delay lines using the data acquisition setup shown in Scheme 5.1B.. The FWHM is ∼400ps, twice the transit time for a pulse across the 40mm anode charge collection fingers.

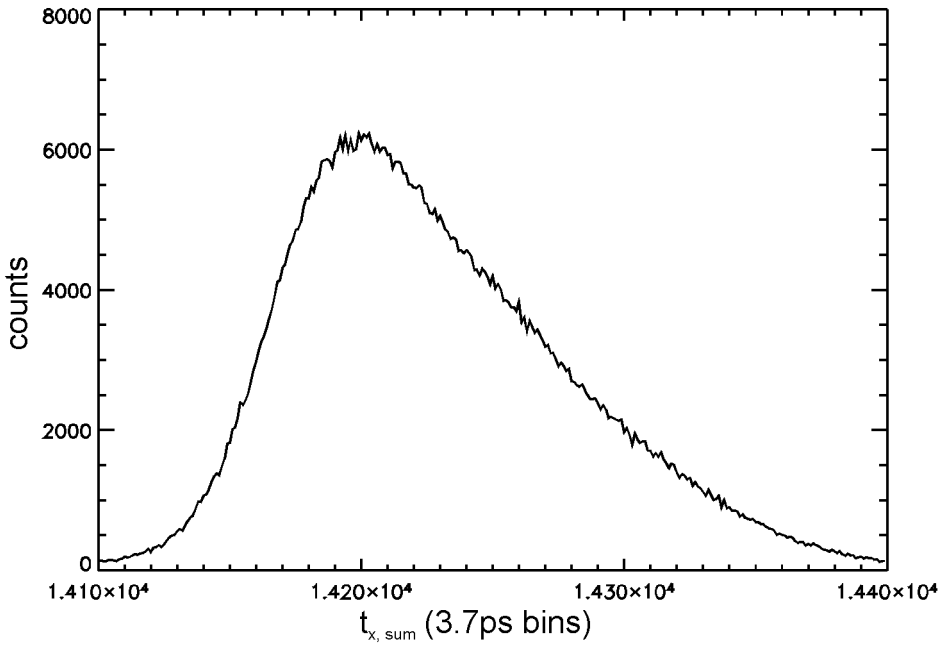

spatial resolution across the face of the detector: resolution at the centre of the detector, where dispersion would be expected to perfectly cancel, is typically better than near the edges, where differences in dispersion between the different ends of the delay lines is greatest.

Non-uniform MCP pulse shape is another possible limiting factor for timing resolution. Average MCP gain can vary quite substantially over the detector face with factors of >2 easily seen even in high quality imaging plates. Also, due to the nature of the electron amplification process, gain variations over small areas of the detector can vary by ∼70% for our MCPs. These gain variations do not vary purely the amplitude of the pulse, they also affect the pulse shapes, which is detrimental to the CF

Figure 5.5: Images correlated with values of $t_{x,sum}$. The numbers label the start bin of $t_{x,sum}$.

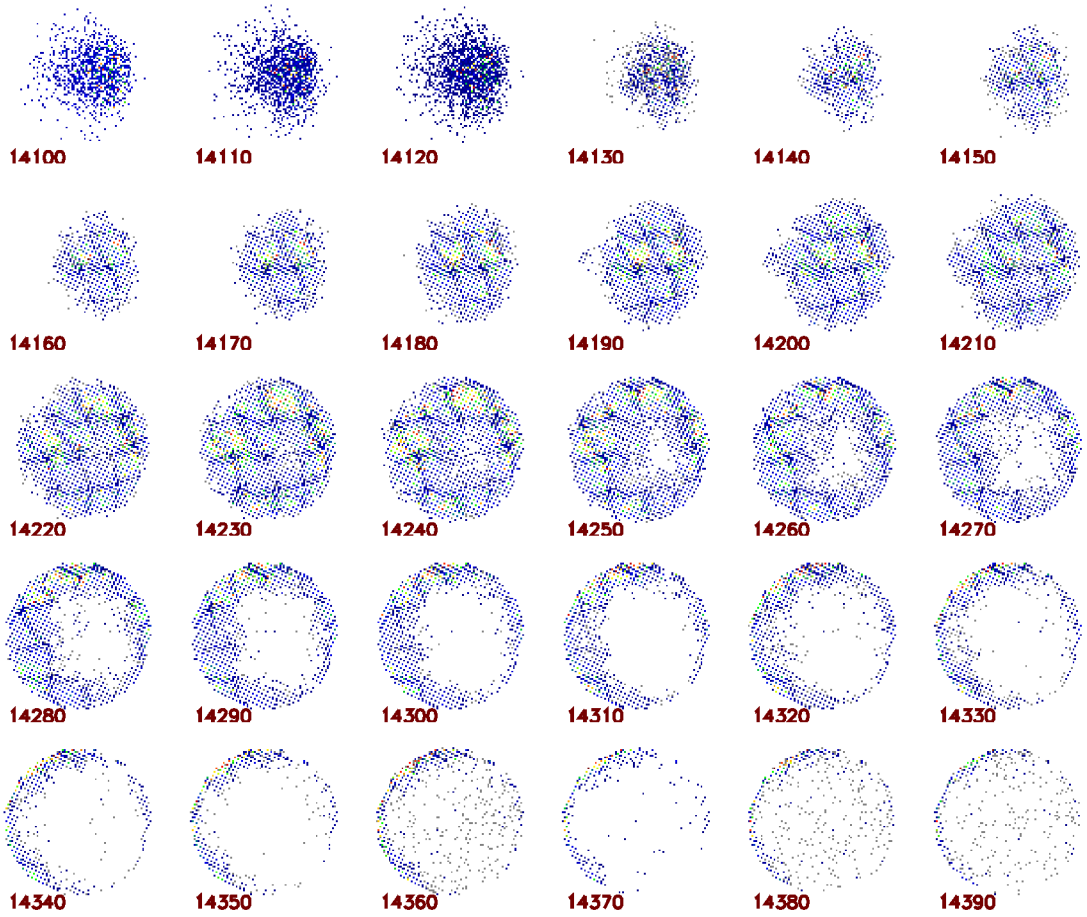

discrimination technique.

Another reason why improved timing resolution might not be possible is that the anode charge collection fingers are open circuit at the end not connected to the delay line. This means that there can be reflections off the open ends that causes finer timing resolution to be lost. This problem might be circumvented by using serpentine delay line anodes that extend over the active area of the detector, thus eliminating the need for the charge collection fingers; or by using helical anodes[83]. However, dispersion effects might prevail with these lengthier anodes.

An additional problem can be caused by dispersion near the edges of the detector. When the signals traveling along the charge collection fingers reach the delay line, they bifurcate resistively towards the ends of the delay line. Thus, when the anode hit is towards one side, the larger portion of the pulse goes towards the end that is closer while the smaller portion traverses the longer distance to the other end. In our detectors, as the pulses exit the anode into the coaxial cabling, an impedance mismatch causes a reflection to be sent back along the delay line. Near the edge of the detector, the reflection of the larger portion of the pulse immediately follows the non-reflected smaller pulse towards the other end of the detector. Dispersion can cause elements of the reflected large pulse to catch up with the non-reflected small pulse and distort the trailing edge of the timing pulse. CF discrimination relies on the shape of both the leading and trailing edges of the pulses. Distortion of the pulse shape is the reason for the waviness of the pinhole mask images near the edge of the detector. The outer millimetre or two of any detector image should be cropped to avoid these distortions.

5.2.6 Measuring ion TOF and electron TOF and position

Resigning ourselves to the fact that we could not obtain better than 200ps timing resolution, we settled on using our two DSTDC modules with their finer resolution for the electron and ion position measurements. The electron TOF was then measured with the Tennelec/Phillips CFD-TDC combination, which easily has 200ps timing resolution. This setup is shown in Scheme 5.2. Measurement with this setup using laser triggering indicated that the electron detector timing resolution of this setup was ∼180ps.

Scheme 5.2: Setup for measuring the electron and ion positions, and electron TOF.

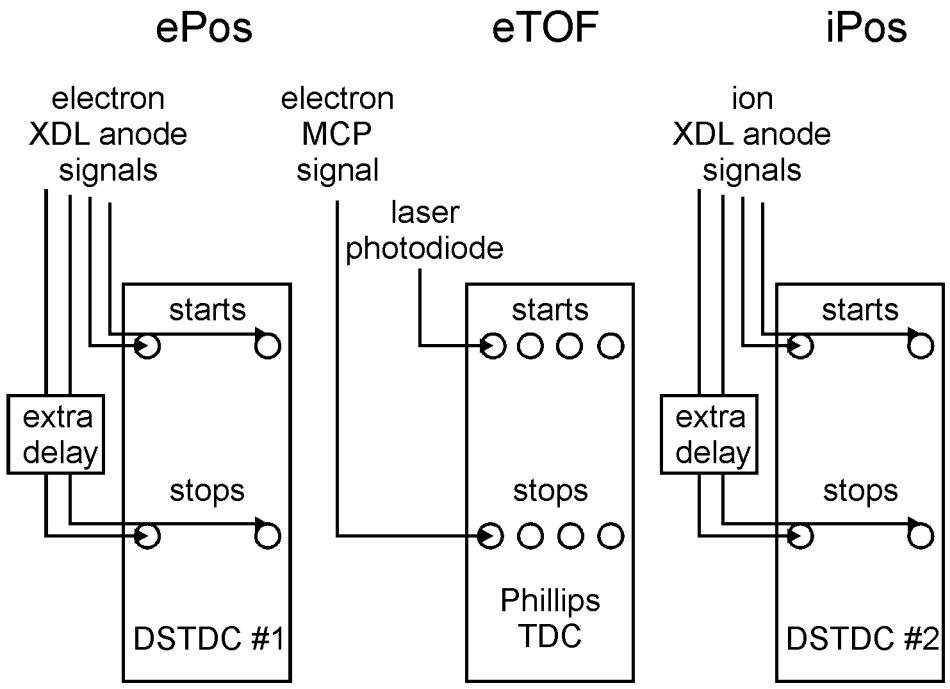

5.2.7 Detector Position CFD Tuning

The preceding timing resolution tests required tuning of the CFD settings for each of the different setups. Only CFD settings for the final setup shown in Scheme 5.2 will be described here. The DSTDC modules have their delays and fractions hardwired onto their printed circuit boards. These were left intact. The remaining parameters to adjust were the 4 walk settings (1 for each anode input) and 2 threshold settings (1 for each anode dimension) for each detector.

All threshold levels were set at -300mV at the front test point for both electron and ion detectors. The actual voltage at the comparator is about 10× less than the front test point plus 10mV. The threshold is usually implemented to cut out low pulse height pulses caused by MCP dark counts. Dark count rates are typically <1 count cm^{-2} s^{-1}. For our CIS experiments, the real events are correlated with the laser so the probability of spurious counts from dark counts is negligible. Therefore, the threshold setting has only to keep out noise along the anode delay lines.

The zero point of the walk adjustments (the walk voltage where the zero crossing comparator inputs are equal) were measured directly by opening the modules and placing a fast oscilloscope probe (Tektronix 6243) on the output of the zero crossing comparator. The voltage at the front panel test point is about 1000× the actual walk voltage. The front panel zero crossing points are given in Table 5.1.

Table 5.1: Front panel zero points of the DSTDC walk adjustments

Channel	Ion Detector (V)	Electron Detector (V)
XStart	-2.31	-1.93
XStop	-2.05	-1.88
YStart	-2.18	-1.97
YStop	-1.96	-1.86

Starting from the walk zero points +0.5V and −0.5V, the walk adjustments were varied while recording images from the detector. To ensure accurate pulse shapes and height distributions, the detectors were illuminated with ions and electrons created from an ion gauge biased to accelerate the particles towards their respective detectors. A pinhole mask with 10μm holes located on a 1mm grid was placed on the detector face. A typical image of the pinhole mask is shown in Figure 5.6. The delay lines are not the same length for each detector dimension. x-y scaling factors of 1.185:1 and 1.290:1 were applied to the electron and ion detector images respectively to restore the images back to a square grid. For both detectors, each scaled pixel corresponds to ∼7.9μm. The final walk settings were determined by minimizing the peak widths of the masked holes at 5 selected locations across the detector. Since the mask hole diameter is below the resolution limit of the detector, the measured peak width of the holes is approximately the detector spatial resolution. An example of the peak cross-section analysis output used to determine the detector resolution is shown in Figure 5.7. The final walk settings for both detectors are given in Table 5.2. Using these settings, the detector spatial resolution averaged over 5 locations on the MCP face was 58μm(x) and 52μm(y) for the ion detector, and 77μm(x) and 82μm(y) for the electron detector. The electron detector resolution is worse because biasing restraints force its anode to float at high voltage rather than being held at ground. This is mitigated by the presence of decoupling capacitors but even if the effective ground plane wobbles by a couple of millivolts, the timing of pulses, and thus the derived positions, can be affected significantly.

The pinhole mask was electroformed from a high precision lithographically produced mould. Thus, the spacing and location of the holes in the mask are quite

accurate. Yet the positions of the holes in the detector images do not form a perfect grid as indicated by the slightly wavy lines of holes in Figure 5.6. This is due to detector and/or electronics INL. A transformation can be applied to spatially correct the wavy mask image back into a perfect grid. Thus, the cumulative effects of INL can be corrected to achieve high accuracy images with correspondingly high resolution. For this purpose, high signal-to-noise images of the pinhole mask were collected for both detectors. Whether or not this correction is necessary will be determined by future experiments.

Table 5.2: Final ion and electron detector DSTDC walk settings

Channel	Ion Detector (V)	Electron Detector (V)
XStart	-1.74	-1.50
XStop	-1.45	-1.44
YStart	-1.31	-1.47
YStop	-0.96	-1.31

5.2.8 Detector Timing CFD Tuning

To tune the Tennelec 454 CFDs used for discrimination of the MCP pick-off pulses, we created precision timed events on the detector face using 300nm ultrashort laser pulses. Again we used a discriminated laser photodiode to Start the Phillips 7187 TDC while using the CFD-discriminated MCP pulses as the Stop. We tuned the CFDs by adjusting the parameters to minimize the width of the MCP pick-off timing histogram. The electron and ion MCP pick-off CFD parameters are shown in Table 5.3. The given timing resolution is the FWHM of the MCP pick-off arrival time histogram.

Figure 5.6: Typical pinhole mask image from the ion detector.

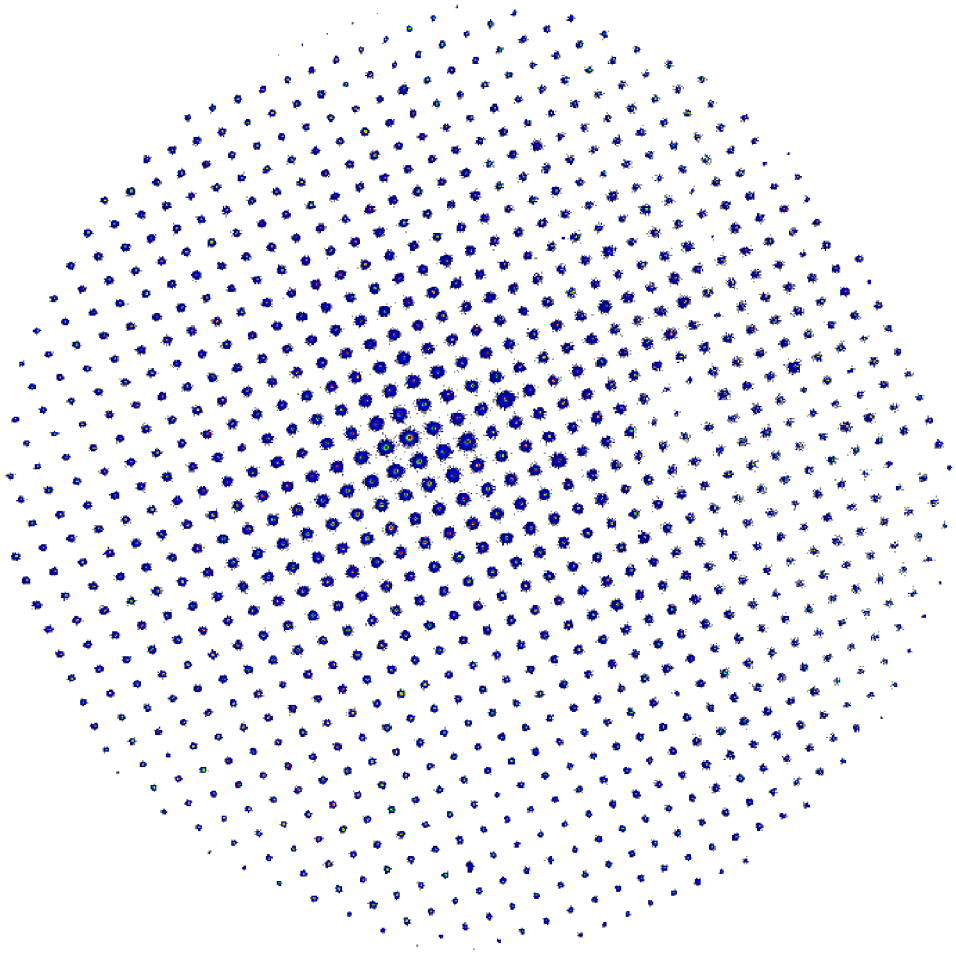

Figure 5.7: Cross-sectional analysis of a detector pinhole image from the ion detector. The plot at the bottom shows the integral across the shorter dimension of the coloured bar.

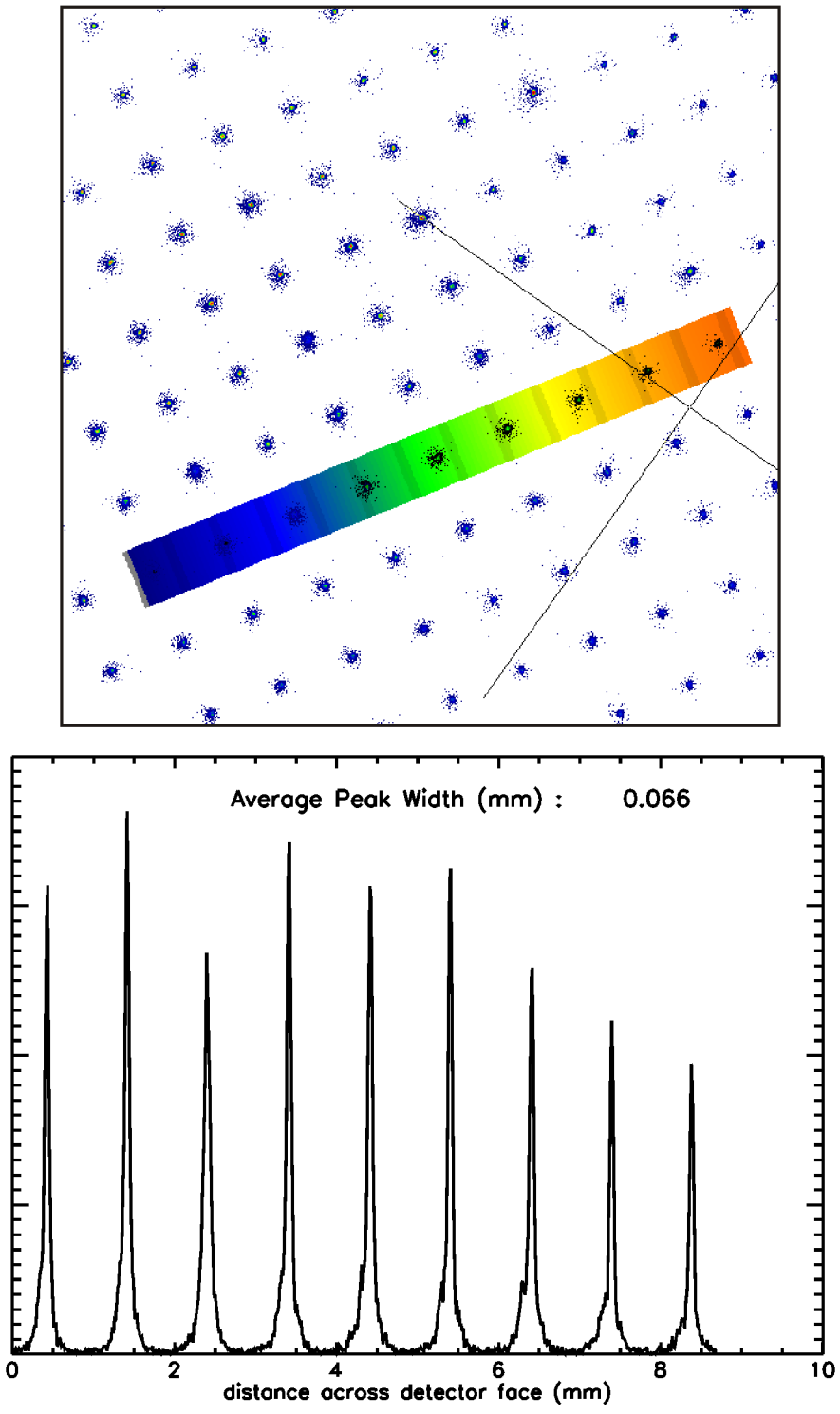

Table 5.3: Tennelec 454 CFD settings for the electron and ion MCP pick-offs

	Electron Detector	Ion Detector	units
walk (Z)	0.0	0.0	mV
external delay	1.5	1.3	ns
fraction (F)	0.4	0.4	
threshold delay	0.75ns	0.75	ns
resolution	200	220	ps

5.3 Data Acquisition Specifics

5.3.1 CAMAC

Our data acquisition (DAQ) system is based on the Computer Aided Measurement And Control (CAMAC) architecture. This data acquisition bus is commonly used in high energy physics. CAMAC is quite an old standard, yet is well suited to our CIS experiment because our photoelectron/photoion measurement requirements parallel those of particle physics experiments. Briefly, one places individual, specialized hardware modules into a CAMAC crate that usually contains 24 slots. Two slots are reserved for the CAMAC controller, which interfaces to other CAMAC crates, VME crates, or in our case, a computer. The controller communicates with the other modules via a dataway hardwired into the backplane of the CAMAC crate. Commands sent from the computer are encoded in a simple, uniform command sequence structure. CAMAC modules are typically designed to take a single piece or set of data during one data acquisition cycle.

The CAMAC controller used in for our setup was the CC32 (Wiener, Plein & Baus GmbH, Burscheid, Germany) interfaced to our computer through a PCIADA card from the same company. Sequenced read and write operations can be executed

on the order of 1-2μs per operation, enabling relatively high speed communication and data transfer rates.

5.3.2 Ion TOF Measurement

For measuring the ion TOF, we used a combination of a Time to Amplitude Converter (TAC) (Ortec 566, Oak Ridge, TN) followed by an 11-bit ADC (LeCroy 2249W). Ion TOFs are typically in the range of several microseconds while the TOF spread, indicating the amount of kinetic energy release (KER), is typically a few 100's of nanoseconds. Therefore, it is desirable to delay the Start trigger for the TAC by several microseconds so that a finer TAC scale can be used to measure the KER more precisely. This delay is long enough that it must be done electronically, however, it is critical that the delay does not jitter or else all benefit of using the finer timing scale is lost.

The scheme we used to minimize the jitter for our TAC Start is shown in Scheme 5.3. Phase locking electronics (SpectraPhysics 3930) lock the femtosecond laser oscillator to a 80MHz reference signal produced by a temperature controlled quartz oscillator. One of the pulses from the oscillator seeds the 1kHz amplifier. These 1kHz pulses are used to conduct the experiments. The 80MHz pulse train is locked to the 1kHz output pulse. Therefore, it is possible to achieve accurate delays in steps of 12.5ns to hundreds of microseconds by simply counting the 80MHz reference clock pulses. This is realized by inputting the 80MHz reference into a discriminator (Phillips Scientific 6904). The input is vetoed by a gate set by a somewhat jittery delay generator (DG535, Stanford Research Systems, Sunnyvale, CA) that opens for exactly one specified 80MHz reference pulse. Only during this gate can the reference

signal trigger output from the discriminator. The output pulse jitter is estimated to be <10ps to very long delays (>1ms). This setup is tolerant of pulse generators that jitter up to 12.5ns, which is easily achievable with standard commercial products.

Scheme 5.3: Scheme for producing low jitter delays

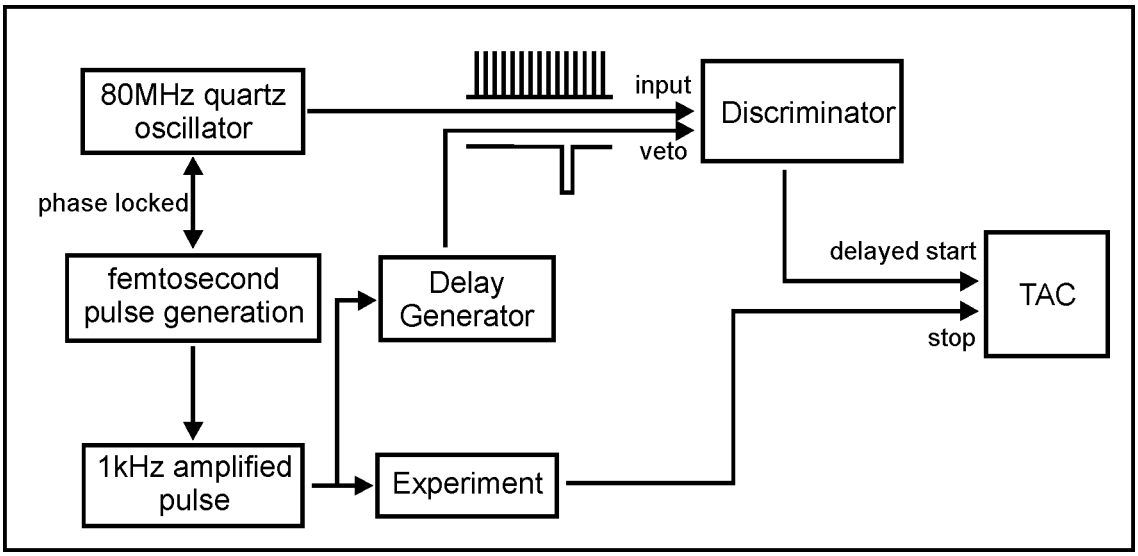

To calculate the TOF spread, the TAC and ADC conversions must be known accurately. The linearity of the TAC was tested using controlled signals from a pulse generator. The plot of voltage output from the TAC versus time difference between the Start and Stop arrival time is linear with slopes, calculated via linear regression, given in Table 5.4. The LeCroy 2249 series ADC's are purely charge integrators that integrate the input channels over the duration of a supplied gate pulse. The gate was supplied from one of the channels of a gate generator (Phillips Scientific 7194, Mahwah, NJ). With a gate width of 127.5ns, the ADC conversion factor is 201.0 ± 0.4 ADC bins / V. As such, the full scale TAC output of 10V roughly translates into a full scale reading on the ADC (11-bits = 2048 bins). Requiring 100μs for digitization of the integrated charge, the LeCroy 2249W ADC is the slowest module on our CAMAC

bus, and thus was used to trigger data readout by the computer.

Table 5.4: Ion TOF Ortec 566 TAC slope

TAC Range (ns)	slope (V/μs)
50	200.9 $\pm$0.4
100	100.3 $\pm$0.1
200	50.11 $\pm$0.04
500	20.98 $\pm$0.01
1000	10.492 $\pm$0.006
2000	5.237 $\pm$0.002

5.3.3 Ion Position and Electron Position and TOF Measurement

For the ion and electron position measurement, each DSTDC interfaces to the CAMAC bus via two 16-bit parallel input modules (BiRa 322, Albuquerque, NM). The transition from two DB25 connectors on the DSTDCs to 16 pair card edge connectors is made via a hand made connector board. The data for each event is present on the parallel output of the DSTDC modules as soon as it becomes available. A hardware clear to the DSTDCs via the connector board clears the fifo buffers and the data available flag prior to the next laser pulse.

The electron TOF measurement by the 12-bit Phillips 7187 TDC directly interfaces to CAMAC.

5.3.4 Ion and Electron Detector Charge Measurement

While the Sensor Sciences anode delay line preamps have high frequency AC amplifiers for the timing signals, they also have a lower frequency ($\sim$1MHz) AC amplifier that

integrates the charge deposited on the anode. The output is a bipolar pulse with total duration of 3-4μs whose amplitude is proportional to the anode charge. The charge pulse is inverted and amplified to drive a 50Ω load by a set of home built amplifiers. The ion and electron charge pulses are input into separate LeCroy 2249A ADC modules digitizing at 10 bits in 60μs. The gates for these measurements are provided by a pair of channels from a Phillips Scientific 7194 Quad Gate Generator.

A typical pulse height distribution is shown in Figure 5.8. Notice how the charge distribution can help differentiate between single hits; double hits, where the anode charge is approximately twice that of single hits; and dark counts, where the anode charge is anomalously low.

Figure 5.8: Typical anode charge pulse height distribution. Counts in region (a) are dark counts; (b) are single detector hits and; (c) are double detector hits. The FWHM in this case is $\sim$65%.

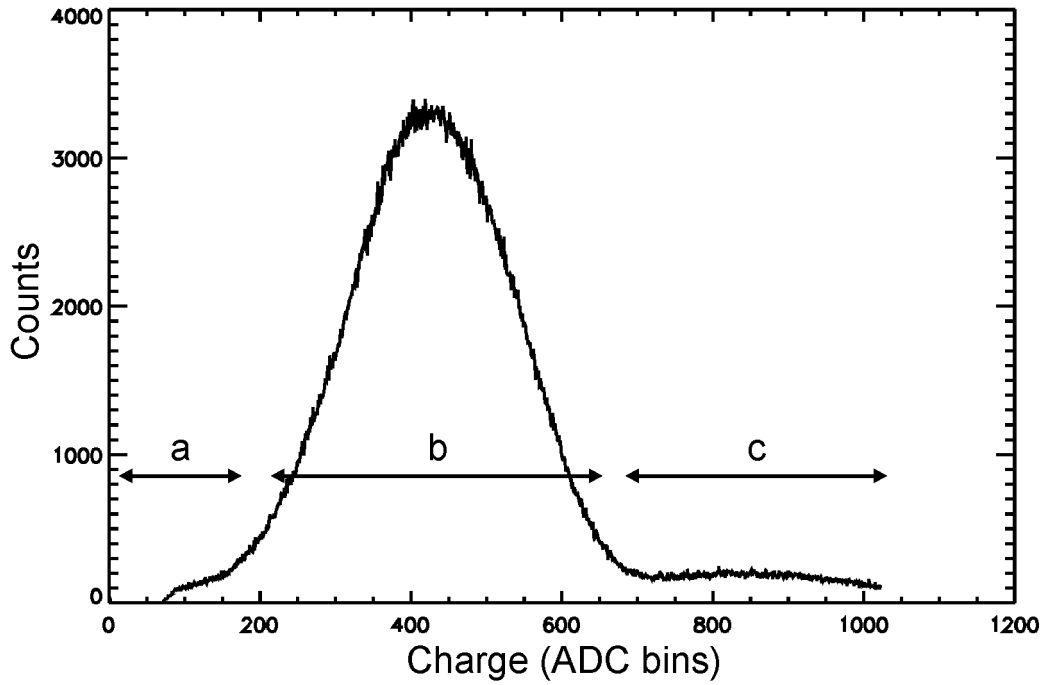

5.3.5 Ion Count Measurement

The modules that measure the ion TOF, position, and charge are implemented to receive one and only one event per laser shot. However, there is the possibility that two or more ions are formed in the interaction region and make their way to the detector. In this case it is ambiguous to which ion the electron correlates. Thus it is necessary to identify and filter out these events. There are two DAQ scenarios depending how different the ion TOFs are. If ions arrive at the detector within $\sim 1\mu$s of each other, the ion charge measurement will be able to distinguish between single and multiple hits. If ions arrive further than $\sim 1\mu$s apart, the charge pulses will be separated in time and the charge measurement will register only a single detector hit. To record these events, we placed a counter (LeCroy 2551 Scaler) on the MCP pick-off line following a long blocking width ($\sim$120ns width) discriminator. The long blocking width discriminator is present to eliminate occasional double pulsing seen from short output discriminators due to triggering on reflections of large MCP pulses.

5.3.6 Laser Counter Measurement

The current laser shot is read by a home-built 24-bit counter that inputs to CAMAC via a parallel connection (BiRa Systems 2322, Albuquerque, NM). Unfortunately, output bits 9 and 10 were switched during building of the module, however this can be easily corrected afterwards using software.

5.4 Data Acquisition Implementation

We were able to fit all of our DAQ modules into a single CAMAC crate. This greatly simplifies computer-instrument communication since all CAMAC modules are accessed in a similar manner. A schematic representation of the DAQ layout is shown in Scheme 5.4. (The diagram is provided for reference only, a full understanding of the diagram in not necessary for the discussion here.) All of the modules except the laser counter are hardware cleared $\sim 995\mu$s after each laser pulse, $\sim 5\mu$s before the next laser pulse. The main source of noise on the signal line in this experiment is the high voltage ion extraction pulse. The high frequencies present on the sharp leading and trailing edges capacitively couple to all nearby signal lines. Extensive gating was implemented to mask out these signals to the greatest extent possible.

Scheme 5.4: CIS Data Acquisition system layout

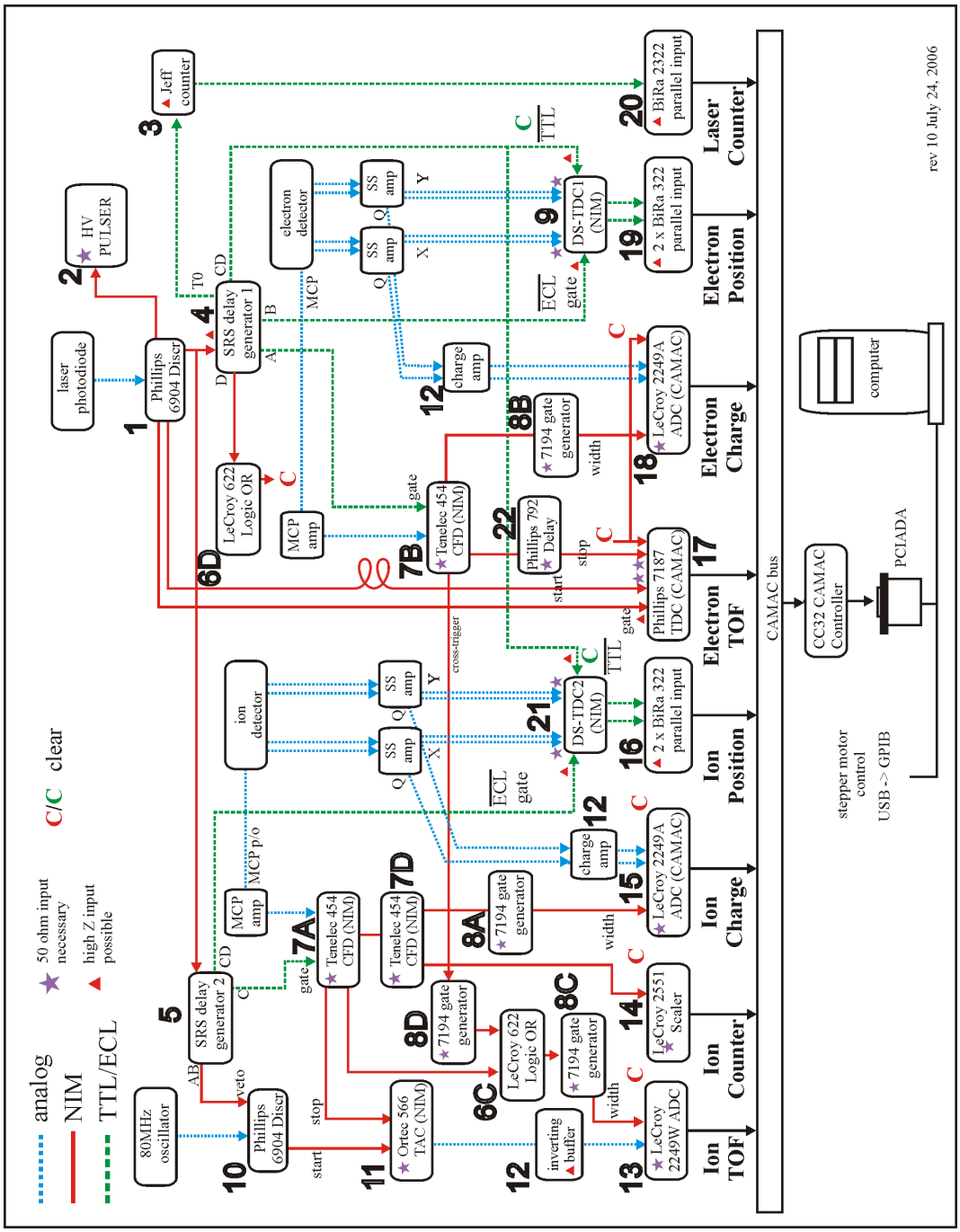

5.5 Signal Timing

A valid event chronology follows:

1. a laser pulse hitting a photodiode generates a Start for both the electron and ion TOF measurements.
2. pump and probe laser pulses generate an ion/electron pair.
3. electron is extracted towards electron detector and causes a hit on the electron detector.
4. electron position pulses travel along delay line. One output of each delay line is delayed so that one pulse always arrives first.
5. electron MCP pulse enters TDC to measure TOF and gate closes.
6. electron position enters front end of DSTDC and gate promptly closes.
7. high voltage pulse extracts ions toward ion detector.
8. electron charge pulses arrive at ADC.
9. ion strikes detector, ion position is measured by DSTDC, ion TOF is measured by TAC, and ion charge is measured by ADC.
10. ion TOF is digitized completing acquisition of all event data.
11. computer program is triggered to read CAMAC modules.
12. computer completes data read.
13. CAMAC crate is cleared and is prepared for next event.

5.6 DAQ Computer and Software

The computer runs asynchronously from the experiment and is interrupt triggered from the CAMAC crate when it receives valid data events. After triggering, the computer must read all of the necessary instruments on the CAMAC bus before the next laser shot. Since our computer runs Windows, there is an inherent difficulty in

controlling the timing of commands. The implementation of the laser shot counter allays this problem. At the start of a data event retrieval, the laser counter is read. After reading all of the instruments, the laser counter is read again. If both laser counter readings are the same, then we are sure that the data is from a single data event. Of course this means that we must discard events that have differing laser count readings, but fortunately, this occurs rarely.

This problem can be overcome with the new CAMAC controller module CC-USB from Wiener, Plein & Baus GmbH, Burscheid, Germany. This controller contains an internal programmable list processor that can execute CAMAC commands and buffer data autonomously. Using this module, computer communication is not timing critical and is only necessary to transfer large chunks of data.

5.6.1 DAQ Software

Currently, the software measures full coincidence events, or just events due to ions or electrons alone. The DAQ software was written in Borland Delphi 5 and consists of 8 primary modules containing >2300 lines of code (none of which will be reproduced here). The program was written to be multi-threaded so that data acquisition does not conflict with such things as screen updates or the user interface. The current version of the program is called "Full_CIS_v1_1.exe". Brief descriptions of the program modules are given here.

main.pas

- Performs global variable initialization.
- The main program module that contains the Form:main.

- Form:main contains all of user input information, including experimental parameters, and locations of instruments within the CAMAC crate.
- Form:main contains the program control (Start/Stop/Pause) user interface.
- Starts the data acquisition thread DAQThread, the plotting thread PlotThread, and the runtime thread RunThread.

DAQThread.pas

- Controls all communication with the CAMAC crate.
- Stores data events in the appropriate arrays.
- Occasionally call SaveDataModule routines to save the data to disk.

PlotThread.pas

- Plots histograms of iPos, ePos, iTOF, iQ, and eQ, and detector images to the screen.
- Updates times and counters on Form:main.

RunThread.pas Very rarely, the DAQThread hangs because it misses the interrupt request from the CAMAC crate. This thread checks that data is constantly being acquired. If it does hang, it kills the DAQThread and restarts it.

globals.pas Contains all global variables used in all of the modules.

camac.pas Contains all function prototypes for accessing CAMAC commands using the DLL "pcicc32_ni.dll".

SaveDataModule.pas Contains all data saving routines.

DataForm.pas Contains definitions, methods, and functions for the windows displaying the real-time histograms and images.

Chapter 6

Background Removal and Spectrometer Calibration

6.1 Introduction

This chapter deals with two steps necessary for performing real CIS experiments: the removal of unwanted signals from the CIS data; and the calibration of the spectrometer. There are many sources of unwanted signals in a typical CIS experiment. Correspondingly, there are several ways of minimizing the effects of these signals by taking appropriate action before, during, and after the experiment. Some of these background sources are demonstrated using 267nm multiphoton ionization of nitric oxide (NO). Before performing a real CIS experiment, it is also necessary to calibrate certain spectrometer parameters to calculate particle momenta and distributions correctly. Simulations are extensively used to determine these parameters.

6.2 Removing Unwanted Data Signals

There are several sources of unwanted signals in the CIS experiment. These include

- events caused by laser light striking the detectors.
- electrons photoemitted from surfaces that are struck by laser light.
- events from photodissociation/photoionization of the background gas.
- multiple hits on the detectors.
- false ion/electron coincidences.
- single laser pulse (ie. non pump-probe) photodissociation/photoionization.

Methods to reduce or remove these effects on distributions and spectra are discussed here.

6.2.1 Photoemission and Scattered Light

Due to the open nature of the electrodes, the spectrometer collects electrons from a large volume not limited to just the interaction region. Stray photoelectrons can be produced via photoemission from UV laser light striking the spectrometer surfaces. Depending on where these electrons are produced, they can be accelerated and detected. Events can also be caused by the UV light directly hitting the detectors. To reduce light scattering, the electrodes in the extraction region were designed to be far apart with a minimum 8mm gap for the laser light to pass through.

The exposed surfaces near the interaction region were coated with either germanium or gold. Work functions for laboratory prepared surfaces of Ge and Au

are reported to be 4.78eV [87] and 4.83eV [88] respectively. Initial tests performed using low intensities ($\sim$1μJ) of 267nm (4.64eV) light in our spectrometer showed prohibitively large numbers of photoemitted electrons and scattered light events (>0.3 per laser shot) that precluded any real molecule measurements. The ability of the 267nm laser light to cause photoemission was rather surprising, considering that the photon energy is below the work functions of both Au and Ge. The observation of photoelectrons was thought to be due to thermal excitation or the presence of surface defects, either of which could lower the work function. Elimination of these bad events required, in addition to the light-masking baffles and entrance/exit window geometries described in Chapter 4, strict control over the quality of the incoming laser beam. After spatial filtering and ensuring that the steering mirrors to the vacuum chamber were defect-free, scattered light/photoemission events were reduced to <0.005 per laser shot at pulse energies up to 3μJ.

The electron TOF spectrum for NO 267nm multiphoton ionization is shown in Figure 6.1. Ionization via two photons (2×4.64eV = 9.29eV) to the ground vibrational ionic state (IP = 9.264eV[89]) yields low energy electrons ($\sim$25meV). This NO photoelectron peak is centred at 1520. Expanding the count axis in Figure 6.1b shows the presence of many additional peaks located before and after the NO photoelectron peak in time. The counts between 0 and 63 are artifacts created by the TDC dithering circuit and should be ignored. Three small peaks preceding the NO peak are seen at 950, 1000, and 1200. The peak at 950 is caused by scattered light directly hitting the detector. The peak at 1000 is due to photoelectrons created in the region between the detector and the electron drift tube. The peak at 1200 is due to photoelectrons created between the ion extraction and ion acceleration grids. These electrons are

born at high negative potential and arrive quickly at the detector. The smeared peaks at 2050 and 2650 are due to photoelectron creation in the electron and ion drift tubes respectively. They arrive at late times because they require a long time to travel out of these field free drift regions. Post-experiment removal of unwanted electrons and scattered light is easily performed since the electron TOF peak of interest is well separated from the other peaks. Electrons that arrive before and after the desired peak can reduce the count rates for the desired peaks if they arrive within the same laser shot. This is because the electron charge ADC will measure multiple hits and the event will have to be discarded. Fortunately, as seen in the figure, the number of these events can be made small.

Figure 6.1c shows a closer view of the NO photoelectron spectrum. It is more asymmetric than expected based on simulations. The shape of this peak is due to deflections of the electrons by the grid meshes, causing smearing of the TOF peak towards longer times. To avoid artifacts caused by the grid deflections, it might be desirable to preferentially select particles that travel towards the detector for data analysis. Similar smearing of the TOF peaks is also seen in the ion TOF spectrum.

6.2.2 Background Gas Photoionization / Photodissociation

Events caused by photoionization of the background gas are easily seen in the 266nm multiphoton ionization image of NO (see Figure 6.2). Desired events are caused by the intersection of the laser and molecular beams. Background gas ionization causes a stripe of events coincident with the projection of the laser beam on the detector. On the electron detector, this stripe passes through the intense central spot of the desired events. On the ion detector, the NO^+ ions produced from the molecular beam are

Figure 6.1: Electron TOF spectrum for NO 267nm multiphoton ionization. The horizontal axis is in 25ps TDC bins. (a) Full TOF spectrum. (b) Full spectrum with expanded y-axis. (c) The NO photoelectron peak. See text for description of peaks.

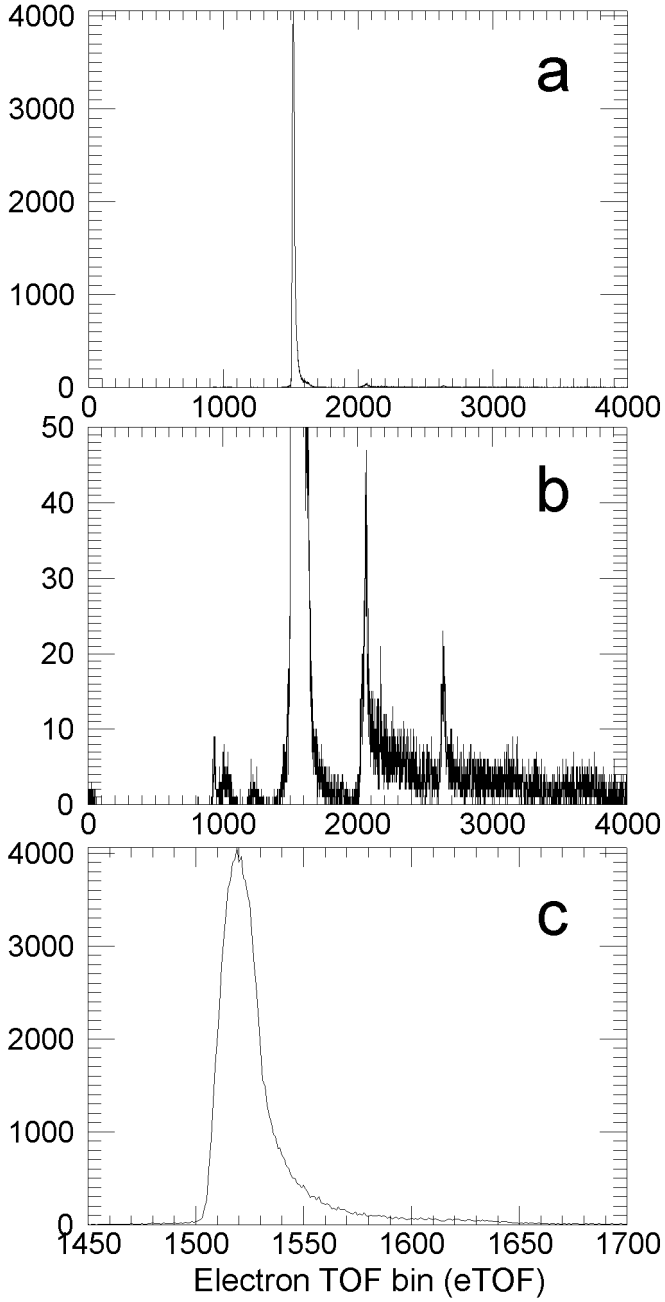

shifted relative to the background stripe because they travel at the average molecular beam velocity. Removal of the background ion events is trivial if they are spatially separated from the ions of interest. Seeding the molecule of interest in helium helps separate the ions by increasing the average molecular beam speed.

If the background events overlap the real events, as is always the case for electrons, there are two solutions. The first is to decrease the background gas pressure. This can be achieved by increasing the pumping speed for the chamber by adding additional pumps, or by decreasing the gas load supplied to the chamber. At 1kHz laser repetition rate, the gas load can be easily decreased by a factor of ~ 100 using a pulsed valve with 10μs opening time. The additional benefits of using a pulsed valve to increasing spectrometer resolution were already discussed in Chapter 4. Additionally, as will be presented in Section 6.3.4, the stability of the molecular beam is important for accurately determining the projection of the origin onto the detector. Running a continuous molecular beam can consume considerable amounts of gas and for long experiments requiring many hours of data acquisition time, the stability of the beam may be compromised. In contrast, a 10μs pulsed molecular beam consumes 100 times less gas volume.

The second solution to removing background events is to subtract their effect from the derived distributions and spectra. For this solution, data sets of background only (BG), and background plus real data (BG+Real), must be collected. To ensure that the background is identical for both data sets, the molecular beam must be flowing for both experiments, however, for the background only data set, the piezoslit must be completely closed to eliminate events from the molecular beam. Both the BG and BG+Real data sets must be subjected to the same calibration and transformation

steps to obtain a distribution (kinetic energy, photoelectron angular, energy correlation, etc). In the final step the BG distribution can be subtracted from the BG+Real distribution to obtain only the Real distribution.

Of the two solutions to reducing background gas effects, the former is superior as it is always better to eliminate background in the first place rather than correct for it afterwards. Subtraction of distributions always leads to increased noise. Also, background subtraction requires the collection of two data sets, thus doubling the experimental time. High quality data sets require many hours of data collection so this becomes an important issue when laser and molecular beam stability factors are considered.

Figure 6.2: Ion and electron images for 267nm multiphoton ionization of NO. Molecular beam ionization events result in the intense spots on the detector. The diffuse, horizontal stripes are due to photoionization of the background gas.

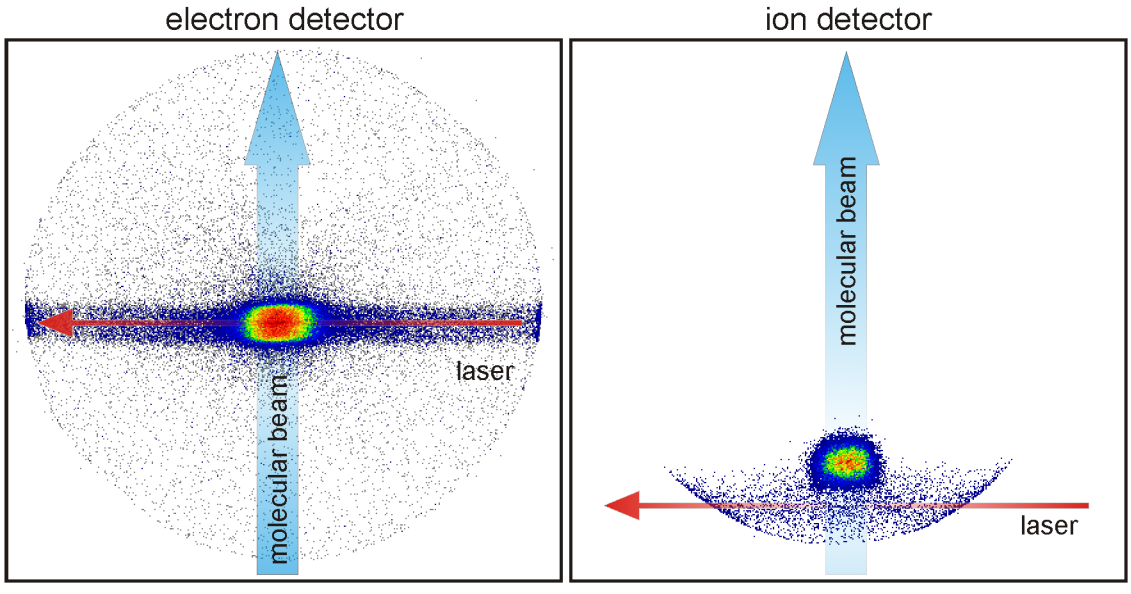

6.2.3 Multiple Detector Hits

The detector charge indicates if multiple ions/electrons hit a detector simultaneously ($<1\mu$s apart). Figure 6.3 shows the ion detector charge distribution for 267nm NO photoionization. The FWHM of the distribution divided by the peak position defines the pulse height distribution, in this case it is 29%. This is significantly narrower than that shown in Figure 5.8 because the ions hit a small region of the detector. From this distribution, single hit events are easily separated from dark counts and double hits. For the ion detector, non-simultaneous ($> 1\mu$s apart) multiple hits are measured by the scaler card.

Figure 6.3: Ion detector charge distribution for 267nm NO photoionization. The FWHM of the distribution divided by the peak position defines the pulse height distribution; in this case it is 29%.

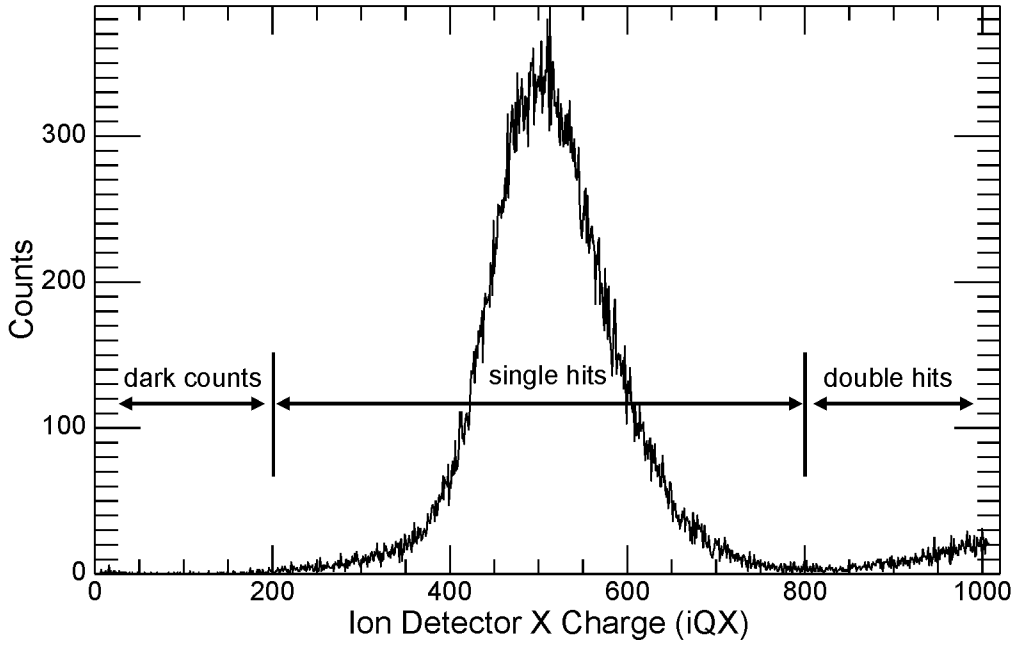

6.2.4 False Coincidences

An electron/ion pair is called a false coincidence if they originate from two different molecules. False coincidence events are completely indistinguishable from true coincidence events. If the detection efficiencies for either of the particles is unity, there are no false coincidences because multiple particle events are eliminated as described previously. In this case data can be collected at a rate up to 1 per laser shot. For our spectrometer, the grids and MCP active area greatly reduces the detection efficiency of both particles, and necessitate a data acquisition rate significantly less than 1 per laser shot. Following the analysis of Stert and coworkers[90], assuming Poisson statistics, the rates of detecting ions and electrons are

$$w_i = \xi_i \overline{n} \tag{6.1}$$

$$w_e = \xi_e \overline{n} \tag{6.2}$$

where ξ_i and ξ_e are the ion and electron detection efficiencies respectively, and $\overline{n}$ is the average number of photoelectron/photoion pairs produced per laser shot. The total coincidence rate, the rate of detecting exactly one electron and one ion from a single laser shot, w_{11} is given by

$$w_{11} = \xi_i \xi_e \overline{n} \left[1 + \overline{n}(1-\xi_e)(1-\xi_i)\right] \times \exp\left[-\overline{n} + \overline{n}(1-\xi_e)(1-\xi_i)\right] \tag{6.3}$$

The true and false coincidence rates, $w_{11}^{(t)}$ and $w_{11}^{(f)}$, are

$$w_{11}^{(t)} = \xi_i \xi_e \overline{n} \times \exp\left[-\overline{n} + \overline{n}(1-\xi_e)(1-\xi_i)\right] \tag{6.4}$$

$$w_{11}^{(f)} = \xi_i \xi_e \overline{n}^2 (1-\xi_i)(1-\xi_e) \times \exp\left[-\overline{n} + \overline{n}(1-\xi_e)(1-\xi_i)\right] \tag{6.5}$$

One of our NO 267nm photoionization data sets yielded 62,531 electron events, 53,930 ion events, and 21,248 coincident events for 373,280 laser shots. Using Equations 6.1 to 6.3, the calculated total detection efficiencies for electrons and ions are

0.45 and 0.39 respectively, and the average number of electron/ion pairs produced per laser shot was 0.37. Assuming grid transmission efficiencies of 0.89 for the 8 lines/mm grids and 0.79 for the 20 lines/mm grids, the electron and ion detector efficiencies are 0.64 and 0.70 respectively. This information is summarized in Table 6.1.

Table 6.1: Electron/Ion Detection Efficiencies.

Particle	Total Detection Efficiency	Grid Efficiency	Detector Efficiency
Electron	0.45	0.70	0.64
Ion	0.39	0.56	0.70

It is experimentally useful to use substitute Equations 6.1 and 6.2 into Equations 6.3 through 6.5 to obtain the total, true, and false coincidence rates as a function of the easily measured electron or ion count rates w_e and w_i. Plots of these coincidence rates as a function of either the electron or ion count rates are shown in Figures 6.4 and 6.5 respectively. The detection efficiencies used are those shown in Table 6.1. As an example, to achieve <10% false coincidences, the total coincidence count rate should be ∼5% of the laser repetition rate. The ratio of true to total coincidences approaches unity for count rates approaching zero. However, the absolute true coincidence rate is small at low count rates. Thus, there is always a compromise when adjusting laser power and molecular beam intensity; higher count rates are desired to collect good signal to noise data, but smaller count rates are needed to avoid large numbers of false coincidences.

6.2.5 Background Signal Subtraction

When performing pump-probe experiments, events are almost always created by photodissociation/photoionization of the target molecules by either the pump or probe

Figure 6.4: (top) Total (w_{11}), true ($w_{11}^{(t)}$), and false ($w_{11}^{(f)}$) coincidence rates versus ion count rate. The electron and ion detection efficiencies are 0.45 and 0.39 respectively. (bottom) The ratio of the number of true coincidences to the total number of coincidences versus ion count rate.

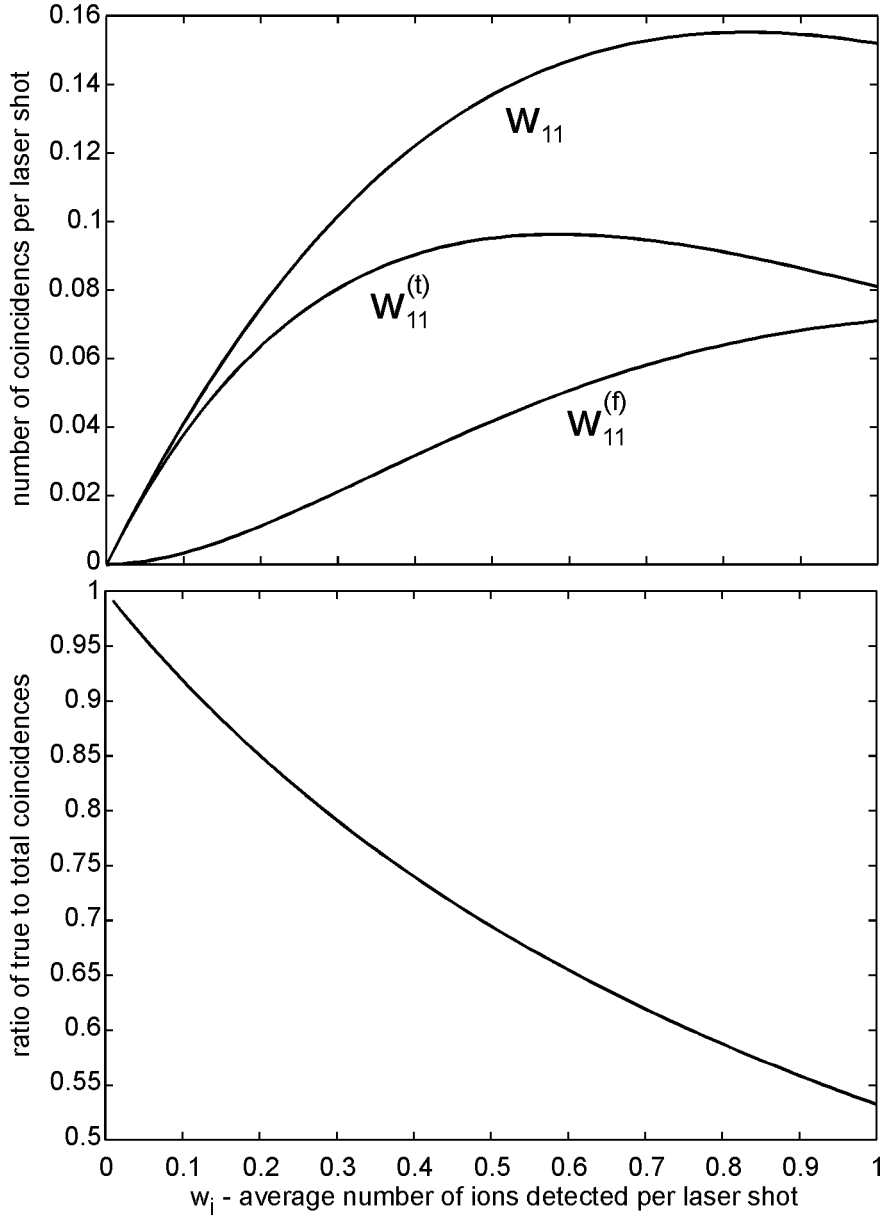

Figure 6.5: (top) Total (w_{11}), true ($w_{11}^{(t)}$), and false ($w_{11}^{(f)}$) coincidence rates versus electron count rate. The electron and ion detection efficiencies are 0.45 and 0.39 respectively. (bottom) The ratio of the number of true coincidences to the total number of coincidences versus electron count rate.

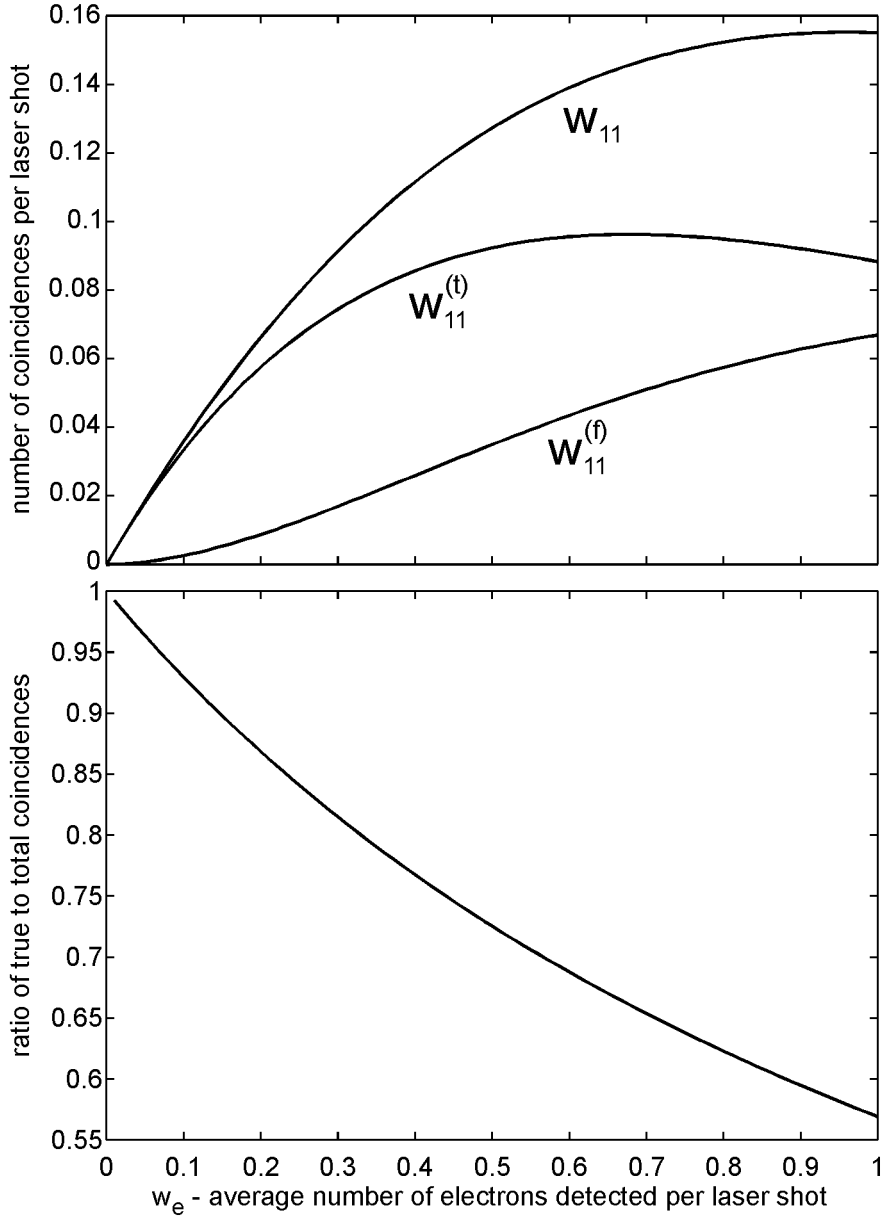

laser alone. One optimally wants to adjust the laser intensities to maximize the signals of interest while minimizing these single pulse backgrounds, however, it is unlikely that all such events can be eliminated. If the amount of single-colour background is significant, it may be necessary to subtract the background from the real data in a similar manner to that described for background gas interference in Section 6.2.2. In this case, it is necessary to measure three data sets: the pump laser alone; the probe laser alone; and the pump and probe lasers together.

It is also possible to subtract distributions due to false coincidences. All coincidence events must be separated into ion and electron measurements and pooled together with events where only a single particle was measured. A data set of false coincidences can then be constructed by recombining these separated measurements in a random fashion. Distributions of these false coincidences can be subtracted from distributions created from events containing both true and false coincidences to yield distributions resulting only from true coincidences. Use of Figures 6.4 or 6.5 can give an estimate of the number of false coincidence events that need to be created. This number can be increased or decreased accordingly to eliminate a feature in a distribution that is known to be an artifact due to false coincidences.

6.3 Spectrometer Calibration

For the electron spectrometer, the unknown parameters that must be calibrated are: 1) the time difference between the photoionization event within the spectrometer and the Start trigger of the TOF measurement, $t_{e,start}$; 2) the projection of the origin onto the detector, $(x,y)_{e,origin}$; and 3) the detector spatial intensity correction function, $I_{e,corr}(x,y)$. Similar parameters $t_{i,start}$, $(x,y)_{i,origin}$, and $I_{i,corr}(x,y)$ are also required

for the ion spectrometer. Additionally, the arrival time of the high voltage pulse at the interaction region, t_{pulse}, and the average molecular beam velocity, v_{beam}, must be calibrated. These parameters must be calibrated by photodissociating or photoionizing molecules with well known energy spectra and/or angular distributions.

6.3.1 Photoelectron and Photofragment Angular distributions

In general, photoelectron angular distributions (PADs) and photofragment recoil distributions can be expressed as a sum of spherical harmonics:

$$I(\theta,\phi) \propto \sum_{L=0}^{L_{max}} \sum_{M=-L}^{L} B_{LM} Y_{LM}(\theta,\phi) \tag{6.6}$$

where $I(\theta,\phi)$ is the intensity per unit of solid angle, $Y_{LM}(\theta,\phi)$ are the spherical harmonics, and the coefficients B_{LM} depend on the experimental geometry, and dynamics of the photodissociation or photoionization. θ is measured with respect to the laboratory frame axis, which for linearly polarized light lies along the laser electric field vector. For single photon processes, the distribution simplifies to the well-known 'beta'-distribution[91]:

$$I(\theta) \propto \quad 1 + \beta P_2(\cos\theta) \tag{6.7}$$

$$P_2(\cos\theta) = \quad \tfrac{1}{2}(3\cos^2\theta - 1) \tag{6.8}$$

where β is the anisotropy parameter, and $P_2(\cos\theta)$ is the second order Legendre polynomial. For purely parallel transitions, $\beta = 2$, producing a $\cos^2\theta$ distribution. For purely perpendicular transitions, $\beta = -1$, producing a $\sin^2\theta$ distribution. Values of β between these two extremes indicate photodissociation or photoionization dynamics. Examples of simulated electron TOF distributions with $\beta = 2, 0, -1$ using linearly

polarized light for electric field vectors oriented parallel and perpendicular to the spectrometer axis are shown in Figure 6.6. The corresponding simulated images are shown in Figure 6.7.

The anisotropy parameter is a function of the energy release. Therefore, the complete photofragment/photoelectron energy and angular distribution is described by

$$\mathcal{P}(E_T, \theta) = P(E_T)\left[1 + \beta(E_T)P_2(\cos\ \theta)\right] \tag{6.9}$$

where E_T is the kinetic energy release.

For n photon processes, the general expressions for photoelectron/photofragment distributions contain even order Legendre polynomial terms up to order $2\times n$ [92].

6.3.2 Electron Axial Momentum Calibration

For the electron spectrometer, the spectrometer voltages and distances between grids are well defined. Additionally, the laser-molecular beam interaction region is sufficiently small and the space focussing conditions such that the only undetermined parameter required for TOF calculation is the time difference between the photoionization event within the spectrometer and the Start trigger of the TOF measurement, $t_{e,start}$. With only one unknown, only one calibration experiment needs to be performed. This can be accomplished by measuring a TOF spectrum from an atom or molecule with a relatively simple PAD. The only information that needs to be gleaned from the PAD is the TOF for an electron with no initial velocity directed along the spectrometer axis as measured by the TDC, $t_{v_0=0,TDC}$. The timing offset is then

$$t_{e,start} = t_{v_0=0,analyt} - t_{v_0=0,TDC} \tag{6.10}$$

Figure 6.6: Simulated single photon $\beta = 2, 0, -1$ photoionization TOF spectra for light polarized parallel and perpendicular to the spectrometer axis. The electron kinetic energy release is 0.78±0.12eV. The extraction field was 12.5V/cm. Each distribution consists of 10^6 electrons.

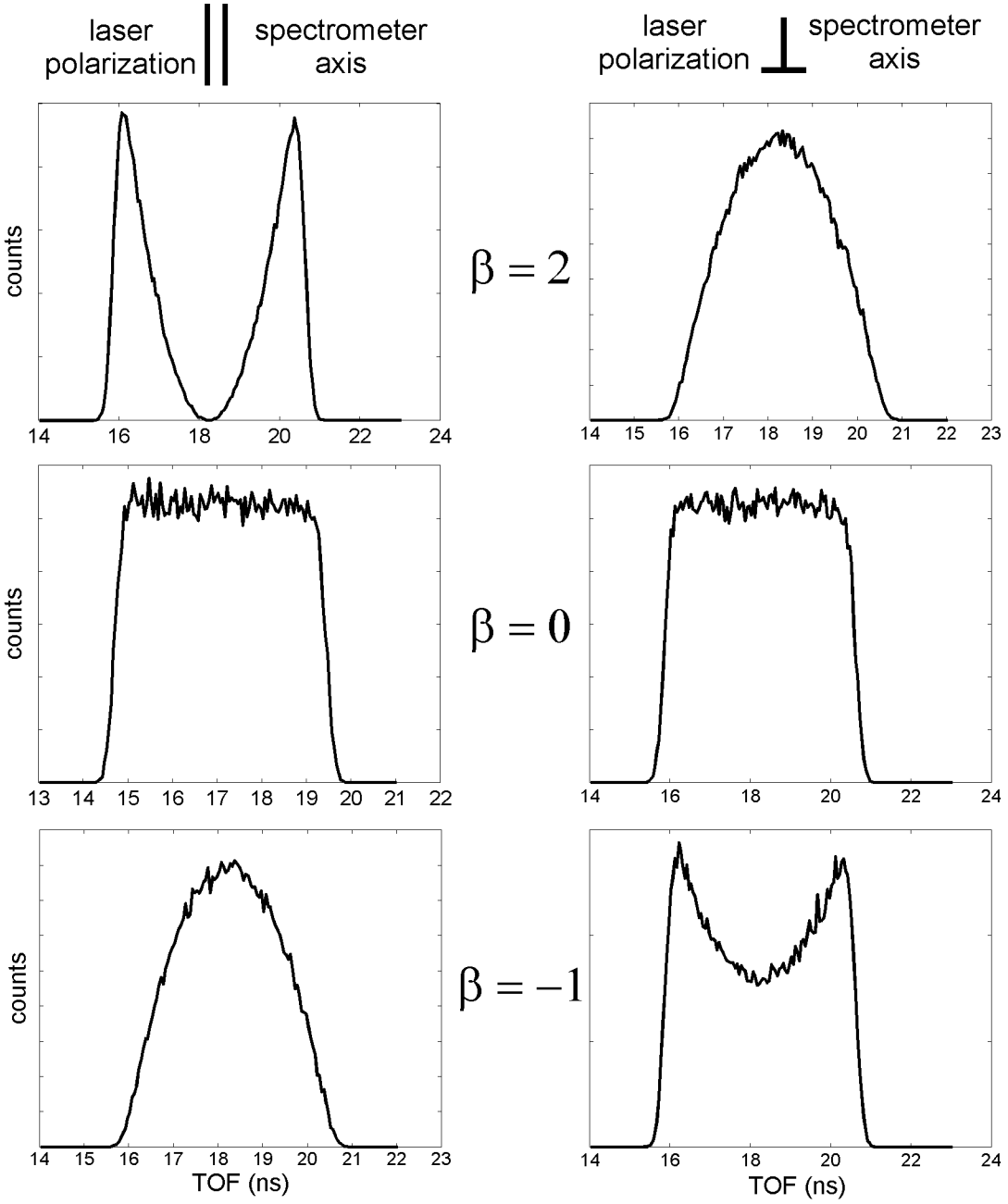

Figure 6.7: Simulated single photon $\beta = 2, 0, -1$ electron images for light polarized parallel and perpendicular to the spectrometer axis. The electron kinetic energy release is 2.0±0.1eV. The extraction field is 12.5V/cm. Each image is constructed from 10^6 electrons. Axes are labeled in mm.

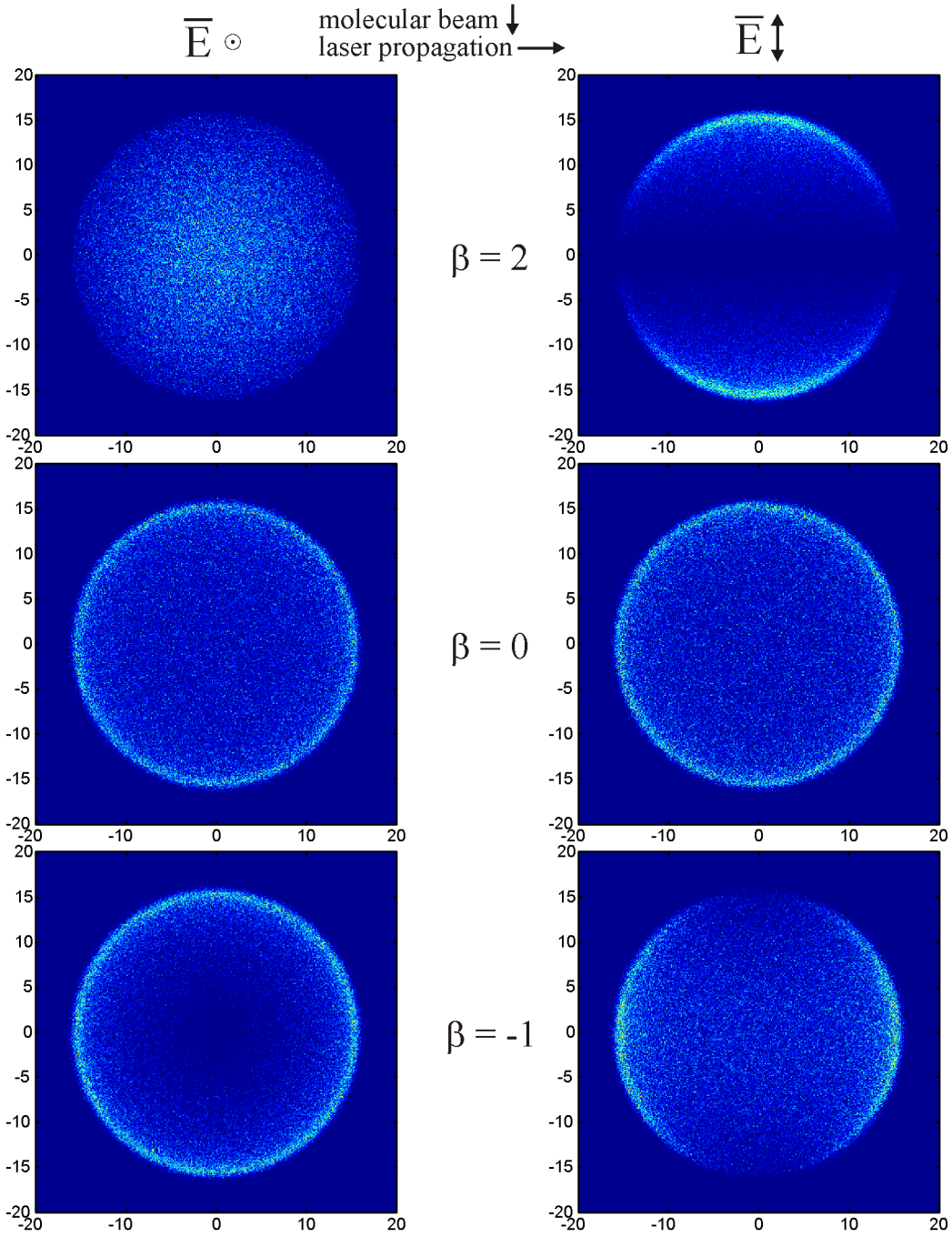

where $t_{v_0=0,analyt}$ is the analytically calculated TOF for an electron passing through the spectrometer with the specified voltages. All TOFs measured by the TDC, TOF_{TDC}, must be shifted to obtain the real TOF, TOF_{real}:

$$TOF_{real} = TOF_{TDC} + t_{e,start} \tag{6.11}$$

$t_{v_0=0,TDC}$ can only be found using an entire TOF distribution. There are several ways of determining $t_{v_0=0,TDC}$ from the TOF distribution. Two of the simplest ways are described here. One is to simply find the median of the TOF distribution. In theory, since equal numbers of electrons will be ejected towards the detector as away from the detector, the median will have TOF equal to $t_{v_0=0,TDC}$. Another way to find $t_{v_0=0,TDC}$ is to fit the central part of the TOF distribution with a polynomial. As seen in Figure 6.6, for linearly polarized light with its electric field vector aligned exactly parallel or perpendicular with the spectrometer axis, the median, and thus $t_{v_0=0,TDC}$, are found near a minimum or a maximum in the TOF distribution (with the exception of isotropic $\beta \approx 0$ distributions).

Using simulated TOF spectra generated assuming a single electron energy and angular distribution given by Equation 6.9, we tested the validity of both of the described methods for obtaining $t_{v_0=0,TDC}$. Electrons were simulated with kinetic energy 0.78±0.03eV for different values of β. 10^6 electrons were simulated for each TOF distribution.

For distributions with large positive β, and laser polarization located along the spectrometer axis, fitting the central part of the TOF distribution with a 3^{rd}-order polynomial and using the minimum as $t_{v_0=0,TDC}$ proved to be quite accurate. For $\beta \gtrapprox 1.5$, the fitted $t_{v_0=0,TDC}$ were better than the timing resolution of the spectrometer. Directly calculating the median is less accurate for $\beta \gtrapprox 1.5$ because there is a dearth of

events near the minimum which causes $t_{v_0=0,TDC}$ to be severely affected by statistical fluctuations. For $\beta \lesssim 1.5$, the situation is reversed. Direct calculation of the median results in an accuracy approximately equal to the spectrometer timing resolution whereas the polynomial fitting method is significantly worse. The polynomial method falters because the minima/maxima become shallow and loosely defined near $\beta = 0$. Also, $t_{v_0=0,TDC}$ skews slightly away from the extrema because on propagating the trajectories through the spectrometer, equally spaced v_{0z} slices do not map to the same number of bins in the TOF spectrum. TOF distributions described by Equation 6.9 obtained with the laser polarization perpendicular to the spectrometer, do not have a minimum in the TOF that reaches zero, so the median method is recommended for determining $t_{v_0=0,TDC}$.

In principle, it is possible to measure absolute TOF timing if scattered laser light causes a detectable event on the detector. In this case, $-t_{e,start}$ is equal to the TDC measured arrival time of the laser event on the detector. In our experiment, scattered light is often a problem that has to be gated out in order to record real data. Also, the ability of the laser to cause events is a function of laser intensity and wavelength, and thus is not always a reliable source. Another method is to use Monte Carlo simulations of trajectories to generate and fit the parameters, including $t_{e,start}$, that determine the measured TOF spectrum.

6.3.3 Ion Axial Momentum Calibration

The ion TOF calibration is slightly more involved because it involves the determination of two parameters, $t_{i,start}$, analogous to that for the electron spectrometer, and t_{pulse}, the arrival time of the high voltage pulse at the interaction region. Since two

parameters are sought, two experiments are required. In the first experiment, the high voltage pulser used to extract the ions from the interaction region must be replaced with a static high voltage source. This eliminates t_{pulse} from the experimental parameters and allows calculation of $t_{i,start}$ as was done for the electron spectrometer. Care must be taken to ensure Wiley-McLaren space focussing voltages within the spectrometer so that time spreading due to the extent of the interaction region is minimized.

The experiment must then be repeated with the high voltage pulser connected and operating. This shifts $t_{v_0=0,TDC}$ to a different time. Determining the amount of this shift allows calculation of t_{pulse} via a fitting procedure. Simulations show that recovery of t_{pulse} from such a fitting procedure is within the timing resolution of the spectrometer.

6.3.4 Radial Momentum Calibration

The detector length calibrations, x-y stretching factors, and distortions were determined using the pinhole mask as described in Chapter 5. Radial velocities are measured by dividing the particle displacement from the projection of the origin onto the detector by the particle TOF. Finding this origin projection is the challenging part of the calibration.

For electrons, as stated in Chapter 3, the molecular beam velocity is insignificant compared to kinetic energy release. Therefore, electron images are approximately centred on the detector with small variations due to laser and/or molecular beam alignment. Finding the exact image centre can be difficult if the photoelectron spectrum of a molecule is not very structured. Therefore, it is desirable to calibrate for

$(x, y)_{e,origin}$ using a molecule that does have a structured photoelectron spectrum, producing complete or partial rings in the detector image. Examples of such rings are seen in the selected β distributions shown in Figure 6.7. For $\beta < 0$ distributions, these spectral rings are more well defined when the laser polarization is parallel to the spectrometer axis, while $\beta > 0$ distributions are sharper when the laser polarization is perpendicular. The centre of the rings defines $(x, y)_{e,origin}$.

In principle, since no radial forces are exerted on the electrons as they traverse the spectrometer, the location and energy of the rings can be used to calibrate the TOF parameters $t_{e,start}$ and $t_{i,start}$. However, the limited spatial resolution of the spectrometer due to effects described in Chapter 3 produces larger uncertainty than the methods described previously.

Finding the projection of the centre of interaction onto the ion detector is complicated by the presence of the average molecular beam velocity which carries the ions along the molecular beam direction. Different ion masses have different TOFs, which means that each mass experiences a different molecular beam velocity displacement on the detector. Care must be taken to monitor the beam generation conditions (stagnation pressure, beam composition, etc.), because these affect the molecular beam velocity, and can vary even during a single experimental run. The easiest way to determine the mean beam velocity is if the molecule under study ionizes to a stable molecular cation. These cations will impact the detector at a single location with some spread due to the beam velocity spread, the finite size of the interaction region, and any small recoil of the ion from the photoionized electron. If the experiment is repeated with a different set of spectrometer voltages, the molecular cations will hit a different location. The two different hit locations accurately define the molecular

beam axis, and also allow calculation of the molecular beam velocity v_{beam}, and the projection of the interaction region onto the detector $(x, y)_{i,origin}$. This procedure is unnecessary if the molecules produce structured photofragment distributions similar to those shown in Figure 6.7. In this case, $(x, y)_{i,origin}$ can be calculated in an analogous manner to the electrons.

6.3.5 Detector Uniformity Calibration

To obtain accurate distributions from the detector, it is necessary to calibrate the spatial dependence of the detector efficiency. The effect of varying spatial detection efficiency on the TOF distributions should be minimal because integration over all spatial coordinates should average out the differences. The projections of the origins onto the detectors are also expected to be minimally affected by variations in spatial detection efficiency. However, the photoelectron and photofragment angular distributions might be expected to be quite sensitive to the detector spatial efficiency. In the imaging community, it is common skip this calibration step and to ameliorate detector efficiency variation by left/right, up/down averaging of the detector image to obtain one quadrant of unique data. This type of symmetrization is only possible if the photophysics of the laser-molecule interactions produce images that are left/right, up/down symmetric. These types of interactions are limited to those where the laser polarizations are parallel, or perpendicular to the spectrometer axis. The infallible method for calibrating spatial detection variation is to use a photoionize/photodissociate molecules for which their photoelectron/photoion energy and angular distributions ($\mathcal{P}(E_T, \theta)$) are known. Simulations can be used to generate the electron and ion images created by these distributions ($I_{e,real}$ and $I_{i,real}$).

The measured images ($I_{e,meas}$ and $I_{i,meas}$), can then be used to calculate the detector spatial intensity correction functions ($I_{e,corr}$ and $I_{i,corr}$):

$$I_{e,corr}(x,y) = \frac{I_{e,real}(x,y)}{I_{e,meas}(x,y)} \tag{6.12}$$

$$I_{i,corr}(x,y) = \frac{I_{i,real}(x,y)}{I_{i,meas}(x,y)} \tag{6.13}$$

These correction functions can then be used to determine the correct weighting of the events in images where energy and angular distributions are unknown. For regions of the detector insufficiently sampled by the image to generate reliable correction functions, the calibration experiment will have to be repeated using different spectrometer voltages to cover the under-represented areas. The whole calibration procedure described here is rather lengthy, so it is not surprising that the symmetrization method is very popular. The decision to perform this rigorous calibration depends on the desired accuracy for the experiment.

Chapter 7

Photodissociation dynamics of the NO Dimer

7.1 Introduction

The preceding chapters have focussed on the machinery involved with designing, constructing, and operating a coincidence imaging spectrometer. This chapter provides an example demonstrating the power of this technique to unravel the photodissociation dynamics of a seemingly simple molecule, the NO dimer.

The nitric oxide dimer $(NO)_2$ is formed from a pair of nitric oxide monomer radicals. The bonding interaction (dissociation energy $\sim$700cm^{-1} [93, 94, 95]) is weak compared to normal covalent bonds, yet stronger than van der Waals interactions. Spectroscopic studies have revealed that the ground state has a *cis*-planar C_{2v} symmetry with θ(N–N–O) = 99.6°, r(N–N) = 2.24 $\AA$, and r(N–O) = 1.16 $\AA$ [96]. This structure, along with the conventional axis definition for the dimer is shown in Figure 7.1. Theoretical analyses of the electronic states predict a plethora of states closely

spaced in energy for both the ground and excited states [97, 98, 99]. The complexity of the calculations has resulted in the NO dimer becoming a theoretical benchmark molecule for testing multiconfigurational effects in molecules.

A broad, featureless absorption band starts at 5.12eV [100] and peaks at approximately 6eV [101, 102]. Excitation to this band can in principle lead to photodissociation of the dimer via three pathways:

$$(NO)_2 \xrightarrow{h\nu_{pump}} (NO)_2^* \rightarrow NO(X^2\Pi) + NO(X^2\Pi) \quad (\Delta E = +0.087eV) \quad (7.1)$$

$$\rightarrow NO(X^2\Pi) + NO(A^2\Sigma^+) \quad (\Delta E = +5.54eV) \quad (7.2)$$

$$\rightarrow NO(X^2\Pi) + NO(B^2\Pi) \quad (\Delta E = +5.78eV) \quad (7.3)$$

The energies indicated are the energies required to dissociate the molecule from the dimer ground state. The molecular orbital (MO) diagrams for the NO(X), NO(A), and NO(B) monomer product states are shown in Figure 7.2 [97]. Removal of the π_{2p}^* electron from the electronic NO($X^2\Pi$) ground state produces the $NO^+(X^1\Sigma^+)$ ionic ground state located 9.264eV above the neutral. The NO($A^2\Sigma^+$) state, 5.45eV above the NO(X) state, is a 3s Rydberg state that upon ionization also correlates to the ionic ground state. The NO($B^2\Pi$) state has doubly excited character and does not ionize to the cationic ground state, preferring instead to ionize to excited states of the NO cation. We chose to perform our experiments using excitation wavelengths between 200nm and 210nm. At 6eV excitation, there is no evidence that (7.1) plays an important role in the photodissociation dynamics. In addition, the NO(B) production channel does not contribute at wavelengths greater than 200nm [103]. Therefore, we focus our experimental and theoretical efforts on the NO(A) production channel described by Equation 7.2.

Figure 7.1: Structure of the NO monomer and conventional axis definition.

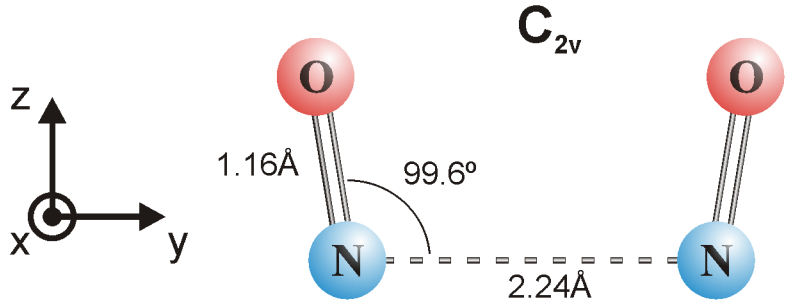

There has been some disagreement in the literature about how the photodissociation to NO(A) + NO(X) products occurs. The absence of structure in the absorption spectrum and fast dissociation timescale led some researchers to conclude that photodissociation to NO(A) + NO(X) occurs directly from a repulsive potential [104]. However, their alignment and vector correlation studies indicated that although the photodissociation occurred mostly within a plane, the product distributions obtained were less than the limiting values expected for a direct dissociation [105, 106, 107]. A time resolved photoelectron spectroscopy study recorded a discrepancy between decay time of the parent $(NO)_2^+$ parent ions (∼320fs) and the rise time of the NO(A) products (∼730fs) [108]. The authors postulated that the photodissociation resulting in NO(A) + NO(X) products proceeded sequentially via an unobserved, $(NO)_2^\dagger$ 'dark' state, *viz*

$$(NO)_2 \xrightarrow{h\nu_{pump}} (NO)_2^* \xrightarrow{\tau_1} (NO)_2^\dagger \xrightarrow{\tau_2} NO(A) + NO(X) \qquad (7.4)$$

High resolution rotational state correlation experiments have confirmed the tendency of the NO(A) reaction channel to occur in the plane[109, 94]. Lifetime effects were cited to be primarily responsible for the $\beta < 2$ photofragment angular distributions.

Figure 7.2: Molecular orbital diagrams for the lowest electronically excited states of nitric oxide. Energies shown are relative to the electronic ground state.

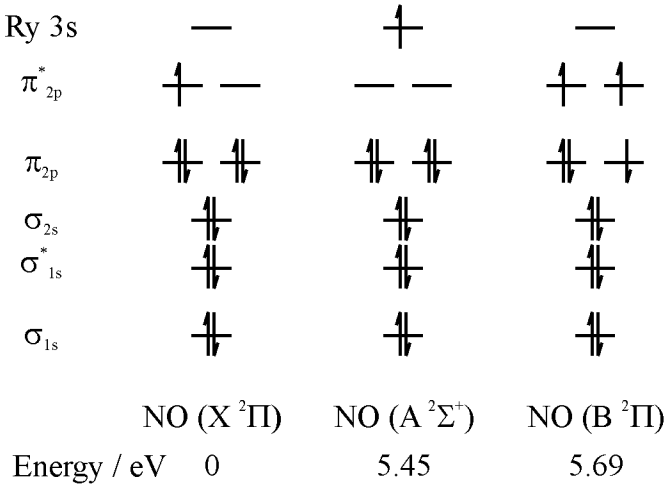

In addition, vibrational predissociation and restricted intramolecular vibrational energy redistribution (IVR) within the molecule were used to explain the observed $\mathbf{v} - \mathbf{J}$ correlations. Recently, a series of time resolved photoelectron and photofragment imaging experiments have suggested that an intermediate 'dark' state is not needed to describe the photodissociation of Equation 7.2, postulating that the NO(A) products are formed by excitation of a valence state, followed by crossing to a dimer 3s Rydberg state which smoothly evolves into the final NO(A) 3s Rydberg state at large inter-NO separations [110, 111, 112]. The proposed existence of the 3s valence state is rationalized by observation of a shift in the NO(A) photoelectron peak at short times. Contrary to the earlier studies, these experiments measured a decay rate of the $(NO)_2^+$ ions that apparently matched the combined rise of the proposed 3s Rydberg + NO(A) states.

Our experiments sought to clarify the NO(A) channel photodissociation dynamics using a combination of time resolved photoelectron spectroscopy (TRPES) and time resolved coincidence imaging spectroscopy (TRCIS). The TRPES experiments were performed using excitation/probe wavelength combinations of 209.6/279.5nm and 200.0/266.7nm. The TRCIS experiments used 208.8nm excitation and 278.4nm probe. In both of these experiments photoionization is used as the probe (see Scheme 7.1). In the case of TRPES, we analyze the photoelectrons generated from ionization of the species along the reaction pathway. The TRPES experiments provide high signal-to-noise time-resolved data to identify the timescales of the dynamics occurring in the molecule. Using this data, we confirm the NO(A) reaction channel occurs via the sequential mechanism described by Equation 7.4. With the TRCIS experiments, we measure the photoelectron and photoion recoil energies and directions of the photodissociation reaction products. At the probe wavelengths used, we also observe dissociative photoionization of the still-bound NO dimer to learn about the evolving dynamics on the excited potential energy surface. Recoil frame photoelectron angular distributions obtained from the TRCIS experiments helped us to identify the electronic symmetry of the intermediate state. With assistance from theoretical calculations, we provide a mechanism that is consistent with all reported experimental and theoretical observations.

Scheme 7.1: Schematic representation of NO dimer photodissociation producing NO(X) + NO(A) photoproducts. The gray arrow represents the disputed chemical dynamics occurring between the initial excitation and the emergence of the NO(A) photoproduct. The blue and red arrows show the possible pump excitation and probe photoionization scenarios.

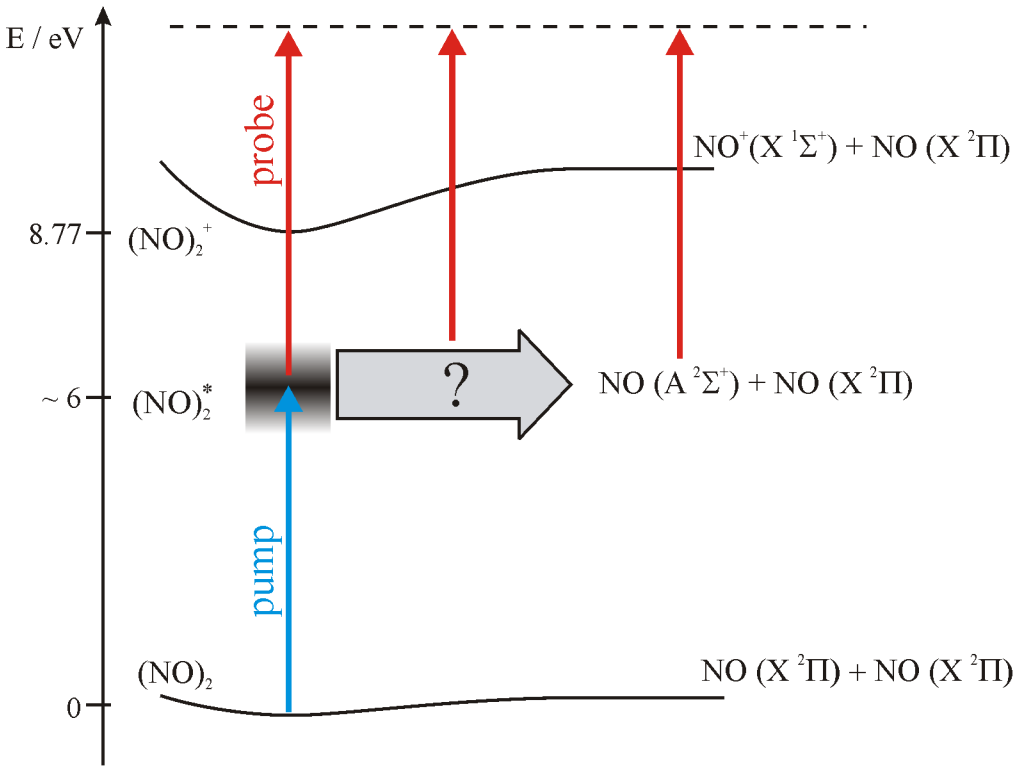

7.2 Experimental

7.2.1 TRPES Experiments

The laser setup and magnetic bottle spectrometer used for the TRPES experiments are detailed in Chapter 2.2. Specific experimental parameters are summarized in Table 7.1.

Around zero pump-probe time delay a strong non-resonant two-photon signal from NO monomers is present , an unavoidable major constituent of the molecular beam

Table 7.1: Experimental parameters for the NO dimer TRPES studies

Parameter	209.6nm + 279.5nm	200.0nm + 266.7nm	Units
Laser Conditions			
Pump pulse energy	2.0	4.9	μJ
Probe pulse energy	11	5.4	μJ
Cross correlation (FWHM)	160	170	fs
Molecular Beam Conditions			
Nozzle diameter	70	100	μm
NO / He gas mixture	15 / 85	30 / 70	%
P_{nozzle}	3.6	1.3	bar
Data Scans			
Scan range	-700 to 3500	-500 to 2000	fs
Scan step size	25	25	fs
Pump-probe events	3.2 $\times 10^6$	5.7 $\times 10^5$	

if clusters no higher than dimers are to be produced. Although the monomer signal had to be subtracted in order to obtain the NO dimer signals, its well characterized sharp peaks were also used as a sensitive *in situ* monitor of: (i) the pump-probe cross-correlation function; (ii) the reproducibility of the absolute pump-probe time delays upon repeated scans; and (iii) the absolute energy calibration of the photoelectron spectrum. High signal-to-noise monomer background spectra were obtained using neat NO molecular beams with stagnation pressures low enough such that no dimer signals were detected. These NO monomer spectra contained between 3.3×10^5 and 8.3×10^5 events. Upon energy calibration, the NO monomer signal was eliminated by scaling the pure monomer spectrum and subtracting it from each dimer scan. Importantly, the 209.6nm and 279.5nm wavelengths were specifically chosen such that the crucial rising part of the sharp NO(A) photoelectron peak was located exactly between the well separated NO monomer $\nu = 1$ and $\nu = 2$ photoelectron peaks. In

this way, any remaining small systematic errors in the subtraction of the NO monomer signals could not affect the kinetic analysis presented here. This is not the case for the 200.0nm + 266.7nm experiment.

7.2.2 TRCIS Experiments

Due to the lengthy development/construction time of our own Coincidence Imaging Spectrometer, the TRCIS experiments were performed using the laser system and apparatus located at Sandia National Laboratories in Livermore, CA. Only a brief description is provided here; more detail can be found in the literature [26, 27]. The experimental geometry is schematically the same as our CIS spectrometer shown in Figure 3.1.

Linearly polarized femtosecond laser pulses at 834nm were produced by regenerative amplification of a Ti:sapphire mode-locked oscillator. The pump pulse at 208.8nm and probe pulse at 278.4nm were generated from harmonics of the amplified fundamental. The maximum pump and probe pulse energies were $\leq 1\mu J$ and $\leq 15\mu J$ respectively, and were reduced so as to minimize ionization signals from each laser beam separately. The pump and probe polarizations were aligned to be parallel, with electric vectors perpendicular to the spectrometer axis. The measured FWHM of the pump-probe cross-correlation function was 290 fs. The beams were co-propagated and focussed into the interaction region using a long focal length lens.

Nitric oxide dimers were formed from a pulsed valve supersonic expansion of 10% NO in helium (stagnation pressure $\sim$3 bar) through a 100μm pinhole nozzle. The molecular beam passed through a 1mm skimmer, a differentially pumped region, and finally into the high vacuum interaction region.

Small coincidence data sets containing approximately 8000 events were taken in the pump-probe delay range of -1000fs to +3800fs in steps of 67fs to record the temporal dynamics. Large coincidence data sets containing approximately 5×10^5 events were collected at pump-probe delays of 50, 130, 330, 590, and 930fs to obtain high quality angular distributions. For the measurements presented here, the experimental conditions were chosen so that the coincidence rate was approximately 0.02 per laser shot. Assuming detection efficiencies similar to our own spectrometer, Figures 6.4 and 6.5 indicate that the false coincidence rate was <5%. This false coincidence count rate is low enough such that even without false coincidence subtraction it does not impact the results presented here..

As in the TRPES experiments, the molecular beam contains unwanted NO monomers. Non-resonant ionization of the monomer produces NO^+ which may be also produced by dissociative ionization of the NO dimer or ionization of the NO(A) photoproduct. However, unlike ionization of the monomer, $(NO)_2$ and NO(A) photoionization produces NO^+ ions with recoil velocity relative to the average molecular beam velocity. Since our coincidence technique measures this recoil velocity, removal of the NO monomer contribution is straightforward.

7.3 TRPES Results, Data Analysis, and Discussion

7.3.1 TRPES - 209.6nm Excitation - General Features

The pump=209.6nm, probe=279.5nm TRPES scan is shown in Figure 7.3. In the 2-dimensional TRPES scan, the number of photoelectrons counted are plotted as a

function of the pump-probe delay time and the binding energy. The binding energy is the sum of the pump and probe photon energies minus the measured photoelectron kinetic energy. The NO monomer signal has been subtracted from the data set.

Figure 7.3: Two views of the pump = 209.6nm, probe = 279.5nm TRPES scan for the NO dimer. The NO monomer spectrum has been subtracted. The scan axes are pump-probe delay time and binding energy. The binding energy is the sum of the pump and probe photon energies minus the measured photoelectron kinetic energy.

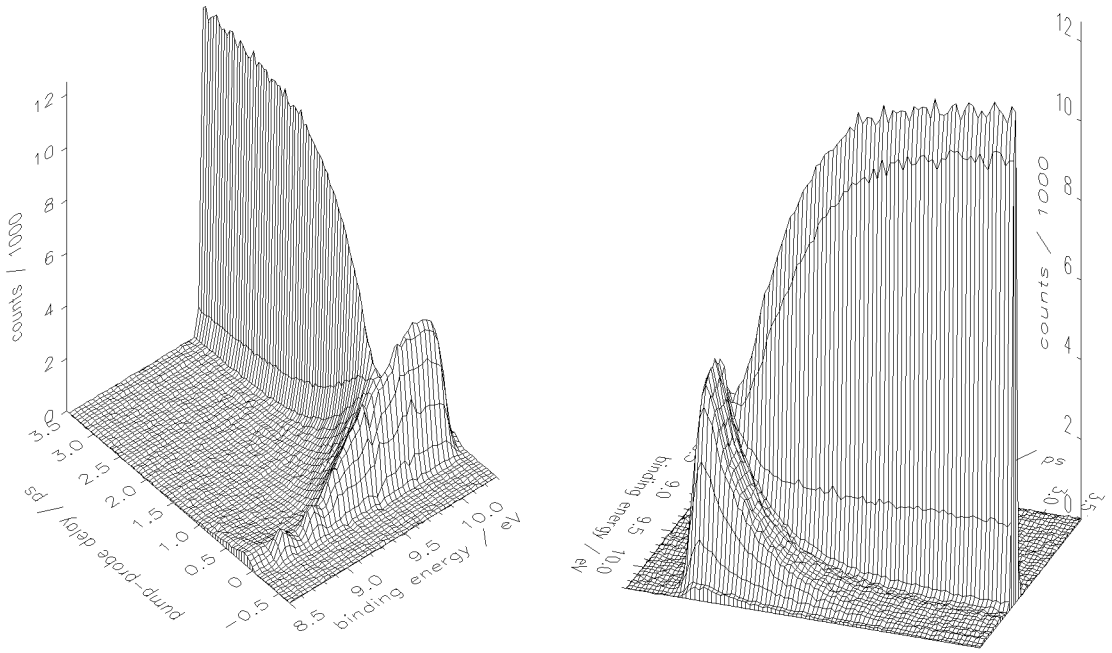

The most prominent features in Figure 7.3 are: (i) a broad, nearly structureless spectrum at early times which decays with time delay; and (ii) a single sharp rising peak which is the only remaining spectral feature at later times. These general features in the NO dimer TRPES spectrum have been observed in previous studies [108, 110, 112]. The broad decaying spectrum is due to photoionization of the excited neutral NO dimer before it fragments into products. The energy difference between the two small peaks at binding energies E_b=8.76 eV and E_b=9.03 eV (energy difference

$= 0.27\text{eV} = 2200\text{cm}^{-1}$) agrees within the resolution of the experiment with published values for the NO symmetric stretching vibration $\nu_1 = 2090\text{cm}^{-1}$ for the $(\text{NO})_2^+(X^2A_1)$ dimer cation[113]. Thus, these two peaks are due to photoionization to $\nu_1 = 0$, and 1 of the dimer cation. The threshold energy $E_b = 9.35\text{eV}$ for dissociative ionization of the dimer, $(NO)_2 + h\nu_{pump} + h\nu_{probe} \rightarrow NO(X) + NO^+(X) + e^-$, is the sum of the dimer dissociation energy ($\sim$0.087eV)[93] and the nitric oxide ionization energy (9.264eV). Therefore, the broad featureless photoelectron band near zero pump-probe delay time and at energies greater than 9.35eV arises from bound-free Franck-Condon transitions to the vibrational continuum lying above the dissociation limit of the $(\text{NO})_2^+(X^1\Sigma^+)$ dimer cation. The sharp rising peak at 9.7eV is due to photoionization of the $\text{NO}(A^2\Sigma^+)$ photofragment. The NO bond length in the $\text{NO}(A^2\Sigma^+)$ 3s Rydberg state is almost identical to that in the $\text{NO}^+(X^1\Sigma^+)$ cation electronic ground state. Therefore, due to Franck-Condon diagonality ($\Delta\nu = 0$), the NO(A) photoelectron spectrum consists almost entirely of a single sharp peak. At long time delays, the high signal-to-noise data permits us to observe the very weak $\Delta\nu \neq 0$ Franck-Condon non-diagonal $\text{NO}^+(X^1\Sigma^+) \leftarrow \text{NO(A)}$ transitions, as described below. It should be noted that the magnetic bottle detection efficiency drops dramatically at low electron kinetic energies (<100meV) so the NO dimer spectrum in Figure 7.3 does not maximize at high binding energies as it does in the TRCIS experiments described later or published elsewhere [114, 110, 111, 112]. However, as no conclusions are drawn from the low kinetic energy region, this does not interfere with the analysis or interpretations discussed here.

Selected slices of the TRPES scan cut parallel to the pump-probe time delay axis are shown in Figure 7.4. It is quickly apparent that these time transients cannot

be fit using a single exponential time constant describing decay of a single initially excited state to a single product state. This is in contrast to previously published results [110, 111, 112]. A full global fit of the scan is not easily performed because initially it is difficult to predict the number of components and the number of time constants involved in producing the observed TRPES scan. We attempted to simplify the fitting problem by first decomposing the TRPES scan into decaying components and rising components.

7.3.2 TRPES - 209.6nm Excitation - Separation into decaying and rising components

Figure 7.5 shows the TRPES scan in Figure 7.3 decomposed into decaying and rising components. The decomposition was made by interpolating the broad decaying NO dimer spectrum across the region of the rising NO(A) photoelectron peak. To minimize the arbitrariness in this decomposition, we proceeded as follows. The shapes of the photoelectron intensity transients above $E_b = 9.80$ eV are all very similar and show no discernable contribution from a rising component which is very prominent just below this binding energy. Therefore we set one anchor point for the interpolation at 9.83 eV. Similarly, we chose the second anchor point at 9.38 eV, the maximum binding energy on the low energy side of the NO(A) peak for which the shape of the photoelectron intensity transient was almost the same as for 9.83 eV, differing only in the absolute magnitude. We then, at each time delay, linearly interpolated the photoelectron spectra between 9.38 eV and 9.80 eV in order to extract the decomposed scan components shown in Figure 7.5.

The TRPES spectrum of Figure 7.5a shows the decay dynamics of the excited

Figure 7.4: Selected time transient slices of the pump = 209.6nm, probe = 279.5nm TRPES scan. The vertical lines are the data point uncertainties obtained from full error propagation analysis. The values of E_b indicate the energy range integrated to obtain the time transient.

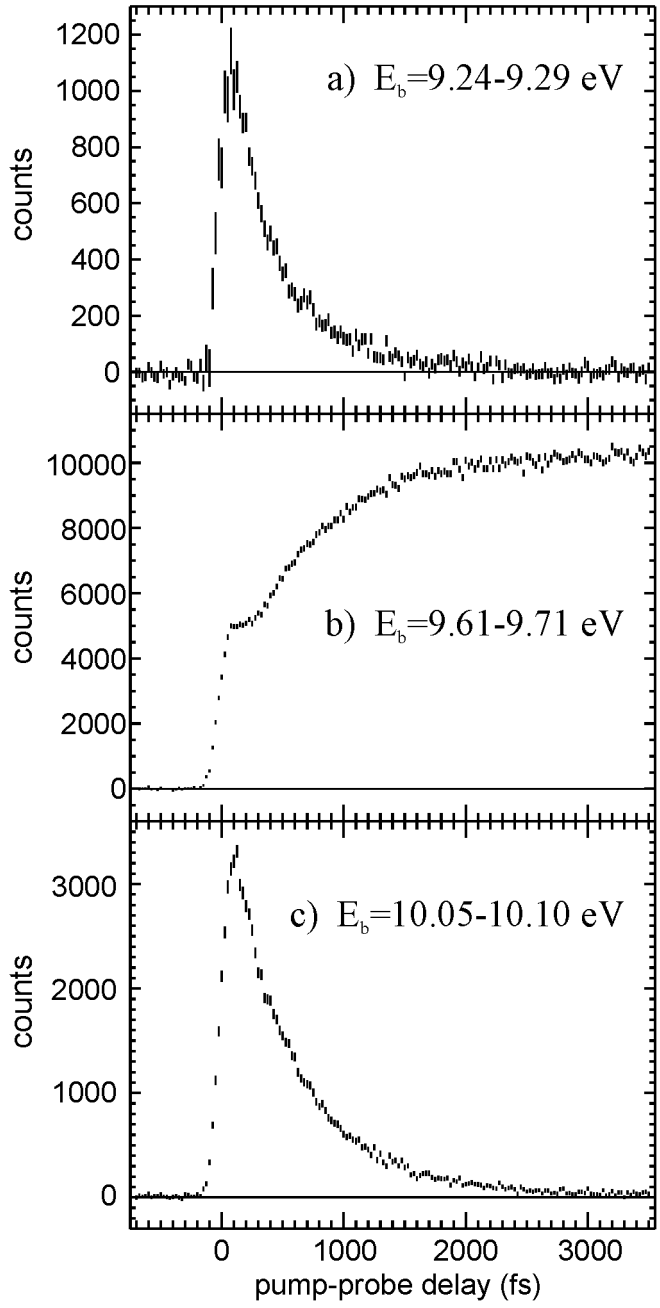

Figure 7.5: a) Decaying and b) rising components of the pump = 209.6nm, probe = 279.5nm TRPES scan. Note the differing binding energy axes.

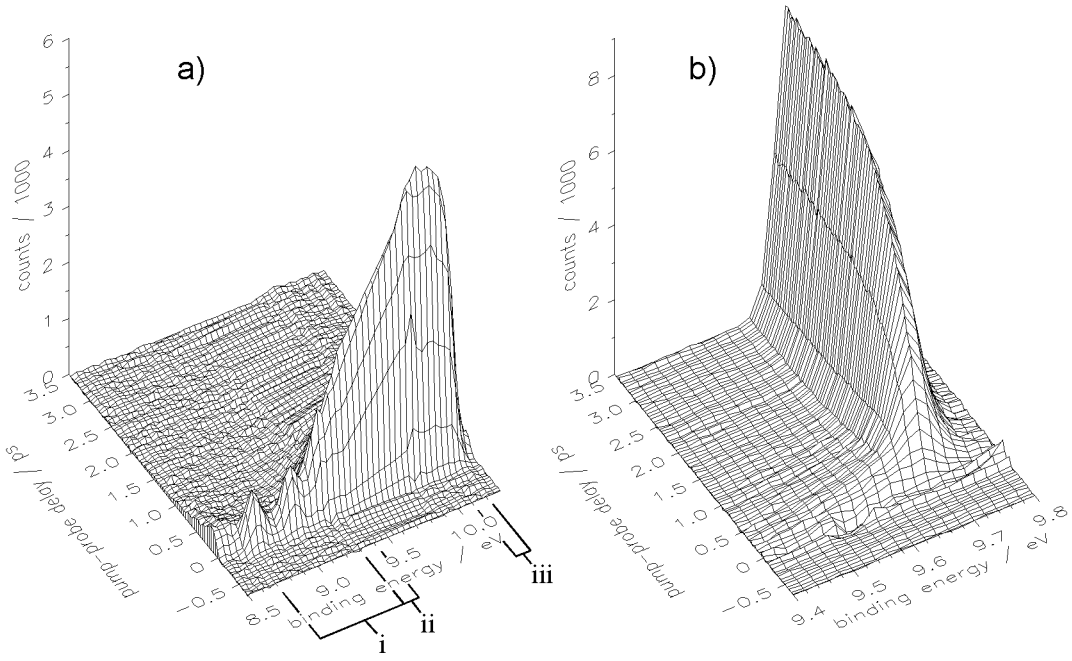

NO dimer as it proceeds to dissociation. The binding energy region labeled (i) corresponds to ionizing transitions to the bound $(NO)_2^+(^2A_1)$ ground state dimer cation. Therefore the integrated photoelectron signal in this region should show the same time behaviour as the $(NO)_2^+$ total ion signal. The binding energy regions labeled (ii) and (iii) correspond to dissociative ionization transitions, producing NO^+ ions.

7.3.3 TRPES - 209.6nm Excitation - NO($A^2\Sigma^+$) product growth dynamics

In Figure 7.5b, one can see an apparent 'tuning' of the rising NO(A) peak with time delay: the peak maximum shifts by about 50 meV and becomes sharper at

longer pump-probe time delays. This 'tuning' behavior of the rising component was previously emphasized [110, 111] and interpreted as the signature of a proposed NO dimer 3s Rydberg state which evolves into the photofragment NO(A) 3s Rydberg channel.

Integration of the rising component in Figure 7.5b along the binding energy coordinate leads to a time transient shown in Figure 7.6. The experimental data clearly shows that the rising edge of the NO(A) peak is offset with respect to zero pump probe delay (which was determined within ±10fs). The solid line in Figure 7.6a is a fit of the final NO(A) product using the sequential model described by Equation 7.4 yielding time constants $\tau_1 = 130 \pm 15$fs and $\tau_2 = 600 \pm 10$fs. These values and errors include the uncertainty in separating the decaying from rising components, as described previously. Figure 7.6b shows the residuals between this fit and the data. As in Chapter 2, the exponentials are convoluted with the instrumental response to obtain the fitting functions. It is important to note that only a sequential model produces a satisfactory fit to the data using only two time constants because a parallel model cannot fit the delayed onset of the NO(A) growth. In order to compare this with earlier results at 210nm excitation, we have plotted the dotted line in Figure 7.6 which shows a single exponential rise curve with a time constant of 330fs. This is the previously reported (apparent) single exponential decay time of the $(NO)_2^+$ cation signal [111, 115]. It can be seen that the fit is poor, confirming the discrepancy between $(NO)_2^+$ parent ion decay and NO(A) product rise times found in previous measurements in our lab [115].

Figure 7.6c presents the result of a single exponential fit to the data, yielding a time constant of 770 ± 20fs. This is in good agreement with the previously reported

single exponential rise time of 730 ± 20fs [115]. However, the fit in Figure 7.6c is not ideal as it leads to systematic deviations from the data at short times (∼200fs) and longer times (1-2ps), as seen in the residual curve in Figure 7.6d. We conclude that the previous assignment as a single rising exponential was made due to poorer signal-to-noise and time resolution. In summary, we reiterate that the rising peak in the TRPES scan is only modeled well with 2 time constants using a sequential model.

7.3.4 TRPES - 209.6nm - Excited $(NO)_2$ decay dynamics

The evidence presented above supporting a two-step sequential dissociation process was based upon the observed growth of the NO(A) products. These conclusions are further corroborated by analyzing the decaying excited $(NO)_2$ photoelectron spectrum. A full global fit using the sequential model on the data in Figure 7.5 sliced into 40meV wide energy slices yields time constants of $\tau_1 = 140 \pm 30$fs and $\tau_2 = 590 \pm 20$fs. The time constants agree quantitatively with the time constants $\tau_1 = 130 \pm 15$fs, and $\tau_2 = 600 \pm 10$fs, obtained from the analysis of the rising NO(A) component.

Selected excited NO dimer time transients from integrated slices of the decomposed scan shown in Figure 7.5a are plotted in Figure 7.7. The solid lines are the sum of the three dashed line components: the cross correlation (CC) component X; and the components of a sequential decay model: A being the initially excited species $(NO)_2^*$; and I being the intermediate excited species $(NO)_2^\dagger$. Only the amplitudes of the components were fit; the two time constants used were $\tau_1 = 140$fs and $\tau_2 = 590$fs. Easily seen is the excellent agreement of the sequential model with the experimental data. The CC component has been observed previously [111, 112]. For reasons detailed below, the CC component has been assigned to non-resonant ionization of the

Figure 7.6: Integrated rising NO(A) time transient from Figure 7.5b. a) The solid line is the final product of a sequential model fit yielding time constants $\tau_1 = 130 \pm 15$fs and $\tau_2 = 600 \pm 10$fs. The dotted line is a single exponential rise with time constant equal to 330fs. c) The solid line is a single rising exponential fit yielding a time constant of 770 ± 20fs. b,d) The residuals between the solid line fits in a) and c) and the experimental data.

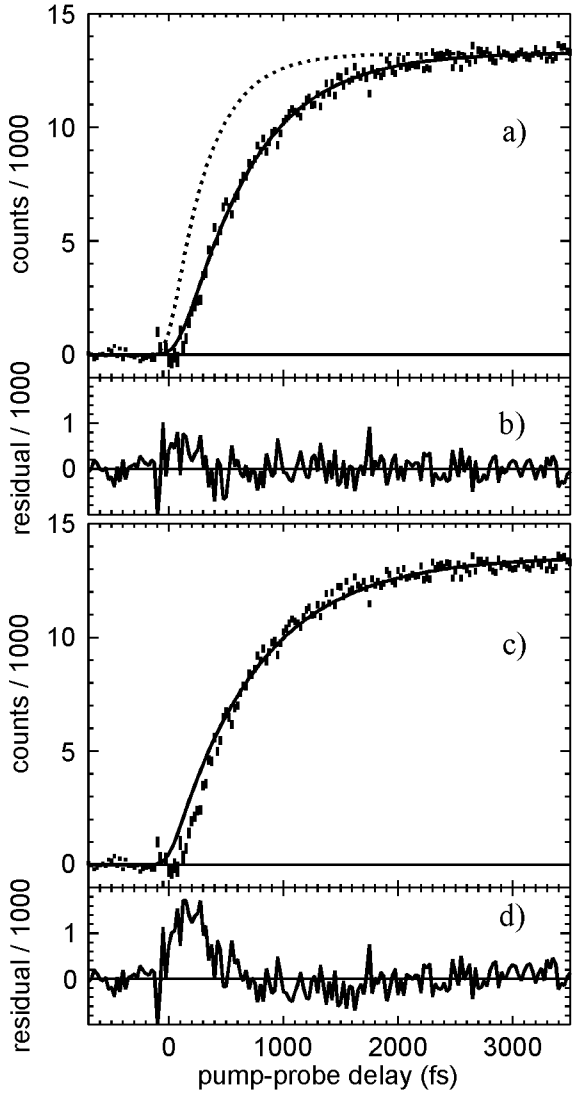

dimer.

The time transient due to ionization to bound $(NO)_2^+$, shown in Figure 7.7a, only occurs in the binding energy region $E_b = 8.7 - 9.3eV$. In this energy region, all three components (*X, A, I*) have significant contributions to the total signal. This can lead to relatively large uncertainties in the time constants, amplitudes of the fit, and even the model chosen for fitting. In fact, Figure 7.7a is reasonably fit using just a cross correlation component and a single exponential decay component with time constant ∼330fs. However, the other energy regions shown in Figures 7.7b and c, consist of *A* and *I* almost exclusively. Therefore, fitting of the photoelectron signals in Figures 7.7b and c enforces the need for the sequential kinetic model to describe the data. Thus, relying solely on the integrated ion $(NO)_2^+$ signal might explain the previously published observation of single exponential kinetics [110, 115]. Only by fitting the entire decaying spectrum is it possible to independently confirm that the sequential model of Equation 7.4 is the appropriate one. As confirmation of the validity the model, the fits of the selected transients presented in Figure 7.4 are shown in Figure 7.8.

7.3.5 TRPES - 209.6nm - Deconvoluted Spectra

The global fit of the complete 209.6nm pump, 279.5nm probe TRPES scan using Equation 7.4 yields time constants $\tau_1 = 140 \pm 30$fs and $\tau_2 = 590 \pm 20$fs. It is shown in Figure 7.9. All features of the spectrum are modeled by the fit, including the apparent shift in the NO(A) spectrum at short times. The independent fits of the NO(A) rising component, and the decaying spectral components unequivocally support the sequential model of Equation 7.4.

Figure 7.7: Decaying excited NO dimer time transients from Figure 7.5a. The decaying scan was integrated over the energy ranges indicated.The solid lines are the sum of the three dashed line components: the cross correlation component X; and the components of a sequential decay model: A being the initially excited species $(NO)_2^*$; and I being the subsequent intermediate excited species $(NO)_2^\dagger$). The two time constants used in the model are $\tau_1 = 140$fs and $\tau_2 = 590$fs.

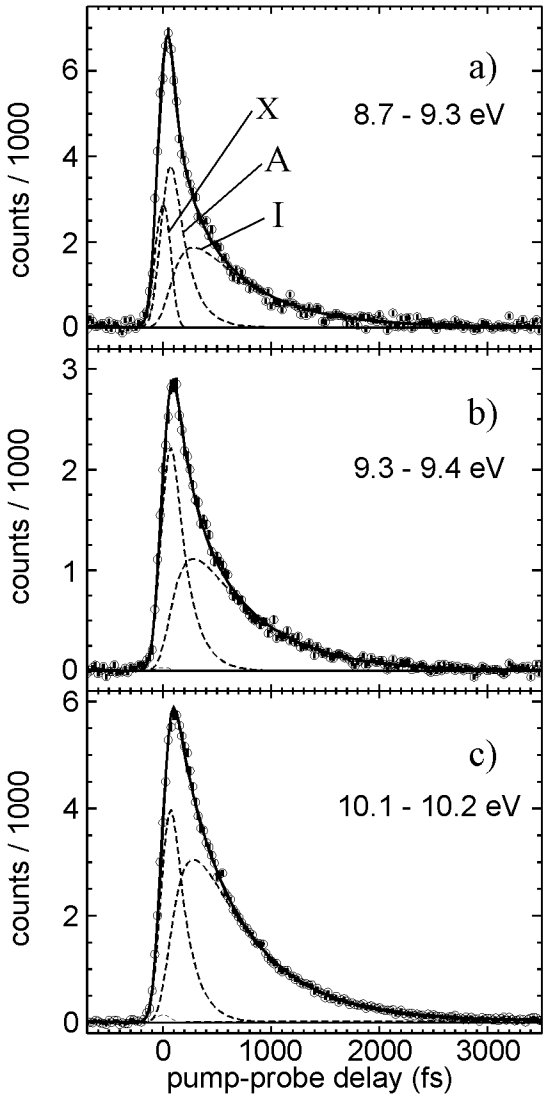

Figure 7.8: Sequential model fits of the time transients from Figure 7.4. Only the amplitudes were fit; the time constants used were $\tau_1 = 130$fs and $\tau_2 = 600$fs. X is the cross correlation component, A is the initially excited species $(NO)_2^*$, I is the intermediate species $(NO)_2^\dagger$, and P is the final NO(A) product.

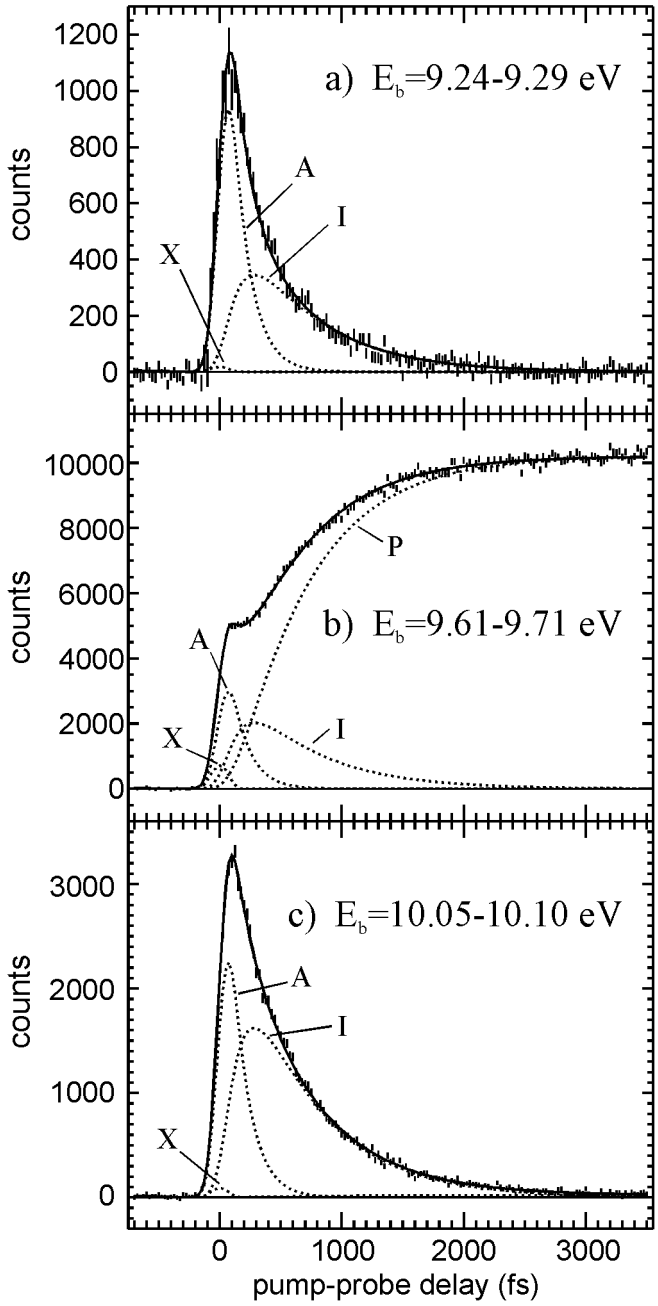

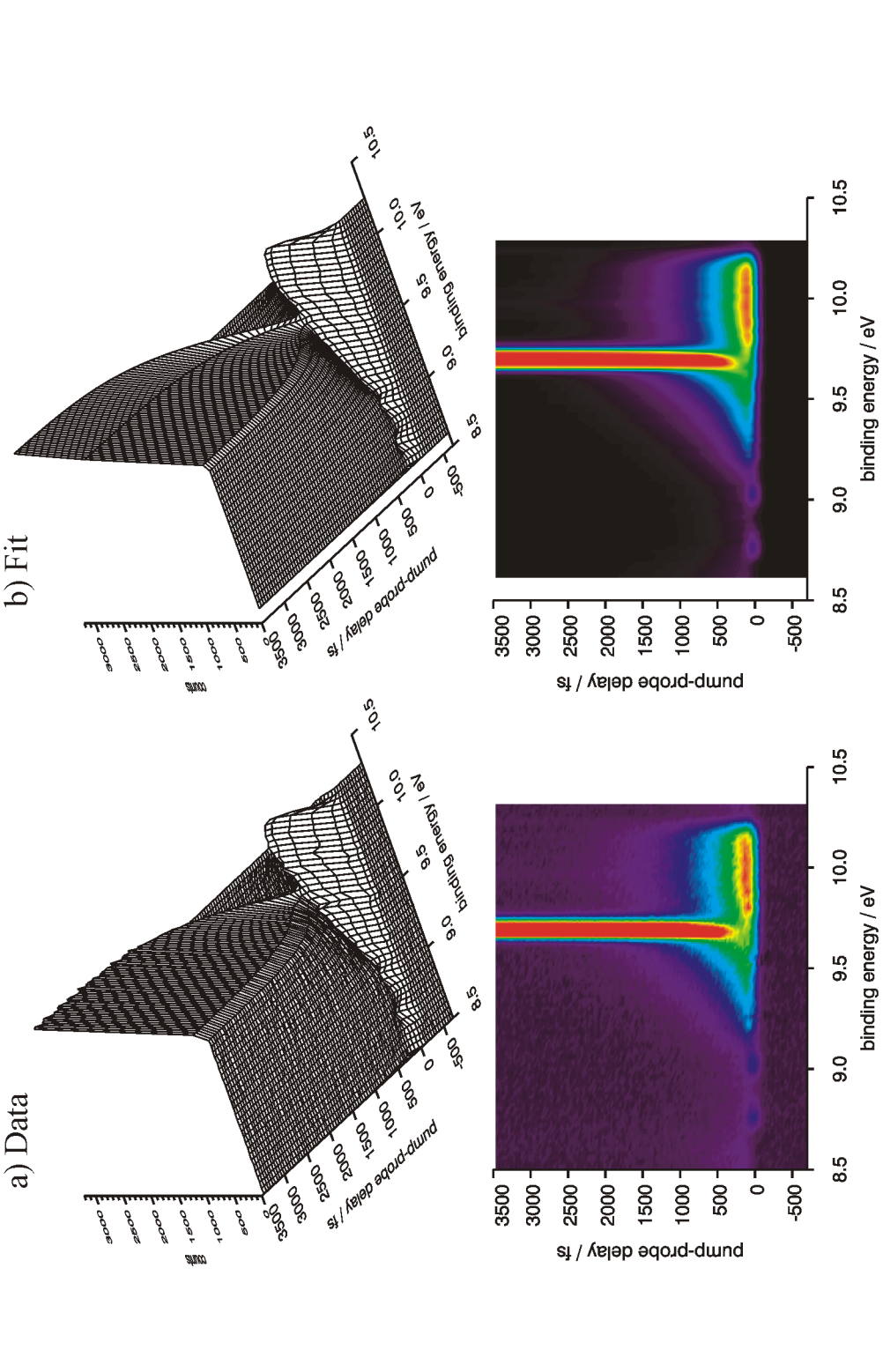

Figure 7.9: a) Data and b) fit of the 209.6nm pump, 279.5nm probe TRPES scan of the NO dimer using a sequential model and $\tau_1 = 140$fs and $\tau_2 = 590$fs.

The spectra obtained from a full global fit of the decomposed scan shown in Figure 7.5a are presented in Figure 7.10. The dotted lines in the region between 9.38 and 9.80eV are interpolated and represent only estimated spectra in these regions. The reason for the uncertainty in this region is because of the small shift in the NO(A) peak at short pump-probe delays, as seen in Figure 7.9b. This shift is not modeled accurately using a global fitting procedure, which relies on fixed spectral shapes of the components. The vertical scales are determined by taking each component's spectrum at the pump-probe delay times where each exhibits its maximum population. For 160fs cross correlation, $\tau_1 = 140fs$ and $\tau_2 = 590fs$, these maximum populations occur at t=0fs for the cross correlation component, 70fs for $(NO)_2^*$, 285fs for $(NO)_2^\dagger$, and t$\rightarrow \infty$ for NO(A).

Figure 7.10a shows the component that follows the cross correlation. Peaks at 8.76 and 9.03eV agree with ionization to the $\nu_1 = 0, 1$ (N–O symmetric stretch) vibrational levels of the stable $(NO)_2^+$ cation [116]. Our $\nu_1 = 2$ peak shows a dip in the center which is an artifact of the NO monomer signal subtraction. (This only impacts the CC spectrum since it is the only other non-resonant ionization signal). The dash-dotted curve in Figure 7.10a shows the subtracted monomer contribution reduced by a factor of $\sim$14. The strong similarity of the CC component with the single photon He(I) photoelectron spectrum [117] suggests that this component is non-resonant ionization of the NO dimer. The CC signal above 9.90eV is likely due to non-resonant ionization to higher lying electronic states of the NO dimer cation.

Figure 7.10b shows the spectra corresponding to the resonantly excited initial state $(NO)_2^*$, and the intermediate state $(NO)_2^\dagger$. The lack of structure in these components, unlike the CC component, suggests that these states have very displaced N=O stretch

coordinates from the neutral and cation ground states. The onset of the $(NO)_2^*$ spectrum occurs around the energy of the dimer cation $\nu_1 = 2$ level whereas the $(NO)_2^\dagger$ spectrum rises at higher energy. This is the most distinguishing feature between the two components and suggests that the NO stretching vibrations play an important role in the excited state dynamics. The intermediate spectrum does not contain significant ionization to the cation $\nu_1 = 2$ vibrational level and must have a geometry even more distorted than the initially excited state. The apparent smooth transition from bound state to dissociative ionization and lack of any threshold effects strongly suggests that all dimer photoionization is into the electronic continuum of the $(NO)_2^+(^2A_1)$ electronic ground state. This single electronic continuum observation is particularly important for the interpretation of the TRCIS data.

The product state spectrum is dominated by the NO(A) $\Delta\nu = 0$ ionization located at 9.69eV. This rising component has been removed as described in section 7.3.2. The remaining features are shown in Figure 7.10c. The main structures are two peaks at 9.99 and 10.25eV. Comparison with the spacing of these peaks with the vibrational spacing of the $NO^+(X^1\Sigma^+)$ state [89] reveals that these peaks are due to non-diagonal Franck-Condon (FC) transitions from the photoionization of the NO($A^2\Sigma^+$) photofragment. Since the NO($A^2\Sigma^+$) Rydberg and the $NO^+(X,^1\Sigma^+)$ ionic states geometries are almost identical, the FC factors for non-diagonal vibrational transitions are extremely small.

In sum, we have shown that at pump=209.6nm, probe=279.5nm, photodissociation of the NO dimer to NO(X) and NO(A) occurs via a sequential two-step dissociation process. Following fast ($\tau_1 = 130 \pm 15$fs) decay of an initially excited dimer state, the intermediate state takes an additional $\tau_2 = 600 \pm 10$fs to finally dissociate

Figure 7.10: Deconvoluted spectra for the 209.6nm pump, 279.5nm probe TRPES scan. a) The cross correlation component spectrum. The dash-dotted line shows the location of the subtracted NO monomer spectrum. b) The initially excited $(NO)_2^*$ (solid) and intermediate $(NO)_2^\dagger$ (dashed) spectra. c) The product NO(A) spectrum. The dotted lines between 9.38 and 9.80eV are interpolated and represent only estimated spectra in these regions. The vertical scales are determined by taking each component's spectrum at the pump-probe delay times where each exhibits its maximum population. This occurs at t=0fs for the cross correlation component, 70fs for $(NO)_2^*$, 285fs for $(NO)_2^\dagger$, and t$\rightarrow \infty$ for NO(A).

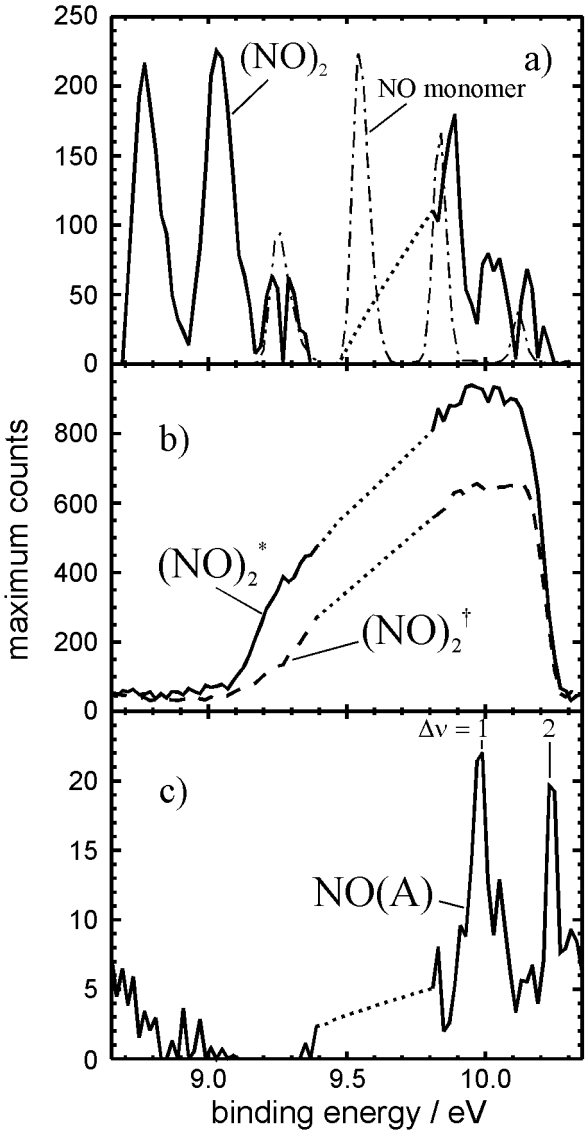

into the NO($A^2\Sigma^+$) + NO($X^2\Pi$) products. The high quality of this data permits us to resolve the apparent discrepancy in the observed timescales between the parent ion decay and the NO(A) fragment rise time. Excitation of the NO stretching mode seems to play an important part in the dissociation process.

7.3.6 TRPES - 200.0nm Excitation

The pump=200.0nm, probe=266.7nm TRPES scan is shown in Figure 7.11. At 200.0nm, the excitation energy (6.20eV) is higher than that at 209.6nm (5.92eV). The general characteristics of the scan are very similar to the scan taken at pump = 209.6nm, probe = 279.5nm. The primary difference between the scans is the significantly faster dynamics at 200.0nm pump. A similar analysis as described previously for the 209.6nm data again arrives at the necessity for two time constants to fit the experimental data well. These time constants were determined to be $\tau_1 = 110 \pm 30$fs and $\tau_2 = 330 \pm 70$fs. The relatively larger uncertainty in the time constants is due to the difficulty in fitting time constants that are close in range. Unlike the time transients plotted in Figure 7.8, the 200.0nm pump time transients cannot distinguish between a sequential or parallel fitting model because they are mathematically equivalent for these transient shapes. However, since we have no evidence to support the parallel model over the sequential model, we conclude that like those at 209.6nm, the 200.0nm dynamics are sequential. The deconvoluted spectra do not provide any greater insight into the processes occurring and are not presented here.

Figure 7.11: Two views of the pump = 200.0nm, probe = 266.7nm TRPES scan for the NO dimer. The NO monomer spectrum has been subtracted. The scan axes are pump-probe delay time and binding energy. The binding energy is the sum of the pump and probe photon energies minus the measured photoelectron kinetic energy.

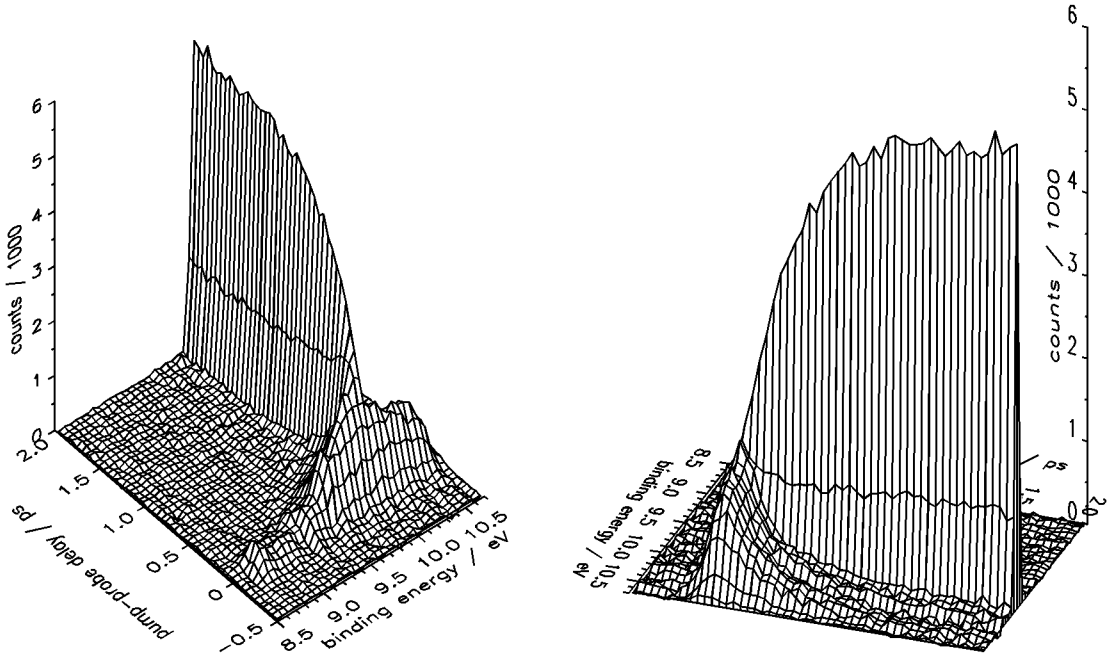

7.3.7 TRPES Summary

The TRPES experiments presented here suggest that the photodissociation of the NO dimer at 209.6nm and 200.0nm occurs via a sequential mechanism:

$$(NO)_2 \xrightarrow{h\nu_{pump}} (NO)_2^* \xrightarrow{\tau_1} (NO)_2^\dagger \xrightarrow{\tau_2} NO(A) + NO(X) \tag{7.5}$$

At 209.6nm excitation, the time constants were determined to be $\tau_1 = 140 \pm 30$fs and $\tau_2 = 590 \pm 20$fs. At 200.0nm excitation, the time constants were determined to be $\tau_1 = 110 \pm 30$fs and $\tau_2 = 330 \pm 70$fs. The lack of structure in the deconvoluted spectra of $(NO)_2^*$ and $(NO)_2^\dagger$ suggest that ionization occurs to vibrationally excited states of the ground state dimer cation $(NO)_2^+(X^2\Sigma^+)$. The $(NO)_2^*$ state has some

Franck-Condon (FC) overlap with $\nu_1 = 2$ of the dimer cation but predominantly dissociatively ionizes. Larger geometry changes in the $(NO)_2^\dagger$ state pushes the FC envelope even higher into the dissociative continuum. This implies an important role for the NO stretching vibrations in the dissociation dynamics.

7.4 TRCIS Results, Data Analysis, and Discussion

7.4.1 Mass Selected Photoelectron Spectra

Figure 7.12 shows the photoelectron spectra at 50fs pump-probe delay correlated with NO^+ ions, and with $(NO)_2^+$ ions. Using pump=208.8nm, and probe=278.4nm, the total energy provided to the system is 10.39eV. The spectra are plotted versus binding energy as before, subtracting the electron kinetic energy from 10.39eV. The mass separation of spectra is only possible using coincident detection of the electrons and ions.

The photoelectron spectrum correlated with NO^+ shown in Figure 7.12a peaks towards the high binding energy threshold, consistent with the TRPES experiments. The NO symmetric stretch vibrational levels for the molecular $(NO)_2^+$ cation assuming a constant level spacing of 2090cm^{-1} [116] are indicated in Figure 7.12b. The inverted vibrational population and the propensity for the excited state for dissociative ionization over molecular ionization confirms the observation that the excited state is geometrically different from the neutral and cationic ground states. Presumably, the initially excited state has significant vibrational energy in the N-O stretching coordinate. As expected, the sum of the two mass correlated spectra resembles the TRPES deconvoluted $(NO)_2^*$ photoelectron spectrum shown earlier in Figure 7.10b. However,

from the different vertical scales in Figure 7.12, it is easy to see how the $(NO)_2^+$ photoelectron signal could be overlooked if only the total photoelectron spectrum was measured.

Figure 7.12: The photoelectron spectrum correlated with a) NO^+, and b) $(NO)_2^+$ ions at 50fs pump-probe time delay. Pump = 208.8nm, probe = 278.4nm. In b) the vibrational energies of the symmetric NO stretch ν_1, are indicated. Contributions due to ionization of the NO monomer have been removed.

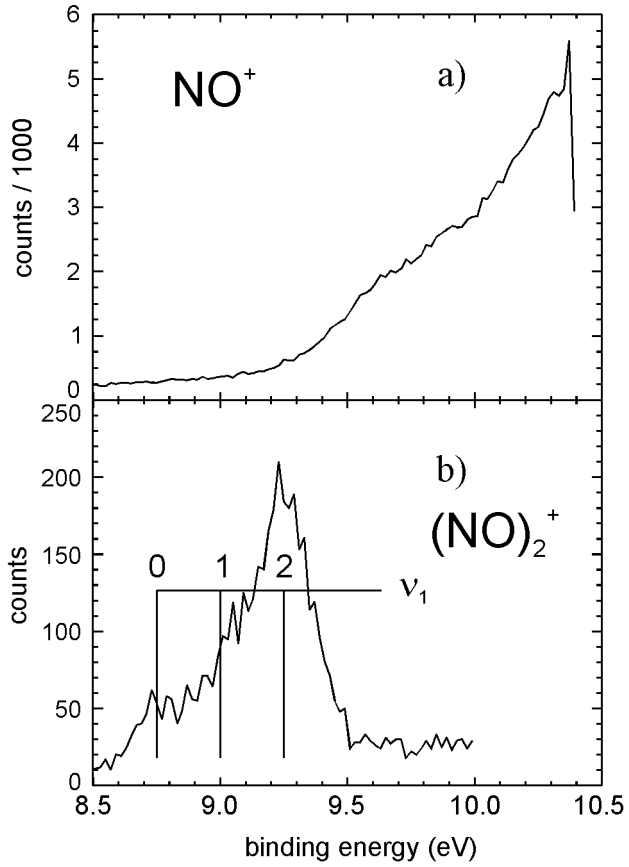

7.4.2 Integrated Ion Transients

The integrated ion time transients for NO^+ and $(NO)_2^+$ using pump = 208.8nm, probe = 278.4nm are shown in Figure 7.13. The contributions due to non-resonant ionization of the NO(X) monomer have been removed. The transients for both ions were obtained from the same data set. NO^+ ions can arise from several sources:

- Non-resonant dissociative ionization of the NO dimer ground state:

$$(NO)_2 + h\nu_{pump} + h\nu_{probe} \rightarrow NO + NO^+ + e^- \tag{7.6}$$

- Dissociative ionization of the NO excited state:

$$\begin{aligned} (NO)_2 + h\nu_{pump} &\rightarrow (NO)_2^* \text{ or } (NO)_2^\dagger \\ (NO)_2^* \text{ or } (NO)_2^\dagger + h\nu_{probe} &\rightarrow NO + NO^+ + e^- \end{aligned} \tag{7.7}$$

- Photoionization of the NO(A) photofragment:

$$\begin{aligned} (NO)_2 + h\nu_{pump} &\rightarrow NO(X) + NO(A) \\ NO(A) + h\nu_{probe} &\rightarrow NO^+ + e^- \end{aligned} \tag{7.8}$$

The integrated NO^+ time transient in Figure 7.13a can show any combination of these NO^+ production channels. The fit using the kinetics model described by Equation 7.4 and time constants of τ_1 = 140fs and τ_2 = 590fs determined from the TRPES 209.6nm experiments is shown by the solid line in the figure. Only the amplitudes of the components were adjusted to construct the fit. Dissociative ionization of the NO excited states and photoionization of the NO(A) photofragment are the primary NO^+ production channels. The fit agrees with the model proposed from the TRPES experiments. The integrated $(NO)_2$ time transient is shown in Figure 7.13b. The data is fit well with a cross-correlation component and $(NO)_2$ excited state components. As before, only the amplitudes of the components were

adjusted.

7.4.3 Electron-ion kinetic energy correlation maps

In the preceding section, it was seen how there are several contributions to the integrated NO^+ time transient. These contributions can be somewhat separated by plotting the correlated ion and electron kinetic energy maps. This map is shown in Figure 7.14. The colour scale indicates the probability of detecting electron and NO^+ ions in coincidence with measured energies of each. The ion kinetic energy, or KER (kinetic energy release) is defined as the sum of the kinetic energies of both fragment monomers which, by conservation of linear momentum, is twice the kinetic energy of the NO^+ fragment that is measured.

The correlation maps contain two major features: a broad, structureless sloping surface that peaks towards zero electron and ion kinetic energy due to dissociative ionization of the dimer (Equation 7.7); and a sharp peak at $E_{electron} = 0.66eV$ that emerges at longer pump probe delays due to ionization of the $NO(A^2\Sigma^+)$ photoproduct (Equation 7.8). The dissociative ionization feature is smooth over the entire accessible energy region including the transition region towards the bound dimer cation. This agrees with the TRPES observation. The lack of any threshold behaviour over the entire photoelectron energy range strongly suggests that all ionization leads to only one electronic state of the cation, namely the $(NO)_2^+(X^2A_1)$ ionic ground state. This point was already suggested previously[111, 100] and will become important in the analysis of the recoil frame photoelectron angular distributions.

Figure 7.13: Integrated ion transients for a) NO^+, and b) $(NO)_2^+$. Pump = 208.8nm, probe = 278.4nm. In a), contributions due to ionization of the NO monomer have been removed. The solid lines are fits adjusting only amplitudes using a sequential model with time constants of 140fs and 590fs. X, A, I, and P are the cross-correlation, initially excited, intermediate, and product components respectively.

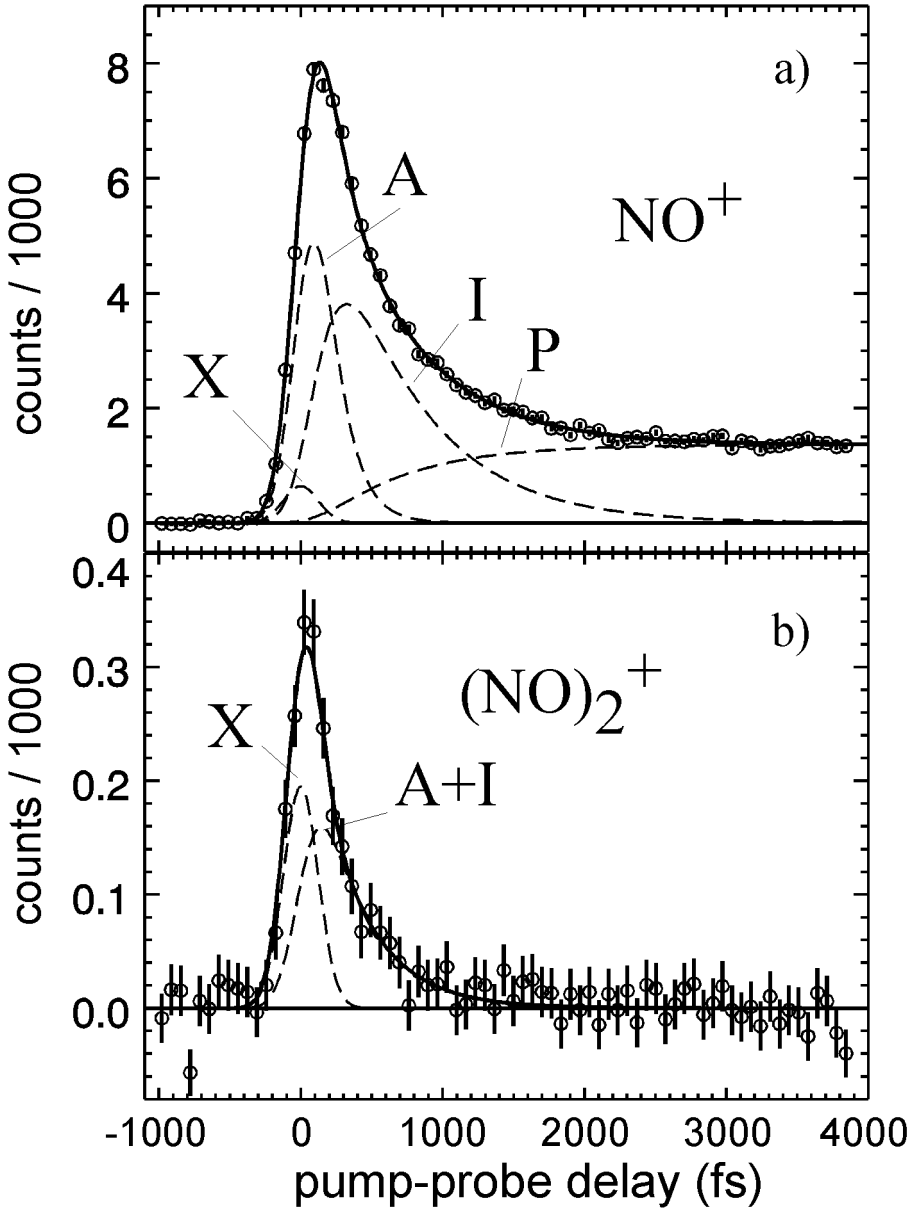

Figure 7.14: Electron-ion energy correlation maps and integrated energy spectra at various pump-probe delay times. The colour map indicates intensity increasing from white to red. Integrated electron and ion kinetic energy spectra are shown beside the axes.

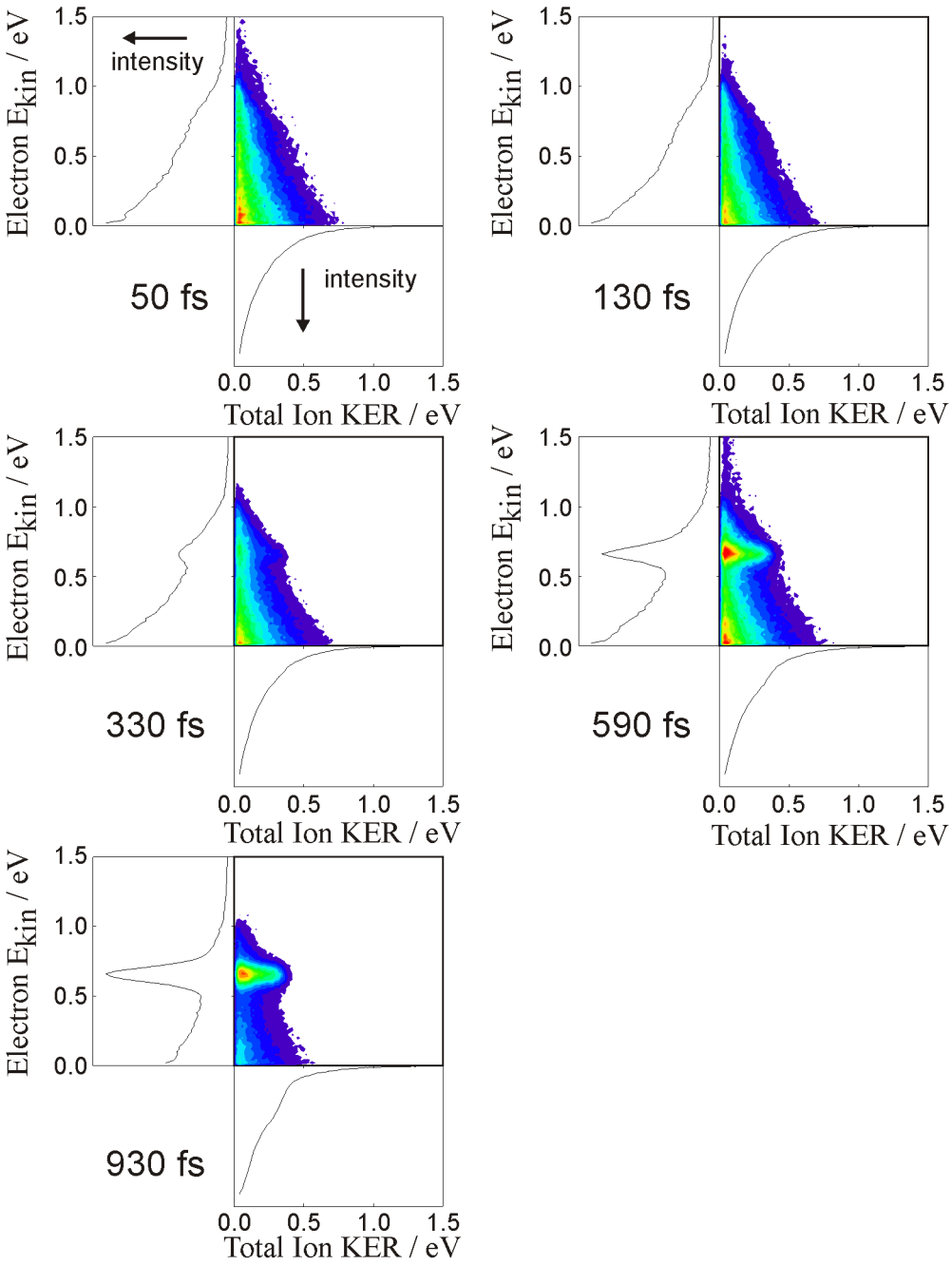

7.4.4 Time Resolved Kinetic Energy Distributions

The overlapping nature of the NO(A) photoelectron peak with the broad distribution of the dissociative ionization photoelectrons (Equation 7.7) obscures the KER spectrum of the ionized NO(A) photoproducts (Equation 7.8). However, separation of the two KER spectra is possible using the following method. Above and below the energy for the NO(A) photoelectron peak, the shape of the ion KER spectrum due to dissociative ionization does not change at different time delays. Thus, the ion KER spectrum due to dissociative ionization under the NO(A) peak is not expected to change shape either. The combined ion KER spectra from the two processes was obtained by integrating the electron kinetic energy between 0.60 and 0.73eV. At 50fs pump probe delay, there is negligible contribution in the ion KER spectrum from ionization of NO(A). Therefore, a scaled replica of this spectrum was subtracted from the ion KER spectra at other time delays. The scaling factor was determined by setting the KER difference spectrum to be zero at KER greater than 0.40eV, the maximum KER for the NO(A) dissociation channel at 208.8nm. Calculated in this way, the difference ion KER spectra are the ones correlated with the NO(X) + NO(A) dissociation channel. These ion KER spectra are shown in Figure 7.15. It is important to note that in this measurement, since dissociation of the dimer occurs before the arrival of the probe pulse, the presented NO(A) ion KER spectra are time-integrations of the product between zero pump probe delay and the times indicated in the figure. The vibrational energy limits for the NO(A) and NO(X) photofragments are shown as vertical dashed lines.

The implications of Figure 7.15 are the following. At all time delays the total

Figure 7.15: Time resolved total ion kinetic energy release of the NO(X) + NO(A) photodissociation channel. Error ranges accounting for statistical and scaling factor errors are indicated with dotted lines. Vibrational energy limits for the photofragments are indicated by vertical dashed lines.

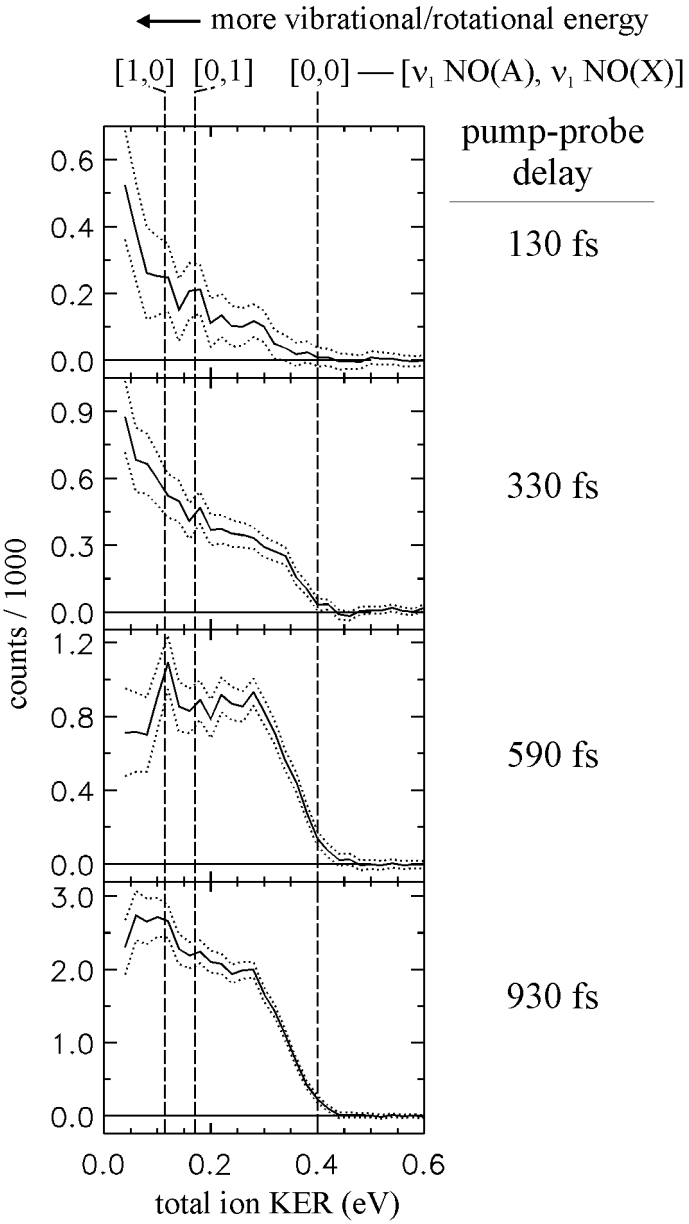

available excess energy is 0.40eV. This corresponds to the difference in energy between the 208.8nm photon and the energies of the NO(X) and NO(A) photoproducts relative to the NO dimer ground state. For all ion KER energies below this limit of 0.40eV, conservation of energy dictates that the remaining energy must be partitioned amongst the internal degrees of freedom, i.e. vibrations and rotations. Low ion KER energies correspond to higher vibrational/rotational excitation and vice versa. At early times, vibrational excitation of the photofragments is prevalent. At later times, more population shifts to the ground vibrational state, but with substantial rotational excitation. Initial excitation of the dimer is mainly in the high frequency NO stretch coordinate and fragmentation is a result of coupling this energy into the inter-monomer coordinate. Products formed at early times have little time to transfer energy to the other modes in the molecule, including the inter-monomer coordinate, and vibrational excitation is retained in the products. Products formed at later times however, have more time to complete the vibrational energy transfer and dissociation leads to less vibrationally excited products. To our knowledge, this is the first direct observation of time-resolved intramolecular vibrational energy redistribution (IVR) using time resolved product state distributions.

7.4.5 Photoelectron and Photofragment Angular Distributions

High resolution studies have looked at the time integrated lab frame (LF) photoelectron angular distributions (PADs) to infer information about the NO dimer photodissociation [107, 109, 94]. More recent studies have looked at the time resolved LF-PADs using femtosecond lasers [110, 111]. It should be stressed that these PADs

are measured *in the lab frame*. The coincidence experiment is also able to measure the LF-PADs. Furthermore, in the axial recoil limit, the recoil frame (RF) PADs can be constructed.

The left side of Figure 7.16 shows the time resolved LF-PADs for the electron kinetic energy range of 0.05-0.50eV corresponding to the dissociative ionization channel. All ion energies were accepted. The laser polarizations, as indicated in the figure, were parallel and define the lab frame axis. The distributions are cylindrically symmetric about lab frame axis. The LF distributions were fit (solid lines) to a Legendre polynomial expansion [118]:

$$I(\theta) \propto \sum_{L_{max}} \beta_L P_L(cos\theta) \tag{7.9}$$

where β_L is the L^{th}-order β parameter, and $P_L(cos\theta)$ is the L^{th}-order Legendre polynomial. Only terms of even L are required to fit the PADs since ionization is equally likely to occur when the electric field is up as when it is down. The distributions were fit to $L_{max} = 4$, as dictated by the nature of the two-photon ionization process [13].

The RF-PADs are shown on the right side of Figure 7.16 for the same energy. To obtain sufficient statistics, NO^+ ions were selected within a $\pm 20^\circ$ cone of the parallel laser polarizations. The emission directions of these ions were defined to be $\theta = 0^\circ$. The directions of the coincidentally detected photoelectrons were histogrammed relative to the ion recoil direction. Selecting the photoelectrons in this way yields cylindrically symmetric PADs about the ion recoil direction (neglecting the small angle between laser polarizations and the ion recoil directions). Since the integrated solid angle for each azimuthally integrated slice scales as $\sin\theta$, the statistics are most favourable around $\theta = 90^\circ$ and least favourable $\theta = 0^\circ$ and $\theta = 180^\circ$. This explains the systematic variation of the error bars from the equator to the poles of the angular

distributions. For RF-PADS, in principle, the value of L_{max} in Equation 7.9 is not predefined by the experiment. However, in practice, contributions of partial waves with very large L_{max} are usually insignificant. Fits of the RF-PADs using Equation 7.9 (solid lines) required the inclusion of terms with $L = 2, 4, 6, 8$. Fits including terms of higher L did not improve the reduced χ^2 value of the fit. The rotational temperature of the molecular beam under these experimental conditions is estimated to be 20K. At this temperature, the average rotation of the dimer about the axes perpendicular to the N-N bond is $\sim 20°$/ps. This does not factor in any slowing of the rotation as the dimer dissociates. Thus, the axial recoil approximation is judged to be valid for this analysis.

Differences between the LF-PADs and RF-PADs are readily apparent. All of the LF-PADs are largely structureless and show little difference across all of the time delays measured. In stark contrast, the RF-PADs show significant structure that varies with time delay. A simple quantitative measure of the change in the RF-PAD structure is shown in Figure 7.17. In this figure, the ratios of PAD intensity at $\theta = 90°$ to the PAD intensity at $\theta = 0°$ are plotted versus the pump-probe delay. The $I(\theta = 90°)/I(\theta = 0°)$ varies between 0.95 and 1.08 for the LF-PADs and between 1.25 and 1.86 for the RF-PADs indicating both the richer structure, and the more obvious time behaviour of the latter.

In the TRPES section, it was argued that all ionization occurs to the ionic electronic ground state. Thus, the changing shape of the RF-PADs is direct evidence of a changing electronic configuration occurring during the NO dimer photodissociation. In Figure 7.17, the population curve of the $(NO)_2^{\dagger}$ intermediate state generated using time constants from the TRPES measurements is overlaid with the RF-PAD intensity

Figure 7.16: Time resolved lab frame (LF) and recoil frame (RF) photoelectron angular distributions (PADs). Electron kinetic energies between 0.05eV and 0.50eV and all ion energies were selected, corresponding to events from the dissociative ionization channel. For the RF-PADs, the recoil direction of the NO^+ fragments is directly downwards. NO^+ ions were selected within a $\pm 20°$ cone of the parallel laser polarizations. The emission directions of these ions were defined to be $\theta = 0°$. The directions of the coincidentally detected photoelectrons are histogrammed relative to the ion recoil direction. The PADs were normalized to the same total flux integrated over all angles. The solid curves are fits to even Legendre polynomial expansions with maximum order $L_{max} = 4$ for the LF-PADs and $L_{max} = 8$ for the RF-PADs.

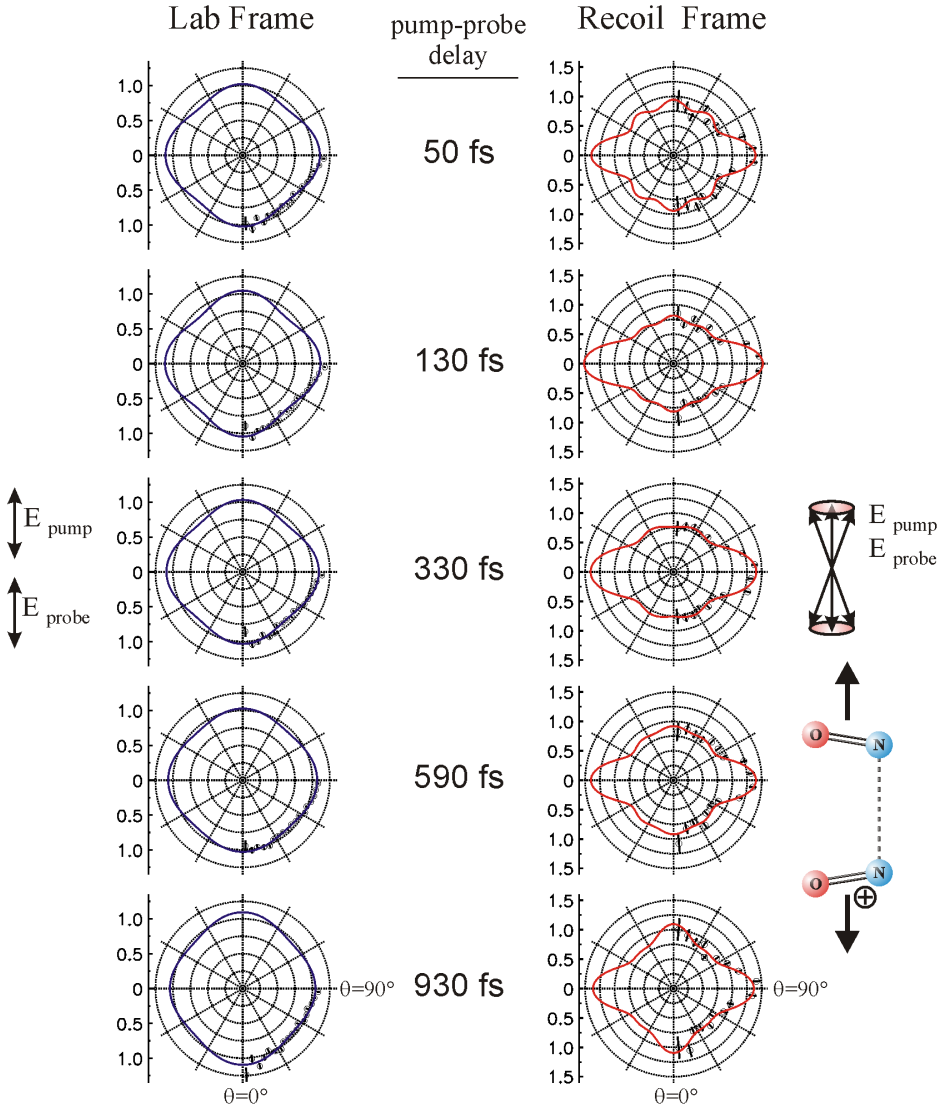

ratio curve. Both curves maximize at approximately the same time, revealing that ionization of the $(NO)_2^{\dagger}$ state leads to a RF-PAD that peaks perpendicular to rather than parallel with the ion recoil and laser polarization vectors.

Figure 7.17: Time dependent ratios of the PAD intensities at $\theta = 90°$ and $\theta = 0°$ shown in Figure 7.16 for the recoil frame (RF, solid), and the lab frame (LF, dotted). The population curve of the $(NO)_2^{\dagger}$ intermediate state using time constants from the TRPES measurements is overlaid (dashed).

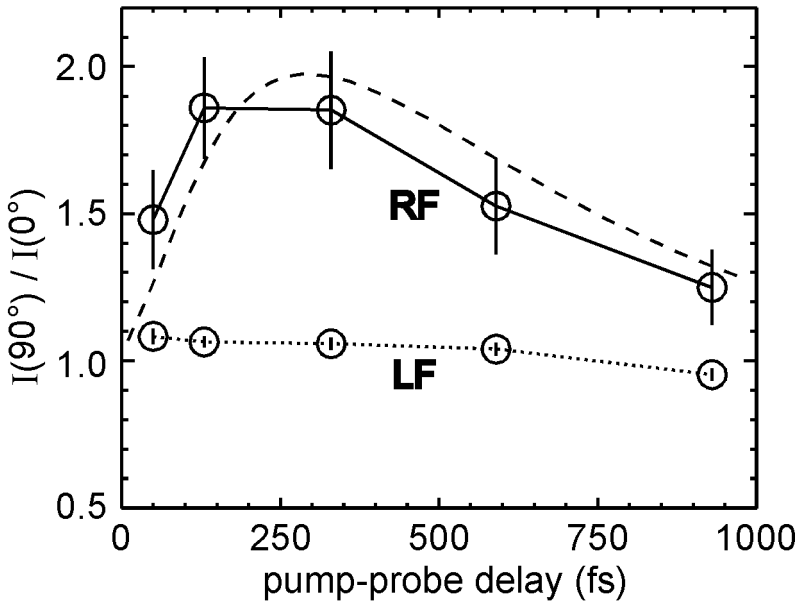

Simple arguments can be used to predict the shapes of the RF-PADs. From arguments presented previously, we assume that the dimer excited states ionize to the totally symmetric closed shell ground state of the monomer cation. For Rydberg states in the absence of core scattering, the RF-PAD is dictated by the selection rule $l = l_0 \pm 1$. If the excited dimer progresses through a 3s type Rydberg state, as suggested by Tsubouchi et al. [112], the RF-PAD should be a p-wave directed along the electric field vector. This is the exact opposite of what we observe in the

RF-PADs presented in Figure 7.16, where most intensity is directed perpendicular to the electric field vector. Therefore, we can rule out significant 3s Rydberg state involvement in the photodissociation dynamics.

Calculations outlined in the following section reveal a state of B_2 symmetry (in the C_{2v} point group) that is initially excited in the NO dimer. The subsequent accessibility of a B_2 symmetry $3p_y$ Rydberg dimer state is also predicted in the same energy region. For ionization of a $3p_y$ orbital, the $\Delta l = \pm 1$ selection rule creates photoelectron distributions with s and d character. Interference between s and d partial wave contributions from atomic-like orbitals can lead to PADs which peak perpendicular to the laser polarization, as was first explained by Cooper and Zare[91]. Based on the perpendicular propensity for ionization quantified in Figure 7.17, we conclude that the intermediate $(NO)_2^{\dagger}$ state is a $3p_y$ Rydberg dimer state. This conclusion is only made possible using the coincidence technique that allows access to the recoil frame PADs.

7.4.6 TRCIS Summary

In summary, using the TRCIS technique, we are able to draw several conclusions about the NO dimer photodissociation. Mass selected photoelectron spectra confirm the large geometry differences between the excited state and the ground and ionic states, and suggest significant N-O stretching excitation in the initially excited state. The time behaviour of the integrated ion transients also agrees with the sequential dissociation model inferred from the TRPES studies. The electron-ion kinetic energy correlation maps allow separation of the ionization channels that result in the formation of NO^+. The lack of any structure or threshold effects in the time resolved spectra

implies that ionization occurs to the ground state of the dimer cation. We are able to separate the time resolved ion KER spectra of the NO(A) neutral dissociation channel from that of the dissociative ionization channel. We find that NO(A) products emitted at early times show higher vibrational excitation than products emitted at later times. To our knowledge, this is the first measurement of time resolved vibrational energy distributions. Time resolved recoil frame photoelectron angular distributions indicate that the electronic nature of the excited NO dimer changes with the same kinetics as the population of the intermediate state. The PAD associated with the maximum intermediate state population has the maximum intensity ratio between electrons emitted perpendicular to the laser polarization, and those emitted parallel. This gives us indications of the symmetries of the excited dimer states that will be discussed in the following sections. Only through the use of the coincidence imaging technique were these measurements possible.

7.5 Electronic Structure of the Excited NO Dimer Intermediates

Collaboration with theoreticians at the University of Southern California and the University of Regina have yielded important results for unraveling the NO dimer photodissociation dynamics [119]. These results are briefly summarized here.

Schematically, the lowest excited NO dimer states can be constructed by combining NO monomers is two different ways: a ground state NO($X^2\Pi$) monomer with a monomer in one of the excited doublet states *A, B, C, D*; or a ground state $NO^+(X^1\Sigma)$ cation with hypothetical electronic states of NO^-. The neutral combinations result in

ER (excimer, exciton-resonance) states, while the charged combinations result in CT (charge-transfer, charge-resonance) states. Calculations were made using complete active space self-consistent field (CASSCF), multireference configuration interaction singles and doubles (MRCISD), and equation-of-motion coupled-cluster (EOM-CC) methods. The most important state responsible for oscillator strength of transitions in the 6eV energy region is the $(\sigma_d^1\sigma_d^{*1})$ CT_1 state, which is of B_2 symmetry. This state mixes with many other states of B_2 symmetry, producing a bright band of states of similar energy. The presence of these states explains the experimentally observed, broad, featureless absorption band of the NO dimer[101].

The lowest-lying state of B_2 symmetry is the $\sigma_d^1 3p_y^1$ $X + A3p_y$ Rydberg state, correlating to NO(X) + NO(A) at large separations. The existence of such a $3p_y$ orbital is easily explained with the aid of Figure 7.18. In the dimer, the NO monomers are quantum mechanically indistinguishable. As the dimer separates, two states are created from in-phase and out-of-phase combinations of the final NO(X) and NO(A) monomer states. The in-phase combination results in a $3s$-type Rydberg orbital of A_1 symmetry, whereas the out-of-phase combination results in the aforementioned $3p_y$-type Rydberg orbital. The direct transition to the $3s$-type Rydberg state is forbidden due to symmetry reasons and must vibronically couple to a B_2 vibration to be somewhat allowed. However, the $3s$-Rydberg state is located located about 0.5eV below the bright CT_1 state and thus can be expected to play little role in the initially excited configuration.

Analysis of the Frank-Condon factors between the ground and excited states suggest that initial excitation populates roughly two to four quanta of energy in the N–O symmetric stretch, and low excitation in the inter-monomer stretch. This is

Figure 7.18: In-phase and out-of-phase MO combinations of the NO(X) and NO(A) photoproducts.

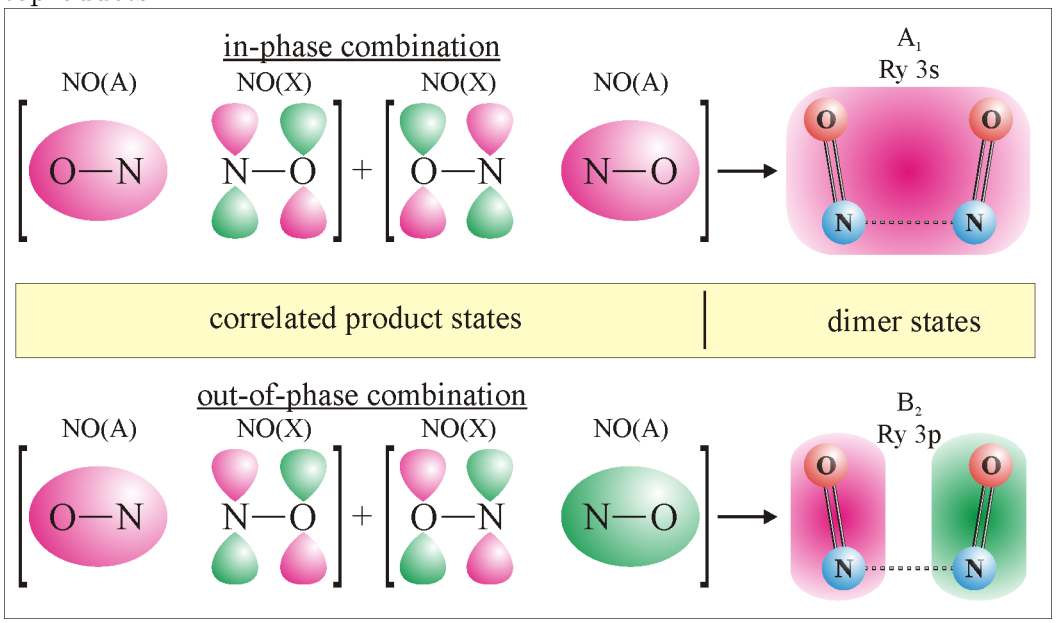

consistent with the time-dependent internal energy distributions presented in Figure 7.15, which show early products still contain a large amount of internal energy. The mixing of the CT_1 and $3p_y$ Rydberg states and their energies are strongly dependent on the N–O (and also N–N) distances within the dimer. Therefore, the excited N–O stretching vibration causes oscillations in the electronic configurations that are CT-like at the maximum r(N–O) turning point, and $3p_y$ Rydberg-like at the minimum r(N–O) turning point. As energy initially deposited into the N–O stretch flows into the ν_3 N-N stretching dissociation coordinate, the electronic configuration becomes less CT-like and more $3p_y$ Rydberg-like.

7.6 Conclusions

Time resolved photoelectron spectroscopy, time resolved coincidence imaging spectroscopy, and *ab initio* calculations were used to unravel the dynamics of the NO dimer photodissociation leading to NO(X) and NO(A) products. The TRPES studies confirmed that the photodissociation occurs via a sequential mechanism $(NO)_2 \xrightarrow{h\nu_{pump}} (NO)_2^* \xrightarrow{\tau_1} (NO)_2^\dagger \xrightarrow{\tau_2} NO(A) + NO(X)$ with time constants determined to be $\tau_1 = 140 \pm 30$fs and $\tau_2 = 590 \pm 20$fs at 209.5nm excitation. Dissociative ionization of the excited states is preferred over ionization to the molecular cation. The lack of structure in the photoelectron spectrum led us to conclude that ionization occurs to the electronic ground state of the cation. The absence of vibrational progressions in the molecular cation photoelectron region suggests that the geometry of the excited state is quite different from that of the neutral and cation ground states.

The TRCIS experiments allowed us to measure mass selected photoelectron spectra, as well as distinguish between NO^+ ions formed by either dissociative ionization or ionization of the NO(A) photoproducts. These types of measurements are only possible using a coincidence measurement method. Vibrational excitement in the N–O stretching coordinate was observed in the excited NO dimer. The TRCIS method also allowed us to measure both lab frame and recoil frame PADs. While the lab frame PADs showed little structure, and little variation with time, the recoil frame PADs showed rich dynamical behaviour. We conclude that these changes are due to changing electronic character of the excited state. *Ab initio* theoretical calculations identified two electronic states of B_2 symmetry, a charge transfer state, responsible for the oscillator strength of the transition, coupled to a $3p_y$ Rydberg state, leading to dissociation of the dimer to NO(X) and NO(A). The changes in the recoil frame

PADs were consistent with ionization of the $3p_y$ Rydberg type state.

We were also able to directly measure time resolved internal energy distributions of the NO(A) photoproducts. Products that are formed at early times have more N–O stretching excitation than products that are formed at later times, which are vibrationally colder. This supports calculations that suggest that photoexcitation initially occurs to states with highly excited N–O stretching vibrations. Dissociation to NO(X) and NO(A) occurs after sufficient time has passed to couple the N–O stretching energy into the inter-monomer stretch.

Chapter 8

Conclusion

Here we have studied the effects of methyl substitution on relaxation rates in the electronically excited α, β-enones acrolein (AC), crotonaldehyde (CR), methylvinylketone (MVK), and methacrolein (MA) using time resolved photoelectron spectroscopy (TR-PES). We observe large differences between the molecules in the relaxation rates from the S_1 surface. The relative relaxation times are: CR $<$ AC $\leq$ MVK $<$ MA. Correlated with the relative relaxation rates in CR and AC is the absence of HCO(X) production in photolysis experiments. Relaxation from the S_1 state is predicted to occur via a conical intersection (CI) with the ground state. The topographies of the S_1/S_0 CI for all of the enones are considerably tilted along the gradient difference vector to approximately the same degree. The geometries of the CI's are also extremely similar, with the terminal methylene carbon twisted by 90° and slightly pyramidalized. Quantitative treatment of the geometrical, energetic, and topographical features of the S_1/S_0 CI's do not indicate any 'structural' differences that might be responsible for the differing relaxation dynamics. We conclude that the differences in relaxation rates between the molecules are due to dynamical factors. Based on

our experimental results, we develop a simple model describing how the nonadiabatic crossing rate through sloped conical intersections is controlled by the relative speeds or frequencies of important motions. Motions that are responsible for reaching the conical intersection geometry, but are not responsible for creating the intersection itself, promote relaxation if they are slow. Conversely, in the coordinates that create the intersection, fast motions promote nonadiabatic crossing. Thus CR has the fastest decay because it has slow motion of the torsional coordinate required to reach the CI, and fast motion through the CI. AC and MVK have slower relaxation rates because they pass by the CI region quickly, not allowing the trajectory to reach the crossing. MA has the slowest decay because like AC and MVK, it passes the CI region quickly. However, MA has an additional hindrance to nonadiabatic decay because it also has a methyl group attached where it slows the motion of one of the intersection coordinates. This study is important because too often only structural parameters are used to predict reaction pathways without consideration of dynamical factors. We hope that this is the first of many studies to explore dynamics occurring near CI's. Just as Polanyi outlined rules for A + BC reactions in his 1972 paper [120], this study begins an exploration to whether a similar set of rules can be developed for nonadiabatic conical intersection dynamics. *Ab initio* calculations employing full dynamical treatments are currently possible for small polyatomics [72] (although still quite computationally taxing), opening new opportunities for combined experimental and computational investigations.

With TRCIS, we hope to develop the emerging field of "femtochemistry from the molecule's point of view". This thesis has outlined the construction of our coincidence imaging spectrometer located at the National Research Council. Coincidence imaging

spectroscopy allows access to measurements not possible using other techniques, such as photoelectron/photoion energy correlation maps, and recoil frame photoelectron angular distributions (RF-PADs). Energy correlation maps allow separation of reaction channels leading to the same products. RF-PADs allow access to the electronic symmetries of the evolving molecular states. We demonstrate the use of TRPES and time resolved coincidence imaging spectroscopy (TRCIS) to elucidate the photodissociation dynamics of the NO dimer at ∼209nm excitation leading to NO(X) and NO(A) products. The TRPES experiments reveal the timescales of the reaction and unequivocally identify the kinetics of the reaction. Theoretical analyses indicate the presence of an optically bright charge transfer state that can couple to a $3p_y$ type Rydberg state. We experimentally observe this state using TRCIS. Additionally, using energy correlation maps, we are able to determine the internal energy, and therefore follow intramolecular vibrational energy redistribution (IVR) in the photofragments. Using this combined TRPES and TRCIS approach, we follow the photodissociation dynamics in unprecedented detail from initial excitation to the final products.

Bibliography

[1] L. R. Khundkar and A. H. Zewail, *Annu. Rev. Phys. Chem.* **41**, 15 (1990).

[2] R. Gonzalez-Luque, M. Garavelli, F. Bernardi, M. Merchan, M. A. Robb, and M. Olivucci, *Proc. Natl. Acad. Sci. USA* **97**, 9379 (2000).

[3] Q. Wang, R. W. Schoenlein, L. A. Peteanu, R. A. Mathies, and C. V. Shank, *Science* **266**, 422 (1994).

[4] T. Schultz, J. Quenneville, B. Levine, A. Toniolo, T. Martinez, S. Lochbrunner, M. Schmitt, J. Shaffer, M. Zgierski, and A. Stolow, *J. Am. Chem. Soc.* **125**, 8098 (2003).

[5] A. Stolow, A. E. Bragg, and D. M. Neumark, *Chem. Rev.* **104**, 1719 (2004).

[6] M. T. Zanni, V. S. Batista, B. J. Greenblatt, W. H. Miller, and D. M. Neumark, *J. Chem. Phys.* **110**, 3748 (1999).

[7] P. Kruit and F. H. Read, *J. Phys. E* **16**, 313 (1983).

[8] A. Stolow, *Annu. Rev. Phys. Chem.* **54**, 89 (2003).

[9] A. E. Bragg, J. R. R. Verlet, A. Kammrath, O. Cheshnovsky, and D. M. Neumark, *Science* **306**, 669 (2004).

[10] R. Mabbs, K. Pichugin, and A. Sanov, *J. Chem. Phys.* **122**, 174305 (2005).

[11] T. Suzuki, *Annu. Rev. Phys. Chem.* **57**, 555 (2006).

[12] T. Seideman, *Annu. Rev. Phys. Chem.* **53**, 41 (2002).

[13] K. L. Reid, *Annu. Rev. Phys. Chem.* **54**, 397 (2003).

[14] R. Schinke, *Photodissociation Dynamics*, Cambridge University Press, 1993.

[15] Z. Xu, B. Koplitz, and C. Wittig, *J. Chem. Phys.* **90**, 2692 (1989).

[16] Y. Huang, Y.-A. Yang, G. He, S. Hashimoto, and R. J. Gordon, *J. Chem. Phys.* **103**, 5476 (1995).

[17] D. J. Gendron and J. W. Hepburn, *J. Chem. Phys.* **109**, 7205 (1998).

[18] G. E. Busch and K. R. Wilson, *J. Chem. Phys.* **56**, 3626 (1972).

[19] R. Vasudev, R. N. Zare, and R. N. Dixon, *J. Chem. Phys.* **80**, 4863 (1984).

[20] X. Yang, J. Lin, Y. T. Lee, D. A. Blank, A. G. Suits, and A. M. Wodtke, *Rev. Sci. Instrum.* **68**, 3317 (1997).

[21] D. W. Chandler and P. L. Houston, *J. Chem. Phys.* **87**, 1445 (1987).

[22] A. J. R. Heck and D. W. Chandler, *Annu. Rev. Phys. Chem.* **46**, 335 (1995).

[23] A. T. J. B. Eppink and D. H. Parker, *Rev. Sci. Instrum.* **68**, 3477 (1997).

[24] C. R. Gebhardt, T. P. Rakitzis, P. C. Samartzis, V. Ladopoulos, and T. N. Kitsopoulos, *Rev. Sci. Instrum.* **72**, 3848 (2001).

[25] D. Townsend, M. P. Minitti, and A. G. Suits, *Rev. Sci. Instrum.* **74**, 2530 (2003).

[26] J. A. Davies, J. E. LeClaire, R. E. Continetti, and C. C. Hayden, *J. Chem. Phys.* **111**, 1 (1999).

[27] R. E. Continetti and C. C. Hayden, *Modern Trends in Chemical Reaction Dynamics: Coincidence Imaging Techniques*, volume 14 of *Advanced Series in Physical Chemistry*, p. 475, World Scientific, 2004.

[28] K. A. Hanold, A. K. Luong, T. G. Clements, and R. E. Continetti, *Rev. Sci. Instrum.* **70**, 2268 (1999).

[29] R. E. Continetti, *Annu. Rev. Phys. Chem.* **52**, 165 (2001).

[30] R. Dorner, V. Mergel, O. Jagutzki, L. Spielberger, J. Ullrich, R. Moshammer, and H. Schmidt-Bocking, *Phys. Rep.* **330**, 96 (2000).

[31] W. Kamke, R. Herrmann, Z. Wang, and I. Hertel, *Z. Phys. D* **10**, 491 (1988).

[32] J. G. Underwood and K. L. Reid, *J. Chem. Phys.* **113**, 1067 (2000).

[33] J. V. Vallerga and O. H. W. Siegmund, *Nucl. Instrum. Methods Phys. Res., Sect. A* **442**, 159 (2000).

[34] O. H. W. Siegmund, M. Lampton, J. Bixler, S. Chakrabarti, J. Vallerga, S. Bowyer, and R. F. Malina, *J. Opt. Soc. Am. A* **3**, 2139 (1986).

[35] F. Bernardi, M. Olivucci, and M. A. Robb, *Pure & Appl. Chem.* **67**, 17 (1995).

[36] M. Ben-Nun and T. J. Martinez, *Chem. Phys.* **259**, 237 (2000).

[37] D. R. Yarkony, *J. Chem. Phys.* **114**, 2601 (2001).

[38] G. J. Atchity, S. S. Xantheas, and K. Ruedenberg, *J. Chem. Phys.* **95**, 1862 (1991).

[39] L. D. Landau, *Phys. Z. Sowjetunion* **2**, 46 (1932).

[40] C. Zener, *Proc. R. Soc.* **A137**, 696 (1932).

[41] M. Reguero, M. Olivucci, F. Bernardi, and M. A. Robb, *J. Amer. Chem. Soc.* **116**, 2103 (1994).

[42] W.-H. Fang, *J. Am. Chem. Soc.* **121**, 8376 (1999).

[43] C. S. Page and M. Olivucci, *J. Comput. Chem.* **24**, 298 (2003).

[44] R. R. Birge and P. A. Leermakers, *J. Amer. Chem. Soc.* **94**, 8105 (1972).

[45] F. Aquilante, V. Berone, and B. O. Roos, *J. Chem. Phys.* **119**, 12323 (2003).

[46] J. C. D. Brand and D. G. Williamson, *Discuss Faraday Soc.* **35**, 184 (1963).

[47] J. M. Hollas, *Spectrochim. Acta* **19**, 1425 (1963).

[48] K. Inuzuka, *Bull. Chem. Soc. Jpn.* **34**, 729 (1961).

[49] G. A. Osborne and D. A. Ramsay, *Can. J. Phys.* **51**, 1170 (1973).

[50] K. W. Paulisse, T. O. Friday, M. L. Graske, and W. F. Polik, *J. Chem. Phys.* **113**, 184 (2000).

[51] R. R. Birge, W. C. Pringle, and P. A. Leermakers, *J. Amer. Chem. Soc.* **93**, 6715 (1971).

[52] H. Shinohara and N. Nishi, *J. Chem. Phys.* **77**, 234 (1982).

[53] M. A. El-Sayed, *J. Chem. Phys.* **38**, 2834 (1963).

[54] G. T. Fujimoto, M. E. Umstead, and M. C. Lin, *J. Chem. Phys.* **82**, 3042 (1985).

[55] B. M. Haas, T. K. M. Minton, P. Felder, and J. R. Huber, *J. Phys. Chem.* **95**, 5149 (1991).

[56] Y.-T. Kao, W.-C. Chen, C.-H. Yu, and I.-C. Chen, *J. Chem. Phys.* **114**, 8964 (2001).

[57] B. F. Parsons, D. E. Szpumar, and L. J. Butler, *J. Chem. Phys.* **117**, 7889 (2002).

[58] J. Shu, D. S. Peterka, S. R. Leone, and M. Ahmed, *J. Phys. Chem. A* **108**, 7895 (2004).

[59] S.-H. Jen and I.-C. Chen, *J. Chem. Phys.* **111**, 8448 (1999).

[60] D. E. Johnstone and J. R. Sodeau, *J. Chem. Soc. Faraday Trans.* **88**, 409 (1992).

[61] J.-C. Loison, S. H. Kable, and P. L. Houston, *J. Chem. Phys.* **94**, 1796 (1991).

[62] A. Fahr, W. Braun, and A. H. Laufer, *J. Phys. Chem.* **97**, 1502 (1993).

[63] J. Pola, Y. Koga, and A. Ouchi, *Tetrahedron* **53**, 3757 (1997).

[64] S. Lochbrunner, J. Larsen, J. Shaffer, M. Schmitt, T. Schultz, J. Underwood, and A. Stolow, *J. Electron Spectrosc. Relat. Phenom.* **112**, 183 (2000).

[65] P. Masclet and G. Mouvier, *J. Electron. Spectrosc. Relat. Phenom.* **14**, 77 (1978).

[66] W.-C. Tam, D. Yee, and C. E. Brion, *J. Electron. Spectrosc. Relat. Phenom.* **4**, 77 (1974).

[67] H. van Dam and A. Oskam, *J. Electron. Spectrosc. Relat. Phenom.* **13**, 273 (1978).

[68] B. O. Roos, *The Complete Active Space Self-Consistent Field Method and its Applications in Electronic Structure Calculations*, p. 399, Advances in Chemical Physics: Ab Initio Methods in Quantum Chemistry II, John Wiley and Sons Ltd., 1987.

[69] K. K. Docken and J. Hinze, *J. Chem. Phys.* **57**, 4928 (1972).

[70] H.-J. Werner, P. J. Knowles, R. Lindh, F. R. Manby, M. Schütz, P. Celani, T. Korona, G. Rauhut, R. D. Amos, A. Bernhardsson, A. Berning, D. L. Cooper, M. J. O. Deegan, A. J. Dobbyn, F. Eckert,

C. Hampel, G. Hetzer, A. W. Lloyd, S. J. McNicholas, W. Meyer, M. E. Mura, A. Nicklass, P. Palmieri, R. Pitzer, U. Schumann, H. Stoll, A. J. Stone, R. Tarroni, and T. Thorsteinsson, MOLPRO, 2002.

[71] J. Quenneville and T. Martinez, *J. Phys. Chem. A* **107**, 829 (2003).

[72] J. D. Coe and T. J. Martinez, *J. Phys. Chem. A* **110**, 618 (2006).

[73] O. Gessner, E. T. H. Chrysostom, A. M. D. Lee, D. M. Wardlaw, M. L. Ho, S. J. Lee, B. M. Cheng, M. Z. Zgierski, I. C. Chen, J. P. Shaffer, C. C. Hayden, and A. Stolow, *Faraday Discuss.* **127**, 193 (2004).

[74] S. Matsika and D. R. Yarkony, *J. Chem. Phys.* **117**, 6907 (2002).

[75] D. Yarkony, *J. Phys. Chem. A* **101**, 4263 (1997).

[76] D. R. Yarkony, *J. Chem. Phys.* **112**, 2111 (2000).

[77] J. Ullrich, R. Moshammer, A. Dorn, R. Dörner, L. P. H. Schmidt, and H. Schmidt-Böcking, *Rep. Prog. Phys.* **66**, 1463 (2003).

[78] W. C. Wiley and I. H. McLaren, *Rev. Sci. Instrum.* **26**, 1150 (1955).

[79] M. Lebech, J. C. Houver, and D. Dowek, *Rev. Sci. Instrum.* **73**, 1866 (2002).

[80] T. Bergmann, T. P. Martin, and H. Schaber, *Rev. Sci. Instrum.* **60**, 792 (1989).

[81] P. Dahl, *Introduction to Electron and Ion Optics*, Academic Press, 1973.

[82] U. Even, J. Jortner, D. Noy, N. Lavie, and C. Cossart-Magos, *J. Chem. Phys.* **112**, 8068 (2000).

[83] I. Ali, R. Dorner, O. Jagutzki, S. Nuttgens, V. Mergel, L. Spielberger, K. Khayyat, T. Vogt, H. Brauning, K. Ullmann, R. Moshammer, J. Ullrich, S. Hagmann, K. O. Groeneveld, C. L. Cocke, and H. Schmidt-Bocking, *Nucl. Instrum. Methods Phys. Res., Sect. B* **149**, 490 (1999).

[84] A. J. Mager, *IEEE Trans. Magnet.* **6**, 67 (1970).

[85] S. M. Freake and T. L. Thorp, *Rev. Sci. Instrum.* **42**, 1411 (1971).

[86] T. J. Sumner, J. M. Pendlebury, and K. F. Smith, *J. Phys. D* **20**, 1095 (1987).

[87] J. A. Dillon and H. E. Farnsworth, *J. Appl. Phys.* **28**, 174 (1957).

[88] P. A. Anderson, *Phys. Rev.* **115**, 553 (1959).

[89] K. Huber and G. Herzberg, *Molecular Spectra and Molecular Structure. IV. Constants of Diatomic Molecules*, Van Nostrand Reinhold Co., 1979.

[90] V. Stert, W. Radloff, C. P. Schulz, and I. V. Hertel, *Eur. Phys. J. D* **5**, 97 (1999).

[91] J. Cooper and R. N. Zare, *J. Chem. Phys.* **48**, 942 (1968).

[92] P. Lambropoulos, *Adv. At. Mol. Phys.* **12**, 87 (1976).

[93] E. Wade, J. Cline, K. Lorenz, C. Hayden, and D. Chandler, *J. Chem. Phys.* **116**, 4755 (2002).

[94] A. B. Potter, V. Dribinski, A. V. Demyanenko, and H. Reisler, *J. Chem. Phys.* **119**, 7197 (2003).

[95] J. Hetzler, M. Casassa, and D. King, *J. Phys. Chem.* **95**, 8086 (1991).

[96] S. G. Kukolich, *J. Mol. Spectrosc.* **98**, 80 (1983).

[97] A. L. L. East, *J. Chem. Phys.* **109**, 2185 (1998).

[98] R. Sayos, R. Valero, J. M. Anglada, and M. Gonzalez, *J. Chem. Phys.* **112**, 6608 (2000).

[99] M. Tobita, S. A. Perera, M. Musial, R. J. Bartlett, M. Nooijen, and J. S. Lee, *J. Chem. Phys.* **119**, 10713 (2003).

[100] V. Dribinski, A. B. Potter, I. Fedorov, and H. Reisler, *Chem. Phys. Lett.* **385**, 233 (2004).

[101] J. Billingsley and A. B. Callear, *Trans. Faraday Soc.* **67**, 589 (1971).

[102] E. Forte and H. Vandenbergh, *Chem. Phys.* **30**, 325 (1978).

[103] H. Reisler, private communication.

[104] O. Kajimoto, K. Honma, and T. Kobayashi, *J. Phys. Chem.* **89**, 2725 (1985).

[105] Y. Naitoh, Y. Fujimura, F. Honma, and O. Kajimoto, *Chem. Phys. Lett.* **190**, 135 (1992).

[106] Y. Naitoh, Y. Fujimura, F. Honma, and O. Kajimoto, *Chem. Phys. Lett.* **205**, 423 (1993).

[107] Y. Naitoh, Y. Fujimura, F. Honma, and O. Kajimoto, *J. Phys. Chem.* **99**, 13652 (1995).

[108] V. Blanchet and A. Stolow, *J. Chem. Phys.* **108**, 4371 (1998).

[109] A. V. Demyanenko, A. B. Potter, V. Dribinski, and H. Reisler, *J. Chem. Phys.* **117**, 2568 (2002).

[110] M. Tsubouchi, C. A. de Lange, and T. Suzuki, *J. Chem. Phys.* **119**, 11728 (2003).

[111] M. Tsubouchi and T. Suzuki, *Chem. Phys. Lett.* **382**, 418 (2003).

[112] M. Tsubouchi, C. A. de Lange, and T. Suzuki, *J. Electron Spectrosc. Relat. Phenom.* **142**, 193 (2005).

[113] B. Urban, A. Strobel, and V. E. Bondybey, *J. Chem. Phys.* **111**, 8939 (1999).

[114] V. Dribinski, A. B. Potter, I. Fedorov, and H. Reisler, *J. Chem. Phys.* **121**, 12353 (2004).

[115] V. Blanchet, M. Z. Zgierski, T. Seideman, and A. Stolow, *Nature* **401**, 52 (1999).

[116] I. Fischer, A. Strobel, J. Staecker, G. Niednerschatteburg, K. Muller-Dethlefs, and V. E. Bondybey, *J. Chem. Phys.* **96**, 7171 (1992).

[117] F. Carnovale, J. B. Peel, and R. G. Rothwell, *J. Chem. Phys.* **84**, 6526 (1986).

[118] S. N. Dixit and P. Lambropoulos, *Phys. Rev. A* **27**, 861 (1983).

[119] S. Levchenko, H. Reisler, A. Krylov, O. Gessner, A. Stolow, H. Shi, and A. East, *J. Chem. Phys.* **125**, 84301 (2006).

[120] J. C. Polanyi, *Acc. Chem. Res.* , 161 (1972).

[121] J. V. Vallerga and J. B. McPhate, Optimization of the readout electronics for microchannel plate delay line anodes, in *Proceedings of the SPIE*, edited by S. Fineschi, C. M. Korendyke, O. H. W. Siegmund, and B. E. Woodgate, volume 4139, pp. 34–42, SPIE, 2000.

Appendix A

Spectrometer Materials

Table A.1: Vacuum compatible materials used in the CIS spectrometer.

Spectrometer Materials		
Material	Composition(%)	Usage
SS316L (A4SS)	C 0.03 max [1] Cr 16 - 18 Fe Balance Mn 2 Mo 2-3 Ni 10-14 P 0.045 max Si 1 max S 0.03 max	- least magnetic SS - most corrosion resistant SS
SS304 (A2SS)	C 0.08 max [1] Cr 18 - 20 Fe balance Mn 2 max Ni 8-10.5 P 0.045 max Si 1 max S 0.03 max	-common 'non-magnetic' SS -very corrosion resistant -also called 18-8 Stainless Steel
⋮	⋮	⋮

Table A.1: (continued)

Spectrometer Materials		
Material	Composition(%)	Usage
AA 6061-T6	Al 97.9 [2] Si 0.60 Cu 0.28 Mg 1.0 Cr 0.20	-high strength aluminum alloy -no zinc content -non-magnetic: used for spectrometer electrodes
CuBe (UNS17200)	Cu 98.1 [3] Be 1.9	- expansion coefficient almost the same as pure copper - used for copper grid mounts
PEEK 30% glass-filled	PolyEther-EtherKetone	- vacuum compatible polymer - glass fiber reinforcement imparts higher stiffness than unfilled. - high dielectric breakdown strength: used as machinable insulating material
Kapton	Polyimide	- high dielectric breakdown strength film: used as insulating film between plates of high voltage
Ceramic	alumina	- use as high voltage insulators: coated with germanium to eliminate surface charging and produce uniform field drop
PTFE	PolyTetra-FluoroEthylene	- machinable plastic.

[1] from www.suppliersonline.com
[2] from www.efunda.com
[3] from www.copper.org

Appendix B

Constant Fraction Discriminator Tuning

B.1 Choosing the Fraction and Delay

The fraction (F) of a CFD is usually defined as the amplitude of the prompt pulse divided by the amplitude of the delayed pulse. Choosing the ideal fraction to give the best timing characteristics depends on the input pulse shape. The fraction analysis which follows is taken from a paper by Vallerga and McPhate[121] .

The difference voltage between the comparator inputs is described by the function $G(t)$

$$G(t) = FV(t) - V(t - t_0) \tag{B.1}$$

where F is the fraction, $V(t)$ is the input pulse, and $V(t - t_0)$ is the input pulse delayed by time t_0. The CFD produces an output logic pulse when G(t) crosses zero.

The error in the crossing time σ_t is caused by voltage noise σ_G at the crossing time T

$$\sigma_t = \frac{\sigma_G}{dG/dt|_T} \tag{B.2}$$

Assuming that the voltage noise at time t, $\sigma_{V(t)}$, is the same as at time $t-t_0$, $\sigma_{V(t-t_0)}$, the error in G is

$$\sigma_G^2 = \left(\frac{dG}{dV(t)}\right)^2 \sigma_{V(t)}^2 + \left(\frac{dG}{dV(t-t_0)}\right)^2 \sigma_{V(t-t_0)}^2 \tag{B.3}$$

$$\sigma_G = \sigma_{V(t)}(F^2+1)^{\frac{1}{2}} \tag{B.4}$$

The derivative of $G(t)$ with respect to time is simply

$$\frac{dG}{dt} = F\frac{dV(t)}{dt} - \frac{dV(t-t_0)}{dt} \tag{B.5}$$

Combining the above equations gives the expression for the error in the crossing time as

$$\sigma_t = \frac{\sigma_{V(t)}(F^2+1)^{\frac{1}{2}}}{F\frac{dV(t)}{dt} - \frac{dV(t-t_0)}{dt}} \tag{B.6}$$

The condition for the optimum value of F can be found by setting the derivative of σ_t with respect to F to be zero and rearranging to give

$$F = -\left(\frac{\left.\frac{dV(t)}{dt}\right|_T}{\left.\frac{dV(t-t_0)}{dt}\right|_T}\right) \tag{B.7}$$

Both derivatives must be taken at the crossing time T. Unfortunately, Equation B.7 is not as helpful as we would like, because the crossing time T is unknown until the delay t_0 is chosen. However, the optimum delay is not known a priori for an arbitrary pulse $V(t)$ so further analysis is required.

B.1.1 Symmetric pulses

For symmetric pulses the slope of the leading edge of $V(t-t_0)$ is always equal to the slope of the trailing edge of $V(t)$, regardless of the delay time chosen. Equation B.7 shows that the optimal fraction is 1. Now that F is known, examination of Equation B.6 shows that the optimum delay time should be chosen such that $V(t)$ and $V(t-t_0)$ cross when their slopes have the largest difference (ie. the maximum absolute slopes). The choice of the correct delay is readily apparent in Figure B.1, where the timing jitter for different external delays are shown. The vertical extent on the prompt (dark blue) and delayed (light blue) pulses represents noise. The pink regions are the regions where the pulses overlap. CFD output is triggered inside the dashed circled region. The timing jitter is the horizontal extent of the triggering region. The timing jitter is minimized when the external delay is approximately half of the total pulse width. For Gaussian shaped pulses, the optimal delay is 85% of the full width half maximum (FWHM) of the pulse.

Figure B.1: Noise timing jitter for symmetric pulses when the external cable delay is (a) optimal, (b) too short, (c) too long. The CFD triggers when the two curves cross within the dashed circle.

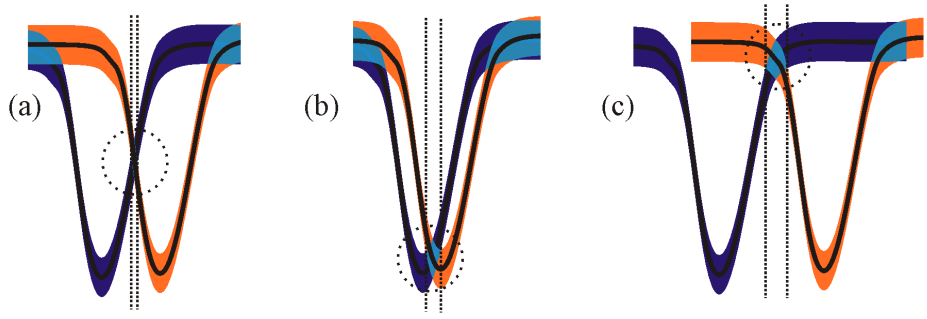

B.1.2 Nonsymmetric pulses

It is difficult to find the absolute optimal delay and fraction for nonsymmetric pulses. Fortunately, a large range of fractions and delays usually gives errors within 1% of each other. The approach that I have found useful is the following:

1. Find the time of maximum slope on the leading edge t_L, and trailing edge t_T, of the pulse to be measured.

2. Calculate the fraction needed to make the maximum slopes cross. $F = V(t_L)/V(t_T)$. (Remember it is the leading edge of the delayed pulse and the trailing edge of the prompt pulse that cross)

3. The delay needed is $t_0 = t_T - t_L$.

4. Calculate the crossing time error σ_t from Equation B.6.

5. Calculate the fraction via Equation B.7. If this fraction matches the fraction calculated in step 2, then you have the optimal fraction and delay. Most likely, they are not consistent so a slightly different F and t_0 are needed. If this is necessary, try adjusting the fraction small amounts, readjusting the delay, and calculating the timing error again. The goal is to minimize timing error.

In general, pulses with fast leading edges and slow trailing edges should have $F < 1$, while pulses with slow leading edges and fast trailing edges should have $F > 1$.

B.2 Walk and Threshold Adjustments

To realize the CFD electronically, two more adjustable parameters must be introduced: the walk and threshold adjustments. The threshold adjustment sets the minimum pulse height necessary to trigger the CFD output. The threshold is typically set just above the noise level of the input.

When the CFD is not receiving input, a small voltage must be applied across the inputs of the zero crossing comparator (ZCC) so that its output does not oscillate. This adjustable voltage is commonly called the walk adjustment. The adjustment of the walk voltage is critical to obtain optimal timing characteristics of the CFD. Ideally, the walk should be as small as possible to retain optimal timing characteristics. However, the walk must be greater than the noise level so that the comparator output does not fluctuate wildly creating spurious triggers.

The walk may be slightly positive or slightly negative. It may be advantageous to choose one polarity over the other to ease in crossing the maximum slopes on the leading and trailing edges of the prompt and delayed input pulses (see previous section). For negative input pulses, large positive walk settings should be avoided to prevent triggering of the prompt pulse with the baseline ahead of the delayed pulse. Figure B.2 depicts various walk settings for a negative input pulse with 100% amplitude variation. Case (a) shows an optimally set walk voltage. Case (b) and (c) show too large walk settings. In the improperly adjusted cases (b) and (c), the timing jitter, indicated between the vertical bars, is larger than the optimal case (a).

Figure B.2: Discrimination timing for input pulses with varying amplitudes (black, red, green, blue, violet corresponding to 50, 75, 100, 125, 150% amplitude respectively) for various walk/delay settings. The output times for the extreme amplitudes are shown with vertical dashed lines. (a) Ideal walk setting. (b) walk setting negative and too large. (c) walk setting positive and too large. In the improperly adjusted cases (b) and (c), the timing jitter indicated between the vertical bars, is larger than the optimal case (a).

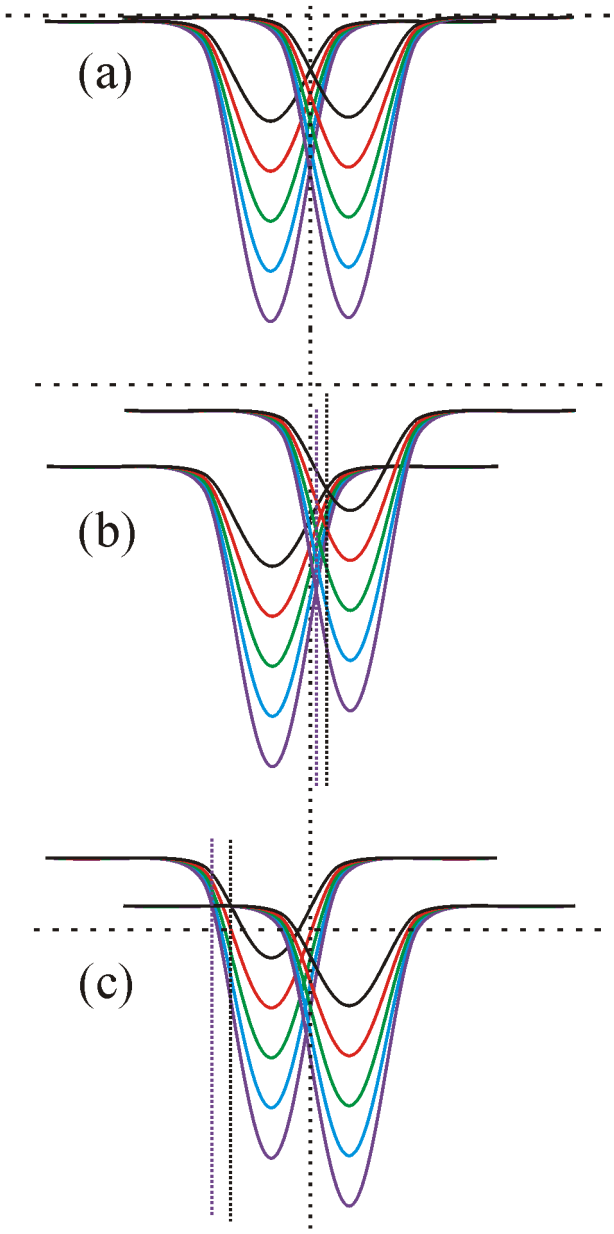

B.3 Electronic Implementation : The Tennelec 454 CFD

B.3.1 CFD Triggering

This and the following sections describe how the technique of constant fraction discrimination is implemented in the commercially available Tennelec/Canberra 454 (T454) CFD. Other implementations, including that found inside the Sensor Sciences DSTDC, are similar. An abbreviated schematic of the Tennelec 454 CFD is shown in Scheme B.1. Refer to the Tennelec manual schematic for a complete diagram.

The operation of the CFD is as follows. A negative input pulse is applied to both the threshold crossing comparator (TCC) and the fraction module. If the input received at the TCC is greater than the threshold voltage at TP2 (which should be the front test point voltage T divided by ten), an ECL pulse is produced which is used to gate the threshold gate (TG). The ECL gate pulse is only produced while the input pulse is greater than the threshold voltage.

Inside the fraction module, the input pulse is split and proper input termination is ensured. One part of the pulse is sent to the zero crossing comparator (ZCC) directly. The other part is routed through an external delay cable and into the other input of the ZCC. The walk adjustment (Z) quiescently keeps the ZCC inverted output HIGH. When the delayed pulse is greater than the prompt pulse, the ZCC output switches state and produces a leading edge which is timed with the zero crossing. This timing edge can only pass through the TG if it coincides with the gate pulse produced by the TCC.

The timing edge is used as the clock signal (CE-bar) for a D-type flip-flop (IC 3)

for which the data input (D) is held high. Thus, the leading edge at Q is carefully timed and passed to the output driving electronics. Q-bar is used to trigger the output width electronics that after a delay set by the front panel W pot, resets the flip-flop via RO.

Scheme B.1: Abbreviated schematic of the Tennelec 454 CFD

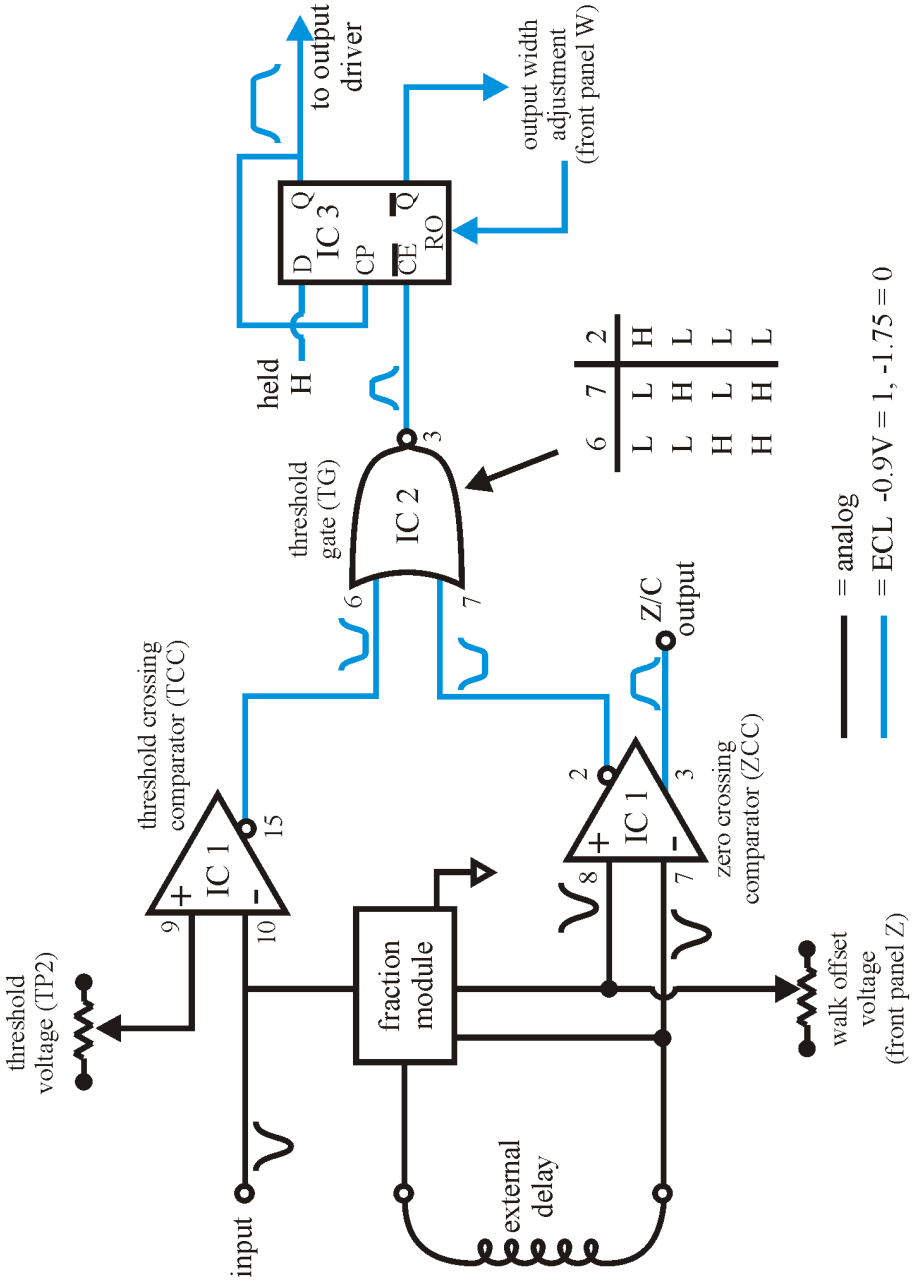

B.3.2 Choosing the Fraction

Inside the T454, the input pulse is split into two at pins 4 and 5 of the Fraction Module (FM). The prompt pulse goes into the non-inverting input of a fast comparator IC1 pin 8 (the Zero-Crossing Comparator, ZCC). The delayed pulse is routed through the external delay cable and into the inverting input of the ZCC, IC1 pin 7. The Fraction Module is schematically illustrated in Scheme B.2.

Scheme B.2: The Tennelec 454 Fraction Module. If $R1 = R2 = R3 = R4 = 50\Omega$, it will have an input impedance of 50Ω and $F = 1$.

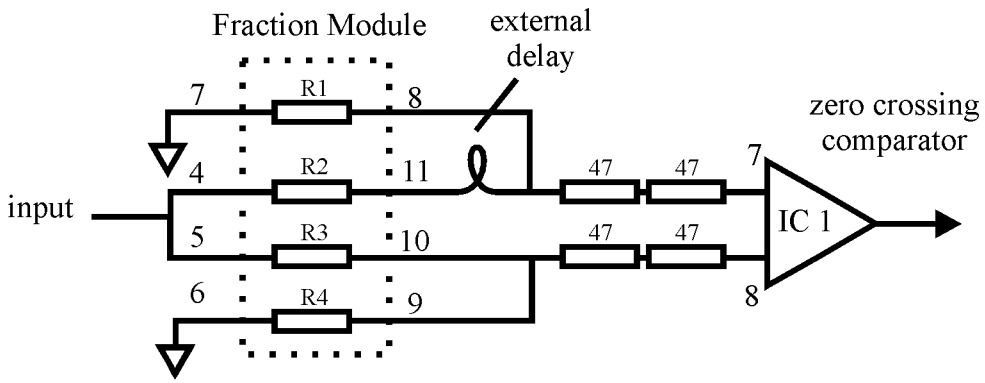

Both the fraction, F and the input impedance of the CFD are determined by the fraction module. The fraction, F is

$$F = \frac{\left(\frac{R4}{R3+R4}\right)}{\left(\frac{R1}{R1+R2}\right)} \tag{B.8}$$

The input impedance R_{in} is

$$\frac{1}{R_{in}} = \frac{1}{R1+R2} + \frac{1}{R3+R4} \tag{B.9}$$

Once F and R_{in} have been chosen, two free variables remain. If $R1$ and $R4$ are

chosen, then

$$R2 = R_{in}\left(\frac{R1}{R4}F + 1\right) - R1 \tag{B.10}$$

$$R3 = R_{in}\left(\frac{R4}{R1}\frac{1}{F} + 1\right) - R4 \tag{B.11}$$

If R2 and R3 are chosen, then

$$R1 = R2\left(\frac{\frac{1}{R_{in}} - \frac{1}{R3} - \frac{1}{R2}}{\frac{1}{R3}(1-F) - \frac{1}{R_{in}}}\right) \tag{B.12}$$

$$R4 = R3\left(\frac{\frac{1}{R_{in}} - \frac{1}{R3} - \frac{1}{R2}}{\frac{1}{R2}(1-\frac{1}{F}) - \frac{1}{R_{in}}}\right) \tag{B.13}$$

B.3.3 Choosing the External Delay Length

Tennelec specifies the internal delay within the T454 to be 600ps. However, module-to-module variations have revealed this to be 450-600ps. This internal delay must be subtracted from the overall delay to obtain the length of cable needed for the external delay.

B.3.4 Adjusting the Walk Compensation (Z)

A simplified version of the walk (or zero crossing adjustment) circuit inside the T454 is shown in Scheme B.3. The voltage measured at the front panel Z test point is the DC bias voltage seen at the ZCC pin 8. The bias voltage seen at the ZCC pin 7 depends on the driving device because the walk biasing contains the signal input line. If the DC output impedance of the driving signal is very high, then the ZCC pin 7 sees one-third of the voltage that pin 8 sees. If the driving output impedance is lower, the voltage at pin 7 is less than one-third that at pin 8. This stresses the importance of measuring or adjusting the walk voltage with the input connected.

Scheme B.3: The Tennelec 454 walk circuit.

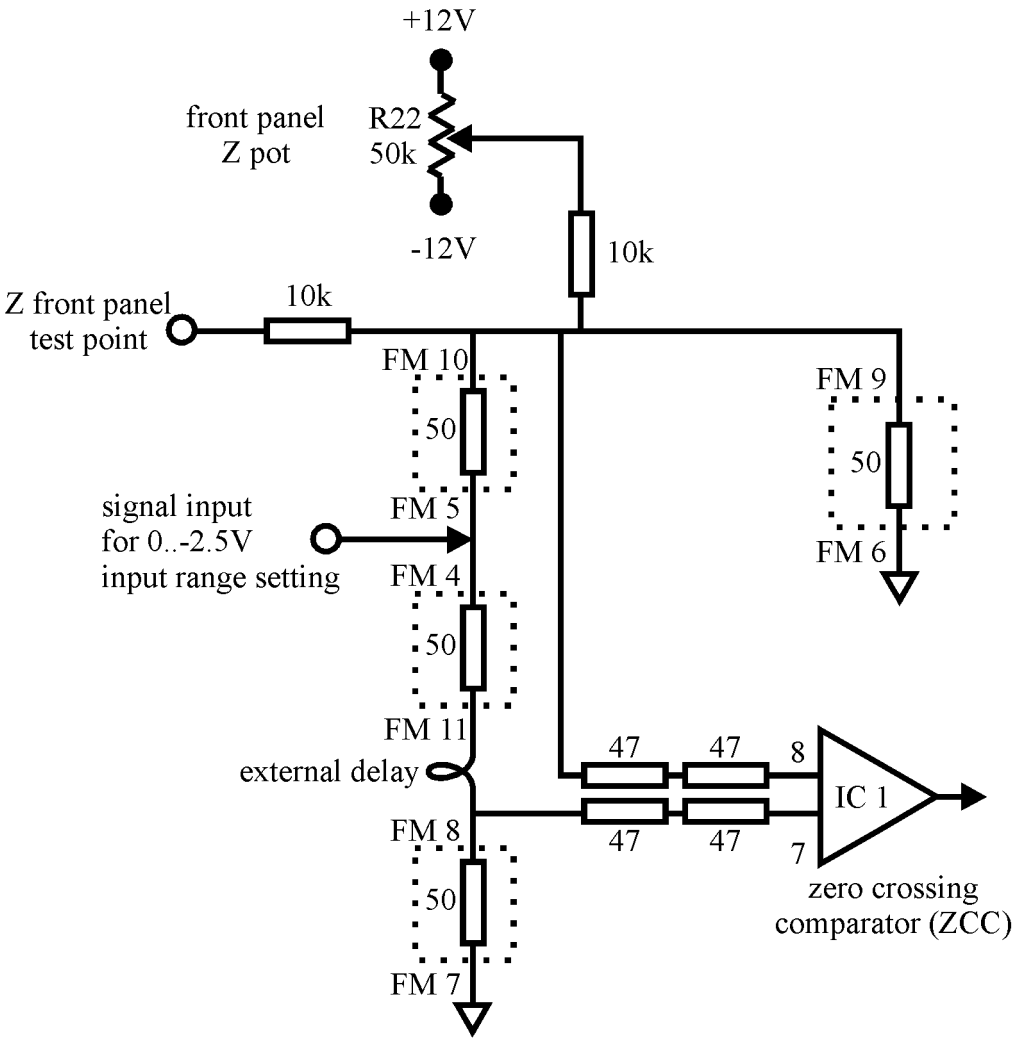

B.3.5 Threshold Adjustment

In the T454, the threshold can be measured directly at TP2 or at the front panel test point (T) which is 10 times greater than the actual voltage at the comparator. As shown in Scheme B.1, the TCC produces a gate pulse when input pulses exceed the threshold voltage. This signal gates the timing signal received from the ZCC. Ideally this part of the circuit should block all pulses with magnitude smaller than the threshold voltage, and let through all pulses with magnitude larger than the threshold voltage. In the T454, while it is true that all pulses smaller than the threshold will be blocked, pulses larger than threshold might not trigger output. When the CFD walk and external delay settings are adjusted correctly, and the input pulse is much larger than the threshold voltage, the CFD behaves correctly (Scheme B.4, Case 1) When the input pulse is small compared to the threshold voltage, the CFD fails to trigger because the gate signal from the TCC closes before the zero crossing occurs.

To alleviate this problem, an extra delay cable (threshold delay) was added between the input and the TCC to delay the gate signal. Practically this is most easily done by first removing R14 from the component side of the board. A length of coaxial cable can be soldered to this resistor and replaced resulting in the cable being between R14 and R68 . The coaxial shield can be grounded via TP2GND and the grounded side of C2.

Another solution suggested by John Vallerga is to add a 39pF capacitor between the TCC input (IC1, pin10) and ground. In this manner, the input signal's high frequencies are attenuated prior to entering the TCC, thus slowing the rise and fall time of the threshold gate pulse and allowing the zero crossing to occur before the gate closes. Unfortunately, the overall signal pulse is attenuated, so the sensitivity

of the TCC is reduced, so small pulses are lost. Thus the chosen capacitor value is extremely critical. Too large capacitance and the input signal is attenuated too much, and too small capacitance and the gate closes before the zero crossing occurs.

When testing, unless unwanted signals overwhelm the CFD, it is best to set the threshold potentiometer to the minimum level so that the walk voltage and delay cable can be adjusted first. After the walk voltage and delay cable length has been optimized, the threshold can be set.

B.4 Summary

In order to adjust a CFD for optimal operation, the following steps should be taken:

1. Choose fraction (F) and external delay: fast leading edge, slow trailing edge - F<1; symmetrical pulse - F=1; slow leading edge, fast trailing edge - F>1.

2. Set the walk (Z) to a small negative or positive voltage. If a constant timing source is available, check on scope that minimum jitter is found.

3. Set Threshold to eliminate unwanted small signals.

4. Iterate all steps adjusting parameters slowly to achieve best resolution.

Achieving optimal resolution requires an extensive amount of time and patience. It is important to realize what resolution is necessary prior to starting CFD tuning to avoid wasting time when other factors in an experiment can limit the resolution more drastically.

Scheme B.4: Timing diagram showing the arrival of the zero crossing edge and the threshold gate signal at the threshold gate. See text for discussion.